UNIVERSITY OF CALIFRONIA
RIVERSIDE

Effect of Support Acidity and Cu Surface Structure on Cu Surface Site Quantification and Non-Oxidative Ethanol Dehydrogenation

A Dissertation submitted in partial satisfaction
of the requirements for the degree of

Doctor of Philosophy

in

Chemical and Environmental Engineering

by

Sergei P. Hanukovich

June 2019

Dissertation Committee:
Dr. Phillip Christopher, Chairperson
Dr. Ian Wheeldon
Dr. Lorenzo Mangolini

The Dissertation of Sergei P. Hanukovich is approved:

_____

_____

_____

Committee Chairperson

University of California, Riverside

ACKNOWLEDGEMENTS

I must first acknowledge advisor, Dr. Phillip Christopher, for not only giving me the opportunity to be a part of his lab, but also guiding me through a rigorous PhD program that has helped me grow dramatically as a researcher. I also appreciate him giving me a level of trust and independence in my work that helped me optimize my growth and prepare me for any of my future endeavors. The last thing that may be taken for granted or overlooked but is not a given for all advisors is Phil's combination of high expectations for my abilities, but also treating me as a human being and being supportive even when results were slow or stagnant. I would also like to thank Dr. Ian Wheeldon and Dr. Lorenzo Mangolini for being a part of my committee and being willing to drive out to Santa Barbara for my defense, which I am very grateful for.

I would also like to thank past and present members of the Christopher lab, specifically the first generation students, Matt Kale and John Matsubu, who were always willing to answer my too many questions, taught me many skills that have been vital to my completing of this dissertation, and always challenged me to work better and more independently. I would also like to thank Talin Avanesian, who although didn't work with me in lab, was a genuine friend who I still talk to today. Additionally, although our paths didn't last long, I want to acknowledge Yibo Jiang for being a very kind person and a pleasure to work with. I will also extend a big shout out to Leo Derita with whom I spent 3 years of long days and nights working in lab and the office, trying to figure out how to make sense of our research and results. With respect to the present members, I would like to thank Insoo Ro for not only being a helping hand, but also providing me with a critical

voice that has helped me improve my research in itself as well as lab skills. I would also like to extend an acknowledgement to all other group members, Chithra Asokan, Ji Qi, Joaquin Resasco. Bhogesh Seemara, Andy Therrien for helping me out in different ways along the way. Finally, it wouldn't be fair if I didn't acknowledge Alan Dang, a UCSB 3rd year undergraduate, who worked with me for over a year, helping me with my research and developing laboratory skills and a critical eye that have aided me with my research. His phenomenal work earned him the role of a 2nd author in the paper published (Hanukovich, S., Dang, A., Christopher, P., *ACS Catal.*,**2019**, *9*, 3537-3550), as shown in Chapter 4.

I would also like to acknowledge the many people along the way who played a role, in part, to help me develop a healthy (~ish) work-life balance through different extracurricular actives. This includes Tyler Lopez who was my gym partner for over a year and really challenged me to improve my strength, techniques, and self-expectations. Also, Leo Derita, who organized soccer scrimmages and games that were many times the highlights of my weeks in addition to watching soccer and playing Fifa together. Additionally, previously mentioned John Matsubu, started out as a senior student in the lab who helped in lab and has now turned into a friend outside of the research group who has helped me immensely throughout grad school, particularly while in Santa Barbara, by just being an overall good friend.

Finally, I could not have done this without my huge, self-labelled, extensive family including my girlfriend Lorette, my mom, my sister, my father and my many other loved ones who I will explicitly call out in the dedication below.

DEDICATIONS

This dissertation, and everything I do, is dedicated to my family including my mother Marina, my sister Xenya, and my father Pavel

And to my extended family of parents and siblings that includes my stepfather, J.J. McKenna, brother Kenneth Woodard and my beautiful Goddaughter Amora, my brother Luis Mukul and his family (Janet, Matthew, Melissa, Simon Jr. and a second mother to me, Irma), my brother Hugo Morel and his family (Isais and my second set of parents, Hugo Sr. and Juliette), my brother William "Will BElieve" Gross, my mentor and second mother Sally Matsuishi and her family (Miya, Rob, Beverly, Ed), my brother Corey Christian, my brother Eddy Gramajo and his fiancé Vanessa, and many others

And finally, a special dedication to Maria Mikell and Vyacheslav "Slava" who believed in me when no one else would. May you both Rest in Paradise

Everything I am and have done, I owe to you all

ABSTRACT OF THE DISSERTATION

Effect of Support Acidity and Cu Surface Structure on Cu Surface Site Quantification and Non-Oxidative Ethanol Dehydrogenation

by

Sergei P. Hanukovich

Doctor of Philosophy, Graduate Program in Chemical and Environmental Engineering
University of California, Riverside, June 2019
Dr. Phillip Christopher, Chairperson

In this dissertation, we have utilized a multi-faceted approach, combining carefully controlled synthesis techniques, qualitative and quantitative surface characterization, as well as rigorous reaction kinetics techniques to elucidate key insights for heterogeneous catalytic processes involving Cu catalysts. Specific focus was placed on developing a comprehensive analysis of the current state-of-the-art Cu surface characterization technique as well as studying the impact of Cu-support interfacial effects on the reaction activity and mechanism of ethanol dehydrogenation.

For Cu surface characterization, the widely accepted assumption that N_2O titration of Cu at mild temperatures only oxidizes metallic Cu to Cu^+ lead to significant overestimation of Cu particle dispersion due to the over-oxidation of Cu sites to Cu^{2+}. As expected, with increasing oxidation temperature, the extent of over-oxidation (relative

concentration of Cu^{2+} sites) increased. This trend was most prominent on smaller Cu particles which were composed mainly of under-coordinated sites. On the other hand, the larger particles, which were more difficult to oxidize required larger oxidation temperatures compared to smaller particles to induce complete titration of the Cu surface. This highlights the difficulty in predicting an optimal N_2O oxidation temperature, as it is Cu particle size dependent. In response to this, a novel technique was proposed, in which NO chemisorption is used to exclusively probe the quantity of Cu^{2+} sites generated after oxidation, as a means of correcting the initial dispersion estimates.

For the second part of this dissertation, it was demonstrated that metal oxide supports with strong Lewis acid sites promoted ethanol dehydrogenation activity over Cu by not only modifying interfacial Cu sites, but also by potentially facilitating the initiation of the reaction mechanism. The results in this work provide a potential bridge to explain the discrepancy in literature about the rate limiting step for ethanol dehydrogenation, but also elucidated the role of support acid sites, specifically at the metal-support interface, in promoting reaction rates. This study may work as a model system for carefully using reaction kinetics to determine the reaction active site, rate limiting step, and corresponding mechanism for future studies of small nanoparticles loaded on active metal oxide supports.

Table of Contents

ABSTRACT OF THE DISSERTATION vii
Chapter 1. Introduction 1
1.1 Summary 1
1.2 Importance of Catalysis on the Global Scale 2
1.3 Fundamentals of Heterogeneous Catalysis 3
1.4 Importance of Cu Catalysts 5
1.5 Importance of Metal Oxide Supports 6
1.5.1 Metal Oxide Support Acid Site Chemistry 6
1.5.2 Metal Oxide Support Base Site Chemistry 8
1.5.3 Cooperative Effects of Acid-Base Pairs 9
1.5.4 Metal Doping to Modify Support Acidity 12
1.5.5 Support Site Poisoning by Ambient Environment 15
1.5.6 Impact of Support Surface Intermediates 16
1.6 Cooperativity Between Cu Catalysts and Their Corresponding Metal Oxide Support 17
1.6.1 Particle Size Effects on Catalyst Activity 18
1.6.2 Support Effects on Catalyst Activity 20
1.7 Optimizing Cu Surface Area Characterization 21
1.8 Conclusions 24
1.9 Dissertation Summary 25
1.10 References 28
Chapter 2. Materials and Experimental Methods 34
2.1 Summary 34
2.2 Materials 34
2.2.1 Gases 34
2.2.2 Chemicals 34
2.2.3 Tools 35
2.2.4 Analytical Instruments 35
2.3 Synthesis Techniques 36
2.3.1 Precursor Impregnation 36

2.3.1.1 Incipient Wetness “Dry” Impregnation 36
2.3.1.2 Wet Impregnation 36
2.3.2 Colloidal Cu Synthesis 37
2.3.3 Galvanic Replacement 38
2.4 Characterization Techniques 38
2.4.1 Site Quantification through Surface Chemisorption and Surface Reactions 38
2.4.1.1 Probe Molecule Pulse Chemisorption 38
2.4.1.2 N_2O – TPR for Cu Surface Characterization 40
2.4.1.3 Probe Molecule Temperature Programmed Desorption 42
2.4.2 BET Surface Area Approximation 42
2.4.3 Diffuse Reflectance Infrared Fourier Transform Spectroscopy (DRIFTS) 43
2.4.3.1 Principles and Design 43
2.4.3.2 CO Probe Molecule IR Spectroscopy 44
2.4.3.3 Pyridine and CO_2 Probe Molecule IR Spectroscopy 45
2.4.4 Transmission Electron Microscopy (TEM) 46
2.4.5 X-Ray Absorption Spectroscopy (XAS) 47
2.4.6 X-Ray Powder Diffraction (XRD) 48
2.4.7 Inductively Coupled Plasma-Absorption Emission Spectroscopy (ICP-AES) 48
2.5 Catalyst Activity and Reaction Kinetics 49
2.5.1 Reactor Design and Automation 49
2.5.2 Reactor System Schematic 50
2.5.3 Analytical Instrumentation – Gas Chromatography 52
2.5.4 Mass and Heat Transfer Limitations and Differential Reactor Regime 54
2.5.5 Differential Reactor and Calculating Reaction Rates 55
2.5.6 Catalyst reactivity, activity, and turn over frequency (TOF) 56
2.5.7 Temperature Dependent Reaction Activity 58
2.5.8 Partial Pressure Dependent Reaction Activity 59
2.5.8.1 Fitting Pressure Dependent Activity to Reaction Mechanism 61
2.6 References 62
Chapter 3. Rigorous Surface Characterization of Supported Cu Catalysts 64
3.1 Summary 64

3.2 Introduction 65
3.3 Materials and Methods 69
3.3.1 Synthesis of Cu catalysts over ZrO_2, TiO_2, and γ-Al_2O_3 69
3.3.2 Cu Particle Dispersion Estimates 69
3.3.2.1 N_2O Titration followed by TPR 69
3.3.2.2 Cryogenic CO TPD 70
3.3.2.3 Cryogenic CO and NO Pulse Chemisorption 71
3.3.3 *In situ* probe molecule IR characterization 71
3.3.3.1 CO and NO probe molecule IR to probe Cu surface structure 72
3.4 Results 73
3.4.1 Comparing dispersion estimates with N_2O-TPR and CO-TPD 73
3.4.2 Identifying and differentiating Cu^+ and Cu^{2+} sites 75
3.4.3 Cu overoxidation as a function of particle size and N_2O temperature 77
3.4.4 NO as a Probe Molecule 81
3.5 Discussion 82
3.6 Work to be completed 87
3.7 Conclusion 88
3.8 References 89
Chapter 4. The Influence of Metal Oxide Support Acid Sites on Cu Catalyzed Non-Oxidative Dehydrogenation of Ethanol to Acetaldehyde 92
4.1 Summary 92
4.2 Introduction 93
4.3 Materials and Methods 97
4.3.1 Synthesis of Cu Catalysts over ZrO_2 and TiO_2 97
4.3.2 Synthesis of Cu Catalyst over Al-ZrO2 97
4.3.3 Cu Dispersion Estimates 98
4.3.4 BET Surface Area 100
4.3.5 X-Ray Diffraction (XRD) 100
4.3.6 Transmission Electron Microscopy (TEM) 100
4.3.7 In-situ IR Probe Molecule Characterization 100
4.3.7.1 Pyridine probe molecule IR to probe surface acidity 101

4.3.7.2 CO probe molecule IR to probe Cu surface structure 102
4.3.8 Steady state ethanol dehydrogenation kinetics 102
4.3.8.1 Ethanol dehydrogenation as a function of temperature 104
4.3.8.2 Ethanol dehydrogenation as a function of ethanol and pyridine pressure 104
4.4 Results 105
4.4.1 Catalyst Characterization 105
4.4.2 The influence of support acidity on ethanol dehydrogenation kinetics 116
4.4.3 Ethanol dehydrogenation dependence on Cu particle size 121
4.4.4 Effect of ethanol partial pressure on ethanol dehydrogenation 124
4.5 Discussion 128
4.6 Conclusion 138
4.7 References 140
Chapter 5. The Effect of Support Acid Sites on the Mechanism for Ethyl Acetate Conversion 147
5.1 Summary 147
5.2 Introduction 147
5.3 Materials and Methods 151
5.3.1 Preparation of Metal Oxide Supports 151
5.3.2 BET Surface Area 151
5.3.3 CO_2 and NH_3 Temperature Programmed Desorption 151
5.3.4 In-situ CO_2 and Pyridine Probe Molecule IR Characterization 152
5.3.5 Steady state ethyl acetate conversion kinetics 153
5.3.5.1 Ethyl acetate conversion as a function of temperature 154
5.3.5.2 Ethyl acetate conversion as a function of EA and H_2O pressure 155
5.4 Results 156
5.4.1 Metal oxide support selection through characterization 156
5.4.2 Effect of support acid and base sites on ethyl acetate conversion 159
5.4.3 Effect of H_2O partial pressure on ethyl acetate conversion 161
5.4.4 Effect of Na dopant on catalyst activity for ethyl acetate conversion 165
5.5 Discussion 167
5.6 Conclusion 169

5.7 References 171
Chapter 6. Conclusions and Future Outlook 174
6.1 Summary 174
6.2 General Conclusions 174
6.3 Outlook on Future Work 176
6.4 Choice of active metals for ethyl acetate hydrogenolysis 177
6.5 Completed work for Pt-Cu single atom alloys 179
6.5.1 Pt-Cu single atom alloy synthesis 179
6.5.2 Pt-Cu single atom alloy characterization 180
6.5.2.1 Inductively coupled plasma 180
6.5.2.2 Probe molecule CO FTIR 181
6.5.2.3 X-ray absorption spectroscopy 183
6.6 Future outlook for Pt-Cu single atom alloys 188
6.7 References 190
Appendix 192
A.1 Reaction Mechanism Derivation (C-H Abstraction as RLS) 192
A.2 Reaction Mechanism Derivation (O-H Abstraction as RLS) 194

List of Figures

Figure 1.1 Schematic of a potential energy plot with uncatalyzed (black) and catalyzed (red) pathways for reactant A and B conversion to product C. The catalyzed process is shown to have multiple reaction steps with $E_{A,1}$ and $E_{A,2}$ corresponding to the activation barriers for steps 1 and 2, respectively. Note $E_{A,1}$ and $E_{A,2}$ are lower in energy than E_A. 4

Figure 1.2 (a) DFT calculations of a γ-Al_2O_3 (110) surface with most relevant sites quoted as Al_n, which corresponds to aluminum atoms surrounded by *n* oxygen atoms and (b) a schematic representation of pyridine adsorption to Lewis acidic metal (M) centers. Reprinted from ref 27 with permission from Elsevier. 7

Figure 1.3 Schematic of carbonates bound to the support surface basic sites in different configurations that correspond to different basic site strengths. 9

Figure 1.4 Scheme of ethanol dehydrogenation to acetaldehyde catalyzed by acid-base pairs on a metal oxide support with a generic label of "M" for the Lewis acidic metal center and "O" for oxygen sites that act as Lewis bases.[26] 10

Figure 1.5 Scheme of initial steps of aldol condensation reaction for acetaldehyde over acid-base pairs on a metal oxide support with a generic label of "M" for the Lewis acidic metal center and "O" for oxygen sites that act as Lewis bases.[26] 11

Figure 1.6. DFT calculations of Zn-doped La_2O_3 (001) showing the effects of the dopant on its local oxygen neighbors making them more reactive and better at dissociating methane. Reprinted with permission from ref 34. Copyright 2013 American Chemical Society. 14

Figure Calculated fraction of sites (surface, perimeter, and corner) and reaction molar turn over frequency (TOF) as a function of particle diameter. Reprinted with permission from ref 56. Copyright 2013 Science AAAS. 20

Figure 1.8 Fraction (f) of under-coordinated (red) and perimeter (blue) sites as a function of metal particle size (d). Reprinted with permission from ref 60. Copyright 2018 American Chemical Society. 21

Figure 2.1 CO Pulse Chemisorption for 0.5 wt% Pt on γ-Al_2O_3. TCD signal as a function of experiment time where ~0.5 cm3 of CO was pulsed every 5 minutes onto Pt standard catalyst. TCD peaks correspond to CO in the effluent that did not adsorb to Pt catalyst. 40

Figure 2.2 Schematic representation of a manual 4-way valve when using a liquid bubbler for FTIR experiments where in orientation **a)** the inlet gas bypasses the bubbler and flows directly into the Harrick reactor and in orientation **b)** the inlet gas flows into the bubbler, bubbles the liquid at its saturation pressure, and carries the vaporized liquid into the Harrick reactor. The two orientations are induced by manually rotating a 4-way valve 90°. 46

Figure 2.3 Home-built reactor apparatus diagram with fully automated, computer-controlled, mass flow controllers (Python), solenoid valves (Python), reactor temperature (Omega CN7800), syringe pump (LabView), and gas chromatograph (SRIGC, Peaksimple). Note that dotted lines correspond to a secondary pathway from the 3-way solenoid valves that effectively bypass the liquid bubbler + sink configuration... 51

Figure 2.4 Home-built wiring system diagram of an Arduino Uno controlled relay that automated 3-way actuated solenoid valves in the reactor system (Figure 2.3) using python code. 52

Figure 2.5 GC spectrum of effluent during ethyl acetate conversion over γ-Al_2O_3 at 340 °C. Each peak corresponds to different products in the effluent: 1-carbon dioxide, 2-ethylene, 3-acetaldehyde, 4-ethanol, 5-ether, and 6-ethyl acetate. The primary axis corresponds to the GC signal of all peaks as a function of column retention time. The secondary axis corresponds to the GC oven temperature at each retention time. 53

Figure 2.6 Reaction rate ($-r_A''$) as a function of inlet gas flow (U) and particle diameter (d_p). It is observed that in the reaction limited regime, rate is independent of U and d_p while in the diffusion limited regime, rate is dependent on either U or d_p or both parameters. Ref 25, ©2016. Reprinted by permission of Pearson Education, Inc., New York, New York. 55

Figure 2.7 Activities of different supported transition metals as a function of the reaction energy for dissociative CO chemisorption. Note that more negative adsorption energies correspond to stronger CO surface adsorption while more positive adsorption energies correspond to weaker CO surface adsorption. Reprinted from ref 27 with permission from Elsevier..... 57

Figure 3.1 A carton schematic of a 3-4 nm Cu particle loaded on ZrO_2 after oxidation by N_2O where Cu is only oxidized to Cu^+ sites, forming a Cu_2O surface layer (Homogeneous Cu_2O Surface), where Cu perimtere sites are overoxidized to Cu^{2+} (CuO at Metal-Support Interface), and where all under-coordinated Cu sites are overoxidized to Cu^{2+} (CuO at Under-Coordinated Sites). 68

Figure 3.2 Cu surface area estimate for 5 wt% Cu/γ-Al_2O_3 with a) N_2O-TPR after 50, 90, and 130 °C N_2O oxidation and b) cryogenic CO-TPD from -120 to 50 °C. For both methods the supported Cu catalyst was pre-treated with 450 °C oxidation followed by 400 °C reduction..... 74

Figure 3.3 Cu surface site estimation for 1 wt% Cu loaded on TiO_2 with a) N_2O-TPR after 90, 125, and 150 °C N_2O oxidation and b) cryogenic CO-TPD from -120 to 50 °C. Further qualitative characterization was performed with c) in situ IR spectra of CO adsorbed at -120 °C and at saturation coverage on 1 wt% Cu/TiO_2. For all methods the supported Cu catalyst was pre-treated with 450 °C oxidation followed by 250 °C reduction. 75

Figure 3.4 In situ IR spectra of a) CO and b) NO adsorbed at -120 °C and at saturation coverage on 1 wt% Cu/ZrO_2 after purging catalyst under Ar at 150 °C for 30 minutes. Note that (b) NO-IR spectra were recorded immediately after (a) CO-IR spectra without changing catalyst bed. 77

Figure 3.5 Probe molecule CO-IR at -120 °C for a) 1 wt% Cu loaded on ZrO_2, c) 2.5 wt% Cu loaded on ZrO_2, and e) 5 wt% Cu loaded on ZrO_2 with varying N_2O oxidation pre-treatments (50 °C, 90 °C, 130 °C) and TPR spectra for b) 1 wt% Cu loaded on ZrO_2, d) 2.5 wt% Cu loaded on ZrO_2 and f) 5 wt% Cu loaded on ZrO_2. Note that all catalysts were reduced at 400 °C for 1 hour prior to exposure to N_2O..... 79

Figure 3.6 Cu surface site estimation for 1 wt% Cu ZrO_2 using cryogenic CO-TPD from -120 to 50 °C with a 10 °C min^{-1} ramp rate. For all methods the supported Cu catalyst was pre-treated with 450 °C oxidation followed by 250 °C reduction..... 81

Figure 3.7 In situ spectra of CO and NO adsorbed at -125 °C and at saturation coverage on 2.5 wt% Cu/ZrO_2 with a) frequency range characteristic of carbonyl and nitrosyl adsorption to Cu and b) frequency range characteristic of nitrate and nitrite surface species. Spectra as a function of increasing temperature are shown within both frequency ranges. Note, the catalyst was only purged with inert Ar at 150 °C to degas the catalyst bed. 82

Figure 4.1 TPR-N_2O with varying temperatures for Cu loaded on ZrO_2. **a)** 1 wt% Cu/ZrO_2, **b)** 1 wt% Cu/ZrO_2[a] (calcined at 350 °C rather than 450 °C), **c)** 2.5 wt% Cu/ZrO_2, **d)** 4.8 wt% Cu/ZrO_2, and **e)** 9.2 wt% Cu/ZrO_2. All catalysts were pre-treated by 450 °C oxidation followed by 400 °C reduction. The results following 90 °C oxidation, including dispersion and particle size estimates, are summarized in Table 4.2. 99

Figure 4.2 External Mass Transfer Effects. Ethanol dehydrogenation rates at 230 °C and 71.5 mbar ethanol as a function of the square root of the superficial velocity. 1 wt% Cu loaded on TiO_2 (Ti) and ZrO_2 (Zr) showed rates that were independent of the superficial velocity in the range of 100 to 300 cm^3 min^{-1}. A superficial velocity of 200 cm^3 min^{-1} was chosen for all kinetic experiments. 103

Figure 4.3 XRD diffractograms of **a)** bare ZrO_2, **b)** 1 wt% Cu loaded on ZrO_2, and **c)** 1 wt% Cu loaded on 0.675Al-ZrO_2. All spectra show that ZrO_2 is in the monoclicic (m) phase. 106

Figure 4.4 In situ IR spectra of pyridine adsorbed at 50 °C and at saturation coverage on **a)** 1 wt% Cu/ZrO_2 pre-treated by 450 °C oxidation followed by 400 °C reduction, **b)** 1 wt% Cu/0.675Al-ZrO_2 pre-treated by 400 °C reduction, and **c)** 1 wt% Cu/0.675Al-ZrO_2 pre-treated in-situ by 450 °C oxidation followed by 400°C reduction. 107

Figure 4.5 In situ IR spectra of pyridine adsorbed at 50°C and at saturation coverage on 1 wt% Cu loaded on ZrO2 pre-treated by **a)** 450 °C oxidation followed by 400 °C reduction and **b)** 400 °C reduction. 1 wt% Cu loaded on TiO2 pre-treated by **c)** 450 °C oxidation followed by 400 °C reduction and **d)** 400 °C reduction. 1 wt% Cu loaded on 0.675Al-ZrO2 pre-treated by **e)** 450 °C oxidation followed by 400 °C reduction and f) 400 °C reduction..... 109

Figure 4.6 In situ IR spectra of pyridine adsorbed at 50°C and at saturation coverage on γ-Al_2O_3 pre-treated by 450 °C oxidation followed by 400 °C reduction. 109

Figure 4.7 In situ IR spectra of pyridine adsorbed at 50°C and at saturation coverage on **a)** ZrO_2 (Zr), **b)** 0.075 wt% Al on ZrO_2, **c)** 0.225 wt% Al on ZrO_2, and **d)** 0.675 wt% Al on ZrO_2. All supports were pre-treated by 450 °C oxidation followed by 400 °C reduction. 110

Figure 4.8 Temperature programmed reduction following N_2O oxidation with varying temperatures (90, 125, and 150 °C) for **a)** 1 wt% Cu/0.025Al-ZrO_2, **b)** 1 wt% Cu/0.225Al-ZrO_2, and **c)** 1 wt% Cu/0.675Al-ZrO_2. All catalysts were pre-treated by 450 °C oxidation followed by 400 °C reduction. The results following 90 °C oxidation, including dispersion and particle size estimates, are summarized in Table 4.2. 112

Figure 4.9 Temperature programmed reduction following N_2O oxidation with varying temperatures (90, 125, and 150 °C) for 1 wt% Cu/TiO_2 pre-treated by 450 °C oxidation followed by 250 °C reduction. The results following 90 °C oxidation, including dispersion and particle size estimates, are summarized in Table 4.2. 112

Figure 4.10 Temperature programmed reduction following N_2O oxidation with varying temperatures (90, 125, and 150 °C) for **a)** 0.5 wt% Cu/0.675Al-ZrO_2, **b)** 1 wt% Cu/0.675Al-ZrO_2[b] (synthesized with wet-impregnation rather than incipient wetness impregnation), **c)** 2.5 wt% Cu/0.675Al-ZrO_2, and **d)** 5 wt% Cu/0.675Al-ZrO_2. All catalysts were pre-treated by 450 °C oxidation followed by 400 °C reduction. The results following 90 °C oxidation, including dispersion and particle size estimates, are summarized in Table 4.2. 113

Figure 4.11 IR spectra of CO adsorbed at -130 °C and at saturation coverage on **a)** 1 wt% Cu loaded on ZrO_2 (Zr) pre-treated in-situ by 450 °C oxidation followed by 400 °C reduction and **b)** 1 wt% Cu loaded on 0.675Al-ZrO_2 pre-treated in-situ by 450 °C oxidation followed by 400 °C reduction. 114

Figure 4.12. a) HAADF STEM image of a cluster of 1 wt% Cu loaded on ZrO_2 and b) EDS mapping of Cu (green) on ZrO_2. EDS mapping of Cu was employed to qualitatively show that Cu was well dispersed on the ZrO_2 surface. c) and d) HR-TEM images of 1 wt% Cu loaded on ZrO_2 on two different particle clusters. Red circles are used as a guide to see ~5nm particles with cuboctahedra or round particle shapes. 115

Figure 4.13 Ethanol turn over frequency (TOF) at 71.5 mbar ethanol as a function of temperature (from 160 to 210 °C) for **a)** 1 wt% Cu on ZrO_2 (Zr), TiO_2 (Ti), and 0.675Al-ZrO_2 and **b)** 1 wt% Cu loaded ZrO_2 with varying Al weight loadings. All catalysts were pre-treated in-situ by 450 °C oxidation followed by 400 °C reduction. 118

Figure 4.14 Ethanol TOF at 71.5 mbar ethanol over 1 wt% Cu/0.675Al-ZrO_2 as a function of temperature for varying in-situ pre-treatments consisting of 450 °C, 150 °C, 50 °C in O_2, and no oxidative pre-treatment, followed by reduction at 400 °C in H_2. 120

Figure 4.15 Ethanol turn over frequency (TOF) for 1 wt% Cu loaded on TiO_2 as a function of temperature for varying in-situ pre-treatments consisting of 450 °C, 150 °C, 50 °C oxidation, and 450 °C treatment in He, all followed by reduction at 400 °C. 121

Figure 4.16 Ethanol TOF at 200 °C and 71.5 mbar ethanol over Cu loaded on ZrO_2 (Zr) and 0.675Al-ZrO_2 as a function of 1/dispersion (~ Cu particle size). The dotted lines show the linear trend to data with corresponding slopes displayed. All catalysts were pre-treated in-situ by 450 °C oxidation followed by 400 °C reduction. 123

Figure 4.17 Ethanol turn over frequency (TOF) as a function of temperature ranging from 160 to 230 °C with 71.5 mbar ethanol feed on **a)** Cu with various dispersions (18 to 76%) loaded on ZrO_2 (Zr), pre-treated by 450 °C oxidation followed by 400 °C reduction, and **b)** Cu with various dispersions (22 to 73%) loaded on 0.675Al-ZrO_2 pre-treated by 450 °C oxidation followed by 400 °C reduction..... 124

Figure 4.18 a) Ethanol TOF at 210 °C as a function of ethanol partial pressure. Primary axis for 1 wt% Cu loaded on 0.675Al-ZrO_2 and TiO_2 (Ti) and secondary axis for 1 wt% Cu loaded on ZrO_2 (Zr). **b)** Ethanol TOF at 210 °C as a function of pyridine partial pressure with a cofeed of 45.5 mbar ethanol. **c)** Ethanol TOF at 210 °C as a function of ethanol partial pressure with a cofeed of 11.7 mbar pyridine. All catalysts were pre-treated in-situ by 450 °C oxidation followed by 400 °C reduction. 127

Figure 4.19 Ethanol dehydrogenation reaction rate on 1 wt% Cu loaded 0.675Al-ZrO_2 as a function of time on stream at 210 °C and with an inlet flow of 45.5 mbar of ethanol. At 480 minutes (8 hours), 11.7 mbar of pyridine was cofed onto the catalyst with 45.5 mbar of ethanol for 2 hours (until 600 minutes). Rates dropped by a factor of 12 and remained constant until the pyridine flow was shut off and dehydrogenation rates returned to their original values, correcting for catalyst deactivation independent of pyridine. 127

Figure 4.20 In-situ IR spectra of CO adsorbed at -130 °C and at saturation coverage on **a)** 1 wt% Cu loaded on 0.675Al-ZrO_2 pre-treated by 400 °C reduction and **b)** on 1 wt% Cu loaded on TiO_2 pre-treated by 450 °C oxidation followed by 400 °C reduction. 129

Figure 4.21 Ethanol turn over frequency (TOF) predicted by a best fit to equation 4.1 plotted against the corresponding experimental ethanol TOF for 1 wt% Cu loaded on ZrO_2 (Zr), TiO_2 (Ti), and 0.675Al-ZrO_2 on a) a parity plot where unity corresponds to goodness of fit and on b) Figure 4.18a showing ethanol TOF as a function of ethanol pressure..... 133

Figure 4.22 Ethanol turn over frequency (TOF) predicted by a best fit to equation 4.2 plotted against the corresponding experimental ethanol TOF for 1 wt% Cu loaded on ZrO_2 (Zr), TiO_2 (Ti), and 0.675Al-ZrO_2 on **a)** a parity plot where unity corresponds to goodness of fit and on **b)** Figure 4.18a showing ethanol TOF as a function of ethanol pressure..... 133

Figure 4.23 Ethanol TOF for 1 wt% Cu over ZrO_2 (Zr), TiO_2 (Ti), and 0.675Al-ZrO_2 predicted from equation 4.1 (C_α-H cleavage as RLS) and equation 4.2 (O-H cleavage as RLS) from microkinetic model of Scheme 4.1 compared to experimental TOF. Inset shows the corresponding TOF comparison for Cu-Zr. Dashed parity lines included as a reference..... 137

Figure 4.24 Ethanol turn over frequency (TOF) predicted by a best fit to equation 4.1 ($\geq$ 45.5 mbar ethanol) and equation 4.2 (< 45.5 mbar ethanol) plotted against the corresponding experimental TOF for 1 wt% Cu loaded on ZrO_2 (Zr), TiO_2 (Ti), and 0.675Al-ZrO_2 on Figure 4.18 (a) showing ethanol TOF as a function of ethanol pressure..... 137

Figure 5.1 External Mass Transfer Effects. Ethyl acetate conversion rates at 340 °C and 40 mbar ethyl acetate as a function of the square root of the superficial velocity in volumetric rate of $cm^3\ min^{-1}$. MgO, ZrO_2, and γ-Al_2O_3 showed rates that were independent of the superficial velocity in the range of 50 to 200 $cm^3\ min^{-1}$. A superficial velocity of 50 $cm^3\ min^{-1}$ was chosen for all kinetic experiments..... 154

Figure 5.2 Temperature programmed desorption studies using a) CO_2 and b) NH_3 as probe molecules that were adsorbed at 50 °C and at saturation coverage. Following adsorption, catalysts were purged in Ar gas while ramping the catalyst temperature from 50 to 450 °C at 10 °C min^{-1}. Note, catalysts were pre-treated with 450 °C oxidation followed by 400 °C reduction..... 156

Figure 5.3 IR spectra of a) CO_2 and b) pyridine adsorbed at 50 °C and at saturation coverage on MgO, γ-Al_2O_3, and ZrO_2 pre-treated in-situ by 450 °C oxidation followed by 400 °C reduction. For a) CO_2 IR, cb, u,

and bb correspond to chelating bidentate, unidentate, and bridging bidentate carbonates, respectively. For b) pyridine IR, zones 1, 2, and 3 correspond to strong, moderate, and weak acid sites, respectively. 159

Figure 5.4 Ethyl acetate conversion rates normalized per catalyst surface area (from BET measurements) at 40 mbar ethyl acetate as a function of temperature from 290 to360 °C for **a)** MgO, **b)** γ-Al_2O_3, and **c**) ZrO_2. All catalysts were pre-treated in-situ by 450 °C oxidation followed by 400 °C reduction. 161

Figure 5.5 Ethyl acetate conversion rates at 340 °C (360 °C for MgO) as a function of water partial pressure with ethyl acetate pressure of 40 mbar. Reaction rates of all observed products: diethyl ether (red), ethylene (green), ethanol (purple), carbon dioxide (green), and acetaldehyde (orange) as a function of H_2O co-feed partial pressure for a) MgO, b) γ-Al_2O_3, and c) m-ZrO_2. All catalysts were pre-treated in-situ by 450 °C oxidation followed by 400 °C reduction. 164

Figure 5.6 Ethyl acetate conversion rates at 340 °C as a function of water partial pressure with ethyl acetate pressure of 40 mbar. Reaction rates of all observed products: diethyl ether (red), ethylene (green), ethanol (purple), carbon dioxide (green), and acetaldehyde (orange) as a function of H_2O co-feed partial pressure for a) γ-Al_2O_3 and b) ZrO_2. All catalysts were pre-treated in-situ by 400 °C reduction only. 165

Figure 5.7 Ethyl acetate conversion rates normalized per catalyst surface area (from BET measurements) at 40 mbar ethyl acetate as a function of temperature from 290 to 340 °C for **a)** 0.5 wt% Na loaded on γ-Al_2O_3, and **c**) 5.0 wt% Na loaded on γ-Al_2O_3. All catalysts were pre-treated in-situ by 400 °C reduction only. The corresponding temperature dependent rates of un-doped γ-Al_2O_3 are shown in Figure 5.4 (b). 167

Figure 6.2 In situ IR spectra of CO adsorbed at 25 °C and at saturation coverage after a 5-minute Ar purge (a) and a 20-minute Ar purge (b) on $PtCu_{300}$ loaded on γ-Al_2O_3 with varying in situ CO treatment temperatures. $PtCu_{300}$ was pre-treated in situ by 400 °C reduction. Note, these IR spectra were recorded before the XAS experiments. 183

Figure 6.3 XAS of $PtCu_{50}/Al_2O_3$ catalysts. (a) XANES and (b) EXAFS spectra collected at 50 °C immediately following $PtCu_{15}$ degassing in He, labelled "$PtCu_{15}$_Native", and immediately following $PtCu_{15}$ reduction at 350 °C, labelled "$PtCu_{15}$_Reduced". 184

Figure 6.4 XAS of $PtCu_{50}/Al_2O_3$ catalysts. (a) XANES and (b) EXAFS spectra collected at 50 °C immediately following $PtCu_{15}$ reduction at 350 °C, CO treatment at 50 °C, and CO treatment at 200 °C. Note the three spectra are nearly identical and lie on top of each other, particularly in the XANES region. 186

Figure 6.5. In situ IR spectra of CO adsorbed at 50 °C and at saturation coverage after a 5-minute Ar purge on a) $PtCu_{15}$ loaded on γ-Al_2O_3 with varying in situ CO treatment temperatures (50 °C and 200 °C) and b) $PtCu_{300}$ loaded on γ-Al_2O_3 with CO treatment at 50 °C. Both PtCu alloys were pre-treated in situ by 400 °C reduction. Note, these IR spectra were recorded after the XAS experiments. 188

List of Tables

Table 3.1 Summary of N_2O-TPR estimates of the number of total active sites at the Cu surface, the corresponding particle dispersion, and estimated Cu particle size for 1.0, 2.5, and 5.0 wt % Cu loaded on ZrO_2 after N_2O pre-treatment at 50, 90, and 130 °C as shown by the TPR peak area in Figure 3.5. 80

Table 4.1 Al Surface Density on ZrO_2. Estimated Al^{3+} surface loading on ZrO_2 (Surface Area: 26 ± 2 m^2/g) based on Al weight loading. 106

Table 4.2 N_2O-TPR based measurements of # of active Cu sites, Cu dispersion, and estimated Cu particle size for Cu loaded over ZrO_2, TiO_2, and Al-ZrO_2. All estimates were made following 90 °C N_2O oxidation. The Cu weight loading for each catalyst is listed. [a] These 1 wt% Cu on ZrO_2 and 0.675Al-ZrO_2 catalysts were used for all kinetic experiments. [b] 1 wt % Cu/ZrO_2 was calcined at 350 °C rather than 450 °C and 1 wt % Cu/0.675Al-ZrO_2 was synthesized via wet impregnation rather than incipient-wetness impregnation. These two catalysts were used exclusively for the particle size dependent measurements. 111

Table 4.3 Ethanol dehydrogenation turn over frequency (TOF) at 200 °C and 71.5 mbar ethanol for 1 wt% Cu on ZrO_2, 0.025Al-ZrO_2, 0.225Al-ZrO2, 0.675Al-ZrO2, and TiO_2. Corresponding temperature dependent results are shown in Figure 4.13. 118

Table 4.4 Ethanol dehydrogenation turn over frequency (TOF) at 200 °C and 71.5 mbar ethanol for 1 wt% Cu on 0.675Al/ZrO_2 with varying in-situ pre-treatment. Corresponding pre-treatment dependent results are shown in Figure 4.14. 120

Table 4.5 Ethanol dehydrogenation turn over frequency (TOF) at 200 °C and 71.5 mbar ethanol for 1 wt% Cu on TiO_2 with varying in-situ pre-treatment. Corresponding pre-treatment dependent results are shown in Figure 4.15 121

Table 4.6 Ethanol dehydrogenation turn over frequency (TOF) at 210 °C and varying inlet pressures of EtOH and pyridine for 1 wt% Cu on ZrO_2, 0.675Al/ZrO_2, and TiO_2. Corresponding pre-treatment dependent results are shown in Figure 4.18. 128

Table 4.7 Equilibrium (K_1 and K_{eff}) and rate (k_2 and k_4) constants for the best fits of equation 4.2 (O-H cleavage as RLS) below 45.5 mbar ethanol and equation 4.1 (C_α-H cleavage as RLS) at and above 45.5 mbar ethanol. $K_{eff} = K_1K_2K_3K_6^{1/2}\ K_7^{1/2}$. 138

Table 5.1 Summary of catalyst acid and base site density from TPD experiments, see Figure 5.2, and the relative acid and base site strength from IR experiments, see Figure 5.3. 159

Table 5.2 Apparent activation barriers for ethyl acetate conversion to diethyl ether (DEE), ethanol (EtOH), ethylene (EY), and carbon dioxide (CO_2) with 40 mbar ethyl acetate between 290 and 360 °C. Corresponding ethyl acetate conversion rates as a function of inverse temperature are shown in Figure 5.4 161

Table 5.3 Summary of rates (10^{10} mol sec^{-1} m^{-2}) at 340 °C and 40 mbar ethyl acetate pressure for ethyl acetate conversion to diethyl ether (DEE), ethanol (EtOH), ethylene (EY), carbon dioxide (CO_2), and acetaldehyde (AcetH) over γ-Al_2O_3, 0.5 wt% Na loaded on γ-Al_2O_3 (0.5Na-Al_2O_3), 5.0 wt% Na loaded on γ-Al_2O_3 (5Na-Al_2O_3), and MgO. 167

Table 6.1 ICP analysis of $PtCu_{100}$ particles post-digestion with aqua regia with nominal weight loading of Cu and Pt shown with respect to the actual weight loading observed through ICP. 181

Table 6.2 ICP analysis of $PtCu_{15}$ and $PtCu_{300}$ particles post-digestion with aqua regia with the observed weight percent shown of Pt and Cu for each nanoparticle 181

Chapter 1. Introduction

1.1 Summary

This chapter provides background on the significance of heterogeneous catalysis in the world today and particularly on the significance of Cu catalysts in working to promote chemistries involved with the conversion of biomass or sugars to higher value products and fuel-like additives. A discussion of the role of metal oxide supported Cu is provided, detailing the individual importance of Cu nanoparticles and metal oxide supports, as well as the potential cooperative effects the two systems can play when in contact with each other. A focus of this chapter is to provide a brief summary of the different types of active sites on metal oxide supports with an overview of how metal oxide support Lewis acid and Lewis base sites can control specific reaction chemistries, especially when the two sites are working cooperatively on the support surface. Additionally, a discussion is provided on how to modify metal oxide support surface acid sites by doping the support surface with specific molecules that can help promote reaction activity.

Due to the increasing interest as well as number of studies on the potential cooperative effects between small Cu particles and their corresponding metal oxide supports, the second half of this chapter is devoted to describing such effects. Cu-support effects are only meaningful where a large fraction of the Cu surface has intimate contact with the support surface. Thus, using simple area to volume ratio logic, it is established that only Cu particles that are less than 6 nm in diameter “feel” significant effects from the Cu-support interface. Examples from literature of how the Cu-support interface can control reaction chemistries is provided as well as the limitations in literature of effectively

characterizing Cu surface area (or particle size) when Cu-support effects are significant. Finally, a brief summary is provided of the effects of particle size and the support on catalyst activity as well as methods of deconvoluting these two effects. Overall, this chapter provides a detailed, but simplified description of all the theory involved with the work discussed in the subsequent chapters.

1.2 Importance of Catalysis on the Global Scale

The field of catalysis has helped develop many technologies that have effectively transformed and benefited human society in the twentieth century. Some of the most important catalytic processes that impact our everyday lives are ammonia synthesis through the Haber-Bosch process that effectively feeds the world, the production of plastics and other polymers, catalytic cracking and reforming for high octane gasoline, and automobile exhaust catalysis for mass emission and pollution control.[1] For example, ammonia synthesis through the Haber-Bosch process has revolutionized the world and allowed for the world's dramatic population growth as it has been estimated that approximately 50% of the world's food production relies on ammonia-based fertilizers.[2]

Typically, catalysis is broken up into three branches: heterogeneous catalysis, homogeneous catalysis, and biocatalysis. Though they share many of the fundamental principles in how they function, each has its own advantages for a variety of applications. With respect to their ability to promote reactions, liquid phase homogeneous catalysts can be active at low temperatures with high product selectivity while heterogeneous catalysts would typically operate at higher temperatures with lower product selectivity. However, heterogeneous catalysis requires much simpler separation and recycling processes, which

can significantly reduce the costs of heterogeneous catalysis compared to homoegeneous catalysis. Finally, whereas the reaction mechanism and active site are well understood and well-defined for homogeneous catalysts, the mechanism and respective active sites are less understood for heterogeneous catalytic systems. This thesis will focus only on heterogeneous catalysis using abundant and cheap active metal catalysts with a focus on elucidating both the reaction mechanism and active sites for given reaction processes.

1.3 Fundamentals of Heterogeneous Catalysis

A chemical reaction involves the conversion of reactant molecules into product molecules with the requirement that the reactants must overcome an inherent activation energy barrier (E_A) for effective conversion. Typically, the energy barrier is overcome through the input of thermal energy, where the rate dependence on system temperature can be expressed as, $\text{rate} \propto k = Ae^{\frac{-E_a}{RT}}$, where k is the reaction rate constant, A is the reaction pre-exponential factor, E_a is the inherent activation barrier, R is the universal ideal gas constant, and T is the system temperature. According to the equation above, reaction rates can either be increased by a larger input of thermal energy or by decreasing the inherent reaction activation barrier. Generally, catalysts can effectively decrease E_A by stabilizing reactant molecule intermediates, forming an alternate pathway to product formation. This phenomenon is shown in Figure 1.1 where, without a catalyst, reactants A and B are shown to be converted to product C after overcoming a substantial E_A. The catalyzed pathway can effectively promote reaction rates by generating a multistep reaction mechanism with lower effective E_A. Note that the minima on the catalyzed reaction pathway represents the

reaction step with the lowest potential energy, corresponding to the stabilization of adsorbates on the catalyst surface.

For mechanistic analysis, the reaction pathway in Figure 1.1 can be broken down into elementary steps involving reactant A and B adsorption to a catalytic surface (steps 1 and 2), A and B surface reaction to produce C (step 3), and product C desorption from the catalytic surface (step 4) as shown below:

$$1)\ A + * \rightleftharpoons A*$$

$$2)\ B + * \rightleftharpoons B*$$

$$3)\ A* + B* \rightarrow C* + *$$

$$4)\ C* \rightleftharpoons C + *$$

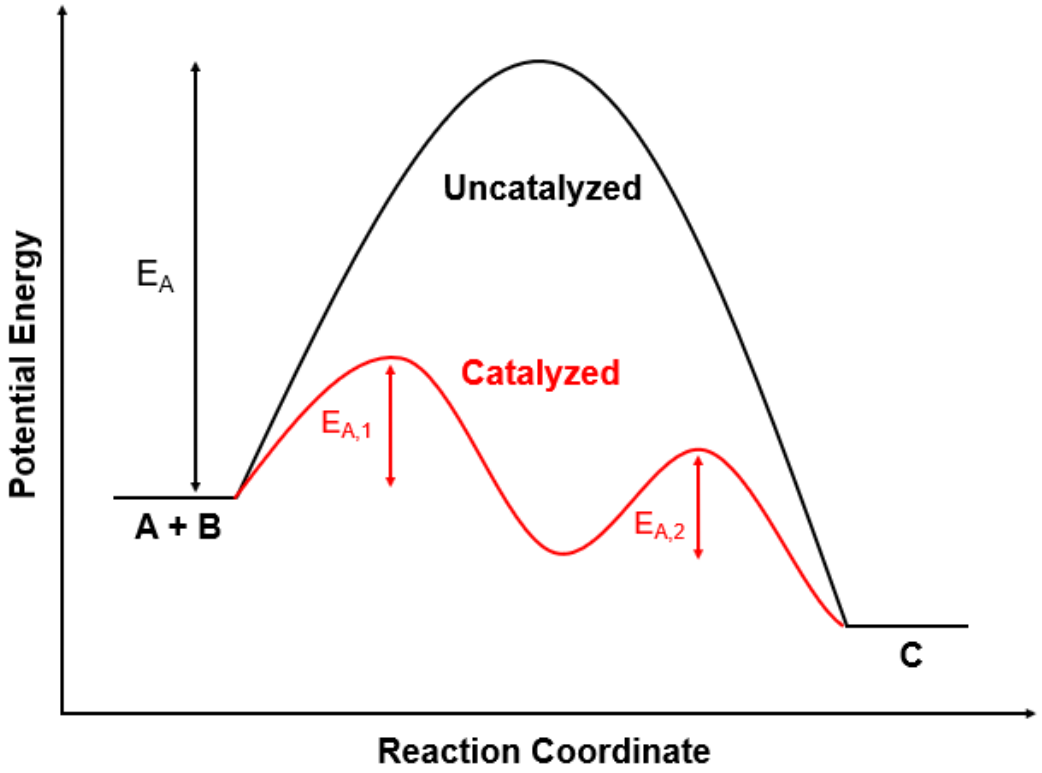

Figure 1.1 Schematic of a potential energy plot with uncatalyzed (black) and catalyzed (red) pathways for reactant A and B conversion to product C. The catalyzed process is shown to have multiple reaction steps with $E_{A,1}$ and $E_{A,2}$ corresponding to the activation barriers for steps 1 and 2, respectively. Note $E_{A,1}$ and $E_{A,2}$ are lower in energy than E_A.

In the reaction scheme above * corresponds to a vacant catalyst adsorption site, A* and B* correspond to the reactants adsorbed to the catalytic surface, and C* corresponds to the product adsorbed to the catalytic surface. Note that each elementary step will have its own rate expression and rate constant. Additionally, for any given catalytic process, there is a rate-limiting step (RLS) that corresponds to the kinetically slowest step in the reaction mechanism, rendering all other steps to be effectively in equilibrium. It should be noted that many chemical reactions have multiple rate determining steps (RDS) as opposed to just one RLS as depicted above. As discussed in more detail in the Appendix, proper reaction elementary steps may be derived into an overall reaction rate expression that can be evaluated against experimental results to validate the proposed mechanism and RLS of a reaction process.

1.4 Importance of Cu Catalysts

Cu catalysts are an important class of materials as Cu is cheap and abundant and Cu is quite selective for the desired products across many important reaction such as propylene epoxidation[3], alcohol dehydrogenation[4], NO_x reduction[5], methanol synthesis from CO and CO_2,[6–12] and has shown potential in performing effective CO oxidation[13,14], a reaction generally conducted over precious metal Pt. Additionally, Cu has been shown to be a quite dynamic catalyst under reaction conditions as the shape of the Cu nanoparticle changes with the introduction of surface adsorbates such as CO, H_2, and H_2O.[15,16]

In this thesis, Cu is primarily used to study the ethanol dehydrogenation reaction mechanism to the production of acetaldehyde. As discussed above, Cu is quite selective towards the ethanol dehydrogenation pathway and this reaction was used to study unique

Cu-support interfacial sites that promoted the reaction activity and modified the Cu active sites.[17] Additionally, this thesis focuses on methods of optimizing Cu surface area characterization to generate more accurate predictions of Cu dispersion, or number of Cu atoms that are at the surface of the Cu nanoparticle, which is important in predicting Cu particle sizes as well as reaction turn over frequency.

1.5 Importance of Metal Oxide Supports

Metal oxide supports are widely used throughout the chemical industry for olefin metathesis[18], alcohol dehydration[19–21], aldol condensation[22], the Lebedev reaction,[23] and numerous other condensation reactions.[24–26] The reaction activity and selectivity of different metal oxide supports for these reactions strongly dependent on the strength and quantity of either their acid or base sites or acid-base site pairs.

1.5.1 Metal Oxide Support Acid Site Chemistry

Support Lewis acid sites are electron withdrawing groups that exist as M^+ species on the support surface (Al^{3+} for Al_2O_3, Zr^{4+} for ZrO_2, etc.) while it also has been suggested that supports, particularly Al_2O_3, have characteristic Brønsted acid sites that are proton donors of the form Al^{3+}-OH.[27] The strength of acid sites is typically correlated with the atoms' local coordination with lower coordination metal atoms corresponding to more reactive, or higher strength acid sites. Figure 1.2 (a) shows a representation of Al^{3+} on Al_2O_3 with coordination to 3 and 4 oxygen neighbors, Al_{III} and Al_{IV}, respectively. In this example, Al_{III} is a stronger acid site than Al_{IV}, which is further supported in literature.[28,29] Additionally, Lewis acid site strength characterization based on the vibrational frequencies of pyridine CCN bonds adsorbed to support acid sites has revealed that in the 8a vibrational

band (1550 – 1650 cm^{-1}), Lewis acidity increases with increasing vibrational frequency.[30,31] A schematic representation of pyridine adsorption to a Lewis acid metal site is shown in Figure 1.2 (b) where the metal site effectively withdraws electrons from the pyridine nitrogen group to induce chemisorption. Using the example in Figure 1.2 (a), the Al_{III} site was calculated to adsorb pyridine with vibrational frequencies above 1620 cm^{-1} while the Al_{IV} was predicted to have frequencies between 1610 and 1617 cm^{-1}.

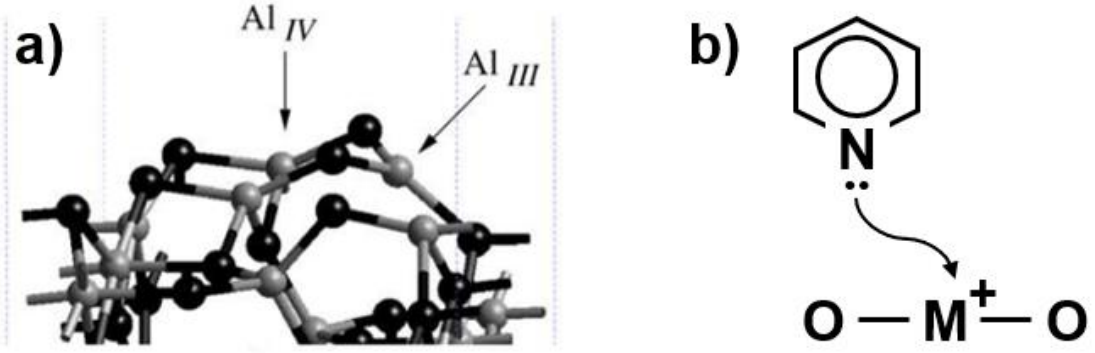

Figure 1.2 (a) DFT calculations of a γ-Al_2O_3 (110) surface with most relevant sites quoted as Al_n, which corresponds to aluminum atoms surrounded by *n* oxygen atoms and (b) a schematic representation of pyridine adsorption to Lewis acidic metal (M) centers. Reprinted from ref 27 with permission from Elsevier.

One example of a common reaction pathway promoted by metal oxide support acid sites is ethanol conversion to either diethyl ether and ethylene or acetaldehyde through the dehydration and dehydrogenation reaction pathways, respectively. Both pathways have been shown to share a common surface intermediate, ethoxy (CH_3CH_2O), which is generated by facile O-H bond cleavage of ethanol over Lewis acid sites on γ-Al_2O_3[20,32], a step shown to have a negligible activation barrier over γ-Al_2O_3 by DFT calculations.[21] This reaction pathway has also been shown to be driven by Brønsted acid sites, where a Brønsted acid O-H group helps to stabilize an ethanol intermediate through a hydrogen bond.[19] On the other hand, C_α-H bond cleavage is much more difficult over γ-Al_2O_3 as

shown by a larger activation barrier, 188 kJ/mol[21] for acetaldehyde formation (dehydrogenation), as well as acetaldehyde rates that were 100-fold lower than those of diethyl ether and ethylene formation (dehydration).[32] This reveals that, as for any catalytic material, it is important to develop a fundamental understanding of the reaction mechanism at the catalytic surface to have some level of predictive power when working to either understand or optimize specific reaction pathways with a given catalytic material.

1.5.2 Metal Oxide Support Base Site Chemistry

Support basic sites, specifically Mg-Al hydrotalcites, are able to catalyze a variety of reactions including: aldol condensation, Michael reaction, cyanoethylation of alcohols, and the nitroaldol reaction.[33] The active sites for these reactions are support Lewis base sites acting as electron donating groups that exist as O atoms on the support surface, where OH^- groups correspond to the weakest base sites, M-O pairs correspond to medium strength base sites, and O^{2-} species correspond to the strongest base sites[33–35] while Brønsted base sites, though of a similar structure, correspond to O-H proton acceptors.[35] Similar to Lewis acid sites and their corresponding metal cations, base site strength varies with O site local coordination where, for example, on MgO, O^{2-} (least coordinated) ions are considered strong basic sites while higher coordinated Mg-O pairs and OH^- groups are considered weaker base sites.[26,35,36] A recent study that employed DFT calculations showed lower coordination O in MgO was able to induce spontaneous dissociative chemisorption of ethanol while higher coordinated O was unable to perform similarly due its inherently lower deprotonation reactivity.[37]

In an analogous way to pyridine for Lewis acid sites, CO_2 can be used as a probe molecule to characterize the strength of basic sites by studying the vibrational frequencies of O-C-O and C-OH of CO_2 adsorbed to different basic sites as shown in Figure 1.3. Literature has shown that upon adsorption to the strongest, intermediate strength, and weakest base sites, CO_2 forms unidentate carbonates (stable > 400 °C), bicarbonates and chelating bidentate carbonates (stable up to 200 °C and 100 °C, respectively), and bridging bidentate carbonates (stable up to 50 °C), respectively.[38] Each carbonate has unique vibrational frequencies and thus can be identified with ease, especially with a corresponding temperature programmed desorption experiment.

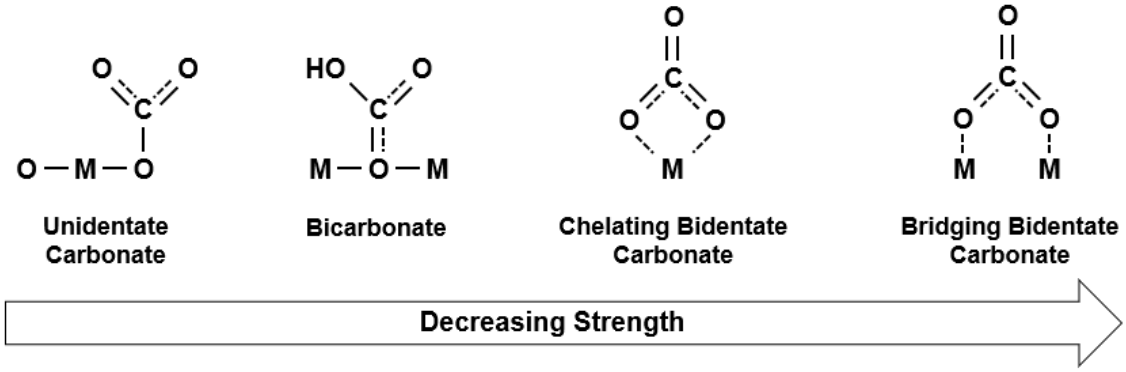

Figure 1.3 Schematic of carbonates bound to the support surface basic sites in different configurations that correspond to different basic site strengths.

1.5.3 Cooperative Effects of Acid-Base Pairs

As can be inferred from the discussions above, very few metal oxide supports will have surfaces that are either exclusively composed of base or acid sites. Two such oxides are MgO, which is exclusively a strongly basic support, and γ-Al_2O_3, which is exclusively a strongly acidic support. However, many other common metal oxide supports, such as ZrO_2 and TiO_2, have a combination of acid and base sites that very in number and strength. The cooperativity between acid and base sites has been widely studied for ethanol

conversion, aldol condensation, and butadiene synthesis from ethanol.[26,37] A simple representation of the cooperative behavior is shown in Figure 1.4 for ethanol dehydrogenation to acetaldehyde where O corresponds to a basic oxygen sites and M corresponds to cationic metal acid sites. Here, ethanol is adsorbed on an acid-base pair with O coordinating to the acid site and the corresponding H coordinating to the nearest base site. This acid-base pair then promotes the cleavage of the O-H bond, forming an ethoxide intermediate. Next, a strong base site can induce C_α-H bond cleavage, converting the ethoxide intermediate to an acetyl intermediate with a carbonyl (C=O) group. Finally, acetyl desorbs as acetaldehyde and the two cleaved H's associatively desorb as hydrogen gas. It should be noted that this reaction pathway is quite similar to that described over Lewis acid sites on γ-Al_2O_3 (section 1.5.1). However, over γ-Al_2O_3 the production of acetaldehyde from ethanol was quite difficult, most likely because the surface of γ-Al_2O_3 does not have strong Lewis base sites than can promote C_α-H bond cleavage.

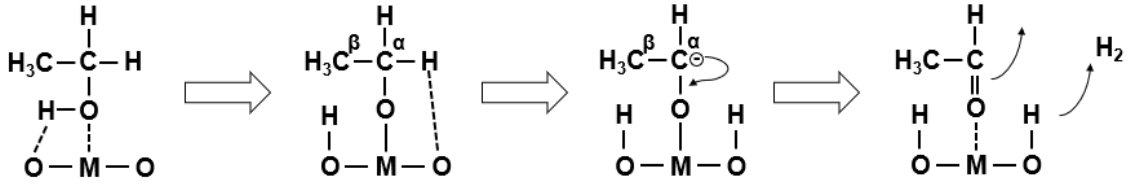

Figure 1.4 Scheme of ethanol dehydrogenation to acetaldehyde catalyzed by acid-base pairs on a metal oxide support with a generic label of "M" for the Lewis acidic metal center and "O" for oxygen sites that act as Lewis bases.[26]

Another class of industrially important reactions that are controlled by acid-base pairs is coupling reactions, known as condensation reactions, which involve C-C bond formation, see Figure 1.5. Here, the acid site attacks the oxygen of a carbonyl, forming an acetyl intermediate. Strong basic sites can then cleave the Cα-H bond, forming a carbo-anion (C-) species that can then attack a carbon on a neighboring acetyl intermediate,

forming new C-C bonds. Though not shown in Figure 1.5, this process leads to the formation of a 4-carbon alcohol with the loss of a water molecule. So, this reaction not only creates a longer chain carbon species but is also able to reduce the effective number of oxygens through the formation of water, two factors that are quite important during the upgrading of platform chemicals to fuel-like products.

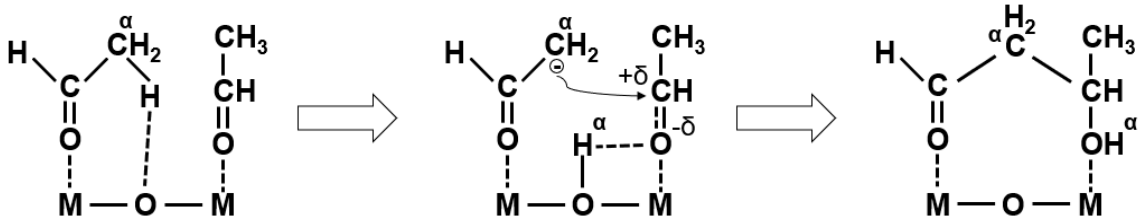

Figure 1.5 Scheme of initial steps of aldol condensation reaction for acetaldehyde over acid-base pairs on a metal oxide support with a generic label of "M" for the Lewis acidic metal center and "O" for oxygen sites that act as Lewis bases.[26]

Although acid-base pairs play an important role in the conversion of platform chemicals to useful products, the impact of both acid-base pair relative strength and quantity on reaction activity and selectivity is currently under investigation over both zeolites and more traditional metal oxide supports. For example, recent studies utilizing density functional theory (DFT) calculations proposed that a combination of strong Lewis acid-weak/medium base pair sites provide the best performance for aldol condensation of ethanol to 1,3-butadiene.[39] The strong Lewis acid sites help stabilize ethanol intermediates on the support surface while a weak/medium base sites promotes proton back-transfer, both helping to promote difficult C_α-H bond activation (see example in Figure 1.5). Additionally, other work focused on studying the effects of the relative quantity of acid-base pairs and showed evidence that a large surface density of acid or base sites (or both) would induce poor butadiene selectivity while selectivity was optimized over catalysts with

a moderate amount of weaker Lewis acid sites and a low amount of stronger base sites.[22,25] Other work has suggested that weak acid-base pairs are optimal for aldol condensation reactions.[40] So, although the optimal acid-base pairs will vary for different reactions, it is clear that understanding the role of these pairs (and how to optimize them) is of particular importance to play a role in helping improve current industrial processes involving condensation reactions.

1.5.4 Metal Doping to Modify Support Acidity

As discussed above, metal oxide supports have been studied to identify the relative strength and quantity of acid and base sites on a support that can optimize reaction activity. As optimization of these acid-base pairs is important, developing a means of controlling and tuning such sites is of high interest. Common techniques in literature for controlling the relative acidity and basicity of support sites have employed the co-precipitation synthesis,[26] the introduction of low and high valence metal dopants,[34,41] and the deposition of nanostructures such as tungsten oxide (WO_x) and rhenium oxide (ReO_x) onto traditional metal oxide supports.[42,43] These three techniques will be discussed in some detail below.

Co-precipitation has been widely employed to create mixed oxides such as Mg-Al with both Lewis acids (characteristic of Al_2O_3) and Lewis bases (characteristic of MgO) on the surface that can be controlled by the relative stoichiometry of Mg and Al.[26,38,44] It was shown through CO_2 probe molecule characterization that the addition of Al to MgO decreased both the relative strength and number of base sites on MgO, likely because the Al sites became coordinated to oxygen atoms on MgO, decreasing the concentration of Mg-O pairs and O^{2-} anions. Similarly, it has been shown that the co-precipitation of MgO

onto SiO_2 actually works to effectively increase the amount of acid and base sites over SiO_2.[25] These examples reveal that the choice of co-precipitation oxide pairs is important as different pairs induce quite different surface effects and thus proper surface acid and base site characterization is essential to understanding these mixed metal oxide supports.

The second technique involves doping a metal oxide support with a different valence metal to induce the formation of unique acid sites on the surface.[34,41,45,46] In this thesis, we primarily focus on adding lower valence dopants (LVD) to metal oxide supports. For example, we dope ZrO_2 (Zr^{4+}) with an Al^{3+} LVD, which induces the substitution of Zr^{4+} with Al^{3+}, creating a local electron deficit in the oxide. This in turn causes the local oxygen atoms to bind more weakly to the doped oxide, making the oxygen atoms more reactive. Consequentially, to counteract the electron deficit, an electron rich atom or molecule may be added to the doped oxide that donates electrons to the surface. In summary, after the addition of a LVD, the doped oxide sites become more electron withdrawing, or stronger Lewis acids.[45] On the other hand, high valence dopants (HVD) promote the generation of strong Lewis bases on metal oxide supports. One example of an HVD is the addition of a Ta^{5+} atom to a ZrO_2 support, though the addition of an HVD to a strongly basic support such as MgO was predicted to have minimal effects.[46] Figure 1.6 shows DFT calculations of LVD zinc doped onto lanthanum oxide, showing how the dopant creates a local electron deficit, weakening the dopant-oxygen bonds and making them more reactive for dissociating the C-H bond of methane.

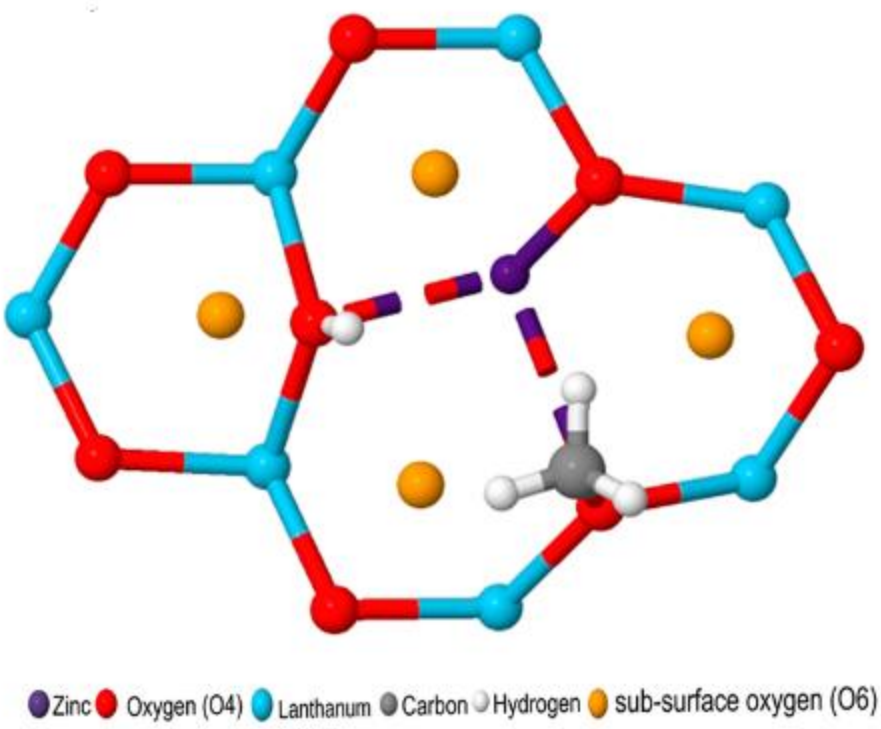

Figure 1.6. DFT calculations of Zn-doped La_2O_3 (001) showing the effects of the dopant on its local oxygen neighbors making them more reactive and better at dissociating methane. Reprinted with permission from ref 34. Copyright 2013 American Chemical Society.

The third technique involves the deposition of WO_x and ReO_x onto more traditional metal oxide supports for the promotion of olefin metathesis, which has been widely studied.[18,42,43,47] Literature studies of WO_x loaded onto ZrO_2 have shown that strong Brønsted acid sites may be generated by partial reduction of WO_x, promoting metathesis activity. Similarly, DFT calculations together with experimental studies of isolated ReO_x loaded on Al_2O_3 showed similar promotional effects on metathesis due to the generation of strongly acidic ReO_x species on the surface. Note that although this thesis only employs the second technique involving metal oxide support doping with LVDs, it is important to highlight the myriad of methods of modifying support acid and basic sites.

1.5.5 Support Site Poisoning by Ambient Environment

Recent reports in literature have suggested that adventitious species that exist in ambient air can effectively poison metal oxide support acid and base sites. It was revealed that TiO_2 can selectively adsorb atmospheric carboxylic acid species forming bidentate intermediates on the surface of the support, which can effectively poison TiO_2 sites from interaction with alcohols.[48] Previous work as well as the work in this thesis (described in more detail in Chapter 4), has shown that reaction activity is intimately linked to the catalyst pre-treatment conditions.[17,36] For example, the conversion of the aldol addition reaction increased dramatically when increasing support pre-treatment temperatures from 200 °C to greater than 400 °C, suggesting the desorption of adventitious surface species such as CO_2, H_2O, and potentially carboxylic acids.[17,35,36,48] Water has also been widely studied as a support surface intermediate, which has been shown to poison acid-catalyzed reactions due to water's propensity to poison strong Lewis acid sites, acting as a competitive inhibitor and significantly decreasing the activity of alcohol dehydration reactions.[20,49] In our work (discussed in Chapter 4), we showed more specifically that pre-treating the catalyst under high temperature oxidation (as opposed to under an inert gas), effectively increased the reaction activity with increasing oxidation temperature, providing further evidence that supports with active acid and base sites are quite sensitive to surface poisoning under ambient conditions. These results provide strong evidence that support materials are not inert to the ambient environment and proper pre-treatment of the supports must be considered when trying to optimize reaction activity.

1.5.6 Impact of Support Surface Intermediates

Though ambient species such as water have been shown to effectively poison strong support acid sites, it has also been reported that the adsorption of water onto a basic support could increase the support reaction activity by generating basic OH^- anions that serve as active sites on the support surface and can promote esterification.[35,50] However, it should be noted that such a phenomenon occurs primarily on weaker basic sites as stronger base sites will be poisoned by water, consistent with the discussion in the previous section.

Many industrially relevant condensation, esterification, and addition reactions require the use of surface intermediates to promote new C-C bond formation to increase the carbon count of the product molecule. Therefore, much work has focused on developing a fundamental understanding on the role of these intermediates under reaction conditions. One common example is aldol condensation of acetaldehyde as previously shown in Figure 1.5. For this process, the surface intermediate (adsorbed acetyl group after C_α-H bond cleavage) is quite similar to the molecule it reacts with (adsorbed acetyl) where, after C_α-H bond activation, the anionic C_α can attack the adjacent acetyl molecule's carbonyl (C=O) group to induce C-C bond formation. This reaction pathway is analogous for aldol condensation of any reactants, as previously described in literature.[50]

The Meerwein-Ponndorf-Verley (MPV) mechanism for the reaction of isopropanol (IPA) with mesityl oxide is an example of a more complex reaction scheme involving the interaction of different surface interemediates.[44] Here IPA was simply used as a hydrogen donor on the support surface to induce selective C=O bond hydrogenation, which is an important step in processes involving the deoxygenation of ester molecules. It should be

noted that H_2O would also be expected to serve as a hydrogen donating species on the surface of supports, though as previously discussed, H_2O is also known to inhibit reaction activity by poisoning surface acid and base sites.

1.6 Cooperativity Between Cu Catalysts and Their Corresponding Metal Oxide Support

Although Cu catalysts and various metal oxide supports individually promote the conversion of many important reactions, there has recently been quite a bit of interest in analyzing the potential cooperative effects on the reaction activity of Cu and its corresponding support, specifically at interfacial Cu sites, where Cu has direct and intimate interactions with the support. One of the most important industrial process involving methanol production from CO_2 has been studied thoroughly over Cu catalysts loaded on ZnO-Al_2O_3 surfaces, a reaction for which the identity of the catalytic active site is in contention. Studies have proposed that the active site consists of Cu sites that are decorated, or interacting, with Zn atoms,[6–8,11] while others have suggested that the support may also act as an active site together with Cu particles, implying the formation of Cu-Zn alloy active sites.[9,10,12] This example highlights the current debate on metal-support effects; whether the support works to promote the reaction pathway by modifying the active metal or by directly participating in the reaction forming a 2-site reaction mechanism. In this dissertation, the focus will be on the former as will be discussed below.

Recently, it was suggested that doping a CuO_x-CeO_2 surface with In_2O_3 could dramatically improve the CO oxidation ability of Cu catalysts by modifying interfacial Cu sites through Cu particle reconstruction.[14] Additionally, it has been proposed that Cu loaded on supports with a large and equal surface density of both acid and base sites,

promotes CO oxidation as the support sites help draw electron density away from interfacial Cu sites, forming Cu^+ sites that are expected to be the active sites for CO oxidation.[51] Similarly, DFT calculation of 4 atom Cu clusters showed that charge transfer from Cu to Cr_2O_3 could induce the formation of interfacial Cu^+ species that stabilize ethanol adsorption, promoting ethanol conversion activity.[52] Ethanol esterification to ethyl acetate was also shown to be a reaction that was directly impacted by interfacial Cu sites.[53,54] These interfacial Cu sites were shown to promote ethyl acetate formation by over an order of magnitude with the effects likely occurring from either the metal and oxide support working in tandem as active sites or the metal acting as a support modified active site.[53] Other work has more broadly expressed that Cu metal-support interactions play a significant role in dictating reaction catalysis.[55] Due to the widely observed promotional effects of metal-support interfacial sites, this thesis will provide a detailed discussion on such effects of interfacial Cu sites that are modified by support acid sites. This thesis will have a focus on how these interfacial sites modify the chemical properties of Cu, as shown through characterization (see Chapter 3 and 4), as well as how these interfacial sites promote ethanol conversion to acetaldehyde (see Chapter 4).

1.6.1 Particle Size Effects on Catalyst Activity

In heterogeneous catalysis, reactions typically occur over catalyst surface sites, as opposed to the sub-surface bulk. Therefore, it is expected that the catalyst particle size can have a direct impact on catalyst activity because particle size dictates the fraction of surface sites that are available for catalysis. In previous work, it was shown that the fraction of different types of surface sites can be generalized based on a power law that was dependent

on the particle diameter, see Figure 1.7.[56] Here, it is shown that different catalyst active sites have different power law dependencies on particle diameter with surface sites, perimeter sites, and corner sites having $d^{-0.9}$, $d^{-1.9}$, and $d^{-2.6}$ dependence on particle size, respectively. It was shown that the reaction activity, or TOF, could also be measured as a function of particle size and the power law could be correlated to suggest which surface sites are the dominant reaction active sites.

Others in literature have used the principles discussed above to show that the catalyst active site can be modified when changing reaction conditions or the catalyst support. For example, Ni loaded on Al_2O_3 was only active at Ni-Al_2O_3 interfacial sites for the dry reforming of methane. On the other hand, for the water gas shift reaction, the entire Ni surface dominated the reaction, with negligible contribution from the interface.[57] Additionally, the water gas shift reaction was studied over Au loaded on Al_2O_3 and TiO_2, showing that when loaded on Al_2O_3 the Au perimeter sites controlled the reaction mechanism while over TiO_2 Au corner sites were dominant.[58] Interestingly, the low coordination, corner sites were shown to be quite more active as evidenced by a 20 fold increase in the reaction activity when Au was loaded on TiO_2. In this thesis, particle size dependence will be used to identify support effects on both the metal active sire and the reaction activity, where it will be proposed that strongly acidic supports can shift metal active sites to the interface while also promoting the reaction activity by over an order of magnitude.

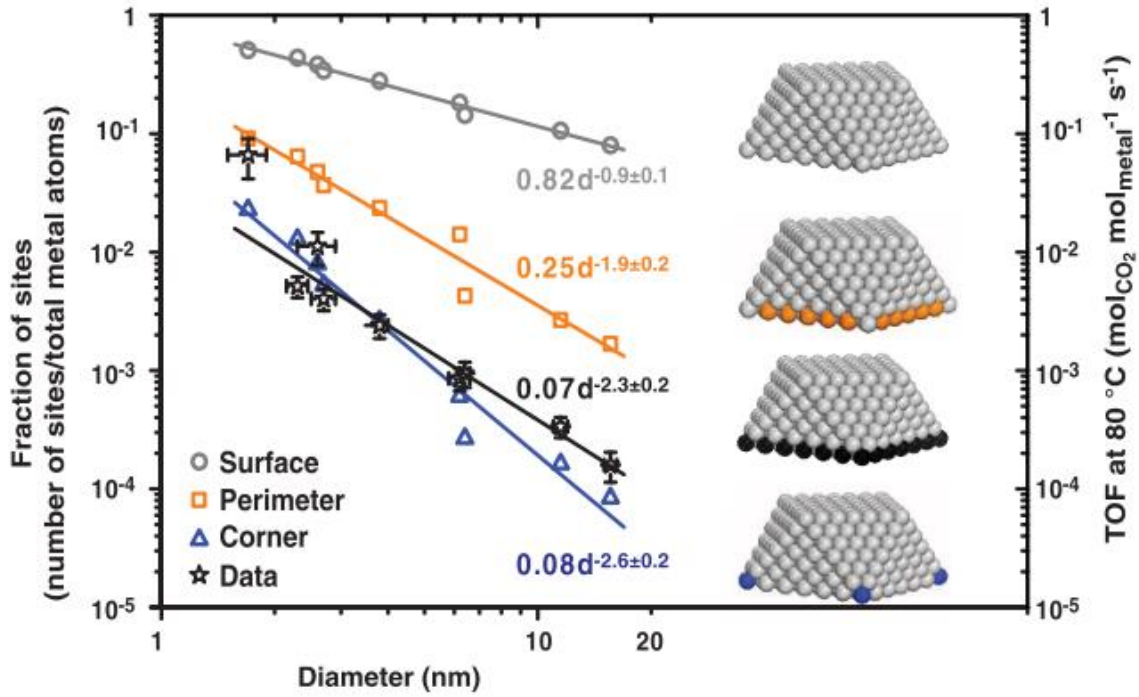

Figure Calculated fraction of sites (surface, perimeter, and corner) and reaction molar turn over frequency (TOF) as a function of particle diameter. Reprinted with permission from ref 56. Copyright 2013 Science AAAS.

1.6.2 Support Effects on Catalyst Activity

Metal oxide supports have also been shown to play a direct role on catalyst reactivity based on the formation of unique interfacial sites. The water gas shift reaction may be used as an example for which Pt particles loaded on TiO_2 have weaker CO binding at the interface as opposed to particles away from the interface.[59] On the other hand, Ni particles loaded on Al_2O_3, had stronger CO, CO_2, and H_2O binding energies than particles away from the interface.[57] These studies reveal that interfacial metal atoms have different properties compared to metal atoms away from the interface, which is why there is quite a lot of interest in studying such effects.

In this thesis, metal particle sizes range from 1 to 10 nm in size, a size range where it is expected that metal-support interfacial sites may still play an important role on the

catalyst reactivity.[60] In this particle size range, with decreasing particle size, the fraction of exposed sites existing as interfacial sites is enhanced, consistent with Figure 1.7. Additionally, in this range of particle sizes, consistent trends in rate, apparent activation barriers, and reaction orders suggest that the interfacial sites are similar in their properties and particle size plays only the role of controlling the relative concentration of metal sites at the interface.[60,61] When studying interfacial effects on catalyst reactivity, it is important to note that undercoordinated surface sites (coordination number <7) in general have inverse particle size dependence (~1/d) that is quite difficult to distinguish from that of perimeter sites (~1/d), as presented in Figure 1.8. To deconvolute interfacial effects on catalyst activity from structure sensitivity effects, it is necessary to study activity as both a function of particle size and with varying supports that are expected to have different effects on interfacial metal sites. This technique is discussed in detail in Chapter 4.

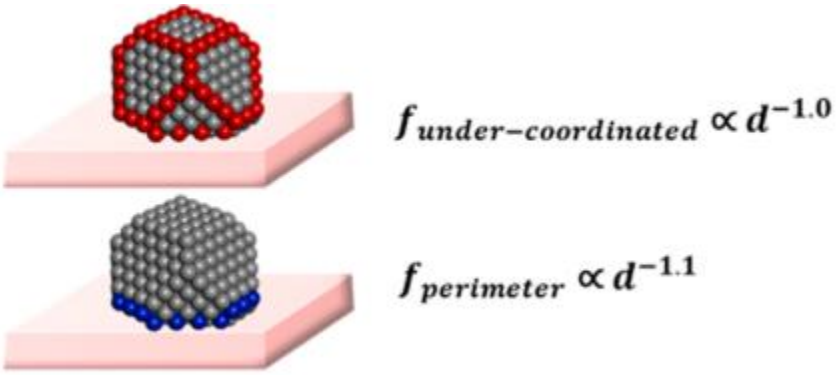

Figure 1.8 Fraction (f) of under-coordinated (red) and perimeter (blue) sites as a function of metal particle size (d). Reprinted with permission from ref 60. Copyright 2018 American Chemical Society.

1.7 Optimizing Cu Surface Area Characterization

As Cu catalysts are used widely in academia and industry, it is important to have well defined methodology for proper characterization of Cu surface area and dispersion for reaction activity measurements. Although the most common characterization technique has

been the use of N_2O titration of surface Cu sites, there exists discrepancy in literature about the optimal titration conditions to facilitate the most accurate predictions of Cu surface area. Typically, it is assumed N_2O selectively oxidizes surface metallic Cu^0 sites to Cu^+. However, the presence of N_2O overoxidation of Cu^0 to Cu^{2+} cannot be excluded and the optimal N_2O oxidation temperature for selective formation of surface Cu^+ has not been established, to the best of our knowledge. To properly optimize N_2O titration of Cu, the titration conditions must be tuned in such a way that surface oxidation occurs over the complete Cu surface and selectively oxidizes Cu sites to Cu^+. Typically, increasing the N_2O oxidation temperature will allow for complete Cu surface oxidation to occur, but will also facilitate Cu overoxidation to Cu^{2+}.

Reports in literature have worked to address this issue and have proposed several different temperatures at which bulk oxidation begins to occur at 70 °C for Cu (34 wt%) loaded on ZnO,[62] at 150 °C for pure Cu, but around 120°C for supported Cu[63], while another report suggested that for Cu (60 wt%) loaded on ZnO/Al_2O_3 below 60 °C Cu surface atoms do not react quantitatively with N_2O while above 90 °C bulk oxidation began to take place.[64] The discrepancies in the proposed optimal N_2O oxidation temperatures are likely due to the characterization of Cu of various sizes (due to different Cu weight loadings) loaded on various metal oxide supports. Additionally, to the best of our knowledge, only one literature study has attempted to deconvolute Cu particle size effects on N_2O oxidation.[55] In this study, it was shown that 4.6 to 20 nm Cu particles loaded on graphite and active carbon behaved identically when treated with N_2O. However, this only suggests that N_2O oxidation is a Cu structure insensitive process, but because there are no

significant electronic interactions between metals and graphite or activated carbon, due to a lack of surface oxygen species, this study does not shed light on how interfacial Cu sites may modify N_2O oxidation.

Cu structure sensitivity and interface effects have previously been studied using probe molecule FTIR. Surface science studies of Cu single and micro crystals have suggested that CO-Cu vibrational frequency increases, or blue-shifts, with either increasing Cu oxidation state or increasing Cu coordination to support oxygen atoms.[65,66] Additionally, the presence of cationic dopant metals such as Mn^{2+} near Cu atoms has been shown to induce the blue-shift of CO-Cu vibrational frequencies due to charge transfer between Mn^{2+} and Cu, where Mn^{2+} withdraws electrons from Cu, making $Cu^{\delta+}$ sites.[67] Such effects may be useful in probing the impact of different types of supports on interfacial Cu, such as comparing a weakly acidic ZrO_2 with that of a strongly acidic Al_2O_3, as discussed in Chapter 4.

CO adsorption to Cu of different oxidation states follows the following trends from strongest adsorption to weakest adsorption: $Cu^+ > Cu^0 > Cu^{2+}$.[68] It has been suggested that CO-Cu^{2+} species only exist at cryogenic temperatures with vibrational frequencies between 2150-2236 cm^{-1}.[66,68] On the other hand, the vibrational frequencies of CO-Cu^+ and CO-Cu^0 generally overlap between 2080 to 2120 cm^{-1}, especially when Cu is well dispersed, and are generally deconvoluted based on CO adsorption strength to the Cu sites.[67] Typically, 1 molecule of CO adsorbs to 1 Cu site, though CO dicarbonyls, $(CO)_2$-Cu^+ have been observed at low temperatures with vibrational frequencies between 2120-2132 cm^{-1} and 2160-2174 cm^{-1}.[65,67] On the other hand, it has been shown that NO binds relatively strongly

to Cu^{2+} species with vibrational frequencies in the region 1845 to 1964 cm^{-1}.[68,69] As CO binds very weakly to Cu^{2+} and NO binds very weakly to both Cu^{+} and Cu^{0} the two probe molecules may be used together to effectively identify the different Cu oxidation states. Using the two probes can be particularly useful when working to study the effects of N_2O oxidation on Cu as the presence of NO-Cu^{2+} vibrational frequencies will provide qualitative evidence of Cu site overoxidation relative to the formation of CO-Cu^{+}.

1.8 Conclusions

From the reported literature, it has become clear that metal oxide supported Cu catalysts are potentially exciting materials for their role in a large variety of reactions as well as their low cost and larger overall abundance. However, more fundamental analyses of such systems are required as a means of developing predictive power with respect to synthesizing these materials in such a way that can either control novel reaction pathways or significantly enhance pathways that have already been well-studied. The careful evaluation of reaction kinetics, together with catalyst surface characterization, is necessary to develop meaningful insights on the effects on surface reactions by the surface structure of active metals, the acid and base sites on supports, and the cooperativity of active metal and support interfacial sites. In recent years, there has been a significant push to develop an understanding of active metal-support effects on reaction activity and selectivity. Through our studies, as described in this thesis, we believe we are adding to the library of knowledge and hope that our generated insights can play a role in motivating future research in the field of Cu and metal oxide support catalysis.

1.9 Dissertation Summary

This dissertation was prepared by using a myriad of techniques as a means of evaluating reaction kinetics together with catalyst surface characterization to elucidate the reaction mechanism and identify the active site for Cu and metal-oxide support catalyzed reactions. Though the primary focus was reaction kinetics, the inconsistencies in literature with respect to the proper characterization of Cu catalyst surface area was studied with the goal of not only elucidating the cause of these inconsistencies, but also with developing a technique to rectify them using a combination of *in-situ* DRIFTS and dynamic pulse chemisorption experiments.

Chapter 2 provides a detailed description of experimental techniques used in this thesis: catalyst synthesis, catalyst characterization and the evaluation of catalyst activity through kinetics studies. Experimental set-up and theory of operation are discussed for catalyst synthesis, dynamic pulse and continuous flow characterization, BET surface area approximation, *in-situ* probe molecule DRIFTS, X-ray absorption spectroscopy, and X-ray powder diffraction. The second half of the chapter focuses on the reactor design along with an explanation of the corresponding kinetic experiments used for this thesis including a schematic of the reactor system and description of the gas chromatograph used to quantify reaction rates.

Chapter 3 presents a discussion of Cu surface area characterization employing CO probe molecule DRIFTS for qualitative characterization and continuous flow N_2O oxidation followed by temperature programmed reduction (TPR) for quantitative characterization. The limitations of Cu site quantification by N_2O-TPR was analyzed and

a potential method of correction for site overestimation by N_2O-TPR was proposed using sub-ambient NO selective pulse chemisorption. The work in this chapter is aimed at improving Cu surface site quantification techniques to achieve higher accuracy dispersion estimates, leading to better catalyst activity evaluation.

Chapter 4 provides a detailed analysis of how Cu-support interfaces can work to promote ethanol dehydrogenation activity by modifying both the rate limiting step of the reaction mechanism as well as the Cu active site. Cu was loaded on different supports that were either weakly acidic or strongly acidic to prove the effects of these acid sites on the catalyst activity using surface characterization together with temperature and pressure dependent reaction rates. The work in this chapter highlights the important role supports can play on reactions that are controlled by an active transition metal when the metal particle size is less than 6 nm. This provides a model for future work studying Cu-support interfacial effects on more complex reactions that are industrially relevant.

Chapter 5 primarily focuses on the role metal oxide support acid and base sites play in the conversion of oxygen-rich molecules. Ethyl acetate conversion is employed as a probe reaction to analyze the impact of acid sites, base sites, or acid-base pairs on the conversion of ethyl acetate to ethanol and/or diethyl ether, which are both meaningful products due to their importance as either higher value chemicals or potential for upgrading to fuel-like products. The aim of this work is to develop a more fundamental understanding of the ethyl acetate deoxygenation reaction mechanism over metal oxide supports as a model for upgrading oxygen rich molecules.

Chapter 6 provides a discussion of the main conclusions of the dissertation and their utility in the field of catalysis. Additionally, this chapter provides a detailed account of unfinished work that was focused on the synthesis and evaluation of Pt-Cu single atom alloys. The single atom alloys have been successfully synthesized and preliminary characterization results suggest a dynamic Pt surface segregation effect when the alloy is under a CO environment. A more rigorous study on the dynamic behavior of the single atom alloys under a CO environment as well as under reaction conditions will help expand the field of single atom catalysis that is quickly growing. Finally, this chapter provides a description of the future outlook of the techniques developed and phenomena discovered in this dissertation.

1.10 References

(1) Adams, C. Applied Catalysis: A Predictive Socioeconomic History. *Top. Catal.* **2009**, *52* (8), 924–934.

(2) Ausfelder, F.; Bazzanella, A.; VanBracki, H.; Wilde, R.; Beckmann, C.; Mills, R.; Rightor, E.; Tam, C.; Trudeau, N.; Botschek, P. Technology Roadmap Energy and GHG Reductions in The. 2013.

(3) Marimuthu, A.; Zhang, J.; Linic, S. Tuning Selectivity in Propylene Epoxidation by Plasmon Mediated Photo-Switching of Cu Oxidation State. *Science* **2013**, *339*, 1590–1593.

(4) Witzke, M. E.; Dietrich, P. J.; Ibrahim, M. Y. S.; Al-Bardan, K.; Triezenberg, M. D.; Flaherty, D. W. Spectroscopic Evidence for Origins of Size and Support Effects on Selectivity of Cu Nanoparticle Dehydrogenation Catalysts. *Chem. Commun.* **2017**, *53* (3), 597–600.

(5) Hadjiivanov, K.; Knözinger, H. FTIR Study of Low-Temperature CO Adsorption on Cu-ZSM-5: Evidence of the Formation of Cu2+(CO)2Species. *J. Catal.* **2000**, *191* (2), 480–485.

(6) Behrens, M.; Studt, F.; Kasatkin, I.; Kühl, S.; Hävecker, M.; Abild-pedersen, F.; Zander, S.; Girgsdies, F.; Kurr, P.; Kniep, B.; et al. The Active Site of Methanol Synthesis over Cu/ZnO/Al2O3 Industrial Catalysts. *Science* **2012**, *759*, 893–898.

(7) Ovesen, C. V.; Clausen, B. S.; Schiøtz, J.; Stoltze, P.; Topsøe, H.; Nørskov, J. K. Kinetic Implications of Dynamical Changes in Catalyst Morphology during Methanol Synthesis over Cu/ZnO Catalysts. *J. Catal.* **1997**, *168* (2), 133–142.

(8) Yoshihara, J.; Campbell, C. T. Methanol Synthesis and Reverse Water-Gas Shift Kinetics over Cu(110) Model Catalysts: Structural Sensitivity. *J. Catal.* **1996**, *161* (2), 776–782.

(9) Fujita, S.; Usui, M.; Ito, H.; Takezawa, N. Mechanisms of Methanol Synthesis from CO2 and CO at Atmospheric Pressure over Cu-ZnO.Pdf. *J. Catal.* **1995**, *157*, 403–413.

(10) Rhodes, M. D.; Bell, A. T. The Effects of Zirconia Morphology on Methanol Synthesis from CO and H 2 over Cu/ZrO2 Catalysts: Part I. Steady-State Studies. *J. Catal.* **2005**, *233* (1), 198–209.

(11) Behrens, M.; Zander, S.; Kurr, P.; Jacobsen, N.; Senker, J.; Koch, G.; Ressler, T.; Fischer, R. W.; Schlögl, R. Performance Improvement of Nanocatalysts by Promoter-Induced Defects in the Support Material: Methanol Synthesis over Cu/ZnO:Al. *J. Am. Chem. Soc.* **2013**, *135* (16), 6061–6068.

(12) Choi, Y.; Futagami, K.; Fujitani, T.; Nakamura, J. Role of ZnO in Cu/ZnO Methanol Synthesis Catalysts - Morphology Effect or Active Site Model? *Appl. Catal. A Gen.* **2001**, *208* (1–2), 163–167.

(13) Liu, W.; Flytzani-Stephanopoulos, M. Total Oxidation with Cu on CeO2 Catalysts.Pdf. *J. Catal.* **1995**, *153*, 304–316.

(14) Zhang, X.; Tian, P.; Tu, W.; Zhang, Z.; Xu, J.; Han, Y.-F. Tuning the Dynamic Interfacial Structure of Copper–Ceria Catalysts by Indium Oxide during CO Oxidation. *ACS Catal.* **2018**, 5261–5275.

(15) Hansen, P. L.; Wagner, J. B.; Helveg, S.; Rostrup-Nielsen, J. R.; Clausen, B. S.; Topsøe, H. Atom-Resolved Imaging of Dynamic Shape Changes in Supported Copper Nanocrystals. *Science* **2002**, *295* (5562), 2053–2055.

(16) Zou, L.; Li, J.; Zakharov, D.; Stach, E. A.; Zhou, G. In Situ Atomic-Scale Imaging of the Metal/Oxide Interfacial Transformation. *Nat. Commun.* **2017**, *8* (1), 1–8.

(17) Hanukovich, S.; Dang, A.; Christopher, P. The Influence of Metal Oxide Support Acid Sites on Cu Catalyzed Non-Oxidative Dehydrogenation of Ethanol to Acetaldehyde. *ACS Catal.* **2019**, *9*, 3537–3550.

(18) Lwin, S.; Keturakis, C.; Handzlik, J.; Sautet, P.; Li, Y.; Frenkel, A. I.; Wachs, I. E. Surface ReOx Sites on Al2O3 and Their Molecular Structure-Reactivity Relationships for Olefin Metathesis. *ACS Catal.* **2015**, *5* (3), 1432–1444.

(19) Knaeble, W.; Iglesia, E. Kinetic and Theoretical Insights into the Mechanism of Alkanol Dehydration on Solid Brønsted Acid Catalysts. *J. Phys. Chem. C* **2016**, *120* (6), 3371–3389.

(20) DeWilde, J. F.; Chiang, H.; Hickman, D. A.; Ho, C. R.; Bhan, A. Kinetics and Mechanism of Ethanol Dehydration on γ-Al2O3: The Critical Role of Dimer Inhibition. *ACS Catal.* **2013**, *3* (4), 798–807.

(21) Christiansen, M. a.; Mpourmpakis, G.; Vlachos, D. G. Density Functional Theory-Computed Mechanisms of Ethylene and Diethyl Ether Formation from Ethanol on γ-Al2O3(100). *ACS Catal.* **2013**, *3* (9), 1965–1975.

(22) Wang, S.; Iglesia, E. Substituent Effects and Molecular Descriptors of Reactivity in Condensation and Esterification Reactions of Oxygenates on Acid-Base Pairs at TiO2and ZrO2Surfaces. *J. Phys. Chem. C* **2016**, *120* (38), 21589–21616.

(23) Ochoa, J. V.; Bandinelli, C.; Vozniuk, O.; Chieregato, A.; Malmusi, A.; Recchi, C.; Cavani, F. An Analysis of the Chemical, Physical and Reactivity Features of MgO-SiO2 Catalysts for Butadiene Synthesis with the Lebedev Process. *Green Chem.* **2016**, *18* (6), 1653–1663.

(24) León, M.; Díaz, E.; Ordóñez, S. Ethanol Catalytic Condensation over Mg-Al Mixed Oxides Derived from Hydrotalcites. *Catal. Today* **2011**, *164* (1), 436–442.

(25) Angelici, C.; Velthoen, M. E. Z.; Weckhuysen, B. M.; Bruijnincx, P. C. A. Influence of Acid-Base Properties on the Lebedev Ethanol-to-Butadiene Process Catalyzed by SiO2-MgO Materials. *Catal. Sci. Technol.* **2015**, *5* (5), 2869–2879.

(26) Di Cosimo, J. I.; Díez, V. K.; Xu, M.; Iglesia, E.; Apesteguía, C. R. Structure and

Surface and Catalytic Properties of Mg-Al Basic Oxides. *J. Catal.* **1998**, *178* (2), 499–510.

(27) Digne, M.; Sautet, P.; Raybaud, P.; Euzen, P.; Toulhoat, H. Use of DFT to Achieve a Rational Understanding of Acid-Basic Properties of γ-Alumina Surfaces. *J. Catal.* **2004**, *226* (1), 54–68.

(28) Kang, M.; Bhan, A. Kinetics and Mechanisms of Alcohol Dehydration Pathways on Alumina Materials. *Catal. Sci. Technol.* **2016**, *6*, 6667–6678.

(29) Chizallet, C.; Digne, M.; Arrouvel, C.; Raybaud, P.; Delbecq, F.; Constentin, G.; Che, M.; Sautet, P.; Toulhoat, H. Insights into the Geometry, Stability and Vibrational Properties of OH Groups on γ-Al2O3, TiO2-Anatase and MgO from DFT Calculations. *Top. Catal.* **2009**, *52* (8), 1005–1016.

(30) Morterra, C.; Magnacca, G. A Case Study: Surface Chemistry and Surface Structure of Catalytic Aluminas, as Studied by Vibrational Spectroscopy of Adsorbed Species. *Catal. Today* **1996**, *27*, 497–532.

(31) Zaki, M. I.; Hasan, M. a.; Al-Sagheer, F. a.; Pasupulety, L. In Situ FTIR Spectra of Pyridine Adsorbed on SiO2-Al2O3, TiO2, ZrO2 and CeO2: General Considerations for the Identification of Acid Sites on Surfaces of Finely Divided Metal Oxides. *Colloids Surfaces A Physicochem. Eng. Asp.* **2001**, *190* (3), 261–274.

(32) DeWilde, J. F.; Czopinski, C. J.; Bhan, A. Ethanol Dehydration and Dehydrogenation on γ-Al2O3: Mechanism of Acetaldehyde Formation. *ACS Catal.* **2014**, *4* (12), 4425–4433.

(33) Xie, W.; Peng, H.; Chen, L. Calcined Mg-Al Hydrotalcites as Solid Base Catalysts for Methanolysis of Soybean Oil. *J. Mol. Catal. A Chem.* **2006**, *246* (1–2), 24–32.

(34) McFarland, E. W.; Metiu, H. Catalysis by Doped Oxides. *Chem. Rev.* **2013**, *113* (6), 4391–4427.

(35) Hattori, H. Solid Base Catalysts: Generation of Basic Sites and Application to Organic Synthesis. *Appl. Catal. A Gen.* **2001**, *222* (1–2), 247–259.

(36) Zhang, G.; Hattori, H.; Tanabe, K. Aldol Addition of Acetone, Catalyzed by Solid Base Catalysts: Magnesium Oxide, Calcium Oxide, Strontium Oxide, Barium Oxide, Lanthanum (III) Oxide and Zirconium Oxide. *Appl. Catal.* **1988**, *36*, 189–197.

(37) Taifan, W. E.; Bučko, T.; Baltrusaitis, J. Catalytic Conversion of Ethanol to 1,3-Butadiene on MgO: A Comprehensive Mechanism Elucidation Using DFT Calculations. *J. Catal.* **2017**, *346*, 78–91.

(38) León, M.; Díaz, E.; Bennici, S.; Vega, A.; Ordóñez, S.; Auroux, A. Adsorption of CO2 on Hydrotalcite-Derived Mixed Oxides: Sorption Mechanisms and Consequences for Adsorption Irreversibility. *Ind. Eng. Chem. Res.* **2010**, *49* (8), 3663–3671.

(39) Fan, D.; Dong, X.; Yu, Y.; Zhang, M. A DFT Study on the Aldol Condensation Reaction on MgO in the Process of Ethanol to 1,3-Butadiene: Understanding the Structure-Activity Relationship. *Phys. Chem. Chem. Phys.* **2017**, *19* (37), 25671–25682.

(40) Climent, M. J.; Corma, A.; Fornés, V.; Guil-Lopez, R.; Iborra, S. Aldol Condensations on Solid Catalysts: A Cooperative Effect between Weak Acid and Base Sites. *Adv. Synth. Catal.* **2002**, *344* (10), 1090–1096.

(41) Connell, G.; Dumesic, J. A. The Generation of Brønsted and Lewis Acid Sites on the Surface of Silica by Addition of Dopant Cations. *J. Catal.* **1987**, *105* (2), 285–298.

(42) Lwin, S.; Li, Y.; Frenkel, A. I.; Wachs, I. E. Nature of WOxSites on SiO2and Their Molecular Structure-Reactivity/Selectivity Relationships for Propylene Metathesis. *ACS Catal.* **2016**, *6* (5), 3061–3071.

(43) Barton, D. G.; Shtein, M.; Wilson, R. D.; Soled, S. L.; Iglesia, E. Structure and Electronic Properties of Solid Acids Based on Tungsten Oxide Nanostructures. *J. Phys. Chem. B* **1999**, *103* (4), 630–640.

(44) Di Cosimo, J. I.; Acosta, A.; Apesteguía, C. R. Gas-Phase Hydrogen Transfer Reduction of α,β-Unsaturated Ketones on Mg-Based Catalysts. *J. Mol. Catal. A Chem.* **2004**, *222* (1–2), 87–96.

(45) Hu, Z.; Li, B.; Sun, X.; Metiu, H. Chemistry of Doped Oxides: The Activation of Surface Oxygen and the Chemical Compensation Effect. *J. Phys. Chem. C* **2011**, *115* (7), 3065–3074.

(46) Metiu, H.; Chrétien, S.; Hu, Z.; Li, B.; Sun, X. Chemistry of Lewis Acid-Base Pairs on Oxide Surfaces. *J. Phys. Chem. C* **2012**, *116* (19), 10439–10450.

(47) Xiaoding, X.; Boelhouwer, C.; Vonk, D.; Benecke, J. I.; Mol, J. C. A Model for the Generation of Active Sites of Rhenium-Containing Metathesis Catalysts. *J. Mol. Catal.* **1986**, *36* (1–2), 47–66.

(48) Balajka, J.; Hines, M.; DeBenedetti, W.; Komora, M.; Pavelec, J.; Schmid, M.; Diebold, U. High Affinity Adsorption Leads to Molecularly Ordered Interfaces on TiO2 in Air and Solution. *Science* **2018**, *361*, 786–789.

(49) Roy, S.; Mpourmpakis, G.; Hong, D.-Y.; Vlachos, D. G.; Bhan, A.; Gorte, R. J. Mechanistic Study of Alcohol Dehydration on γ-Al2O3. *ACS Catal.* **2012**, *2* (9), 1846–1853.

(50) Wang, S.; Iglesia, E. Substituent Effects and Molecular Descriptors of Reactivity in Condensation and Esterification Reactions of Oxygenates on Acid-Base Pairs at TiO2 and ZrO2 Surfaces. *J. Phys. Chem. C* **2016**, *120* (38), 21589–21616.

(51) Manriquez, M. E.; Lopez, T.; Gomez, R. Co Oxidation on Cu/MgO-SiO2 Sol-Gel Derived Catalysts. *J. Sol-Gel Sci. Technol.* **2003**, *26* (1–3), 853–857.

(52) Zhang, M.; Huang, Y.; Li, R.; Li, G.; Yu, Y. A DFT Study of Ethanol Adsorption and Dehydrogenation on Cu/Cr2O3 Catalyst. *Catal. Letters* **2014**, *144* (11), 1978–1986.

(53) Ro, I.; Liu, Y.; Ball, M. R.; Jackson, D. H. K.; Chada, J. P.; Sener, C.; Kuech, T. F.; Madon, R. J.; Huber, G. W.; Dumesic, J. A. Role of the Cu-ZrO 2 Interfacial Sites for Conversion of Ethanol to Ethyl Acetate and Synthesis of Methanol from CO 2 and H 2. *ACS Catal.* **2016**, *6*, 7040–7050.

(54) Freitas, I. C.; Damyanova, S.; Oliveira, D. C.; Marques, C. M. P.; Bueno, J. M. C. Effect of Cu Content on the Surface and Catalytic Properties of Cu/ZrO 2 Catalyst for Ethanol Dehydrogenation. *J. Mol. Catal. A Chem.* **2014**, *381*, 26–37.

(55) Chatterjee, R.; Kuld, S.; van den Berg, R.; Chen, A.; Shen, W.; Christensen, J. M.; Jensen, A. D.; Sehested, J. Mapping Support Interactions in Copper Catalysts. *Top. Catal.* **2019**.

(56) Cargnello, M.; Doan-Nguyen, V. V. T.; Gordon, T. R.; Diaz, R. E.; Stach, E. A.; Gorte, R. J.; Fornasiero, P.; Murray, C. B. Control of Metal Nanocrystal Size Reveals Metal-Support Interface Role for Ceria Catalysts. *Science* **2013**, *341* (6147), 771–773.

(57) Foppa, L.; Margossian, T.; Kim, S. M.; Mueller, C.; Copéret, C.; Larmier, K.; Comas-Vives, A. Contrasting the Role of Ni/Al2O3 Interfaces in Water-Gas Shift and Dry Reforming of Methane. *J. Am. Chem. Soc.* **2017**, *139*, 17128–17139.

(58) Shekhar, M.; Wang, J.; Lee, W.-S.; Williams, W. D.; Kim, S. M.; Stach, E. A.; Miller, J. T.; Delgass, W. N.; Ribeiro, F. H. Size and Support Effects for the Water–Gas Shift Catalysis over Gold Nanoparticles Supported on Model Al2O3 and TiO2. *J. Am. Chem. Soc.* **2012**, *134* (10), 4700–4708.

(59) Aranifard, S.; Ammal, S. C.; Heyden, A. Nature of Pt n/CeO 2 (111) Surface under Water-Gas Shift Reaction Conditions: A Constrained Ab Initio Thermodynamics Study. *J. Phys. Chem. C* **2012**, *116* (16), 9029–9042.

(60) Ro, I.; Resasco, J.; Christopher, P. Approaches for Understanding and Controlling Interfacial Effects in Oxide Supported Metal Catalysts. *ACS Catal.* **2018**, *8*, 7368–7387.

(61) Kale, M. J.; Christopher, P. Utilizing Quantitative in Situ FTIR Spectroscopy to Identify Well-Coordinated Pt Atoms as the Active Site for CO Oxidation on Al2O3-Supported Pt Catalysts. *ACS Catal.* **2016**, *6* (8), 5599–5609.

(62) Sengupta, G.; Gupta, D. J.; Kundu, M. L.; Sen, S. P. Effect of Reduction Conditions upon Metal Area in CuO-ZnO Catalyst. *J. Catal.* **1981**, *225*, 223–225.

(63) Osinga, T. J.; Linsen, B. G.; van Beek, W. P. The Determination of the Specific Copper Surface Area in Catalysts. *J. Catal.* **1967**, *7* (3), 277–279.

(64) Chinchen, G. C.; Hay, C. M.; Vandervell, H. D.; Waugh, K. C. The Measurement of Copper Surface Areas by Reactive Frontal Chromatography. *J. Catal.* **1987**, *103*

(1), 79–86.

(65) Scarano, D.; Bordiga, S.; Lamberti, C.; Spoto, G.; Ricchiardi, G.; Zecchina, A.; Otero Areán, C. FTIR Study of the Interaction of CO with Pure and Silica-Supported Copper (I) Oxide. *Surf. Sci.* **1998**, *411* (3), 272–285.

(66) Boccuzzi, F.; Ghiotti, G.; Chiorino, A. CO Adsorption on Small Particles of Cu Dispersed on Microcrystalline ZnO. *Surf. Sci.* **1985**, *156*, 933–942.

(67) Subramanian, N. D.; Kumar, C. S. S. R.; Watanabe, K.; Fischer, P.; Tanaka, R.; Spivey, J. J. A DRIFTS Study of CO Adsorption and Hydrogenation on Cu-Based Core-Shell Nanoparticles. *Catal. Sci. Technol.* **2012**, *2* (3), 621–631.

(68) Hadjiivanov, K.; Knozinger, H. FTIR Study of CO and NO Adsorption and Coadsorption on a Cu/SiO2 Catalyst: Probing the Oxidation State of Copper. *Phys. Chem. Chem. Phys.* **2001**, *3* (6), 1132–1137.

(69) Milushev, A.; Hadjiivanov, K. FTIR Study of CO and NOx Adsorption and Co-Adsorption on Cu/Silicalite-1. *Phys. Chem. Chem. Phys.* **2001**, *3* (23), 5337–5341.

Chapter 2. Materials and Experimental Methods

2.1 Summary

This chapter details catalyst synthesis, characterization, and reactivity techniques. Additionally, the theory of operation of all analytical instruments and techniques is discussed, including pulse chemisorption, BET surface area approximation, probe molecule FTIR, X-ray absorption spectroscopy, X-ray powder diffraction, and gas chromatography. Detailed schematics of the reactor system, Arduino automation, and liquid bubbling using a 4-way valve are included for clarity. Finally, a short discussion is provided on how reaction rates are recorded with the gas chromatograph and how those results are used to evaluate reaction kinetics, both in terms of apparent activation barriers and the generation of pressure dependent rate expressions.

2.2 Materials

2.2.1 Gases

All gases used were ordered from Airgas. For ex-situ calcination: 20% (±2%) O_2/N2. For reaction experiments: He (UHP, 99.999%), H_2 (UHP, 99.999%), and O_2 (UHP, 99.999%). For volumetric chemisorption experiments: UHP He, Ar (UHP, 99.999%), UHP O_2, 10% (±2%) H_2/Ar, 10% (±2%) CO_2/He, 10% (±2%) CO/He, 10% (±2%) NH_3/He, 1000 ppm (±2%) N_2O/Ar, and 1000 ppm (±2%) NO/He. For probe molecule IR experiments: UHP Ar, UHP O_2, 10% H_2/Ar, 10% CO_2/He, 10% (±2%) CO/Ar, and 0.5% (±2%) NO/Ar.

2.2.2 Chemicals

Catalyst Synthesis: copper (II) nitrate trihydrate ($Cu(NO_3)_2$*$3H_2O$, Sigma-Adrich, 99% purity, CAS: 10031-43-3), aluminum nitrate nonahydrate ($Al(NO_3)_3$*$9H_2O$, Sigma-

Aldrich, 99.997% trace metal basis, CAS: 7784-27-2), ZrO_2 (US Research Nanomaterials, high purity 99.95%, 20 nm, Stock # US3659, CAS: 1314-23-4), TiO_2 (rutile, US Research Nanomaterials, high purity 99.9+%, 30 nm, Stock # US3520, CAS: 13463-67-7), HPLC grade water (J.T. Baker, CAS: 7732-18-15). Characterization: pyridine (anhydrous, 99.8%, Sigma-Aldrich, CAS: 110-86-1) Reaction: pyridine, ethanol (molecular biological grade, Fisher Scientific, CAS: 64-17-5), ethyl acetate (99.9%, Extra Dry, Acros Organics, CAS: 141-78-6).

2.2.3 Tools

Reactor Design: ½" Glass Tube Reactor, 2" x 2" x 4" Aluminum Block, 1" x 2" x 4" Ceramic Insulation. Temperature Control: PID Controller (CN7800, Omega Engineering), CN7800A Software (Omega Engineering), Heating Trace (Omega Engineering), Heating Cartridges (McMaster-Carr), Thermocouples (Omega Engineering). Flow Control: PowerPod-400 (Teledyne Hastings), 3-way solenoid valves (McMaster-Carr), 3-way valves (Swagelok), 4-way valve (Swagelok), Arduino Uno (Amazon).

2.2.4 Analytical Instruments

Characterization: AutoChem 2920 (Micromeritics), 3Flex Porosimeter (Micromeritics), Nicolet iS10 FTIR (Fisher Scientific), Praying Mantis diffuse reflectance adapter (ThermoFisher Scientific), Low Temperature Reactor (Harrick), Inductively Coupled Plasma Atomic Emission Spectrometer (ThermoFisher Scientific), Panalytical Empyrean Powder Diffractometer (Malvern Panalyitcal), FEI Titan (ThermoFisher Scientific). Reactions: MG #3 GC (SRI Instruments), Gemini 88 Plus (KD Scientific).

2.3 Synthesis Techniques

2.3.1 Precursor Impregnation

2.3.1.1 Incipient Wetness "Dry" Impregnation

In dry impregnation (DI), a metal precursor solution, generally an inorganic salt, is added to a metal oxide support with a volume of solution that corresponds to the cumulative volume of the pores on the support material. Typically, discovering the proper amount of solution needed to fill the support pores can be easily calculated by simply adding water dropwise to a known amount of support powder until the support has been completely wetted and forms a gel-like paste. The driving force for metal deposition on the support is the capillary pressure difference across the hemispherical meniscus in a pore, which is represented by the Young-Laplace equation.[1] The benefits of this impregnation technique is it is simple and economical due to the limited use of potentially expensive active components. However, DI is limited by the solubility of the metal precursor, though carrying out consecutive impregnations can be used to overcome this limitation.[2]

2.3.1.2 Wet Impregnation

Wet impregnation (WI) involves using an excess of solution with respect to the support pore volume when depositing the precursor. Typically, WI consists of creating a metal support colloid in excess solution with continuous stirring. The precursor is added slowly (or at any desired injection speed) to the support colloid and left to age for a certain time while stirring, after which it can be filtered and dried. WI is particularly useful when precursor-support interactions are important to the catalyst synthesis and can be support and precursor concentration dependent.[2]

2.3.2 Colloidal Cu Synthesis

The colloidal Cu synthesis technique was employed to synthesize small Cu nanoparticles with a small size distribution, as described previosuly.[3–6] First, Cu nitrate can be mixed in HPLC grade water (forming a light blue solution) for 1 hour under argon gas protection. Next, PVP in a 1:200 (Cu:PVP) molar ratio is mixed in with the Cu nitrate solution for 45 minutes. PVP is a well-known polymer used in colloidal synthesis to control the size and shape of nanomaterials due to PVP's nitrogen and oxygen polar groups. In this system, the polar groups donate electron lone-pairs to Cu^{2+}, forming Cu^{2+}-PVP complexes. Due to the strong adsorption of Cu to PVP, PVP acts as a polymeric capping agent, helping induce the formation of small and uniform Cu clusters.[7] After mixing PVP with the Cu nitrate solution, 0.1M ascorbic acid was added and stirred for 1 hour. Ascorbic acid is a well-known reducing agent due to its ability to scavenge free radicals and reactive oxygen molecules, which allows it to not only reduce Cu^{2+} ions to Cu^0, but also aids in protecting Cu^0 particles from oxidation.[7,8] After mixing the Cu solution with ascorbic acid for 1 hour, the solution began turning light red, indicating that Cu was being reduced. Then, to further promote Cu reduction to Cu^0, 0.4M $NaBH_4$ was added to the Cu solution dropwise, immediately turning the solution to a dark brown color. Finally, after stirring with $NaBH_4$ for 1 hour, γ-Al_2O_3 was added to the colloid suspension and stirred overnight to promote Cu^0 deposition onto the support.

Next, the Cu/Al_2O_3 colloids are vacuum filtered and the Cu filtride is rinsed with 10 mL of HPLC water before leaving in a 60 °C oven to fully dry. After drying, the supported Cu powder is sieved and calcined for 4 hours at 350 °C to burn off PVP. The

supported Cu catalyst was then fully prepared and ready for Pt deposition through galvanic replacement, as described below.

2.3.3 Galvanic Replacement

When it is desired to selectively deposit a dilute metal onto a host metal (as opposed to onto the support) galvanic replacement (GR) has shown to be quite effective.[3,4,9] GR utilizes metal reduction potential as a driving force to induce selective surface deposition. In this thesis, GR was employed to selectively deposit dilute Pt species onto Cu nanoparticles to create Pt-Cu single atom alloys (SAA). First, Cu nanoparticles were synthesized through a colloidal synthesis technique as described above. Next, after reducing surface Cu to Cu^0 *in situ* in H_2, chloroplatinic acid (Pt^{4+}) was added to the Cu^0 solution and stirred at 100 °C for 30 minutes. The reduction potential for Cu (Cu^{2+}/Cu^0) is +0.34 V, which is lower than that of $PtCl_6^{2-}$ (Pt^{4+}/Pt^0), +0.68 V indicating that there exists a positive driving force for Pt^{4+} precursors to be reduced by the Cu host metal through the replacement reaction below. Consequentially, all Pt species (previously in solution) are deposited onto the Cu host metal while surface Cu^0 is reduced to Cu^{2+}, forming Cu chloride in solution, as shown by equation 2.1.

$$2Cu^0(s) + H_2PtCl_6(aq) \rightarrow 2CuCl_2(aq) + 2HCl(aq) + Pt^0(s) \qquad \textbf{equation 2.1}$$

2.4 Characterization Techniques

2.4.1 Site Quantification through Surface Chemisorption and Surface Reactions

2.4.1.1 Probe Molecule Pulse Chemisorption

Probe molecule chemisorption is a characterization technique that may be used to measure metal catalyst dispersion over a given support. Selection of the probe molecule

depends on the specific metal catalyst being studied, although carbon monoxide (CO) is the most commonly used probe molecule for catalytic surfaces due to its surface sensitivity and well-studied adsorption stoichiometry and strength. In this thesis, probe molecule pulse chemisorption is run in a Micromeritics AutoChem 2920, which systematically injects a pulse, of a known and constant volume, into an inert gas stream that then passes over the catalyst material. Figure 2.1 below presents a depiction of the experimental results for a CO pulse chemisorption experiment over a 0.5 wt% platinum (Pt) loaded over a metal oxide support, gamma-alumina (γ-Al_2O_3), which was a standard with a known dispersion provided by Micromeritics. 10% CO/He was pulsed into a constant stream of He every 5 minutes, after which the CO pulse flowed over the Pt catalyst and any CO that flowed out of the reactor was measured by an in-line thermal conductivity detector (TCD).

In Figure 2.1, no CO peak is visible until ~10 minutes, although CO was pulsed into the reactor at ~ 0 minutes and ~ 5 minutes. A lack of CO in the effluent after the first 2 pulses revealed that the Pt catalyst adsorbed all the CO molecules from both pulses, thus not allowing any residual Pt to escape through the effluent. Then, at ~ 10 minutes a small fraction of CO was able to escape into the effluent as the Pt surface began to be saturated with CO adsorbates. After one more pulse ~ 15 minutes, the TCD signal of CO became constant after each sequential CO pulse, indicating that no more CO molecules were adsorbing to the Pt surface, and all the CO introduced into the reactor was able to flow as the effluent into the TCD detector. By using the known volume of CO injected during each pulse, the total number of CO adsorbed to the Pt surface can be calculated by measuring the amount of CO that failed to flow into the thermal conductivity detector (TCD), where

for the first 2 pulses, the entire loop volume failed to flow into the TCD. Note, the dispersion calculation here was performed with a CO:Pt adsorption stoichiometry of 1:1.

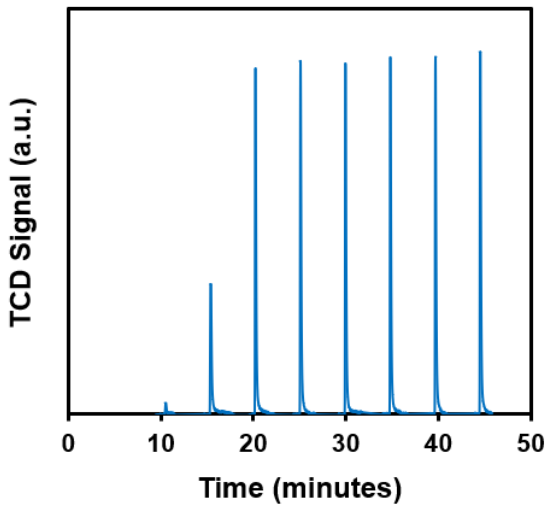

Figure 2.1 CO Pulse Chemisorption for 0.5 wt% Pt on γ-Al_2O_3. TCD signal as a function of experiment time where ~0.5 cm3 of CO was pulsed every 5 minutes onto Pt standard catalyst. TCD peaks correspond to CO in the effluent that did not adsorb to Pt catalyst.

2.4.1.2 N_2O – TPR for Cu Surface Characterization

Since Cu only weakly adsorbs CO, CO chemisorption is not a feasible technique for Cu surface characterization.[10–12] Therefore, in this thesis, an alternative technique has been established in which nitrous oxide (N_2O) oxidation coupled with temperature programmed reduction (TPR) are employed as probes for Cu characterization.[13,14] In this technique, native, oxidized Cu is first completely reduced to Cu^0 by treating the catalyst with hydrogen (H_2) gas at elevated temperatures, producing water (H_2O), equation 2.2. Next, Cu^0 is titrated with N_2O gas to effectively oxidize all surface Cu^0 sites to Cu^+ by forming cuprous oxide (Cu_2O), equation 2.3. Finally, a temperature programmed reduction is conducted to effectively reduce all surface Cu_2O back to Cu^0, forming H_2O, equation 2.4.

$$CuO + H_2 \Rightarrow Cu^0 + H_2O \qquad \textbf{equation 2.2}$$

$$2Cu^0 + N_2O \Rightarrow Cu_2O + N_2 \qquad \textbf{equation 2.3}$$

$$Cu_2O + H_2 \Rightarrow 2Cu^0 + H_2O \qquad \textbf{equation 2.4}$$

The quantity of Cu^+ sites generated during N_2O oxidation was used to estimate the number of active Cu surface sites. Using reaction stoichiometry, total H_2 consumed during TPR was used to directly approximate the number of active Cu sites with the assumption that 1 mole H_2 consumed corresponded to 2 moles of active Cu sites. This was then used to measure the expected Cu particle dispersion with $D = Cu_S/Cu_T$ where D represents dispersion, Cu_S represents the estimated number of active surface Cu through TPR and Cu_T represents the total number of Cu sites as estimated by nominal weight loading. Cu particle dispersion was then used to approximate the average particle diameter of Cu with equation 2.5 below, which assumed a hemispherical Cu particle geometry with the flat portion of the particle considered inaccessible. M is the Cu molecular mass (63.55 g/mol), D is the fractional dispersion of Cu, ρ is the Cu metal density (8.94 g/cm^3), σ is the surface area per Cu atom (6.85 Å^2/atom), and N_0 is Avogadro's constant (6.02x10^{23} molecules/mol). Other work has employed a similar methodology, but directly measured N_2 produced in equation 2.3 by cooling the effluent to 77K as a means of quantifying Cu surface sites.[15] Alternatively, H_2 chemisorption on Cu at low temperatures and high pressures has been employed to estimate Cu metal dispersion.[16]

$$d_P = \frac{6M}{D\rho\sigma N_0} \qquad \textbf{equation 2.5}$$

2.4.1.3 Probe Molecule Temperature Programmed Desorption

While CO pulse chemisorption and N_2O titration followed by TPR are effective methods for quantifying active metal surface areas, support acid and base sites require NH_3 and CO_2 as probe molecules, respectively. For both probe molecules, experiments begin with catalyst pre-treatment followed by the introduction of the probe molecule at 50 °C for 30 minutes to reach complete surface saturation. Next, an inert gas is used to purge out any physi-sorbed species before starting the temperature programmed desorption (TPD). Finally, the TPD is run under an inert gas environment with a constantly increasing temperature ramping at 10 °C/minute. It is expected that the effluent leaving the catalyst surface is the probe molecule and the higher the temperature at which the probe molecule desorbs from the surface, the stronger is the acid or base site. Additionally, the TPD peak area representing the number of probe molecules (NH_3 or CO_2) can be used to quantify the total number of acid or base sites on the surface, respectively, with the assumption that each probe molecule adsorbs to the support surface with a probe molecule to active site ratio of 1:1.

2.4.2 BET Surface Area Approximation

The Brunauer-Emmette-Teller (BET) theory enables an experimental determination of the number of molecules required to form monolayer coverage on an adsorbate surface. By increasing the system pressure, monolayer coverage by the adsorbates on the material's surface is approached, which allows for the approximation of the specific surface area of the material, as described by equation 2.6 where W and W_m are the adsorbed and monolayer weights, P and P_0 are the equilibrium and saturation pressures,

and c is the BET constant, which is dependent on heat of adsorption and the system temperature. Plotting the left-hand side of equation 2.6 versus (P/P_0), the slope, s, and y-intercept, i, can be used to calculate W_m where $W_m = 1/(s+i)$. Finally, W_m can be used to calculate the specific surface area as shown by equation 2.7 where S is the specific surface area, N is Avogadro's number ($6.022 * 10^{23}$ molecules/mole), A_x is the cross-sectional adsorbate area, M is the adsorbate molecular weight, and m is the sample mass. [17]

$$\frac{1}{W\left[\frac{P}{P_0}-1\right]} = \frac{1}{W_m C} + \frac{C-1}{W_m C}\left(\frac{P}{P_0}\right) \qquad \textbf{equation 2.6}$$

$$S = \frac{W_m N A_x}{M} \qquad \textbf{equation 2.7}$$

2.4.3 Diffuse Reflectance Infrared Fourier Transform Spectroscopy (DRIFTS)

2.4.3.1 Principles and Design

Throughout this thesis, diffuse reflectance infrared Fourier transform spectroscopy (DIRFTS) was utilized as a primary tool for qualitative characterization of catalyst and metal oxide support surfaces. IR spectroscopy is a particularly powerful characterization technique as it can act as a sensitive probe of the interaction between sorbed molecules and the catalysts with a large signal to noise ratio.[18,19] A variety of probe molecules may be used for catalyst characterization with requirements consistent of the probe molecule having a dipole moment as well as the ability to chemisorb to the desired surface and/or site.

DRIFTS is an IR based technique, which recollects light that is diffusely scattered by the loaded sample and then collimates the light back to a coherent signal using a set of parabolic mirrors. DRIFTS is advantageous over other FTIR techniques as it is quite easy

to prepare and does not require the samples to be IR transparent. Throughout this thesis, IR spectra will be measured both above and below ambient temperatures, where a custom-made Harrick reactor with an attached liquid nitrogen dewar is used to reach catalyst bed temperatures near -130 °C. This same reactor is also able to operate at elevated temperatures up to approximately 500 °C. Note that for all IR experiments, argon was used as the inert gas because it has a low thermal conductivity, making it more facile to heat and cool the reactor and maintain stable cryogenic temperatures.

2.4.3.2 CO Probe Molecule IR Spectroscopy

CO probe molecule FTIR has been employed widely to study the surface characteristics of various supported metal catalysts. In this thesis, CO-IR was employed mainly to study the surfaces of Cu catalysts. Due to the weak CO adsorption binding energy on Cu surfaces, all CO probe molecule IR experiments were conducted at cryogenic (~ -130 °C) temperatures. To reach stable cryogenic temperatures, all active gases were balanced with Ar (low thermal conductivity) under a vacuum pressure of (-95 kPag) while filling a liquid nitrogen dewar that is directly connected to Low Temperature Harrick Reactor.

Prior to lowering the temperature and saturating the Cu surface with CO, the Cu catalyst was treated accordingly (see Chapter 4) with a combination of either *in-situ* reduction or *in-situ* oxidation followed by reduction. Following reduction, the catalyst temperature was dropped to ~ -130 °C under a continuous stream of Ar, until the temperature became stable. Next, a catalyst background was collected in the Ar environment, which would then be automatically subtracted from the subsequent spectra

taken with exposure to CO. After collection of the background, CO was flowed over the catalyst until no change in the CO-IR spectra was observed (10-15 minutes). Next, Ar was flowed over the catalyst until no change in the CO-IR spectra was observed (10-15 minutes) to purge any gas phase or phys-sorbed CO species. The spectra observed after purging in Ar are the ones that are presented throughout this thesis.

2.4.3.3 Pyridine and CO_2 Probe Molecule IR Spectroscopy

Pyridine and CO_2 probe molecule IR were conducted in an analogous manner to that of CO probe molecule IR, except all spectra were taken at elevated temperatures. Note that because pyridine was stored in the liquid phase, a bubbler was used to effectively vaporize pyridine at its vapor pressure under ambient conditions (~2.3%) as depicted in Figure 2.2. Just as with CO probe molecule IR, after *in-situ* catalyst pre-treatment, the catalyst temperature was reduced to and held at 50 °C and the probe molecule (pyridine of CO_2) was flowed over the catalyst until no change in the probe-IR spectra was observed followed by an Ar purge with the same conditions. The spectra observed after purging in Ar are the ones that are presented throughout this thesis.

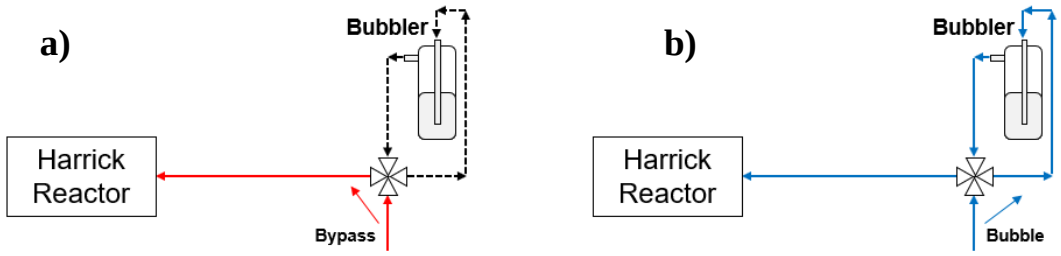

Figure 2.2 Schematic representation of a manual 4-way valve when using a liquid bubbler for FTIR experiments where in orientation **a)** the inlet gas bypasses the bubbler and flows directly into the Harrick reactor and in orientation **b)** the inlet gas flows into the bubbler, bubbles the liquid at its saturation pressure, and carries the vaporized liquid into the Harrick reactor. The two orientations are induced by manually rotating a 4-way valve 90°.

2.4.4 Transmission Electron Microscopy (TEM)

High resolution transmission electron microscopy (HR-TEM) is a technique employed to provide morphological, compositional, and crystallographic information for metal nanoparticle surfaces. TEM transmits a focused, high energy beam of electrons through a sample, where the electrons scatter off the atomic nuclei of the sample. The use of electrons is a powerful tool in microscopy because electron wavelengths are smaller than the atomic separations of solids, which allows for the extraction of morphological and structural information of the sample at the atomic scale.[20] In Chapter 4 of this dissertation, HR-TEM was employed to show the morphology of Cu nanoparticles loaded on a ZrO_2 support.

Scanning Transmission Electron Microscopy (STEM) combines the principles of TEM and scanning electron microscopy (SEM), which allows it to scan a finely focused beam of electrons across a sample and spatially correlate signals including secondary electrons, scattered beam electrons, X-rays, and electron energy loss that cannot be accomplished by the TEM an energy dispersive X-ray spectrometer (EDS), elemental

mapping of surface species can be performed by observing the differences in their z-contrast (average atomic mass). In STEM-EDS, the X-ray spectrometer can detect characteristic x-rays that are emitted by atoms in the sample as they are ionized by an electron beam.[21] Overall, STEM-EDS is a powerful tool to estimate particle size for nanoparticles, as well as the particle size of bulk metal alloys, where differences in z-contrast can be used to deconvolute different metal species in the microscopy images. In this dissertation, STEM-EDS had a limited use to confirm the presence of small, well-dispersed Cu species on a ZrO_2 support, see Chapter 4.

2.4.5 X-Ray Absorption Spectroscopy (XAS)

X-ray absorption spectroscopy (XAS) can provide the details of the local structure and change in local structure of very dilute or atomically dispersed metal species that would otherwise be unobservable with other characterization techniques due to their limits in sensitivity. X-ray absorption near edge structure (XANES) spectroscopy probes the unoccupied local density of states making it sensitive to the local geometry of a metal center, its corresponding oxidation state, and its interactive with different adsorbates.[22] However, using XANES alone to directly obtain structural information is difficult due to the limited resolution of the technique. Therefore, a second technique, extended X-ray absorption fine structure (EXAFS) spectroscopy is used, which can provide details on local metal coordination. In this dissertation, XANES is used to determine the oxidation state of Pt species in PtCu single atom alloys while EXAFS is used to determine the local Pt coordination to neighboring O, Cu, and Pt species, see Chapter 6.

2.4.6 X-Ray Powder Diffraction (XRD)

X-ray diffraction is a technique used to reveal the structural orientation, or phase, of a given compound by observing how X-rays are scattered from the atoms of a crystalline solid with long range order. The governing principle is that when an X-ray beam encounters three dimensional atoms in a given compound, most of the X-rays will destructively interfere and effectively cancel each other out. However, in some specific directions the X-rays will interfere constructively and reinforce one another, a phenomenon that can be observed by an XRD instrument, which measures the intensity of scattered waves as a function of scattering angle. Note that the scattering angle is defined in terms of the Bragg law as shown by equation 2.8, where θ is the scattering angle, d is the distance between the atomic planes, n is a positive integer, and λ is the wavelength of the incident wave.

$$2d\sin\theta = n\lambda \qquad \textbf{equation 2.8}$$

2.4.7 Inductively Coupled Plasma-Absorption Emission Spectroscopy (ICP-AES)

ICP characterization is used for elemental analysis of liquid samples to quantitatively determine the concentration of a given element in an unknown solution on the order of parts per million (ppm) or parts per billion (ppb). During ICP analysis, plasma is used to ionize a compound, exciting electrons into higher energy, excited states. When the electrons relax to lower energy levels, they release energy in the form of light at characteristic wavelengths or emission lines that are element dependent. The intensity of the respective emission line is directly proportional to the element's concentration in solution in the ppm and ppb range. In Chapter 6 of this dissertation, ICP is employed to confirm the relative quantity of Pt and Cu in the as-synthesized PtCu single atom alloys.

2.5 Catalyst Activity and Reaction Kinetics

2.5.1 Reactor Design and Automation

In this thesis, all reaction experiments were conducted in a home-built continuous flow packed bed reactor with fine temperature and gas/liquid flow control. All inlet gases were Ultra High Purity (UHP) grade gases such as O_2 and H_2 for pre-treatment and He, which acted as a carrier gas for liquids and was used to control active gas partial pressures. All gases were regulated by mass flow controllers (MFCs) and introduced into the reactor through an intricate system made up of primarily 1/8" stainless steel tubing, three-way (both manual and automated), and four-way valves. All liquid reactants were biology grade or HPLC grade for H_2O and were fed by flowing inert He through a liquid bubbler or across a syringe pump.

All gas lines downstream of the MFCs mixed in a cross immediately before being flowed into the reactor. Note that three actuated solenoid valves were designed to allow for automated control of the flow through the bubblers and each MFC was automated by USB control using an MFC PowerPod. The actuated valves and PowerPod communicated with the computer through a home-made python code. The MFCs could also be used to flow gas across the syringe pump, which was controlled by the computer using the National Instruments Labview software. Note that all lines carrying gasified liquid were heat traced and maintained at elevated temperatures (~160 °C) when the system was active as a means of preventing the liquid from condensing while traveling through the tubing.

The reactor system consisted of a ½" glass tube with catalyst loaded vertically using quartz wool as a seat. The tube was housed inside an aluminum block that held the reactor

firmly in place and provided fast and even heat transfer across the catalyst bed through conduction. Note that custom NPT ferrules were used to connect the stainless-steel tubing to the glass reactor. Three additional holes were drilled perpendicular to the reactor through the aluminum bock, which housed two vertically spaced 100W, 240V heating cartridges (catalyst was centered in between the vertical spacing of the cartridges) and a k-type thermocouple sitting vertically in between the two cartridges. The heaters were controlled using an Omega Engineering programmable PID controller that could not only effectively control temperature, but also log the observed temperature (through the thermocouple), using software provided by Omega. Note that the entirety of the aluminum block was also covered by ½" thick and rigid ceramic insulation sheets that were cut to the appropriate size to house the block, reactor, heaters, and thermocouple. Through a temperature calibration using an independent thermocouple, the observed temperature gradient was less than 5 °C, showing accurate temperature control. A schematic of the reactor system is provided below in Figure 2.3.

2.5.2 Reactor System Schematic

The reactor system design shown in Figure 2.3 was employed to effectively flow liquid phase reactants into a packed bed, heterogeneous reactor. Helium was used as the carrier gas for each bubbler containing different liquids (i.e. H_2O and EtOH) while 3-way solenoid valves were employed as means to automate the reaction experiments, particularly with partial pressure dependent studies where the flow into the bubbler was varied (between different mass flow controllers) to effectively control the inlet partial pressure of the active gas. Other 4-way and 3-way valves simply allow for the user to bypass either a

bubbler or the reactor itself, respectively. A check valve was connected to the reactor effluent to allow for effective reactor bypassing by preventing back flow, up through the reactor. Additionally, a syringe pump (automated with LabView software) was connected to the inlet of the reactor directly with a manual 2-way shut-off valve that allowed for the isolation of the syringe pump from the reactor when the pump was not in use. Finally, a simple schematic of the reactor itself was shown with the cylindrical glass reactor held in an aluminum block surrounded by insulation.

The automation design using an Arduino Uno controlled relay was shown in Figure 2.4 where the wiring is explicitly described. Communicated from Arduino to computer was established through USB and Python code was used to control and automate the solenoid valves. Note that each individual solenoid valve was connected to its own relay port (each relay has 4 ports), though an example of only one solenoid valve connection is displayed.

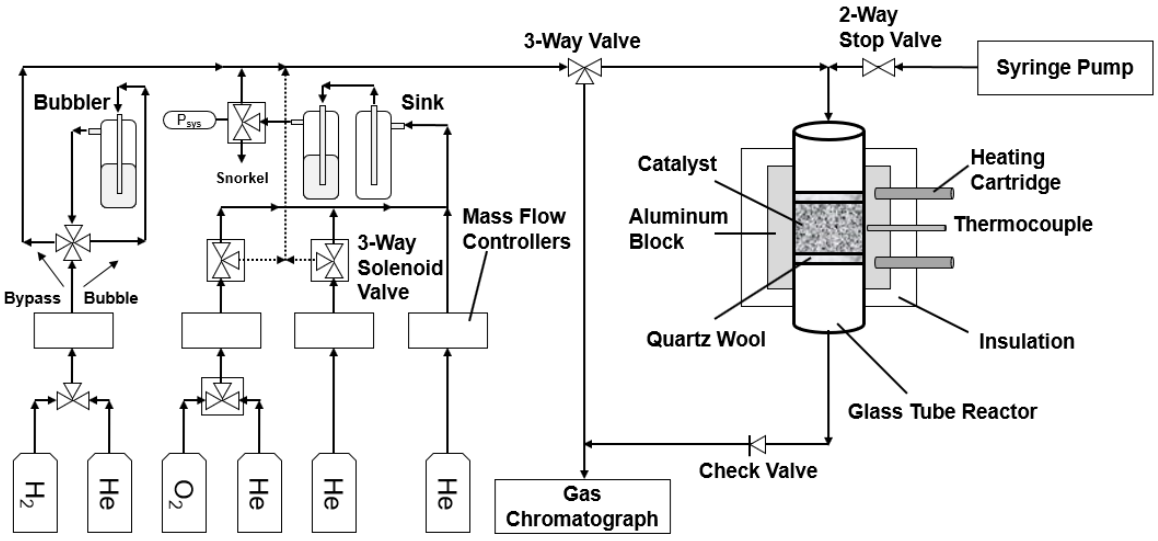

Figure 2.3 Home-built reactor apparatus diagram with fully automated, computer-controlled, mass flow controllers (Python), solenoid valves (Python), reactor temperature (Omega CN7800), syringe pump (LabView), and gas chromatograph (SRIGC, Peaksimple). Note that dotted lines correspond to a secondary pathway from the 3-way solenoid valves that effectively bypass the liquid bubbler + sink configuration.

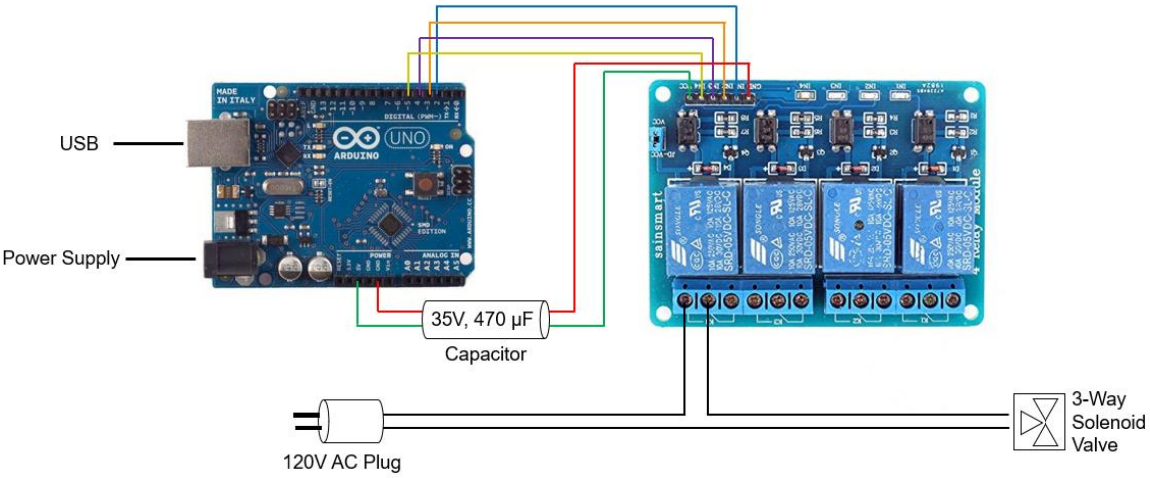

Figure 2.4 Home-built wiring system diagram of an Arduino Uno controlled relay that automated 3-way actuated solenoid valves in the reactor system (Figure 2.3) using python code.

2.5.3 Analytical Instrumentation – Gas Chromatography

In this thesis, all reaction experiment results were obtained using gas chromatography (GC). Chromatography is a technique that works to separate components of a mixture by a series of equilibrium operations that results in the separation of the mixture entities based on their differential sorption between the stationary phase with a large surface area and a mobile phase.[23] For the GC used in this system, the mobile phase is He inert gas and the stationary phase is a packed Haysep D column. Mixture gases are separated based on their sorption ability with more polar molecules and molecules with higher C number trending towards longer sorption. A flame ionization detector (FID) is used downstream of the Haysep D to measure the concentration of gases produced from the reactor. The FID combusts all products with a hydrogen flame and measurements are reported as methane produced. Therefore, careful calibration was important both for identifying specific molecules' retention times (the amount of time it took for the molecule to pass through the Haysep D) as well as detector sensitivity factor to specific gases.

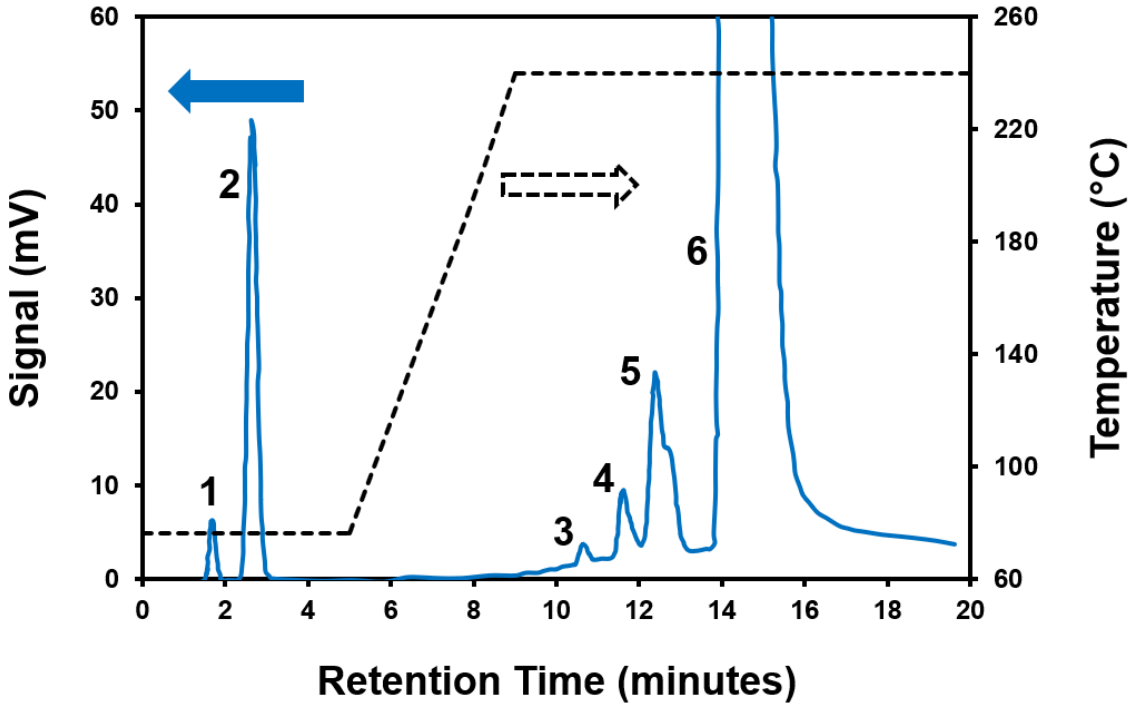

Figure 2.5 GC spectrum of effluent during ethyl acetate conversion over γ-Al_2O_3 at 340 °C. Each peak corresponds to different products in the effluent: 1-carbon dioxide, 2-ethylene, 3-acetaldehyde, 4-ethanol, 5-ether, and 6-ethyl acetate. The primary axis corresponds to the GC signal of all peaks as a function of column retention time. The secondary axis corresponds to the GC oven temperature at each retention time.

Figure 2.5 provides an example of a GC spectra using a Haysep D column and an FID to measure the concentration of products in the effluent of ethyl acetate conversion over γ-Al_2O_3. Here, the primary axis corresponds to the signal intensity in millivolts while the secondary axis corresponds to the GC oven and Haysep D column temperature, both plotted against the column retention time in minutes. Initially, the oven is maintained at a mild 76 °C to effectively separate light molecules in the effluent such as CO, CO_2, ethane, and ethylene. As shown in the spectrum above, CO_2 (peak 1) and ethylene (peak 2) had retention times of 1.7 and 2.6 minutes, respectively. Note that all peaks were identified by introducing a pure stream of the desired molecule into the GC and then matching the observed peak retention time with what is observed under reaction conditions. Next,

because the other products were expected to be heavier molecules (C_2 and C_4 molecules) and more polar (alcohol and carbonyl groups), the oven temperature was increased to 240 °C at a rate of 40 °C/min to make these molecules mobile in the Haysep D column, thus reducing the observed retention times for each molecule. Acetaldehyde (peak 3, 10.6 min), ethanol (peak 4, 11.6 min), and diethyl ether (peak 5, 12.4) were the 3 other products observed. Note that the large peak (peak 6) with a retention time of 14.0 minutes corresponded to ethyl acetate from the reactant stream, as only a small percentage of the ethyl acetate was converted into the 5 observed products.

2.5.4 Mass and Heat Transfer Limitations and Differential Reactor Regime

Prior to making kinetic measurements as reported in this thesis, preliminary tests were employed to ensure that reaction results were only dependent on intrinsic reaction kinetics as opposed to mass or heat transfer effects. As previously discussed, mass and heat transfer effects can modify the apparent activation barriers, inducing experimental deviation from the intrinsic reaction barrier.[24–26] When heterogenous reaction rates are dependent only on the surface reaction kinetics, the rates are independent of the velocity of the inlet gas flow and the catalyst particle size. However, when particles have large pore volumes, the reaction rates become inversely dependent on the particle size, suggesting the rates are limited by internal diffusion effects. Additionally, when the particle diameter is large, the rates become dependent on both particle size and the inlet gas velocity, suggesting the rates are limited by external diffusion effects (and potentially internal diffusion effects). The transition from the reaction limited regime to the diffusion limited regime can be visualized in Figure 2.6. Figure 2.6 also offers a means of controlling

reaction and catalyst parameters as a means of achieving rates controlled in the reaction limited regime by either increasing the inlet gas velocity (U) or decreasing the catalyst particle size, d_p.

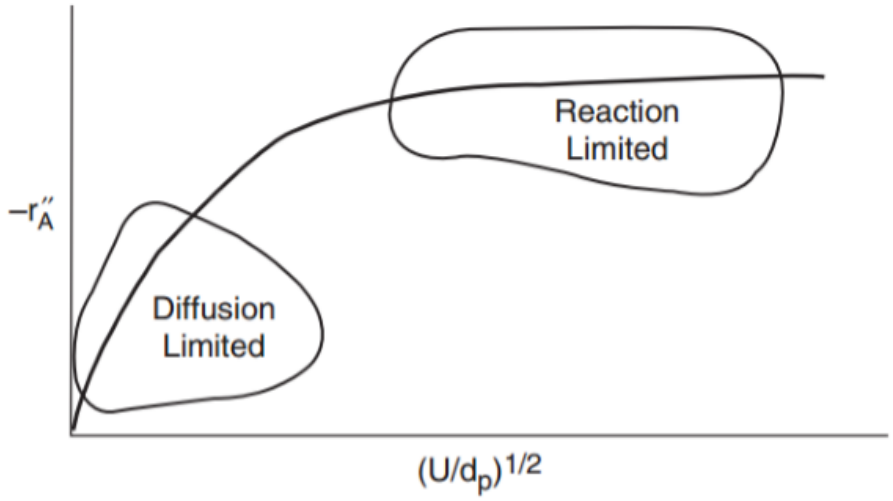

Figure 2.6 Reaction rate ($-r_A''$) as a function of inlet gas flow (U) and particle diameter (d_p). It is observed that in the reaction limited regime, rate is independent of U and d_p while in the diffusion limited regime, rate is dependent on either U or d_p or both parameters. Ref 25, ©2016. Reprinted by permission of Pearson Education, Inc., New York, New York.

2.5.5 Differential Reactor and Calculating Reaction Rates

Operating under the differential reactor regime for packed bed reactors requires the reaction conversion to be low (<10%), allowing for the assumption that the reactant concentration throughout the bed is constant and that the reactor operates in an isothermal manner.[25] This allows for the reactor design equation to be a linear expression as represented by equation 2.9 in terms of reactant A, where $-r_A$ is the reaction rate, F_{A0} is the inlet molar flow rate, X is reactant conversion, and W is the packed bed (catalyst) mass.

$$-r_A\left(\frac{mol}{s*g_{cat}}\right) = \frac{F_{A0}*X}{W} \qquad \textbf{equation 2.9}$$

2.5.6 Catalyst reactivity, activity, and turn over frequency (TOF)

In this thesis, catalyst reactivity will be defined as the ability of a catalytic surface to attack, through adsorption or dissociation, a reactant molecule. Catalyst activity will be defined as the ability of the catalyst surface to convert reactants into desorbed products. For example, if a catalytic surface is extremely reactive, it will bind reactants very strongly and the catalytic surface will become effectively poisoned by surface intermediates, which limits catalyst activity, a phenomenon that is well studied for CO oxidation over Pt nanoparticles.[3] On the other hand, if a catalytic surface is particularly unreactive, then the reactants will not adsorb onto the catalyst surface and no products will be formed. Thus, there exists a tradeoff between catalyst reactivity and it's corresponding reaction activity that has been summarized previously by of a "volcano" plot depicting CO methanation activity plotted against the dissociative CO adsorption energy, or catalyst reactivity, see Figure 2.7.[27] Here it is shown that whereas Pt and Pd are not reactive enough when inducing CO dissociative adsorption, Re is too reactive, and metals such as Ru and Co are the ideal choices as their CO dissociative adsorption energies lie somewhere in between the other metals and show the maximum reaction activity.

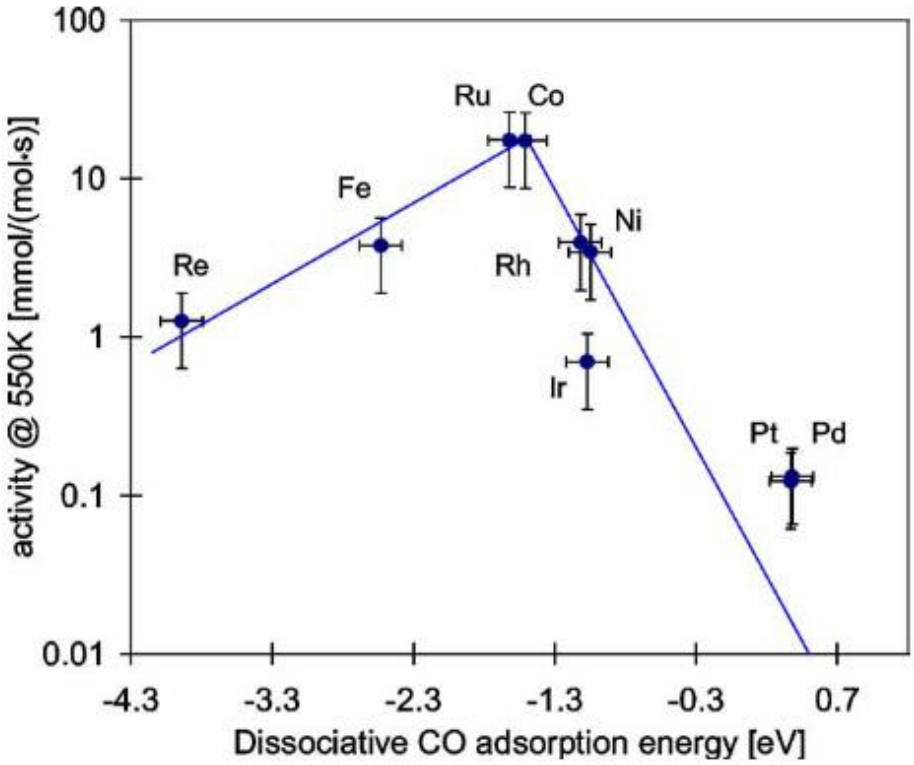

Figure 2.7 Activities of different supported transition metals as a function of the reaction energy for dissociative CO chemisorption. Note that more negative adsorption energies correspond to stronger CO surface adsorption while more positive adsorption energies correspond to weaker CO surface adsorption. Reprinted from ref 27 with permission from Elsevier.

In this thesis, catalyst activity will be presented as turn over frequency (TOF) as opposed to molar reaction rates because TOF corresponds to the inherent activity of individual surface atoms. TOF can be measured by evaluating the reaction rates as a function of the total number of metal sites exposed at the surface. The fraction of metal surface sites can be qualitatively approximated to be proportional to the surface area to volume ratio of the particle, or $\frac{c}{r}$, where r is the radius (or side length) of the bulk particle and c is a constant that will vary with the particle shape. This expression shows that with decreasing particle size ($\propto$ r), the fraction of surface sites approaches 1 while with decreasing particle size, the fraction of surface sites decreases. Therefore, it is important to

measure either the particle size or the surface site quantity directly as explained preciously in sections 2.4.1.1 and 2.4.1.2. Calculating TOF from reaction rates is straightforward as shown by equation 2.10 below. Note that "reaction rates" and "number of active sites" were measured on a per-gram basis for consistency.

$$\text{TOF}\ (s^{-1}) = \text{Rate}\left(\frac{\text{molecules}}{s*g_{cat}}\right) * (\#\ \text{of Active Sites})^{-1}\left(\frac{g_{cat}}{\text{molecules}}\right) \quad \textbf{equation 2.10}$$

2.5.7 Temperature Dependent Reaction Activity

Temperature dependent kinetics were conducted to predict the apparent activation barrier of a reaction over a specific catalytic material. Additionally, temperature dependent studies allowed for the determination of a maximum temperature limit, above which the catalyst particles would begin to sinter or coke. Catalyst sintering occurs at elevated temperatures, typically under reactive gas flow, in which catalyst particles become mobile on the support surface and begin to agglomerate, forming larger catalyst particles. Since reaction kinetics are a surface phenomenon, increasing the size of catalyst particles will inherently decrease the total number of the catalysts surface active sites, which will then decrease reaction rates and create non-Arrhenius temperature dependent functionality. Coking is a second phenomenon that occurs at elevated temperatures where significant buildup of carbon intermediates begins to occur, which effectively poisons catalytic active sites, inducing a decrease in reaction rates as well as rate instability (non-steady state conditions). All reactions in this thesis were run under conditions where catalyst sintering and coking were minimal, unless otherwise stated.

Temperature dependent kinetics were typically performed after catalyst pre-treatment and activation, where pre-treatment involved *in-situ* oxidation (high temperature

oxygen treatment), *in-situ* reduction (high temperature hydrogen treatment), and activation involving holding the catalyst under the most severe reaction conditions during the temperature dependent analysis (highest active gas pressure and highest reactor temperature) for 8 hours, to allow for catalyst deactivation to proceed and for rates to reach steady state. Generally, the temperature range was relatively small (~50 °C) and each temperature step had a range of 10 °C. After activation, the catalyst was held under each temperature for 2 hours to allow for the reaction to reach steady state and to also obtain multiple data points as each point took ~20-24 minutes to obtain from the GC. Then, apparent activation energies were determined by plotting the log of the reaction rate as a function of 1/RT, where R is the energy gas constant (8.3145 J/mol/K) and T is the reaction temperature. Because the reaction rate is directly proportional to the rate constant, the activation barriers can be determined according to the Arrhenius expression as depicted below (equation 2.11). When this expression is linearized (equation 2.12) the slope of rate as a function of 1/RT gives the apparent activation barrier (E_{app}) with a corresponding constant, C, that correspond to the log of the pre-exponential factor (A) and the partial pressure dependence of the reactants.

$$\text{rate} \propto k = Ae^{-E_{app}/RT} \qquad \textbf{equation 2.11}$$

$$\ln(\text{rate}) = -E_{app}\frac{1}{RT} + C \qquad \textbf{equation 2.12}$$

2.5.8 Partial Pressure Dependent Reaction Activity

Reactant partial pressure dependent studies were conducted to study the reaction mechanism over catalytic surfaces. Typically, reaction rates are directly proportional to the equilibrium constant, k and reactant partial pressures (P_A and P_B) as shown by equation

2.13, where α and β are the undetermined reaction orders of the reaction over a given catalyst. Linearizing equation 2.13 by applying the log function to each side gives an expression that can be easily plotted to evaluate each reactant's reaction orders (equation 2.14):

$$\text{rate} = kP_A^{\alpha}P_B^{\beta} \qquad \textbf{equation 2.13}$$

$$\ln(\text{rate}) = \ln(k) + \alpha\ln(P_A) + \beta\ln(P_B) \qquad \textbf{equation 2.14}$$

For example, to determine the reaction order of A, P_A is varied while keeping P_B and the reaction temperature constant. Then, ln(rate) is plotted against ln(P_A) where α is the slope. The same analysis can be performed for reactant B by keeping P_A and temperature constant. The experimental determination of reaction orders is important when justifying the proposed reaction mechanisms based on a series of elementary steps, but the estimation of the reaction orders may be complicated when the catalyst has a non-negligible surface coverage of reaction intermediates, which will decrease the observed reaction order.

For example, the rate law defined by equation 2.13 can be modified to include the potential effects of surface coverage by intermediates, as shown in equation 2.15, where "$1+K_AP_A$" and "$1+K_BP_B$" are simplified expressions corresponding to the surface coverages of A and B intermediates, respectively. As indicated by this new rate law, when K_AP_A or K_BP_B become non-zero (corresponding to large surface coverage by intermediates), the effective reaction orders for both reactants will decrease below their intrinsic values. This is an important phenomenon because when metal oxide supports act as reaction active sites, typically the surface coverage plays a prominent role on the rate

law and the corresponding reaction order.[28] Note that the derivations of all rate expressions in the subsequent chapters of this theses will be shown in the appendix.

$$\text{rate} = \frac{kP_A^{\alpha}P_B^{\beta}}{(1+K_AP_A)(1+K_BP_B)} \qquad \textbf{equation 2.15}$$

2.5.8.1 Fitting Pressure Dependent Activity to Reaction Mechanism

After generating a rate expression as a function of pressure based on a proposed reaction mechanism, it is necessary to evaluate the fit of the rate expression to experimental results. The known values for the rate expression are the reaction rate, the reactant inlet pressures, and the reaction orders of the reactants (assumed based on reaction stoichiometry). The remaining unknowns in the rate expression are the rate constant, k, and the equilibrium constants K_i. The Excel Solver add-on was employed to approximate these unknowns by minimizing the χ^2 of the experimentally observed rates compared to the predicted rates from the rate expression, as shown below by equation 2.16. To begin the optimization process, initial guesses were applied for the rate and equilibrium constants. Next, Excel Solver was used to guess values for the rate and equilibrium constants until χ^2 was minimized, providing the best guess for the rate and equilibrium constants. Note that graphing the predicted rates on top of the experimental rates provides a visual representation of the consistency of the rate expression fit with experimental data.

$$\chi^2 = \sum_i \left| \frac{(Rate_{fit,i} - Rate_{exp,i})^2}{Rate_{exp,i}} \right| \qquad \textbf{equation 2.16}$$

2.6 References

(1) Munnik, P.; De Jongh, P. E.; De Jong, K. P. Recent Developments in the Synthesis of Supported Catalysts. *Chem. Rev.* **2015**, *115* (14), 6687–6718.

(2) Pinna, F. Supported Metal Catalysts Preparation. *Catal. Today* **1998**, *41*, 129–137.

(3) Liu, J.; Lucci, F. R.; Yang, M.; Lee, S.; Marcinkowski, M. D.; Therrien, A. J.; Williams, C. T.; Sykes, E. C. H.; Flytzani-Stephanopoulos, M. Tackling CO Poisoning with Single-Atom Alloy Catalysts. *J. Am. Chem. Soc.* **2016**, *138* (20), 6396–6399.

(4) Marcinkowski, M. D.; Darby, M. T.; Liu, J.; Wimble, J. M.; Lucci, F. R.; Lee, S.; Michaelides, A.; Flytzani-Stephanopoulos, M.; Stamatakis, M.; Sykes, E. C. H. Pt/Cu Single-Atom Alloys as Coke-Resistant Catalysts for Efficient C-H Activation. *Nat. Chem.* **2018**, *10* (3), 325–332.

(5) Lucci, F. R.; Liu, J.; Marcinkowski, M. D.; Yang, M.; Allard, L. F.; Flytzani-Stephanopoulos, M.; Sykes, E. C. H. Selective Hydrogenation of 1,3-Butadiene on Platinum-Copper Alloys at the Single-Atom Limit. *Nat. Commun.* **2015**, *6*, 1–8.

(6) Shan, J.; Liu, J.; Li, M.; Lustig, S.; Lee, S.; Flytzani-Stephanopoulos, M. NiCu Single Atom Alloys Catalyze the C–H Bond Activation in the Selective Non-Oxidative Ethanol Dehydrogenation Reaction. *Appl. Catal. B Environ.* **2018**, *226* (June 2017), 534–543.

(7) Yu, W.; Xie, H.; Chen, L.; Li, Y.; Zhang, C. Synthesis and Characterization of Monodispersed Copper Colloids in Polar Solvents. *Nanoscale Res. Lett.* **2009**, *4* (5), 465–470.

(8) Wu, C.; Mosher, B. P.; Zeng, T. One-Step Green Route to Narrowly Dispersed Copper Nanocrystals. *J. Nanoparticle Res.* **2006**, *8* (6), 965–969.

(9) Boucher, M. B.; Zugic, B.; Cladaras, G.; Kammert, J.; Marcinkowski, M. D.; Lawton, T. J.; Sykes, E. C. H.; Flytzani-Stephanopoulos, M. Single Atom Alloy Surface Analogs in Pd0.18Cu15 Nanoparticles for Selective Hydrogenation Reactions. *Phys. Chem. Chem. Phys.* **2013**, *15* (29), 12187.

(10) Hadjiivanov, K.; Knozinger, H. FTIR Study of CO and NO Adsorption and Coadsorption on a Cu/SiO2 Catalyst: Probing the Oxidation State of Copper. *Phys. Chem. Chem. Phys.* **2001**, *3* (6), 1132–1137.

(11) Sato, S.; Takahashi, R.; Kobune, M.; Inoue, H.; Izawa, Y.; Ohno, H.; Takahashi, K. Dehydration of 1,4-Butanediol over Rare Earth Oxides. *Appl. Catal. A Gen.* **2009**, *356* (1), 64–71.

(12) Subramanian, N. D.; Kumar, C. S. S. R.; Watanabe, K.; Fischer, P.; Tanaka, R.; Spivey, J. J. A DRIFTS Study of CO Adsorption and Hydrogenation on Cu-Based Core-Shell Nanoparticles. *Catal. Sci. Technol.* **2012**, *2* (3), 621–631.

(13) Tu, Y.; Chen, Y. Effects of Alkali Metal Oxide Additives on Cu/SiO2 Catalyst in

the Dehydrogenation of Ethanol. *Ind. Eng. Chem. Res.* **2001**, *40*, 5889–5893.

(14) Bond, G. C.; Namijo, S. N. An Improved Procedure for Estimating the Metal Surface Area of Supported Copper Catalysts. *J. Catal.* **1989**, *118* (2), 507–510.

(15) Ro, I.; Liu, Y.; Ball, M. R.; Jackson, D. H. K.; Chada, J. P.; Sener, C.; Kuech, T. F.; Madon, R. J.; Huber, G. W.; Dumesic, J. A. Role of the Cu-ZrO 2 Interfacial Sites for Conversion of Ethanol to Ethyl Acetate and Synthesis of Methanol from CO 2 and H 2. *ACS Catal.* **2016**, *6*, 7040–7050.

(16) Medina, J. C.; Figueroa, M.; Manrique, R.; Rodríguez Pereira, J.; Srinivasan, P. D.; Bravo-Suárez, J. J.; Baldovino-Medrano, V.; Jimenez, R.; Karelovic, A. Catalytic Consequences of Ga Promotion on Cu for CO 2 Hydrogenation to Methanol. *Catal. Sci. Technol.* **2017**, *7*, 3375–3387.

(17) Lowell, S.; Shields, J. .; Thomas, M. A.; Thommes, M. *Characterization of Porous Solids and Powders: Surface Area, Pore Size and Density*; 2004.

(18) Ryczkowski, J. IR in Cataylisis Review. *Catal. Today* **2001**, *68*, 263–381.

(19) Tamura, M.; Shimizu, K. I.; Satsuma, A. Comprehensive IR Study on Acid/Base Properties of Metal Oxides. *Appl. Catal. A Gen.* **2012**, *433–434*, 135–145.

(20) Su, D. S. Special Issue: Advanced Electron Microscopy for Catalysis. *ChemCatChem* **2013**, *5* (9), 2543–2545.

(21) Friel, J. J.; Lyman, C. E. X-Ray Mapping in Electron-Beam Instruments. *Microsc. Microanal.* **2006**, *12*, 2–25.

(22) Hoffman, A. S.; Sokaras, D.; Zhang, S.; Debefve, L. M.; Fang, C. Y.; Gallo, A.; Kroll, T.; Dixon, D. A.; Bare, S. R.; Gates, B. C. High-Energy-Resolution X-Ray Absorption Spectroscopy for Identification of Reactive Surface Species on Supported Single-Site Iridium Catalysts. *Chem. - A Eur. J.* **2017**, *23* 14760–14768.

(23) Grob, R.; Barry, E. *Modern Practice of Gas Chromatography*; 2004.

(24) Koros, R. M.; Nowak, E. J. A Diagnostic Test of the Kinetic Regime in a Packed Bed Reactor. *Chem. Eng. Sci.* **1967**, *22* (3), 470.

(25) Fogler, H. S. *Elements of Chemical Reaction Engineering, 5th*; 2016.

(26) Allian, A. D.; Takanabe, K.; Fujdala, K. L.; Hao, X.; Truex, T. J.; Cai, J.; Buda, C.; Neurock, M.; Iglesia, E. Chemisorption of CO and Mechanism of CO Oxidation on Supported Platinum Nanoclusters. *J. Am. Chem. Soc.* **2011**, *133* (12), 4498–4517.

(27) Matthiesen, J.; Christensen, C. H.; Sehested, J.; Bligaard, T.; Nørskov, J. K.; Dahl, S. The Brønsted–Evans–Polanyi Relation and the Volcano Curve in Heterogeneous Catalysis. *J. Catal.* **2004**, *224* (1), 206–217.

(28) Knaeble, W.; Iglesia, E. Kinetic and Theoretical Insights into the Mechanism of Alkanol Dehydration on Solid Brønsted Acid Catalysts. *J. Phys. Chem. C* **2016**, *120* (6), 3371–3389.

Chapter 3. Rigorous Surface Characterization of Supported Cu Catalysts

3.1 Summary

Optimization of Cu surface characterization for particle dispersion estimates is important to help probe potential Cu-support interfacial effects that are highly sensitive to proper surface characterization, especially for small Cu particles (< 5nm). Although N_2O titration of Cu surfaces has been widely used to estimate Cu particle dispersion, an important question remains as to the accuracy of the technique with surface overoxidation and bulk oxidation providing over-estimates of the number of active Cu species. In this work, the question is addressed through various characterization techniques by performing in situ cryogenic CO and NO probe molecule FTIR, temperature and particle size dependent N_2O-TPR, and cryogenic CO-TPD experiments. Through characterization at cryogenic temperatures, it is shown that for Cu loaded on ZrO_2, N_2O overoxidation of Cu^0 to Cu^{2+} induces over-estimation of Cu particle dispersion. Additionally, it is revealed that Cu overoxidation occurs more readily on smaller Cu particles while achieving complete surface oxidation of Cu^0 to Cu^+ is more difficult on larger Cu particles. Finally, NO is used as a probe molecule to quantify the number of Cu^{2+} that were over-oxidized by N_2O to correct the initial dispersion estimates from N_2O-TPR. This work develops insights into discrepancies in literature regarding the optimal N_2O oxidation temperature for Cu characterization and provides a method of quantifying the degree of overoxidation as a means of improving the accuracy of Cu dispersion estimates.

3.2 Introduction

Supported Cu catalysts are have catalytic activity for many important reactions such as CO hydrogenation to methanol,[1–3] alcohol dehydrogenation,[4–6] electro-conversion of CO_2 to fuels,[7] and methanol carbonylation.[8] Due to Cu's utility for a wide range of reactions, it is important to develop a method that accurately and consistency predicts the number of active surface Cu sites as a means of understanding the true catalytic efficiency of the material. Normalizing reaction rates by the quantity of active surface Cu sites provides the intrinsic activity of Cu sites, typically presented as turn over frequency (TOF) in s^{-1}, and when measured as a function of particle size can also help to shed light on whether the entire Cu surface or specific Cu facets dominate the reaction pathway.[4,9,10] One specific reaction for which careful estimation of reaction TOF based on Cu surface area can help elucidate the active site is methanol formation from syngas, typically run over $Cu/ZnO/Al_2O_3$ catalysts. Currently, the active site for this process is in contention between Zn modifying the active site, undercoordinated Cu through electron transfer,[11–14] or Cu and Zn both acting as bifunctional active sites.[15–17]

The most common techniques used to quantify the number of active surface Cu species are H_2-TPD and N_2O oxidation. Another potential technique involves CO chemisorption (and CO-TPD), which must be performed at cryogenic temperatures due to CO having a low binding energy to Cu surfaces.[18] Recent surface science studies have predicted that the CO chemisorption stoichiometry was 2:1 (CO:Cu) on close-packed (111) and (110) surfaces[19]. However, in this work, which focuses on small Cu surfaces, with many under-coordinated facets, the CO to Cu stoichiometry was assumed to be 1:1, which

would serve as a complimentary, lower bound of surface site quantification. H_2-TPD experiments are typically performed at high pressure (20 bar) with a H_2O TPD peak positioned at 25 °C.[20] The resulting stoichiometry for H_2 adsorption onto Cu surfaces has been approximated to be close to 3:1 (Cu:H_2)[20,21] as well as 4:1[22,23], while a study utilizing a combination of experimental and computational experiments has reported values of 2.2:1 (Cu:H_2) for small Cu particles (~1.4 nm in size).[24] These discrepancies in predicted stoichiometry are likely due to particle size effects across the different studies, a phenomenon briefly discussed in previous work.[24]

The second characterization technique involves using N_2O frontal chromatography or oxidative titration. Under moderate to mild oxidation conditions, N_2O is expected to selectively oxidize surface metallic Cu^0 to Cu_2O (Cu^+) species with an expected stoichiometry of 2:1 (Cu:O). The key assumptions in this technique are that N_2O will not over-oxidize Cu^0 to CuO (Cu^{2+}), that N_2O will not oxidize sub-surface Cu species, and that N_2O will not interact with the corresponding Cu support. Eliminating direct support oxidation by N_2O is straightforward, as non-reducible support may be used (i.e. ZrO_2, SiO_2, carbon, etc.). Additionally, in a recent study, DFT calculations were performed, suggesting that surface overoxidation is much more favorable than bulk oxidation, revealing that N_2O oxidation of Cu is in fact predominantly a surface catalyzed reaction.[24] Therefore, it is expected that when using N_2O to probe Cu dispersion over non-reducible supports, the main consistently is a result of Cu overoxidation, decreasing the effective Cu:O stoichiometry from 2:1 to 1:1.

To obtain accurate Cu surface site quantification and particle dispersion, N_2O must oxidize the entire Cu surface. Generally, increasing the N_2O oxidation temperature is expected to achieve complete surface oxidation. However, increasing the N_2O oxidation temperature also activates Cu site overoxidation to Cu^{2+}, changing the expected Cu:O stoichiometry to 1:1. Many previous studies have tried to identify the optimal N_2O oxidation temperature that would allow for complete and selective oxidation of a reduced Cu surface to Cu^{+}. However, there exists discrepancy in literature with reports utilizing N_2O oxidation temperatures between -15 and 35 °C,[21,22,25,26] between 50 and 60 °C,[2,6,18,20,27,28] and 90 °C,[3,24,29–31], which raises the question as to the reason for such discrepancies as well as a means to evaluate overoxidation of Cu surfaces by N_2O.

In previous work, Cu particle size was varied over a high surface area graphite and activated carbon supports, showing little Cu particle size dependence of surface site quantification by N_2O, suggesting that N_2O titration is Cu structure insensitive.[20] Additionally, it is expected that reducible supports such as TiO_2 and CeO_2 can be directly oxidized by N_2O, which would induce overestimation of the Cu particle dispersion.[20,21,26] On the other hand, it has been suggested that interactions of a support with interfacial Cu sites through electron transfer can play an indirect role during N_2O titration of Cu.[4,20] It should be noted that many previous studies focused on optimizing N_2O titration experiments over large Cu particles that are larger than 15 nm[26,28] or Cu weight loadings greater than 10%.[21,22,27,30], which are expected to experience minimal metal-support interface effects.

To the best of our knowledge, no studies have been conducted of Cu particle size dependence over metal oxide supports with small enough particle sizes (<6 nm) where it is expected that Cu-support interactions or Cu surface sensitivity could have a direct impact on N_2O titration results over Cu surfaces. In this work, we qualitatively and quantitatively show the impact of Cu particle size in promoting Cu surface overoxidation during N_2O titration. It should be noted that differentiating the effects of Cu-support interactions or structure sensitivity on N_2O surface oxidation was beyond the scope of this work. The corresponding schematic of the two different effects is shown below in Figure 3.1. We achieve this by conducting probe molecule CO and NO IR at cryogenic temperatures to identify Cu^+ vs. Cu^{2+} species with varying Cu particle size and N_2O titration temperature as well as N_2O-TPR experiments to estimate Cu dispersion and particle sizes of each Cu catalyst and at each N_2O treatment. Finally, NO pulse chemisorption is used to quantify the number of surface Cu^{2+} species to correct for Cu:O stoichiometry and produce highly accurate Cu dispersion and particle size estimates.

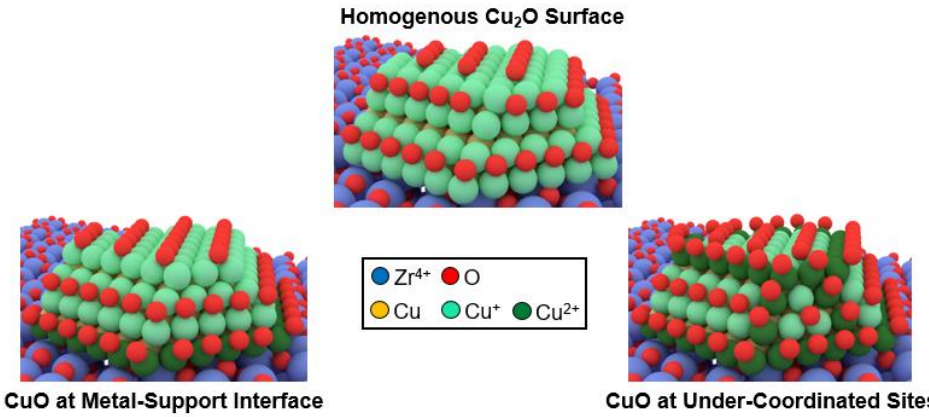

Figure 3.1 A carton schematic of a 3-4 nm Cu particle loaded on ZrO_2 after oxidation by N_2O where Cu is only oxidized to Cu^+ sites, forming a Cu_2O surface layer (Homogeneous Cu_2O Surface), where Cu perimtere sites are overoxidized to Cu^{2+} (CuO at Metal-Support Interface), and where all under-coordinated Cu sites are overoxidized to Cu^{2+} (CuO at Under-Coordinated Sites).

3.3 Materials and Methods

3.3.1 Synthesis of Cu catalysts over ZrO_2, TiO_2, and γ-Al_2O_3

In a typical synthesis, copper (II) nitrate trihydrate ($Cu(NO_3)_2$) was dissolved in HPLC grade water and added to ZrO_2, TiO_2, and γ-Al_2O_3 through incipient wetness impregnation with Cu weight loadings of 1%, 2.5%, and 5%. The paste was mixed and dried overnight in an oven at 60 °C. The catalyst particles were then crushed and sieved to a powder finer than 75 μm and calcined in dry air in a furnace at 450 °C for 4 hours.

3.3.2 Cu Particle Dispersion Estimates

3.3.2.1 N_2O Titration followed by TPR

Cu dispersion was estimated using a Micromeritics AutoChem 2920 instrument. In each experiment, 100 mg of catalyst was placed in a quartz u-tube. The catalyst was first degassed in Ar flowing at 50 mL min^{-1} at 150 °C for 30 minutes after which it was reduced *in-situ* with 10% H_2/Ar flowing at 50 mL min^{-1} at 400 °C for 1 hour. Following these steps, Cu was fully reduced, after which the catalyst was oxidized with 1000 ppm N_2O/Ar flowing at 50 mL min^{-1} at 50 °C for 30 min. The catalyst was then degassed with Ar at 50 mL min^{-1} for 30 min. Next, after allowing the TCD baseline to reach a stable value of zero (its baseline), the catalyst was treated with 10% H_2/Ar (50 mL min^{-1}) through a temperature programmed reduction (TPR) experiment, in which the catalyst was heated from 50 °C to 400 °C at a rate of 10 °C/min. N_2O oxidation followed by TPR was repeated two more times with N_2O oxidation temperatures of 90 and 130 °C, respectively, with the catalyst being cooled down to 50 °C in Ar after each N_2O oxidation.

Multiple N_2O oxidation temperatures were selected as there is discrepancy in literature regarding the optimal temperature that will induce selective and complete Cu^0 oxidation to Cu^+ without subsequent over oxidation. Thus, the aim of this work is to discuss the effects of N_2O oxidation temperature on the Cu particle dispersion estimates as a result of particle size effects for which there are competing effects with overoxidation and complete surface oxidation both having N_2O temperature and Cu particle size dependencies. An in-line TCD was used to measure H_2 consumption as a function of temperature during the TPR. A cold trap was cooled down to ~ -80 °C by mixing isopropyl alcohol (IPA) with liquid nitrogen (LN2) to trap H_2O generated during TPR as a means of protecting the TCD filaments from oxidation. The quantity of Cu^+ sites generated during N_2O oxidation was used to estimate the number of active Cu surface sites as described in section 2.3.1.2 and equation 2.4.

3.3.2.2 Cryogenic CO TPD

CO temperature programmed desorption (TPD) experiments were carried out in an AutoChem 2920 instrument. For each experiment, 100 mg of the support Cu was loaded into a quartz u-tube reactor, degassed in He at 150 °C for 30 minutes and then reduced in 10% H_2/Ar at 400 °C for 1 hr (both gases at 50 mL min^{-1}). After reduction, the catalyst was cooled in He to a temperature of -120 ± 3 °C, where it was expected that CO would chemisorb to the Cu particle at near complete surface coverage. Upon reaching -120 °C, 10% CO/He was flowed over the catalyst for 30 minutes, after which He was flowed over the catalyst for 30 minutes to purge any weakly bound CO-Cu species (both gases at 50 mL min^{-1}). After purging, the catalyst was heated up to 50 °C at a rate of 10 °C/min, in He,

and the effluent was monitored with an in-line TCD that was calibrated to provide quantitative measurements of CO that was desorbed from the Cu surface.

3.3.2.3 Cryogenic CO and NO Pulse Chemisorption

Probe molecule pulse chemisorption experiments were performed using an AutoChem 2929 instrument with a fixed gas loop volume of ~0.5 cm^3. The catalyst was first reduced in 10% H_2/Ar at 400 °C and then cooled down to -120 °C in He. After stabilizing the temperature at -120 °C, the gas loop was filled with 10% CO/He or 1% NO/He gas was subsequently injected into the He stream passing over the catalyst. An in-line TCD was used to monitor the effluent stream, a change in signal would correspond to the probe molecules that did not chemisorb to the catalyst and left through the reactor effluent. Probe molecule gas injections were performed until the TCD peaks became constant, indicating the catalyst surface was fully saturated with the probe molecule.

3.3.3 *In situ* probe molecule IR characterization

In-situ IR Spectroscopy was carried out using a Nicolet iS10 FTIR spectrometer with a mercury cadmium telluride (MCT) detector cooled by LN2. HFC-202 and HFC-302 mass flow controllers (Teledyne Hastings) controlled gas flow rates to the reactor bed in a Harrick Low Temperature Reaction chamber with ZnSe windows mounted inside a ThermoScientific Praying Mantis diffuse reflectance adapter set. All gases were passed across a cold trap maintained between -30 to -50 °C with an IPA/LN2 mixture, a Drierite desiccant to absorb trace moisture and a carbonyl trap made of SiO_2 chips heated to 250 °C. N_2 gas was fed through the Praying Mantis to expel gas phase molecules outside of the reaction chamber to minimize noise generated by gas phase signatures in the background.

Diffuse Reflectance Infrared Fourier Transform Spectroscopy (DRIFTS) was employed to generate spectra showing absorbance as a function of vibrational frequency (cm^{-1}). Note that absorbance was calculated by taking the log of inverse reflectance (Abs = log(1/R)), as previously discussed.[32] The reaction chamber bed was first filled with a filler material, ZrO_2. Next, approximately 15-20 mg of the desired catalyst was loaded onto the filler to generate a flat and homogenous layer of the catalyst at the lip of the chamber bed. Background spectra were collected for the pre-treated catalyst under Ar at -130 °C for CO probe molecule IR and were subtracted from the spectra taken with the adsorbed probe molecule.

3.3.3.1 CO and NO probe molecule IR to probe Cu surface structure

For CO-IR experiments, catalysts were first treated in inert Ar gas (50 mL min^{-1}) at 150 °C for 30 min. The catalysts were then cooled down to -130 °C with a constant flow of Ar under vacuum with a gauge pressure of -90 kPa. Once the reaction chamber reached a stable temperature of -130 °C and a background spectrum was collected at that temperature, 10% CO/Ar at 50 mL min^{-1} was introduced to the catalyst. 10% CO/Ar was flowed over the catalyst until the IR spectrum was constant with time (~10-20 min), after which Ar was used to purge the chamber until the spectrum was constant with time (~10-20 min). This first set of spectra were representative of the CO-IR of the "native" Cu catalyst. Once constant spectra were obtained under Ar purge, 0.5% NO/Ar was flowed over the catalyst until the IR spectrum was constant with time (~10-20 min), after which Ar was used to purge the chamber until the spectrum was constant with time (~10-20 min). The catalyst was then heated up to 400 °C and reduced in 10% H_2/Ar for 1 hr. Following

reduction, the catalyst was treated with subsequent CO and NO gas at -130 °C and the cycle was repeated with 50 °C, 90 °C, and 130 °C N_2O oxidative pre-treatments. Note that reduction was performed after each CO/NO exposure cycle and N_2O pre-treatment was conducted after catalyst reduction.

3.4 Results

3.4.1 Comparing dispersion estimates with N_2O-TPR and CO-TPD

N_2O is the typical technique employed to estimate Cu particle dispersion, but because there is discrepancy in the reported optimal N_2O oxidation temperature, several temperatures were tested in this chapter: 50, 90, and 130 °C. Figure 3.2 (a) shows the corresponding TPR spectra of a N_2O-TPR experiment for 5 wt% Cu loaded on γ-Al_2O_3, with Cu particle dispersion predicted to be 8, 13, and 26% after N_2O oxidation at 50, 90, and 130 °C, respectively. Cryogenic (~ 120 °C) CO-TPD experiments were performed to develop an internal comparison of Cu dispersion estimates without the use of a surface reaction. Figure 3.2 (b) shows a CO-TPD (10 °C min^{-1}) spectrum for 5 wt% Cu/Al_2O_3 with two peaks centered at -100 °C and -40 °C and with a peak area corresponding to 16% Cu dispersion. The dispersion estimates of 16% from CO-TPD in Figure 3.2 (b), agreed well with the N_2O-TPR estimate after 90 °C N_2O oxidation, as shown in Figure 3.2 (a). Note that Cu dispersion from CO-TPD was calculated with the assumption that the CO:Cu stoichiometric ratio was 1:1, which serves as a complimentary, lower bound approximation for Cu dispersion with respect to the N_2O-TPR experiments.

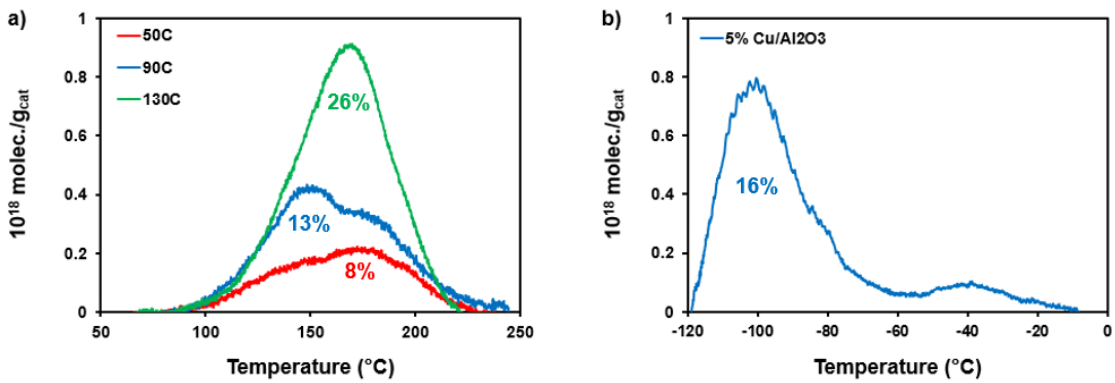

Figure 3.2 Cu surface area estimate for 5 wt% Cu/γ-Al_2O_3 with a) N_2O-TPR after 50, 90, and 130 °C N_2O oxidation and b) cryogenic CO-TPD from -120 to 50 °C. For both methods the supported Cu catalyst was pre-treated with 450 °C oxidation followed by 400 °C reduction.

Next, N_2O-TPR with the corresponding CO-TPD experiments were also run for 1 wt% loaded on reducible, rutile TiO_2. Here, after reduction, the catalyst was oxidized with N_2O at 90, 125, and 150 °C, with the corresponding TPR spectra after each oxidation step, as shown in Figure 3.3 (a). The predicted Cu dispersion was 43, 60, and 55% after 90, 125, and 150 °C N_2O oxidation, respectively. In an independent experiment, cryogenic CO-TPD was run for the same catalyst with the peak area corresponding to the number of CO molecules that desorbed from the catalyst surface, see Figure 3.3 (b). Since TiO_2 is well known to form carbonates at cryogenic temperatures, it was necessary to first deconvolute the contribution of CO molecules that desorbed from Ti^{4+} to the TPD peak area. To address this issue, cryogenic probe molecule CO-IR was employed, see Figure 3.3 (c), which effectively identified carbonyls adsorbed onto TiO_2 and Cu surfaces with vibrational frequencies at 2184 cm^{-1} and 2100 – 2140 cm^{-1}, respectively.[33] The catalyst was then heated gradually from -110 °C to 0 °C while taking spectra every 10 °C. Three carbonate species were differentiable based on their respective adsorption energies with the Cu-CO species with a vibrational frequency of 2125 cm^{-1} desorbing first, followed by the Ti^{4+}-CO species

at 2184 cm^{-1}, while the Cu-CO species at 2111 cm^{-1} had the strongest CO adsorption energy. Based on the CO-IR results, three peaks, each corresponding to the different carbonate species, were fit to the CO-TPD spectra with the lowest and highest temperature peaks corresponding to CO that desorbed from the Cu surface and the peak at -80 °C corresponding to CO desorbed from the TiO_2 support surface. By adding the two fitted peaks that corresponded to CO desorption from Cu, the particle dispersion was estimated to be 42%, which was nearly identical to the TPR estimate after N_2O oxidation at 90 °C (43 %).

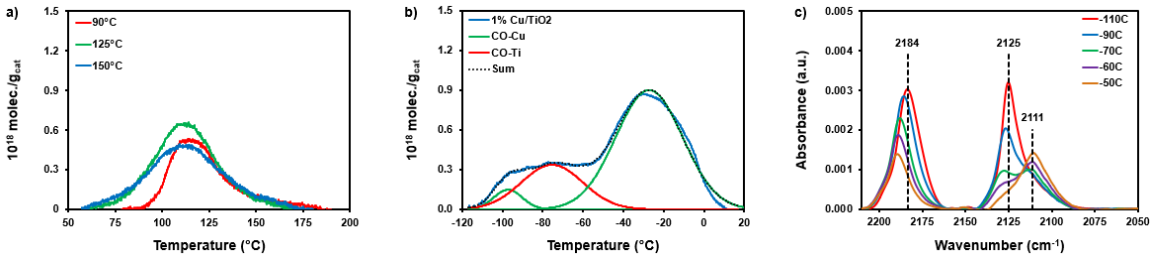

Figure 3.3 Cu surface site estimation for 1 wt% Cu loaded on TiO_2 with a) N_2O-TPR after 90, 125, and 150 °C N_2O oxidation and b) cryogenic CO-TPD from -120 to 50 °C. Further qualitative characterization was performed with c) in situ IR spectra of CO adsorbed at -120 °C and at saturation coverage on 1 wt% Cu/TiO_2. For all methods the supported Cu catalyst was pre-treated with 450 °C oxidation followed by 250 °C reduction.

3.4.2 Identifying and differentiating Cu^+ and Cu^{2+} sites

As previously described in literature, CO can be used most effectively as a probe molecule for Cu^+ surface site characterization at near ambient temperatures while sub-ambient temperature CO characterization is necessary to qualify metallic Cu^0 sites.[34,35] Typically, vibrational frequencies of CO adsorbed to Cu^+ and Cu^0 overlap in the range 2090-2140 cm^{-1}, particularly for well-dispersed Cu particles, though it is expected that CO chemisorbed to Cu^+ should have higher (blue-shifted) vibrational frequencies. On the other hand, because CO is easily evacuated from Cu^{2+} sites, even at cryogenic temperatures, NO

has been proposed to be a useful probe molecule that selectively chemisorbs to Cu^{2+} sites, with NO-Cu^{2+} being stable even at ambient temperatures.[34,36] Figure 3.4 (a) shows a CO probe molecule IR spectrum at -120 ℃ with two distinct vibrational frequencies at 2184 cm^{-1} and 2097 cm^{-1}, which were assigned to CO-Cu^{2+} and CO-Cu^{+} species, respectively. No peak was assigned to CO-Cu^{0} species because the Cu catalyst was stored under an ambient environment and it was expected the Cu surface would have remained oxidized. Next, after CO chemisorption onto the Cu surface, NO was introduced to the Cu catalyst, see Figure 3.4 (b), inducing the disappearance of the CO-Cu^{2+} band at 2184 cm^{-1} and the appearance of a new stretch at 1850 cm^{-1}, which was assigned to NO chemisorbed to Cu^{2+} sites. Note that the CO stretch at 2097 cm^{-1}, corresponding to CO-Cu^{+} species, remained unaffected by the introduction of NO gas. This selective displacement of CO on Cu^{2+} sites by NO shows that the NO-Cu^{2+} bond is stronger than its carbonyl analog, as reported in literature, while the CO-Cu^{+} bond is stronger than its nitrosyl analog.[36] The results summarized in Figure 3.4 provide strong evidence that the utilization of CO and NO as probe molecules can help to identify and differentiate cationic Cu species (Cu^{+} and Cu^{2+}) during cryogenic IR surface characterization of Cu nanoparticles.

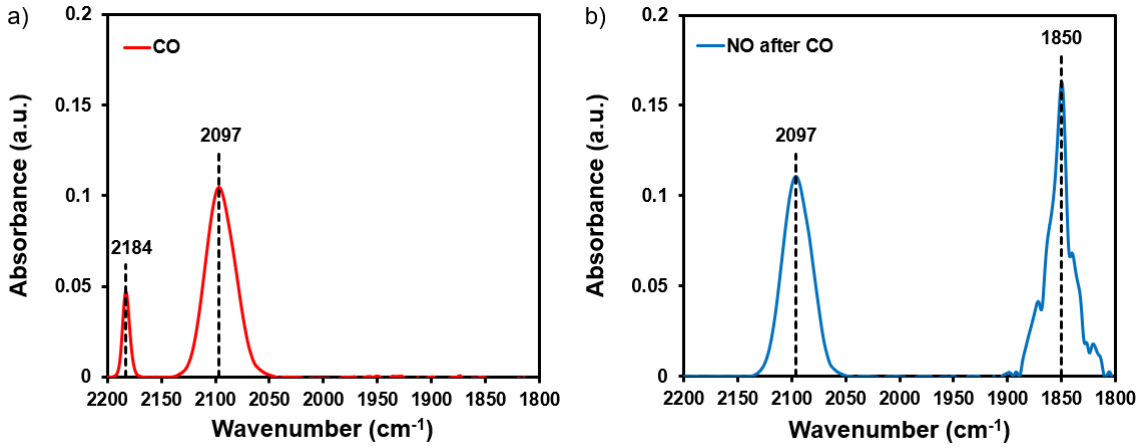

Figure 3.4 In situ IR spectra of a) CO and b) NO adsorbed at -120 °C and at saturation coverage on 1 wt% Cu/ZrO_2 after purging catalyst under Ar at 150 °C for 30 minutes. Note that (b) NO-IR spectra were recorded immediately after (a) CO-IR spectra without changing catalyst bed.

3.4.3 Cu overoxidation as a function of particle size and N_2O temperature

To study the effects of N_2O oxidation temperature on Cu nanoparticles, CO probe molecule IR at -120 °C was employed to identify the oxidation state of Cu sites after N_2O treatment. Figure 3.5 (a) and (b) show CO-IR spectra after 50 °C, 90 °C, and 130 °C N_2O treatment of pre-reduced 1.0, 2.5, and 5.0 wt% Cu loaded on ZrO_2, respectively. ZrO_2 was chosen as the support because it is inert to CO adsorption even at the cryogenic temperatures used in this chapter. The spectra revealed that overoxidation of Cu to Cu^{2+} is dependent on the N_2O oxidation temperature as well as the Cu particle size. In Figure 3.5 (a) there is a clear trend for the stretch at 2184 cm^{-1}, which does not appear until Cu is oxidized with N_2O at 90 °C and continues to grow after 130 °C N_2O treatment. A similar trend is observed for 2.5 wt% Cu/ZrO_2, for which Cu overoxidation begins during N_2O oxidation at 90 °C, as evidenced by the formation of a CO-Cu^{2+} stretch at 2185 cm^{-1}, see Figure 3.5 (c). However, the relative absorbance of the CO-Cu^{2+} for 2.5 wt% Cu/ZrO_2 was noticeably lower than that for 1 wt% Cu/ZrO_2 after equivalent treatment. Similar to 1 wt%

Cu/ZrO_2, the CO-Cu^{2+} for 2.5 wt% Cu/ZrO_2 grows as the N_2O oxidation temperature is increased to 130 °C, though again to a lesser extent. On the other hand, for 5 wt%/ZrO_2, no significant contribution from the CO-Cu^{2+} was observed until after 130 °C N_2O oxidation, after which a small CO-Cu^{2+} stretch with a vibrational frequency of 2190 cm^{-1} appeared, see Figure 3.5 (e). The combined CO-IR results provide qualitative evidence that with increasing particle size, Cu becomes less prone to N_2O overoxidation, up to 130 °C.

The corresponding quantitative analysis of 1.0, 2.5, and 5.0 wt% Cu/ZrO_2 is shown in Figure 3.5 (b), (d), and (e), respectively, where the area under the peak of the TPR spectra is representative of the total number of exposed surface sites of the Cu nanoparticle. For the three catalysts, the predicted total number of surface Cu sites increased with increasing N_2O oxidation temperature. Qualitatively comparing low temperature CO-IR and the N_2O-TPR spectra for 1 wt% Cu/ZrO_2, see Figure 3.5 (a) and (b), it was clear that the formation of Cu^{2+} sites (CO vibrational frequency of 2184 cm^{-1}) trended directly with the increase in the N_2O-TPR peak area. On the other hand, when comparing the CO-IR and N_2O-TPR spectra for 5 wt % Cu/ZrO_2, see Figure 3.5 (e) and (f), there was minimal formation of Cu^{2+} sites on the Cu particle surface even after increasing N_2O oxidation temperature. However, the TPR peak area increased as a function of N_2O oxidation temperature, suggesting that for larger Cu particles, overoxidation to Cu^{2+} sites was not the dominant reason for the observed trends. Note that the observed trends during characterization of 2.5 wt% Cu/ZrO_2 fell in between those of the 1.0 and 5.0 wt% Cu/ZrO_2 catalysts. The results of cryogenic CO-IR and N_2O-TPR highlight the potential difficulty with identifying an

optimum N_2O oxidation temperature for Cu surface characterization, as Cu particle size plays a role on the impact of overoxidation as a function of N_2O oxidation temperature.

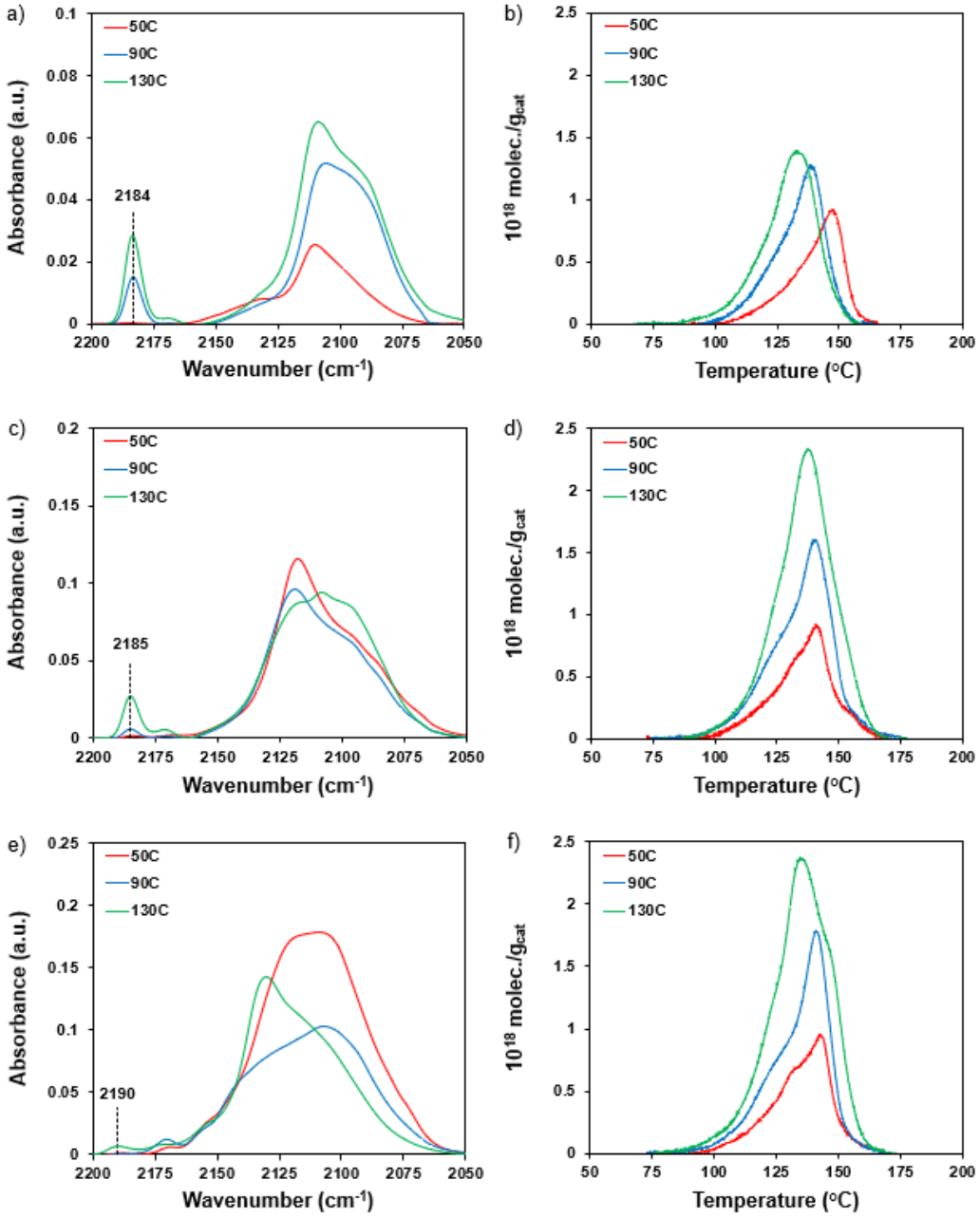

Figure 3.5 Probe molecule CO-IR at -120 °C for a) 1 wt% Cu loaded on ZrO_2, c) 2.5 wt% Cu loaded on ZrO_2, and e) 5 wt% Cu loaded on ZrO_2 with varying N_2O oxidation pre-treatments (50 °C, 90 °C, 130 °C) and TPR spectra for b) 1 wt% Cu loaded on ZrO_2, d) 2.5 wt% Cu loaded on ZrO_2 and f) 5 wt% Cu loaded on ZrO_2. Note that all catalysts were reduced at 400 °C for 1 hour prior to exposure to N_2O.

All N_2O-TPR results from Figure 3.5 are summarized in Table 3.1 with the number of active sites calculated from the TPR peak area as well as the predicted Cu particle dispersion and size for each catalyst and after each N_2O oxidation temperature. The results in Table 3.1 show that at a given N_2O oxidation temperature, the Cu dispersion estimates decreased with increasing Cu weight loading, as expected. Additionally, the dispersion estimates of a given catalyst increased with increasing N_2O oxidation temperature, which was qualitatively consistent with CO-IR spectra observed in Figure 3.5.

Catalyst/Treatment	Number of Active Sites (10^{18} molec./g_{cat})	Dispersion (%)	Estimated Particle Size (nm)
1 wt% Cu/ZrO_2/50 °C	42.1	44.4	2.3
1 wt% Cu/ZrO_2/90 °C	63.3	66.9	1.6
1 wt% Cu/ZrO_2/130 °C	74.0	78.1	1.3
2.5 wt% Cu/ZrO_2/50 °C	46.4	19.6	5.3
2.5 wt% Cu/ZrO_2/90 °C	88.6	37.4	2.8
2.5 wt% Cu/ZrO_2/130 °C	130.8	55.2	1.9
5 wt% Cu/ZrO_2/50 °C	50.9	10.7	9.6
5 wt% Cu/ZrO_2/90 °C	80.3	17.0	6.1
5 wt% Cu/ZrO_2/130 °C	144.0	30.4	3.4

Table 3.1 Summary of N_2O-TPR estimates of the number of total active sites at the Cu surface, the corresponding particle dispersion, and estimated Cu particle size for 1.0, 2.5, and 5.0 wt % Cu loaded on ZrO_2 after N_2O pre-treatment at 50, 90, and 130 °C as shown by the TPR peak area in Figure 3.5.

To develop an internal comparison to the Cu dispersion estimates for 1, 2.5, and 5 wt% Cu/ZrO_2 catalysts, see Figure 3.4 and Table 3.1, cryogenic CO-TPD experiments were run for each catalyst as shown in Figure 3.6. In Figure 3.6 (a), the predicted Cu dispersion for 1 wt% Cu/ZrO_2 was 50%, which was consistent with the estimate from N_2O-TPR after 50 °C N_2O oxidation. To summarize, the Cu dispersion estimates with N_2O-TPR and CO-TPD suggested that the optimal N_2O oxidation temperature varied with both Cu particle size and its corresponding metal oxide support.

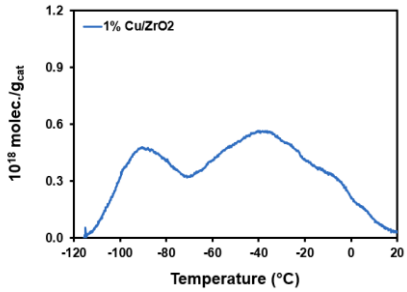

Figure 3.6 Cu surface site estimation for 1 wt% Cu ZrO_2 using cryogenic CO-TPD from -120 to 50 °C with a 10 °C min^{-1} ramp rate. For all methods the supported Cu catalyst was pre-treated with 450 °C oxidation followed by 250 °C reduction.

3.4.4 NO as a Probe Molecule

With the demonstration that overestimation of Cu dispersion was likely due to the formation of Cu^{2+} species during N_2O-TPR experiments, NO was employed as a probe molecule to selectively quantify the number of Cu^{2+} sites for each catalyst studied after different N_2O oxidation temperatures. The first choice was to run a cryogenic NO-TPD experiment, analogous to the CO-TPD experiments shown in Figures 3.1, 3.2, and 3.5. However, as shown in Figure 3.7 (b), with increasing temperature adsorbed NO species did not simply desorb from the Cu surface, but also began forming nitrate and nitrite species as evidenced by the formation of strong absorption bands in the frequency range 1200-1700 cm^{-1}.[36,37] The formation of these species would convolute the approximation of the number of adsorbed NO species on Cu^{2+}, due to potential changes in adsorbate to surface site stoichiometry, and would only add more error to the Cu dispersion estimates.

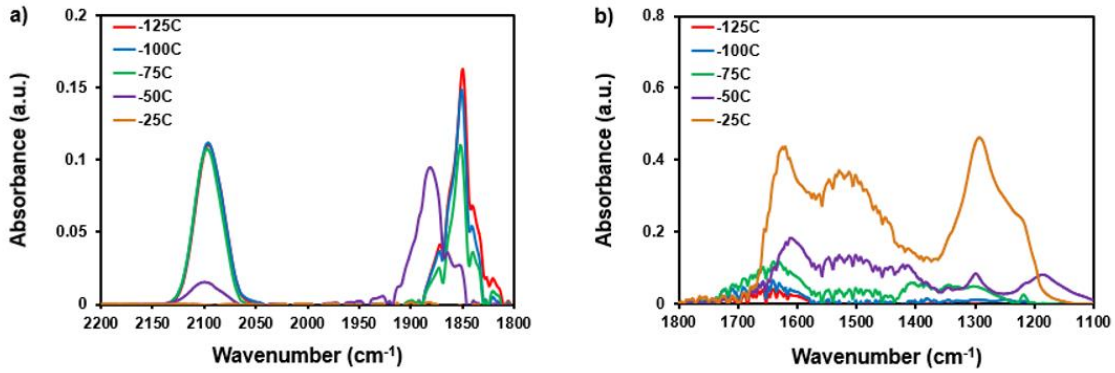

Figure 3.7 In situ spectra of CO and NO adsorbed at -125 °C and at saturation coverage on 2.5 wt% Cu/ZrO_2 with a) frequency range characteristic of carbonyl and nitrosyl adsorption to Cu and b) frequency range characteristic of nitrate and nitrite surface species. Spectra as a function of increasing temperature are shown within both frequency ranges. Note, the catalyst was only purged with inert Ar at 150 °C to degas the catalyst bed.

3.5 Discussion

The combination of in-situ quantitative (N_2O-TPR, CO-TPD) and qualitative (cryogenic IR) characterization measurements suggested that the typical method of estimating Cu particle dispersion through N_2O titration is susceptible to over-estimation due to the formation of Cu^{2+} sites on the Cu surface as opposed to the assumed Cu^{+} sites. The question that must be addressed is whether the formation of Cu^{2+} sites after N_2O titration can be identified and if these sites can be quantified to correct Cu dispersion estimates using N_2O-TPR as a Cu surface characterization technique.

It should be noted that dispersion estimates from CO-TPD experiments were conducted with the assumption that each surface Cu atom adsorbed one CO molecule, 1:1 CO to Cu ratio. Previous surface science studies of CO molecules adsorbed to close-packed Cu (111) and (110) surfaces showed that the CO surface coverage reached a maximum of 0.52, corresponding to a bulk average of one CO-Cu linear bond for every two Cu species, or a 1:2 CO to Cu ratio.[19] However, since the Cu particles discussed in this dissertation are

quite small, it is expected that the particle surfaces will be composed of many undercoordinated sites (steps, edges, etc.) that would be expected to have higher CO adsorption energies and CO surface coverages, approaching a value of 1 (1:1 CO to Cu ratio). However, CO-TPD still served as a useful comparison for the estimation of Cu dispersion as its underestimation of particle dispersion would serve a complimentary role to the overestimation of dispersion using N_2O-TPR.

N_2O-TPR experiments, together with cryogenic CO-TPD, were used to estimate the dispersion of 5 wt% Cu/Al_2O_3 (Figure 3.2), 1 wt% Cu/TiO_2 (Figure 3.3), and 1 wt% Cu/ZrO_2 (Figure 3.5 and 3.6). The dispersion estimates were in good agreement when titration with N_2O at 90 °C for 5 wt% Cu/Al_2O_3 and 1 wt% Cu/TiO_2 and at 50 °C for 1 wt% Cu/ZrO_2. These experiments served as an example to show that the optimal N_2O temperature is potentially support dependent and that even at 90 °C oxidation, the dispersion estimate for 1 wt% Cu/ZrO_2 had increased by 20% compared to after 50 °C oxidation, see Table 3.1. This raises the question of whether the support can play a direct role in influencing N_2O titration estimates (i.e. metal-support interface effects) or if N_2O titration is sensitive to the Cu surface structure.

To address this question, it was first necessary to be able to identify the formation of Cu^{2+} species after N_2O overoxidation and distinguish them from the expected Cu^{+} species. Probe molecule IR at cryogenic temperatures revealed that NO and CO can be used to probe the different Cu oxidation states, as shown in Figure 3.4. Here, CO chemisorption onto 1 wt% Cu/ZrO_2 revealed absorption bands at 2097 and 2184 cm^{-1}, which were assigned to $CO\text{-}Cu^{+}$ and $CO\text{-}Cu^{2+}$, respectively. As discussed previously in

literature, NO selectively chemisorbs to Cu^{2+} sites and effectively displaces any carbonyl species.[36,38] So, to confirm the site assignment of Cu-Cu^{2+} species at 2184 cm^{-1} NO introduced to the catalyst, which immediately induced the disappearance of the band at 2184 cm^{-1} (CO-Cu^{2+}) with the corresponding appearance of a band at 1850 cm^{-1}, which was characteristic of NO-Cu^{2+} species. This experiment with CO replacement by NO worked to confirm the site assignment of the band at 2184 cm^{-1}. Notably, after the introduction of NO the CO-Cu^{+} band was unaffected, suggesting that the CO-Cu^{+} binding energy is larger than that of NO-Cu^{+}, which allowed CO-Cu^{+} species to be resistant to a NO environment. On the other hand, the NO-Cu^{2+} binding energy is larger than that of CO-Cu^{2+}, which allowed for the facile displacement of CO by NO over Cu^{2+} sites. These results revealed that under cryogenic temperatures, the co-adsorption of the two probe molecules allowed NO to selectively bind to Cu^{2+} while CO selectively bonded to Cu^{+} (and Cu^{0}).

The relative strength of the CO and NO binding energies on Cu^{2+} can be rationalized by the interaction of the molecular orbitals of the two probe molecules with that of Cu^{2+}.[39] The lone electron pairs of CO are transferred through its σ-orbital to the d-orbital (d^9) of Cu^{2+}. However, due to its unfilled d-orbital, Cu^{2+} does not participate in d-electron back-donation, making the CO-Cu^{2+} quite weak and more electrostatic in nature. On the other hand, NO has an extra electron compared to CO, which is a lone electron in its π*-orbital that is easily transferred to the Cu d-orbital of Cu^{2+}, forming a stronger bond that allows for selective adsorption of NO when compared to CO. Additionally, because Cu^{+} and Cu^{0} have completely filled d-orbitals, d^{10}, d-electron back-donation is possible, creating stronger CO-Cu adsorption energies compared to that on Cu^{2+} sites. However, the

filled d-orbitals prevent interaction with NO, which no longer can donate its lone pair electron in the π*-orbital to the Cu metal, making NO unlikely to chemisorb to either Cu^+ or Cu^0 sites. To summarize the relative strengths of CO and NO bonds to Cu sites of different oxidation states, the expected trend of CO binding energy to different Cu surfaces follows: $Cu^+ \approx Cu^0 >> Cu^{2+}$ and follows the opposite order for NO: $Cu^{2+} >> Cu^+ \approx Cu^0$, which is consistent with literature and the cryogenic IR results in Figure 3.4.

By establishing cryogenic CO-IR as a viable technique for identifying Cu^{2+} species, CO was used as a probe molecule to study both the impact of N_2O oxidation temperature and Cu particle size on Cu surface overoxidation. To elucidate the impact of N_2O oxidation temperature on overoxidation of the Cu surface to Cu^{2+}, as opposed to Cu^+, cryogenic CO-FTIR spectra were recorded after N_2O oxidation at 50, 90, and 130 °C for 1 wt% Cu/ZrO_2, see Figure 3.5 (a). A clear trend was observed with the absorbance of the CO-Cu^{2+} band at 2184 cm^{-1} increasing with increasing N_2O oxidation temperature. Notably, no CO-Cu^{2+} was detected after N_2O oxidation at 50 °C, suggesting that there exists a certain thermally driven activation barrier for Cu surface overoxidation. Analogous experiments were run for larger Cu particle sizes for 2.5 wt% and 5.0 wt% Cu/ZrO_2, see Figure 3.5 (c) and (e), respectively, showing that the extent of Cu overoxidation, based on the relative absorbance of CO-Cu^{2+} species at 2185-2190 cm^{-1}, was reduced with increasing weight loading, or particle size. These results reveal that N_2O induced Cu overoxidation to Cu^{2+} is not only temperature dependent, but is also sensitive to the Cu particle structure, where overoxidation appeared to be more difficult on flatter Cu surfaces that are more characteristic of larger Cu particles.

Interestingly, although the relative amount of Cu^{2+} species was low for 2.5 wt% and 5.0 wt% Cu after N_2O oxidation at 50 and 90 °C, the corresponding N_2O-TPR spectra, see Figure 3.5 (d) and (f) and Table 3.1, showed significant increases in the corresponding dispersion estimates for each Cu particle. This suggested that for larger Cu particles, it became more difficult to fully oxidize the entire particle surface, and thus higher N_2O oxidation temperatures were needed to achieve full surface oxidation. Therefore, it becomes evident that the N_2O temperature has two competing effects where it is first necessary to increase the temperature high enough to titrate every surface Cu site, but also keep the temperature low enough to avoid any Cu site overoxidation. The picture is further as the particle size dependent results in Figure 3.5 suggest that the optimal N_2O oxidation temperature is also Cu particle size dependent as it becomes more difficult to titrate all surface Cu sites for larger and more well-coordinate Cu structures.

It becomes clear that due to the particle size effects discussed above, it would be increasingly difficult and tenuous to find the optimal N_2O oxidation temperature at which complete and selective surface oxidation of Cu^0 to Cu^+ occurs over different Cu catalysts. Thus, we propose that it is more feasible to titrate the Cu surface with N_2O at higher oxidation temperatures to ensure complete surface oxidation at the expense of some overoxidation of Cu^+ to Cu^{2+}. This temperature can be easily identified by conducting cryogenic CO-IR of the given catalyst at multiple N_2O oxidation temperatures, as shown in Figure 3.5. Next, N_2O-TPR can be employed to generate an initial guess at the Cu dispersion with the assumption that all Cu was oxidized to Cu^+ only. Finally, NO can then be chemisorbed to the Cu^{2+} sites that were formed after N_2O oxidation to quantify the

number of the Cu^{2+}, which would be used to correct the Cu dispersion initially estimated with N_2O-TPR. Equations 3.1-3.3 show a simple set of equations that summarize the process by which NO will be used to correct Cu dispersion estimates.

$$H_2 \text{ consumed (TPR Peak Area)} = 2 * (\text{Number of Surface Cu Sites})$$

$$\text{NO Consumed} = \text{Number of Surface } Cu^{2+} \text{Sites}$$

$$\text{Corrected Estimate} = 2 * (H_2 \text{ Consumed} - \text{NO Consumed}) + \text{NO Consumed}$$

3.6 Work to be completed

Although the above results and discussion provide meaningful insight into the overoxidation of Cu sites during N_2O-TPR characterization, the final step to quantify the extent of overoxidation to correct dispersion estimates has yet to be completed. With the help of a postdoctoral fellow in our lab, Insoo Ro, we are confident we will be able to complete the set of experiments needed to complete the story in this chapter. First, cryogenic CO-TPD experiments will be completed for 2.5 wt% and 5 wt% Cu/ZrO_2 catalyst, included in Figure 3.6 and compared to the corresponding N_2O-TPR measurements. Second, NO pulse chemisorption will be employed to quantify the number of Cu^{2+} sites generated after successive Surface oxidation with N_2O for 1 wt%, 2.5 wt%, and 5 wt% Cu/ZrO_2, as well as 5 wt% Cu/Al_2O_3. The NO pulse chemisorption measurements will then be used to correct the corresponding N_2O-TPR dispersion estimates as described at the end of the discussion, section 3.5. Finally, STEM-EDS images will be obtained at UC Riverside with the help of Krassimir Bhozilov to generate an external prediction of Cu particle size and dispersion, which will be compared to the

corrected dispersion estimates to show that the method developed in this chapter was able to effectively correct the overestimation of Cu dispersion due to surface overoxidation.

3.7 Conclusion

This chapter elucidated the role of Cu surface overoxidation during surface characterization through N_2O oxidation, highlighting quantitative limitations of the technique. Quantitative analysis was performed by using N_2O-TPR with varying N_2O temperature at 50, 90, and 130 °C together with cryogenic CO-TPD (-120 to 50 °C) to develop a reasonable approximation of Cu dispersion when loaded on ZrO_2, γ-Al_2O_3, and rutile TiO_2. The combination of cryogenic (-120 °C) CO and NO probe molecule IR were used to identify the Cu carbonyl stretch around 2184 cm^{-1} as corresponding to CO-Cu^{2+} species, which was used to present a clear trend of the growth of such carbonyls with increasing N_2O oxidation temperature. Additionally, ZrO_2 supported Cu particle size dependent studies revealed that surface oxidation of Cu is more facile on smaller particles and overoxidation is limited on larger Cu particles. However, complete partial oxidation of the surface is also more difficult on larger particles, meaning the optimal N_2O oxidation temperature is likely to be quite different on different sized Cu nanoparticles. Therefore, a new technique using NO chemisorption was proposed as a means of quantifying Cu surface overoxidation and correcting dispersion estimates. This work demonstrates a novel technique to improve Cu surface characterization to estimate particle dispersion and is expected to be beneficial for future work involving Cu catalysis kinetics, especially in the limit of small Cu particles.

3.8 References

(1) Chinchen, G.; Denny, P.; Jennings, J.; Spencer, M.; Waugh, K. Synthesis of Methanol: Part 1. Catalysts and Kinetics. *Appl. Catal.* **1988**, *36*, 1–65.

(2) Ud Din, I.; Shaharun, M. S.; Subbarao, D.; Naeem, A. Synthesis, Characterization and Activity Pattern of Carbon Nanofibers Based Copper/Zirconia Catalysts for Carbon Dioxide Hydrogenation to Methanol: Influence of Calcination Temperature. *J. Power Sources* **2015**, *274*, 619–628.

(3) Jansen, W. P. A.; Beckers, J.; Heuvel, J. C. V. D.; Gon, A. W. D. V.D.; Bliek, A.; Brongersma, H. H. Dynamic Behavior of the Surface Structure of Cu/ZnO/SiO2 Catalysts. *J. Catal.* **2002**, *210*, 229–236.

(4) Hanukovich, S.; Dang, A.; Christopher, P. The Influence of Metal Oxide Support Acid Sites on Cu Catalyzed Non-Oxidative Dehydrogenation of Ethanol to Acetaldehyde. *ACS Catal.* **2019**, *9*, 3537–3550.

(5) Tu, Y. J.; Chen, Y. W. Effects of Alkaline-Earth Oxide Additives on Silica-Supported Copper Catalysts in Ethanol Dehydrogenation. *Ind. Eng. Chem. Res.* **1998**, *37*, 2618–2622.

(6) He, X.; Wang, Y.; Zhang, X.; Dong, M.; Wang, G.; Zhang, B.; Niu, Y.; Yao, S.; He, X.; Liu, H. Controllable in Situ Surface Restructuring of Cu Catalysts and Remarkable Enhancement of Their Catalytic Activity. *ACS Catal.* **2019**, *9*, 2213–2221.

(7) Li, C. W.; Ciston, J.; Kanan, M. W. Electroreduction of Carbon Monoxide to Liquid Fuel on Oxide-Derived Nanocrystalline Copper. *Nature* **2014**, *508*, 504–507.

(8) Narsimhan, K.; Michaelis, V. K.; Mathies, G.; Gunther, W. R.; Griffin, R. G.; Roman-Leshkov, Y. Methane to Acetic Acid over Cu-Exchanged Zeolites: Mechanistic Insights from a Site-Specific Carbonylation Reaction. *J. Am. Chem. Soc.* **2015**, *137*, 1825–1832.

(9) Cargnello, M.; Doan-Nguyen, V. V. T.; Gordon, T. R.; Diaz, R. E.; Stach, E. A.; Gorte, R. J.; Fornasiero, P.; Murray, C. B. Control of Metal Nanocrystal Size Reveals Metal-Support Interface Role for Ceria Catalysts. *Science* **2013**, *341*, 771–773.

(10) Ro, I.; Resasco, J.; Christopher, P. Approaches for Understanding and Controlling Interfacial Effects in Oxide Supported Metal Catalysts. *ACS Catal.* **2018**, *8*, 7368–7387.

(11) Behrens, M.; Studt, F.; Kasatkin, I.; Kühl, S.; Hävecker, M.; Abild-pedersen, F.; Zander, S.; Girgsdies, F.; Kurr, P.; Kniep, B.; et al. The Active Site of Methanol Synthesis over Cu/ZnO/Al2O3 Industrial Catalysts. *Science* **2012**, *759*, 893–898.

(12) Ovesen, C. V.; Clausen, B. S.; Schiøtz, J.; Stoltze, P.; Topsøe, H.; Nørskov, J. K. Kinetic Implications of Dynamical Changes in Catalyst Morphology during

Methanol Synthesis over Cu/ZnO Catalysts. *J. Catal.* **1997**, *168*, 133–142.

(13) Yoshihara, J.; Campbell, C. T. Methanol Synthesis and Reverse Water-Gas Shift Kinetics over Cu(110) Model Catalysts: Structural Sensitivity. *J. Catal.* **1996**, *161*, 776–782.

(14) Behrens, M.; Zander, S.; Kurr, P.; Jacobsen, N.; Senker, J.; Koch, G.; Ressler, T.; Fischer, R. W.; Schlögl, R. Performance Improvement of Nanocatalysts by Promoter-Induced Defects in the Support Material: Methanol Synthesis over Cu/ZnO:Al. *J. Am. Chem. Soc.* **2013**, *135*, 6061–6068.

(15) Fujita, S.; Usui, M.; Ito, H.; Takezawa, N. Mechanisms of Methanol Synthesis from CO2 and CO at Atmospheric Pressure over Cu-ZnO. *J. Catal.* **1995**, *157*, 403–413.

(16) Rhodes, M. D.; Bell, A. T. The Effects of Zirconia Morphology on Methanol Synthesis from CO and H 2 over Cu/ZrO2 Catalysts: Part I. Steady-State Studies. *J. Catal.* **2005**, *233*, 198–209.

(17) Choi, Y.; Futagami, K.; Fujitani, T.; Nakamura, J. Role of ZnO in Cu/ZnO Methanol Synthesis Catalysts - Morphology Effect or Active Site Model? *Appl. Catal. A Gen.* **2001**, *208*, 163–167.

(18) Bond, G. C.; Namijo, S. N. An Improved Procedure for Estimating the Metal Surface Area of Supported Copper Catalysts. *J. Catal.* **1989**, *118*, 507–510.

(19) Hollins, P.; Pritchard, J. Interactions of CO Molecules Adsorbed on Cu(111). *Surf. Sci.* **1979**, *89*, 486–495.

(20) Chatterjee, R.; Kuld, S.; van den Berg, R.; Chen, A.; Shen, W.; Christensen, J. M.; Jensen, A. D.; Sehested, J. Mapping Support Interactions in Copper Catalysts. *Top. Catal.* **2019**.

(21) Fichtl, M. B.; Hinrichsen, O. On the Temperature Programmed Desorption of Hydrogen from Polycrystalline Copper. *Catal. Letters* **2014**, *144*, 2114–2120.

(22) Hinrichsen, B. O.; Genger, T.; Muhler, M. Chemisorption of N2O and H2 for the Surface Determination of Copper Catalysts. *Chem. Eng. Technol.* **2000**, *23*, 956–959.

(23) Muhler, M.; Nielsen, L. P.; Törnqvist, E.; Clausen, B. S.; Topsøe, H. Temperature-Programmed Desorption of H2 as a Tool to Determine Metal Surface Areas of Cu Catalysts. *Catal. Letters* **1992**, *14*, 241–249.

(24) Larmier, K.; Tada, S.; Comas-Vives, A.; Copéret, C. Surface Sites in Cu-Nanoparticles: Chemical Reactivity or Microscopy? *J. Phys. Chem. Lett.* **2016**, *7* (16), 3259–3263.

(25) Sengupta, G.; Gupta, D. J.; Kundu, M. L.; Sen, S. P. Effect of Reduction Conditions upon Metal Area in CuO-ZnO Catalyst. *J. Catal.* **1981**, *225*, 223–225.

(26) Liu, Z.; Li, J. P. H.; Qi, X.; Dai, Y.; Yang, Y. Applying Low Temperature Titration for Determination of Metallic Sites on Active Oxide Supported Catalysts. *Catal. Sci.*

Technol. **2019**, *9*, 2008–2018.

(27) Chinchen, G. C.; Hay, C. M.; Vandervell, H. D.; Waugh, K. C. The Measurement of Copper Surface Areas by Reactive Frontal Chromatography. *J. Catal.* **1987**, *103* (1), 79–86.

(28) Tu, Y.; Chen, Y. Effects of Alkali Metal Oxide Additives on Cu/SiO2 Catalyst in the Dehydrogenation of Ethanol. *Ind. Eng. Chem. Res.* **2001**, *40*, 5889–5893.

(29) Ro, I.; Liu, Y.; Ball, M. R.; Jackson, D. H. K.; Chada, J. P.; Sener, C.; Kuech, T. F.; Madon, R. J.; Huber, G. W.; Dumesic, J. A. Role of the Cu-ZrO2 Interfacial Sites for Conversion of Ethanol to Ethyl Acetate and Synthesis of Methanol from CO2 and H2. *ACS Catal.* **2016**, *6*, 7040–7050.

(30) Luys, M.; Van Oeffelt, P. H.; Brouwer, W.; Pijpers, A. P.; Scholten, J. J. F. Surface and Sub-Surface Oxidation of Copper and Supported Copper Catalysts by Nitrous Oxide. *Appl. Catal.* **1989**, *46*, 161–173.

(31) Scholten, J. J. F.; Konvalinka, J. A. Reaction of Nitrous Oxide with Copper Surfaces. Application to the Determination of Free-Copper Surface Areas. *Trans. Faraday Soc.* **1969**, *65*, 2465.

(32) Sirita, J.; Phanichphant, S.; Meunier, F. Quantitative Analysis of Adsorbate Concentrations by Diffuse Reflectance FT-IR. *Anal. Chem.* **2007**, *79*, 3912–3918.

(33) Panayotov, D. A.; Burrows, S. P.; Yates, J. T.; Morris, J. R. Mechanistic Studies of Hydrogen Dissociation and Spillover on Au/TiO 2: IR Spectroscopy of Coadsorbed CO and H-Donated Electrons. *J. Phys. Chem. C* **2011**, *115* (45), 22400–22408.

(34) Hadjiivanov, K.; Knözinger, H. FTIR Study of Low-Temperature CO Adsorption on Cu-ZSM-5: Evidence of the Formation of Cu2+(CO)2Species. *J. Catal.* **2000**, *191* (2), 480–485.

(35) Subramanian, N. D.; Kumar, C. S. S. R.; Watanabe, K.; Fischer, P.; Tanaka, R.; Spivey, J. J. A DRIFTS Study of CO Adsorption and Hydrogenation on Cu-Based Core-Shell Nanoparticles. *Catal. Sci. Technol.* **2012**, *2*, 621–631.

(36) Hadjiivanov, K.; Knozinger, H. FTIR Study of CO and NO Adsorption and Coadsorption on a Cu/SiO2 Catalyst: Probing the Oxidation State of Copper. *Phys. Chem. Chem. Phys.* **2001**, *3*, 1132–1137.

(37) Hadjiivanov, K. I. Identification of Neutral and Charged NxOy Surface Species by IR Spectroscopy. *Catal. Rev. - Sci. Eng.* **2000**, *42*, 71–144.

(38) Hadjiivanov, K.; Dimitrov, L. IR Spectroscopy Study of CO and NOx Adsorption on a Cu/Zr-HMS Catalyst. *Microporous Mesoporous Mater.* **1999**, *27* (1), 49–56.

(39) Fu, Y.; Tian, Y.; Lin, P. A Low-Temperature IR Spectroscopic Study of Selective Adsorption of NO and CO on CuO/γ-Al2O3. *J. Catal.* **1991**, *132*, 85–91.

Chapter 4. The Influence of Metal Oxide Support Acid Sites on Cu Catalyzed Non-Oxidative Dehydrogenation of Ethanol to Acetaldehyde

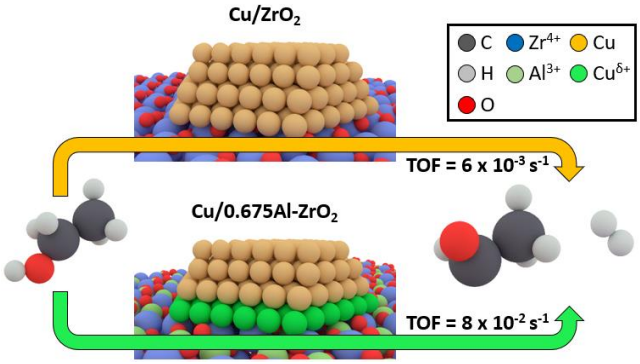

4.1 Summary

Selective ethanol dehydrogenation to acetaldehyde is an important reaction because acetaldehyde is a useful commodity chemical and can serve as a building block to produce other high value products. Cu surfaces are known to selectively convert ethanol to acetaldehyde by driving sequential dehydrogenation steps. However, there remain questions regarding the rate-limiting step in the reaction and the role acidic supports play in promoting catalytic activity. In this work, both questions are addressed by performing kinetic measurements as a function of support acid characteristics, Cu dispersion, reaction temperature, ethanol pressure, and in-situ pyridine poisoning. By coupling kinetic measurements with probe molecule infrared spectroscopy and microkinetic modeling, it is shown that at low ethanol partial pressure (~ 1 mbar) the reaction rate is minimally dependent on the support, with a rate limiting step of O-H cleavage occurring with similar turn over frequency on all Cu surface sites. In contrast, at high ethanol partial pressure (~70 mbar), the Cu surface becomes poisoned with reactive intermediates, and supports with strong Lewis acidity (TiO_2 and Al-doped ZrO_2 supports) promote the rate of ethanol

conversion to acetaldehyde by over an order of magnitude compared to supports with weak acidity (ZrO_2). It is further inferred that at high ethanol pressure for Cu catalysts on supports with strong Lewis acidity, the rate limiting step switches to C_α-H cleavage occurring at interfacial $Cu^{\delta+}$ sites, while the initial O-H cleavage occurs on support acid sites. This demonstrates that the role of support acid sites and the rate limiting step for ethanol dehydrogenation on Cu catalysts are dependent on reaction conditions and more generally provides an understanding of how active metals and acidic supports could act cooperatively to drive catalytic processes.

4.2 Introduction

Aldehydes are key building blocks for the production of many high value chemicals such as 1-butanol, ethyl acetate, and C8 aromatics.[1,2] They are generally produced through the oxidative dehydrogenation of alcohols over heterogeneous noble-metal catalysts, which results in high energy costs due to the required water separation from the effluent.[3] Non-oxidative dehydrogenation of alcohols to aldehydes is an alternative reaction that has the potential to avoid the high costs associated with separating water while also producing H_2 as a byproduct.[3–5] Non-oxidative dehydrogenation of ethanol to acetaldehyde is of particular importance due to the industrial value of acetaldehyde, the use of acetaldehyde in the aldol condensation reaction to form long chain hydrocarbons from biomass-based feedstock, and as a model system that can be used to understand more complex processes.[2,6–12]

Cu is the most commonly studied supported metal catalyst for ethanol dehydrogenation due to its high selectivity toward acetaldehyde production.[1,4,8,13–25] The

mechanism of this reaction has been studied in detail, which is initiated via ethanol adsorption onto Cu surfaces, followed by cleavage of the O-H bond, forming a surface ethoxide intermediate. The ethoxide is then converted to a surface acetyl intermediate through the cleavage of a C_α-H bond, followed by acetaldehyde desorption. C_α-H bond activation has been proposed to be the rate limiting step (RLS) for ethanol dehydrogenation based on surface science studies with well-defined Cu crystals,[4,26] kinetic studies on supported Cu catalysts,[20] and theoretical studies.[27] The same RLS was proposed for the dehydrogenation of methanol to formaldehyde through surface science studies of various Cu crystals.[25,28–32] However, a recent density functional theory (DFT) based analysis calculated the anhydrous dehydrogenation of methanol, ethanol, 1-propanol, and 1-butanol to their respective aldehyde products on Cu(110).[5] This analysis was executed at low surface coverage and concluded that only for methanol dehydrogenation was C_α-H bond activation the RLS, while for $C_{2\text{-}4}$ alcohols the RLS shifted to O-H bond cleavage. This difference in RLS was attributed to a less stable acetyl intermediate (formaldehyde) for methanol, which increased the barrier for C_α-H bond activation by at least 0.5 eV compared to the same step for C_2-C_4 molecules.

In addition to unresolved questions regarding the RLS of non-oxidative ethanol dehydrogenation on Cu surfaces, the potential role of the oxide support in promoting Cu reactivity is not well understood, even though acid sites on commonly used metal oxide supports are known to drive ethanol dehydration. A DFT based analysis of ethanol dehydration over γ-Al_2O_3 showed that O-H bond cleavage was facile, with an activation barrier less than 1 kJ/mol, while C_α-H bond cleavage had a significantly larger activation

barrier of 188 kJ/mol.[33] The calculations also showed that ethanol dehydrogenation to acetaldehyde had an activation barrier that was 33 kJ/mol larger than ethanol dehydration to form diethyl ether or ethylene. This was consistent with experimental research showing that although ethanol dehydrogenation on γ-Al_2O_3 followed an analogous reaction pathway to that described for Cu,[33–37] the selectivity for dehydrogenation was <1% with the active acid sites primarily promoting ethanol dehydration through more facile C-O bond cleavage and ethanol dimerization reactions.[34,38–40] Thus, it is well documented that acidic metal oxide supports can easily activate O-H bonds, while Cu is quite selective for C_α-H bond activation to form acetaldehyde from ethanol, which occurs with a much lower barrier compared to on acidic metal oxide supports. This raises the question of whether Cu and acidic metal oxide supports can work cooperatively to promote ethanol dehydrogenation to acetaldehyde.

A few reports in literature have proposed cooperation between acidic supports and metal clusters for driving ethanol conversion reactions. DFT calculations of 4 atom Cu clusters on Cr_2O_3 surfaces have shown that charge transfer from Cu to Cr_2O_3 could induce the formation of interfacial Cu^+ species that stabilize ethanol adsorption.[41] Experimental studies at high ethanol conversion have similarly proposed that interfaces formed between support Lewis acid sites and interfacial Cu^+ species could promote ethanol conversion to ethyl acetate.[1,42,43] In addition to evidence for support influence on the reactivity of Cu in ethanol conversion, experimental analyses of supported Ag and Pt catalysts have proposed that acidic sites on the support could play a direct role in ethanol conversion by facilitating O-H activation and further that direct support participation in the reaction mechanism could

modify selectivity.[8,44] Although there is evidence that support acidity can influence the reactivity of Cu nanoparticles for ethanol conversion, the mechanism of this effect, whether the support modifies the interfacial Cu properties or directly participates in the reaction mechanism, remains unclear.

In this work, we quantitatively and mechanistically elucidate the influence of oxide support acidity on ethanol dehydrogenation by Cu nanoparticles. This was achieved by performing temperature, ethanol pressure, and pyridine titration dependent kinetic measurements on catalysts consisting of Cu with varying dispersion deposited on ZrO_2, Al doped ZrO_2 (Al-ZrO_2) and TiO_2 supports. Pyridine probe molecule infrared (IR) spectroscopy was used to demonstrate that the addition of Al to ZrO_2 and controlled catalyst oxidative pre-treatment induced the formation of strong Lewis acid sites consisting of 4-fold coordinated (Al_{IV}) Al^{3+}. CO probe molecule IR demonstrated that supports with stronger Lewis acid sites (TiO_2 and Al-ZrO_2) promoted the formation of interfacial Cu sites with cationic character. Comparison of the ethanol dehydrogenation activity under kinetically controlled reaction conditions at low ethanol pressure showed that catalysts exhibit similar turn over frequency (TOF), where at increased ethanol pressure Cu nanoparticles on more acidic supports (TiO_2 and 0.675Al-ZrO_2) exhibited more than an order of magnitude enhancement in TOF. Cu particle size dependent measurements at high ethanol pressure showed enhanced TOF for smaller Cu particle sizes on 0.675Al-ZrO_2 and constant TOF as a function of particle size on ZrO_2, suggesting that the strong Al_{IV} Lewis acid sites induced a predominant participation of interfacial Cu sites in the RLS. These observations in conjunction with kinetic modeling led to the conclusion that at low ethanol

pressure, the reaction proceeds on relatively clean Cu surfaces through a RLS of O-H cleavage with minimal influence of support acidity. At high ethanol pressures, it is proposed that reactive intermediates poison the Cu surface and that on supports with strong Lewis acid sites the reaction initiates through O-H cleavage on the support followed by the RLS of C_α-H cleavage occurring at Cu-support interfacial sites. This work demonstrates that the influence of support acid sites on ethanol dehydrogenation by Cu is important at high ethanol pressure where Lewis acid sites act both through direct participation in the mechanism and to influence the nature of interfacial Cu sites.

4.3 Materials and Methods

4.3.1 Synthesis of Cu Catalysts over ZrO_2 and TiO_2

In a typical synthesis, copper (II) nitrate trihydrate ($Cu(NO_3)_2$) was dissolved in HPLC grade water and added to ZrO_2 or TiO_2 through incipient wetness impregnation. The paste was mixed and dried overnight in an oven at 60 °C. The catalyst particles were then crushed and sieved to a powder finer than 75 μm and calcined in dry air in a furnace at 450 °C for 4 hours.

4.3.2 Synthesis of Cu Catalyst over Al-ZrO2

Al-doped ZrO_2 supports were synthesized by first dissolving aluminum nitrate nonahydrate ($Al(NO_3)_3*9H_2O$) in 20 mL HPLC grade water. Next, 3 g of ZrO_2 was suspended in 60 mL HPLC grade water on an evaporating dish by stirring at 250 rpm. Fifteen milliliters (15 mL) of the Al precursor solution was slowly (2.5 mL/hour) added to the ZrO_2 solution with a syringe pump. Once the precursor was added, the solution was heated to 90 °C and left stirring at 250 rpm until all the solvent was evaporated. The Al-

ZrO_2 support was then crushed and sieved down to a powder finer than 75 μm and calcined at 450 °C for 4 hours. Finally, Cu was added to Al-ZrO2 by incipient-wetness impregnation as described previously in section 4.3.1.

4.3.3 Cu Dispersion Estimates

Cu dispersion was estimated using a Micromeritics AutoChem 2920 instrument. In each experiment, 0.05 g of catalyst was placed in a quartz u-tube. The catalyst was first degassed in Ar flowing at 50 mL min^{-1} at 150 °C for 30 minutes after which it was oxidized in-situ with O_2 flowing at 50 mL min^{-1} at 450 °C for 1 hour and reduced in-situ with 10% H_2/Ar flowing at 50 mL min^{-1} at 400 °C for 1 hour. Following these steps, Cu was fully reduced, after which the catalyst was oxidized with 1000 ppm N_2O/Ar flowing at 50 mL min^{-1} at 90 °C for 1 hour. The catalyst was then degassed with Ar at 50 mL min^{-1} for 30 min. Following N_2O oxidation of Cu, the temperature was decreased to 50 °C under Ar flow (50 mL min^{-1}). The catalyst was then treated with 10% H_2/Ar (50 mL min^{-1}) through a temperature programmed reduction (TPR) experiment, in which the catalyst was heated from 50 °C to 450 °C at a rate of 10 °C min^{-1}. N_2O oxidation followed by TPR was repeated two more times with N_2O oxidation temperatures of 125 and 150 °C, respectively. Multiple N_2O oxidation temperatures were selected as there is discrepancy in literature regarding the optimal temperature that will induce selective and complete Cu^0 oxidation to Cu^+ without subsequent over oxidation. It was observed here that for larger Cu loadings (>2.5%) that the inferred Cu dispersion was independent of N_2O exposure temperature. However, for lower Cu loadings with higher dispersions, N_2O exposure at 125 and 150 °C gave >100% dispersion estimates, suggesting over oxidation of the Cu surface, see Figure 4.1. Thus, all

dispersion estimates were derived from 90 °C N_2O exposure, which is consistent with previous reports in literature.[42,45–48] An in-line TCD was used to measure H_2 consumption as a function of temperature during the TPR. A cold trap was cooled down to ~ -80 °C by mixing isopropyl alcohol (IPA) with liquid nitrogen (LN2) to trap H_2O generated during TPR as a means of protecting the TCD filaments from oxidation. The quantity of Cu^+ sites generated during N_2O oxidation was used to estimate the number of active Cu surface sites as described in section 2.3.1.2 and equation 2.4.

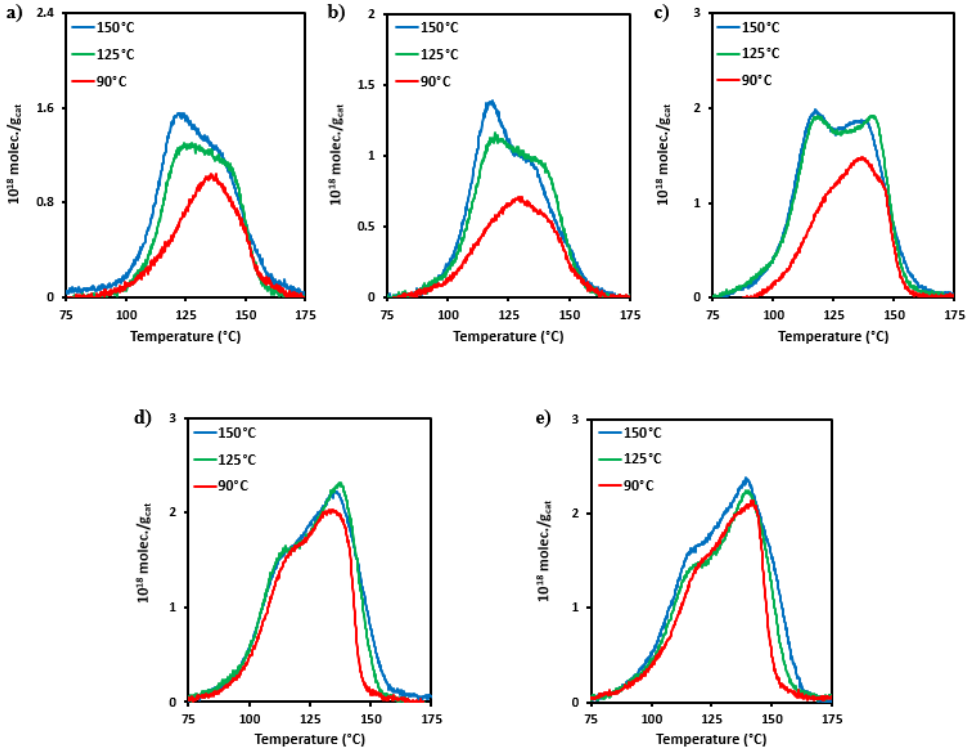

Figure 4.1 TPR-N_2O with varying temperatures for Cu loaded on ZrO_2. **a)** 1 wt% Cu/ZrO_2, **b)** 1 wt% Cu/ZrO_2[a] (calcined at 350 °C rather than 450 °C), **c)** 2.5 wt% Cu/ZrO_2, **d)** 4.8 wt% Cu/ZrO_2, and **e)** 9.2 wt% Cu/ZrO_2. All catalysts were pre-treated by 450 °C oxidation followed by 400 °C reduction. The results following 90 °C oxidation, including dispersion and particle size estimates, are summarized in Table 4.2.

4.3.4 BET Surface Area

Specific surface area based on the Brunaeur-Emmett-Teller (BET) theory was measured for ZrO_2 and 0.025 Al-ZrO_2, 0.225Al-ZrO_2, and 0.675Al-ZrO_2 using a Micromeritics 3Flex Porosimeter.

4.3.5 X-Ray Diffraction (XRD)

XRD diffractograms with a wavelength of 0.154 nm (Cu K-alpha, 8.04 keV) of ZrO_2, 1 wt % Cu/ZrO_2, and 1 wt% Cu/0.675Al-ZrO_2 were recorded in the 2θ range of 10 to 70° using a PANalytical Empyrean Powder Diffractometer.

4.3.6 Transmission Electron Microscopy (TEM)

High resolution TEM (HR-TEM) and scanning electron microscopy (STEM) imaging was performed at 200 kV accelerating voltage on a Thermo Scientific Talos G2 200X instrument. STEM images were recorded with a Fischione high grade angle annular dark field (HAADF) detector. Specimens prepared from a suspension in DI water were deposited on Molybdenum grids coated with lacey carbon.

4.3.7 In-situ IR Probe Molecule Characterization

In-situ IR Spectroscopy was carried out using a Nicolet iS10 FTIR spectrometer with a mercury cadmium telluride (MCT) detector cooled by LN2. HFC-202 and HFC-302 mass flow controllers (Teledyne Hastings) controlled gas flow rates to the reactor bed in a Harrick Low Temperature Reaction chamber with ZnSe windows mounted inside a ThermoScientific Praying Mantis diffuse reflectance adapter set. All gases were passed across a cold trap maintained between -30 to -50 °C with an IPA/LN2 mixture, a Drierite desiccant to absorb trace moisture and a carbonyl trap made of SiO_2 chips heated to 250

°C. N_2 gas was fed through the Praying Mantis to expel gas phase molecules outside of the reaction chamber to minimize noise generated by gas phase signatures in the background. Diffuse Reflectance Infrared Fourier Transform Spectroscopy (DRIFTS) was employed to generate spectra showing absorbance as a function of vibrational frequency (cm^{-1}). Note that absorbance was calculated by taking the log of inverse reflectance (Abs = log(1/R)), as previously discussed.[49] The reaction chamber bed was first filled with a filler material, ZrO_2 for Cu/ZrO_2 or $Cu/Al\text{-}ZrO_2$ and rutile TiO_2 for Cu/TiO_2. Approximately 15-20 mg of the desired catalyst was loaded onto the filler to generate a flat and homogenous layer of the catalyst at the lip of the chamber bed. Background spectra were collected for the pre-treated catalyst under Ar at 50 °C for pyridine probe molecule IR and at -130 °C for CO probe molecule IR, and were subtracted from the spectra taken with the adsorbed probe molecule. In all cases no surface carbonate species were detected in the background spectrum of the freshly pretreated catalysts, suggesting the bands between 1450 and 1650 cm^{-1} exclusively corresponded to adsorbed pyridine on support acid sites.

4.3.7.1 Pyridine probe molecule IR to probe surface acidity

For pyridine-IR experiments, catalysts were either reduced with 10% H_2/Ar (100 mL min^{-1}) at 400 °C for 1 hour or oxidized with O_2 (100 mL min^{-1}) at 450 °C for 1 hour and then reduced. The catalysts were then cooled under Ar (50 mL min^{-1}) and held at 50 °C, after which Ar was bubbled through pyridine to deliver the probe molecule to the reaction chamber. It was assumed that equilibrium between the gas and liquid phase was achieved in the bubbles. Pyridine was delivered to the reaction chamber until the

absorbance saturated (~20 min). The chamber was then purged with Ar until the spectra remained constant (~20 min) to remove any gas phase or physisorbed pyridine.

4.3.7.2 CO probe molecule IR to probe Cu surface structure

For CO-IR experiments, catalysts were either reduced with 10% H2/Ar (100 mL min^{-1}) at 400 °C for 1 hour or oxidized with O2 (100 mL min-1) at 450 °C for 1 hour and then reduced. The catalysts were then cooled down to -130 °C with a constant flow of Ar (50 mL min^{-1}) under vacuum with a gauge pressure of -90 kPa. Once the reaction chamber reached a stable temperature of -130 °C, 10% CO/Ar at 50 mL min^{-1} was introduced to the catalyst. 10% CO/Ar was flowed over the catalyst until the IR spectrum was constant with time (~10 min), after which Ar was used to purge the chamber until the spectrum was constant with time (~10 min).

4.3.8 Steady state ethanol dehydrogenation kinetics

Prior to testing the dehydrogenation activity of all Cu catalysts, it was necessary to ensure that mass transfer effects were minimized through the co-impregnation of each catalyst with SiO_2 gel. 50 mg of the calcined catalyst was mixed with 200 mg of SiO_2 gel and suspended in 30 mL of HPLC grade water in a round bottom flask. The suspension was sonicated for 30 min and stirred overnight. The flask was then transferred to a rotary evaporator and vacuum-dried over a 30 min period at 200 rpm with a bath temperature of 80 °C and a vacuum pressure of ~170 mbar. The corresponding dehydrogenation rates for 1 wt% Cu/ZrO_2 and 1 wt% Cu/TiO_2 were independent of superficial velocity (Figure 4.2) showing mass transfer effects were negligible. 200 mL min^{-1} was selected as the superficial velocity for all kinetic experiments. To prevent heat transfer and/or pressure drop effects

on the reaction rates, 90 mg of the co-impregnated catalyst was further diluted by physically mixing with 900 mg of SiO_2 sand. The diluted catalyst was then loaded into a 1/2" quartz reactor packed with quartz wool and held within a rectangular aluminum block for optimized heat transfer. A home-made temperature controller was used to achieve desired reaction temperatures. All gas flows were controlled by mass flow controllers and an in-line bubbler was used to deliver gas phase ethanol was used to bubble ethanol and used as a diluent to control the ethanol partial pressure. The reaction effluent was quantified in a GC that injected the effluent once every 20 minutes and a 6' Haysep D column was used to separate species with quantification by in-line thermoconductivity (TCD) and flame ionization detectors (FID). Ethanol conversion was kept less than 5% for all studies to ensure the system was in the differential reactor regime.

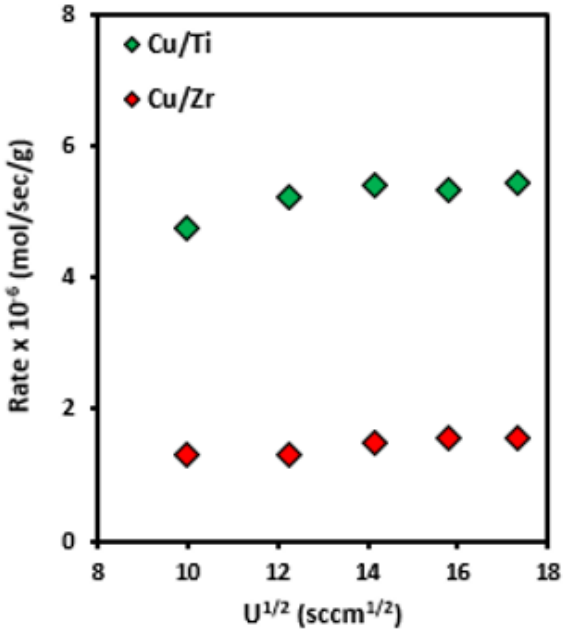

Figure 4.2 External Mass Transfer Effects. Ethanol dehydrogenation rates at 230 °C and 71.5 mbar ethanol as a function of the square root of the superficial velocity. 1 wt% Cu loaded on TiO_2 (Ti) and ZrO_2 (Zr) showed rates that were independent of the superficial velocity in the range of 100 to 300 cm^3 min^{-1}. A superficial velocity of 200 cm^3 min^{-1} was chosen for all kinetic experiments.

4.3.8.1 Ethanol dehydrogenation as a function of temperature

For temperature dependent dehydrogenation experiments catalysts were pre-treated either by reduction at 400 °C for 1 hr with H_2 at 50 mL min^{-1} or by oxidation at 450 °C for 1 hr with O_2 at 50 mL min^{-1} followed by reduction. Following pre-treatment, catalysts were activated by flowing 71.5 mbar ethanol at 230 °C with a superficial velocity of 200 mL min^{-1} for 8 hrs. After activation, the reactor was cooled to and maintained at 180 °C for 2 hours under a constant feed of 71.5 mbar of ethanol. Next, the temperature was increased to (2 °C min^{-1}) and held at 190 °C for 2 hours and this was repeated for each 10 °C step up to 230 °C.

4.3.8.2 Ethanol dehydrogenation as a function of ethanol and pyridine pressure

For ethanol pressure dependent dehydrogenation experiments, 1 wt% Cu/ZrO_2, $Cu/0.675Al\text{-}ZrO_2$ and Cu/TiO_2, were pre-treated by oxidation at 450 °C for 1 hour followed by reduction at 400 °C for 1 hour, with catalyst activation induced by 71.5 mbar ethanol at 210 °C for 8 hrs. After activation, while maintaining a constant temperature of 210 °C, the ethanol partial pressure was successively decreased from 71.5 mbar to 1.3 mbar in steps of 6.5 mbar by adjusting the flow rates of He that bubbled ethanol and He that acted as a diluent. The reaction system was held at each pressure for two hours to allow steady state to be reached and conversion was held at or under 5% at all conditions.

For pyridine pressure dependent dehydrogenation experiments, catalysts were pre-treated and activated in the same protocol as described above except with 45.5 mbar ethanol. After catalyst activation, He was introduced into a second bubbler holding

pyridine, to co-feed 1.95 mbar pyridine with 45.5 mbar ethanol into the reactor. After holding for 2 hours, the pyridine pressure was increased to 11.7 mbar in steps of 1.95 mbar (each pyridine pressure was held for 2 hours) while maintaining constant ethanol pressure (45.5 mbar), reaction temperature (210 °C), and superficial velocity (200 mL min^{-1}). After holding the system at 11.7 mbar of pyridine for 2 hours the ethanol pressure was decreased from 45.5 down to 6.5 mbar in steps of 6.5 mbar while maintaining a constant pyridine pressure (11.7 mbar), reaction temperature, and superficial velocity.

4.4 Results

4.4.1 Catalyst Characterization

The effects of metal oxide acidity on ethanol dehydrogenation were analyzed by supporting Cu nanoparticles on ZrO_2, TiO_2, and Al-ZrO_2 to vary the acid site concentration and strength. ZrO_2 and TiO_2 were chosen as they have similar surface acid site concentrations, but the Lewis acid sites on TiO_2 are known to be considerably stronger than on ZrO_2 based on NH_3 temperature programmed desorption,[50] and in-situ pyridine titration experiments.[51] Alternatively, it has been shown that surface doping of ZrO_2 by $Al(NO_3)_3$ enables the systematic deposition of Lewis sites that are stronger than the Lewis acid sites native to ZrO_2.[52–54] To control the amount of Al-derived Lewis acid sites on ZrO_2, different Al weight loadings were prepared, 0.025, 0.225, and 0.675 wt%, which correspond to Al surface densities of 0.21 Al/nm^2, 1.92 Al/nm^2, and 5.78 Al/nm^2, respectively (Table 4.1). Based on the unit cell size of Al_2O_3, it was expected that the ZrO_2 surface was essentially covered by a monolayer of Al^{3+} sites at 0.675 wt%. Note that the addition of Cu or Al to ZrO_2 did not change the ZrO_2 phase, which remained monoclinic, see Figure 4.3.[55]

Al Loading (wt%)	Al Surface Density (atoms/nm^2)
0.025	0.21
0.225	1.93
0.675	5.78

Table 4.1 Al Surface Density on ZrO_2. Estimated Al^{3+} surface loading on ZrO_2 (Surface Area: 26 ± 2 m^2/g) based on Al weight loading.

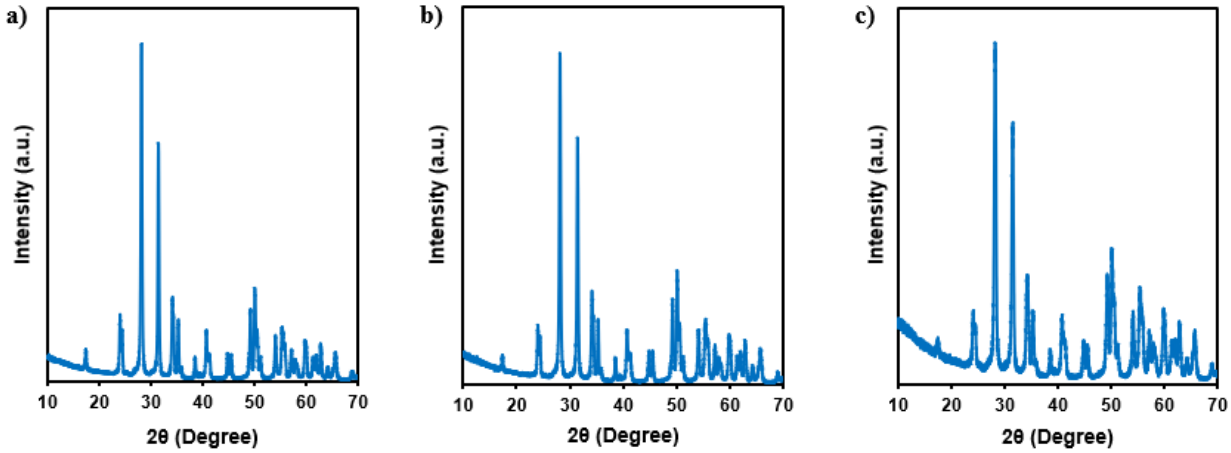

Figure 4.3 XRD diffractograms of **a)** bare ZrO_2, **b)** 1 wt% Cu loaded on ZrO_2, and **c)** 1 wt% Cu loaded on 0.675Al-ZrO_2. All spectra show that ZrO_2 is in the monoclicic (m) phase.

In-situ pyridine probe molecule IR was employed to examine differences in the types of acid sites existing on the supports. Figure 4.4 and 4.5 show IR spectra of pyridine adsorbed at saturation coverage to the various catalysts with pre-treatment by either reduction in H_2 at 400 °C or oxidation in O_2 at 450 °C followed by reduction. Figure 4.4 shows the IR spectra for adsorbed pyridine on Cu/ZrO_2 pre-treated by oxidation followed by reduction and Cu/0.675Al-ZrO_2 following both pre-treatments, specifically in the frequency region (1550-1650 cm^{-1}) where vibrational modes are assigned to pyridine adsorption on Lewis acid sites termed ω_{8a} in literature (the full spectra are shown in Figure 4.5).[56–64] It has been shown previously that the strength of Lewis acid sites in the ω_{8a} band region increases with increasing vibrational frequency.[56,63,64]

Vibrational modes observed at 1573 and 1603 cm^{-1} for pyridine adsorbed to Cu/ZrO_2 shown in Figure 4.4(a) are consistent with literature reports and are associated with Lewis acid sites of weak and medium strength, respectively.[56,64] For $Cu/0.675Al\text{-}ZrO_2$ that was pre-treated by in-situ oxidation followed by reduction, new pyridine stretches at 1592 and 1617 cm^{-1} were observed, which correspond to weak and strong Lewis acid sites, respectively.[56,64] In Figure 4.5, it is shown that no other significant differences existed in the pyridine IR for Cu/ZrO_2 and $Cu/0.675Al\text{-}ZrO_2$ outside of the 1550-1650 cm^{-1} region. The stretch at 1617 cm^{-1} has previously been assigned to pyridine adsorption on a 4-fold coordinated Al^{3+} site that exhibits strong Lewis acidity.[56]

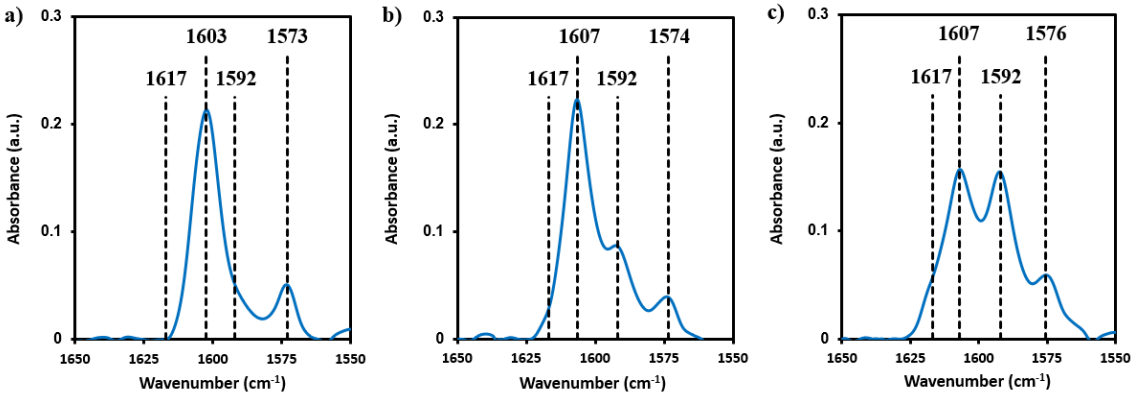

Figure 4.4 In situ IR spectra of pyridine adsorbed at 50 °C and at saturation coverage on **a)** 1 wt% Cu/ZrO_2 pre-treated by 450 °C oxidation followed by 400 °C reduction, **b)** 1 wt% $Cu/0.675Al\text{-}ZrO_2$ pre-treated by 400 °C reduction, and **c)** 1 wt% $Cu/0.675Al\text{-}ZrO_2$ pre-treated in-situ by 450 °C oxidation followed by 400°C reduction.

Although the strongest Lewis acid on Al_2O_3 have been reported to be associated with a vibrational frequency at 1621-1625 cm^{-1} in adsorbed pyridine, as shown in Figure 4.6, in the scope of this discussion we will label the band at 1617 cm^{-1} as a 'strong Lewis acid site' in comparison to the weak Lewis acid sites inherent to the ZrO_2 support.[56,65] Interestingly, the 1617 cm^{-1} pyridine stretch was only observed at the highest tested Al

loading on ZrO_2 (0.675 wt%), see Figure 4.7, and only when the catalyst was pre-treated in-situ by 450 °C oxidation followed by 400 °C reduction, see Figure 4.4(c). It is hypothesized that at 0.675 wt% Al, the generation of strong Lewis acid sites was the result of the formation of contiguous Al^{3+} sites, while the in-situ oxidative pre-treatment cleaned the surface from adsorbed adventitious species generated by exposure to the environment.[66] Alternatively, the pyridine stretch at 1592 cm^{-1} was present on Al-ZrO_2 at the lower weight loadings, see Figure 4.7, and was present on Cu/0.675Al-ZrO_2 at lower intensity when the catalyst was not oxidized in-situ prior to reduction. Note that outside of a small decrease in the relative intensity of the pyridine stretch at 1617 cm^{-1} for 1 wt% Cu/0.675Al-ZrO_2, the addition of Cu to the supports had little impact on the pyridine-IR spectra (see Figure 4.4 and Figure 4.7). Based on the pyridine IR analysis, it was concluded that Al doping of ZrO_2 and controlled in-situ pre-treatment effectively varied the existence and strength of acid sites on the support. In comparison, the pyridine IR spectra for 1 wt% Cu/TiO_2 (see Figure 4.5) showed a broadening of the ω_{19b} band vibrational modes (1440 – 1460 cm^{-1}) compared to both 1 wt% Cu/ZrO_2 and 1 wt% Cu/0.675Al-ZrO_2, consistent with the existence of strong Lewis acid Ti^{4+} sites that do not exist for the other two supports.[67]

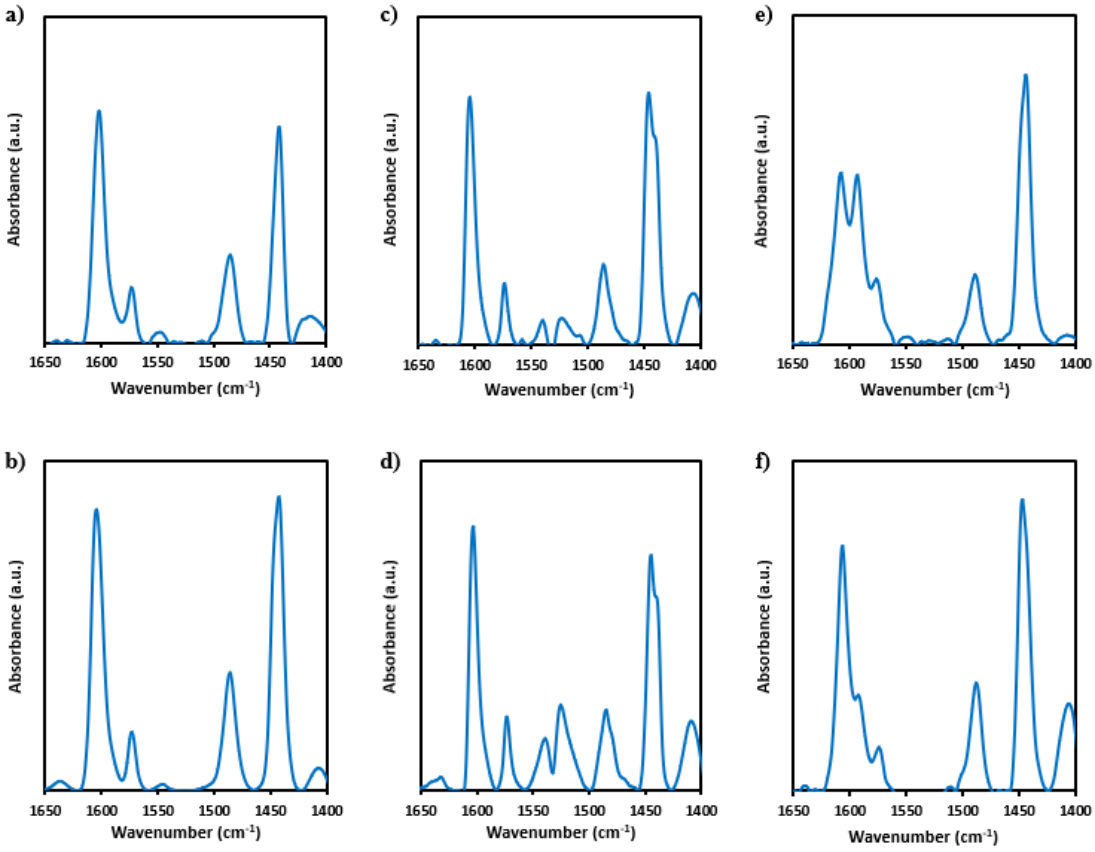

Figure 4.5 In situ IR spectra of pyridine adsorbed at 50°C and at saturation coverage on 1 wt% Cu loaded on ZrO2 pre-treated by **a)** 450 °C oxidation followed by 400 °C reduction and **b)** 400 °C reduction. 1 wt% Cu loaded on TiO2 pre-treated by **c)** 450 °C oxidation followed by 400 °C reduction and **d)** 400 °C reduction. 1 wt% Cu loaded on 0.675Al-ZrO2 pre-treated by **e)** 450 °C oxidation followed by 400 °C reduction and f) 400 °C reduction.

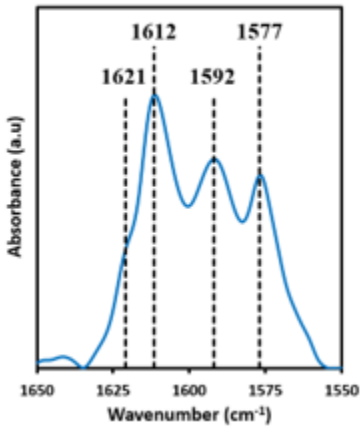

Figure 4.6 In situ IR spectra of pyridine adsorbed at 50°C and at saturation coverage on γ-Al_2O_3 pre-treated by 450 °C oxidation followed by 400 °C reduction.

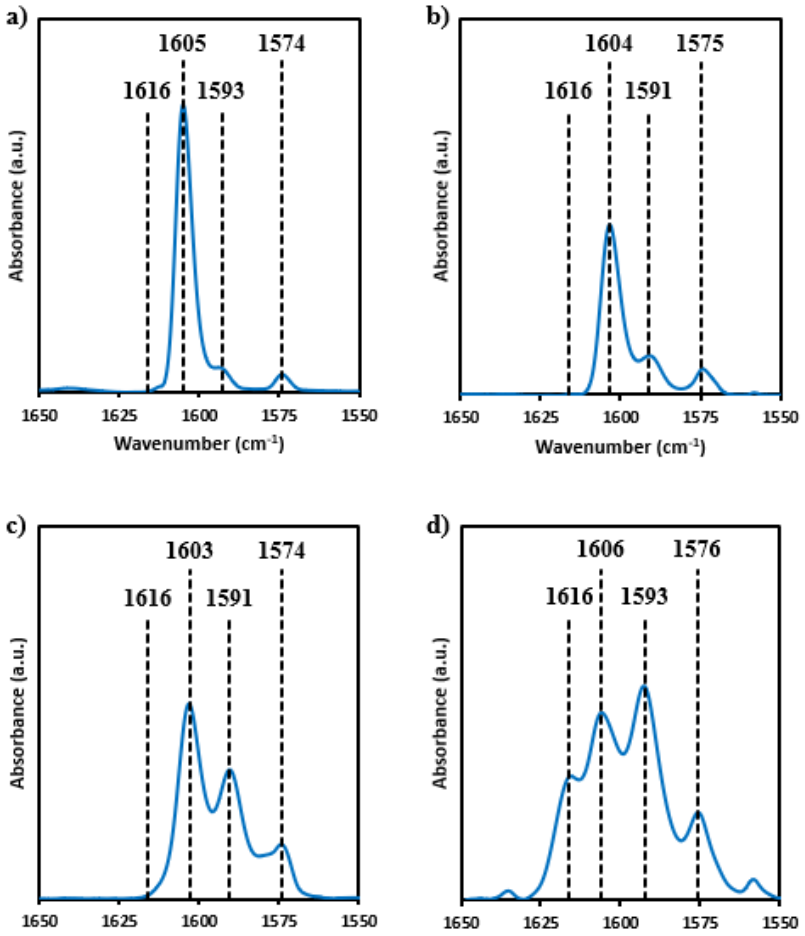

Figure 4.7 In situ IR spectra of pyridine adsorbed at 50°C and at saturation coverage on **a)** ZrO_2 (Zr), **b)** 0.075 wt% Al on ZrO_2, **c)** 0.225 wt% Al on ZrO_2, and **d)** 0.675 wt% Al on ZrO_2. All supports were pre-treated by 450 °C oxidation followed by 400 °C reduction.

Cu was impregnated onto all supports (TiO_2, ZrO_2, 0.025Al-ZrO_2, 0.225 Al-ZrO_2, 0.675Al-ZrO_2) at 1 wt% through incipient wetness impregnation. N_2O titration of the Cu surfaces followed by temperature-programmed reduction was used to quantify Cu dispersions, which are shown in Table 4.2. 1 wt%, Cu was well dispersed across all supports with similar estimated particle sizes ranging from 1.4 to 2.3 nm in diameter. Keeping Cu particle size similar and small across the different supports made it possible to probe the effects of support acidity on ethanol dehydrogenation activity without the potential influence of Cu particle size effects. Cu of varying dispersion (particle size) was

also deposited onto ZrO_2 by varying weight loading and synthetic approach, with dispersion ranging from 76% (~1.4 nm particles) to 18% (~5.9 nm particles), see (Table 4.2, Figure 4.1). Similarly, Cu weight loading and synthetic approach were varied to produce a range of Cu dispersions (particle sizes) on 0.675Al-ZrO_2, ranging from 73% (~1.4 nm particles) to 22% (~4.6 nm particles), see (Table 4.2, Figure 4.10).

Catalyst	**# Active Sites (10^{18} molec./g_{cat})**	**Dispersion (%)**	**Particle Size (nm)**
1 wt% Cu/ZrO_2[a]	72.4	76.2	1.4
1 wt % Cu/ZrO_2[b]	65.0	68.6	1.5
2.5 wt% Cu/ZrO_2	105.6	44.5	2.3
4.8 wt% Cu/ZrO_2	149.8	32.9	3.1
9.2 wt% Cu/ZrO_2	153.0	17.6	5.9
1 wt% Cu/0.025Al-ZrO_2	64.6	68.1	1.6
1 wt% Cu/0.225Al-ZrO_2	40.8	43.1	2.4
0.5 wt% Cu/0.675Al-ZrO_2	25.0	52.7	2.0
1 wt% Cu/0.675Al-ZrO_2[a]	69.2	73.0	1.4
1 wt% Cu/0.675Al-ZrO_2[b]	42.8	45.1	2.3
2.5 wt% Cu/0.675Al-ZrO_2	149.4	31.5	3.3
5 wt% Cu/0.675Al-ZrO_2	212.6	22.4	4.6
1 wt% Cu/TiO_2	40.8	43.1	2.4

Table 4.2 N_2O-TPR based measurements of # of active Cu sites, Cu dispersion, and estimated Cu particle size for Cu loaded over ZrO_2, TiO_2, and Al-ZrO_2. All estimates were made following 90 °C N_2O oxidation. The Cu weight loading for each catalyst is listed. [a] These 1 wt% Cu on ZrO_2 and 0.675Al-ZrO_2 catalysts were used for all kinetic experiments. [b] 1 wt % Cu/ZrO_2 was calcined at 350 °C rather than 450 °C and 1 wt % Cu/0.675Al-ZrO_2 was synthesized via wet impregnation rather than incipient-wetness impregnation. These two catalysts were used exclusively for the particle size dependent measurements.

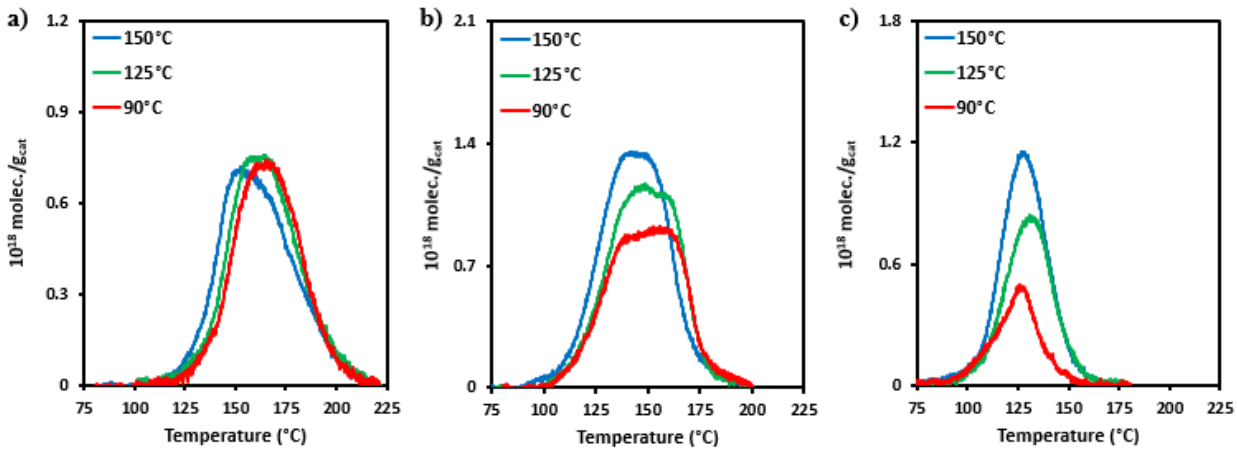

Figure 4.8 Temperature programmed reduction following N_2O oxidation with varying temperatures (90, 125, and 150 °C) for **a)** 1 wt% Cu/0.025Al-ZrO_2, **b)** 1 wt% Cu/0.225Al-ZrO_2, and **c)** 1 wt% Cu/0.675Al-ZrO_2. All catalysts were pre-treated by 450 °C oxidation followed by 400 °C reduction. The results following 90 °C oxidation, including dispersion and particle size estimates, are summarized in Table 4.2.

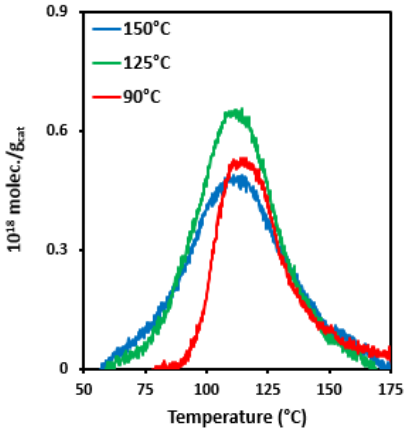

Figure 4.9 Temperature programmed reduction following N_2O oxidation with varying temperatures (90, 125, and 150 °C) for 1 wt% Cu/TiO_2 pre-treated by 450 °C oxidation followed by 250 °C reduction. The results following 90 °C oxidation, including dispersion and particle size estimates, are summarized in Table 4.2.

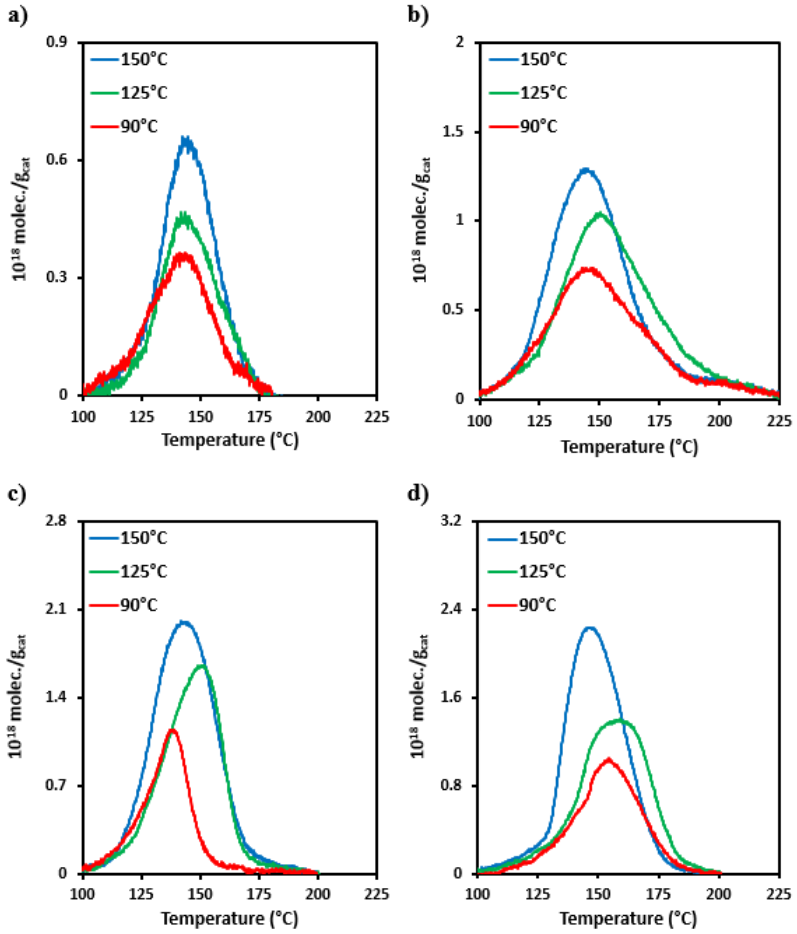

Figure 4.10 Temperature programmed reduction following N_2O oxidation with varying temperatures (90, 125, and 150 °C) for **a)** 0.5 wt% Cu/0.675Al-ZrO_2, **b)** 1 wt% Cu/0.675Al-ZrO_2[b] (synthesized with wet-impregnation rather than incipient wetness impregnation), **c)** 2.5 wt% Cu/0.675Al-ZrO_2, and **d)** 5 wt% Cu/0.675Al-ZrO_2. All catalysts were pre-treated by 450 °C oxidation followed by 400 °C reduction. The results following 90 °C oxidation, including dispersion and particle size estimates, are summarized in Table 4.2.

In-situ CO probe molecule IR was employed to gain insights into support-induced changes in the characteristics of Cu particles. All spectra were recorded at cryogenic temperatures (~ -130 °C) due to the weak affinity for CO binding to Cu.[36,68,69] Figure 4.11 shows IR spectra for CO adsorbed to 1 wt% Cu/ZrO_2 and Cu/0.675Al-ZrO_2 (these catalysts have almost identical Cu dispersions) after pre-treating the catalyst with 450 °C oxidation followed by 400 °C reduction. On both catalysts, prominent CO stretches at 2101 cm^{-1} and

2122-2124 cm^{-1} were observed along with a small shoulder at 2138 cm^{-1}. CO adsorbed to Cu/0.675Al-ZrO_2 showed a relative increase in the intensity of the stretch at 2122-2124 cm^{-1}, as compared to Cu/ZrO_2. The CO stretch at 2101 cm^{-1} is consistent with literature reports of CO adsorbed to metallic Cu^0 sites.[36,70] Surface science studies have shown that CO stretches on Cu(111) blue-shift from 2074-2077 cm^{-1} to 2115 cm^{-1} after the Cu surface is oxidized and further blue-shift to 2137 cm^{-1} over a roughened, oxidized Cu(110) surface.[71,72] Based on these observations, the CO stretches at 2122-2124 cm^{-1} and 2138 cm^{-1} were assigned to adsorption on cationic $Cu^{\delta+}$ sites. With the expectation that during pre-treatment the Cu surface was fully reduced, it is argued that $Cu^{\delta+}$ sites exist at the metal-support interface with Lewis acid sites drawing electron density away from interfacial Cu sites.[73,74]

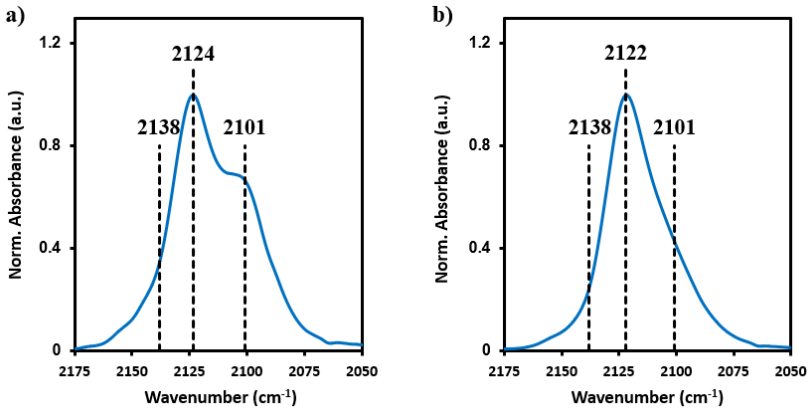

Figure 4.11 IR spectra of CO adsorbed at -130 °C and at saturation coverage on **a)** 1 wt% Cu loaded on ZrO_2 (Zr) pre-treated in-situ by 450 °C oxidation followed by 400 °C reduction and **b)** 1 wt% Cu loaded on 0.675Al-ZrO_2 pre-treated in-situ by 450 °C oxidation followed by 400 °C reduction.

Additionally, HAADF STEM was employed to show, with elemental mapping of Cu (Figure 4.12a-b), that Cu particles on 1 wt% Cu/ZrO_2 were well dispersed on the support, though not atomically dispersed as no CO vibrational frequency was observed at 2199 cm^{-1}, see Figure 4.11.[75] HR-TEM provided further evidence that Cu existed as

particles on the support with a cuboctahedron or round shape (Figure 4.12c-d), consistent with previous reports.[76,77]

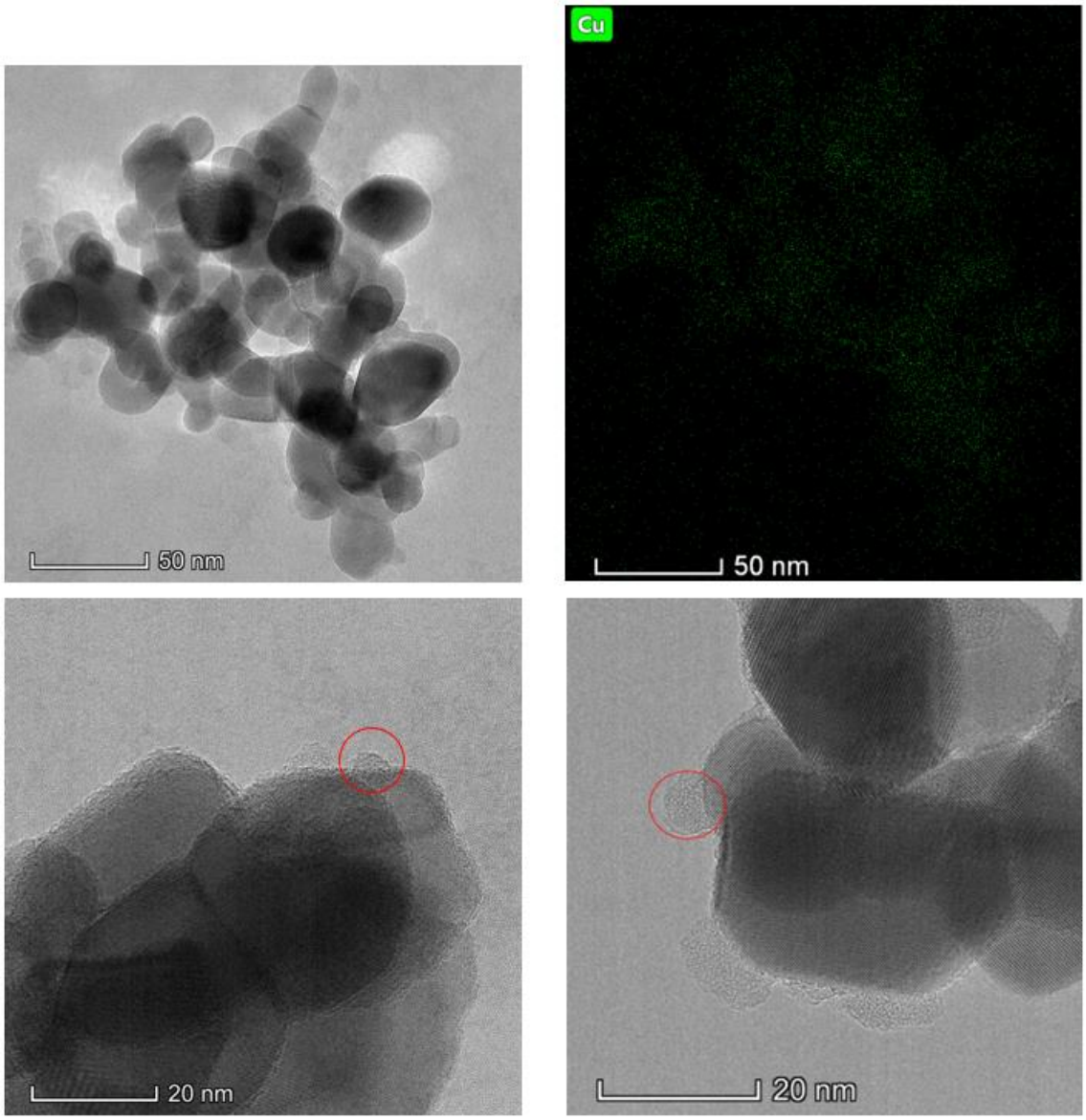

Figure 4.12. a) HAADF STEM image of a cluster of 1 wt% Cu loaded on ZrO_2 and b) EDS mapping of Cu (green) on ZrO_2. EDS mapping of Cu was employed to qualitatively show that Cu was well dispersed on the ZrO_2 surface. c) and d) HR-TEM images of 1 wt% Cu loaded on ZrO_2 on two different particle clusters. Red circles are used as a guide to see ~5nm particles with cuboctahedra or round particle shapes.

To summarize the catalyst characterization, Cu was loaded onto ZrO_2, TiO_2, and Al-ZrO_2, which had varying acidity. In-situ pyridine probe molecule FTIR identified the

formation of strong Al^{3+} (Al_{IV}) sites on 0.675Al-ZrO_2 after 450 °C oxidation and 400 °C reduction, showing that a combination of Al loading and in-situ pre-treatment are responsible for generating strong Lewis acid sites. Cu was loaded at similar dispersion across all supports and with varying Cu dispersion over ZrO_2 and 0.675Al-ZrO_2 catalysts. Based on CO probe molecule IR, it was proposed that strong Lewis acid sites on 0.675Al-ZrO_2 effectively withdrew charge from interfacial Cu sites, producing more cationic Cu sites as compared to the ZrO_2 supported catalyst.

4.4.2 The influence of support acidity on ethanol dehydrogenation kinetics

To compare the activity of the 1 wt% Cu catalysts as a function of support, ethanol dehydrogenation was executed at an ethanol partial pressure of 71.5 mbar diluted in He following pre-treatment of the catalysts with in-situ oxidation at 450 °C followed by reduction 400 °C. Total flow rate dependent measurements were made to ensure the rate of mass transport to the catalysts surface did not influence the observed kinetics, examples of which are shown for 1 wt% Cu/ZrO_2 and Cu/TiO_2 in Figure 4.2. Ethanol conversion was maintained below 5% in all experiments, ensuring differential kinetics. Temperature dependent ethanol dehydrogenation TOF for 1 wt% Cu/TiO_2, Cu/ZrO_2 and Cu/0.675Al-ZrO_2 between 180 and 230 °C are shown in Figure 4.13 (a).

Using 200 °C (0.254 mol/kJ) as an example, 1 wt% Cu/TiO_2 showed a dehydrogenation TOF of (6.22 ± 0.01) x 10^{-2} s^{-1} and 1 wt% Cu/0.675Al-ZrO_2 showed a TOF of (8 ± 1) x 10^{-2} s^{-1}, which were respectively 11 and 15-fold enhanced compared to the TOF over 1 wt% Cu/ZrO_2 of (0.55 ± 0.09) x 10^{-2} s^{-1}. These results are summarized in Table 4.3. In all measurements, the selectivity towards acetaldehyde was 100% within

experimental error, as acetaldehyde was the only measurable product. The corresponding activation barriers were 71 ± 2 kJ/mol for 1 wt% Cu/TiO_2, 60 ± 8 kJ/mol for 1 wt% Cu/0.675Al-ZrO_2, and 73 ± 5 kJ/mol for 1 wt% Cu/ZrO_2, consistent with barriers reported in literature ~70 kJ/mol.[5,44,78]

Figure 4.13(b) shows temperature dependent TOF for 1 wt% Cu on ZrO_2, 0.025Al-ZrO_2, 0.225 Al-ZrO_2, and 0.675Al-ZrO_2 to highlight the influence of additional Lewis acid sites generated by Al addition on ZrO_2. It was observed that the TOF at 200 °C was only mildly enhanced due to the addition of 0.025% and 0.225% Al to ZrO_2, with the most significant enhancement observed at the highest Al loading of 0.675%. The trends observed via pyridine IR suggest the strength of the support acid sites plays a key role in controlling the ethanol TOF. Given the increased strength of acidic sites on 0.675Al-ZrO_2 and TiO_2 compared to ZrO_2, but the retained 100% acetaldehyde selectivity within experimental error, Figure 4.13 provides evidence that support acidity promotes ethanol conversion, while Cu controls the reaction pathway and product selectivity, suggesting cooperative behavior.

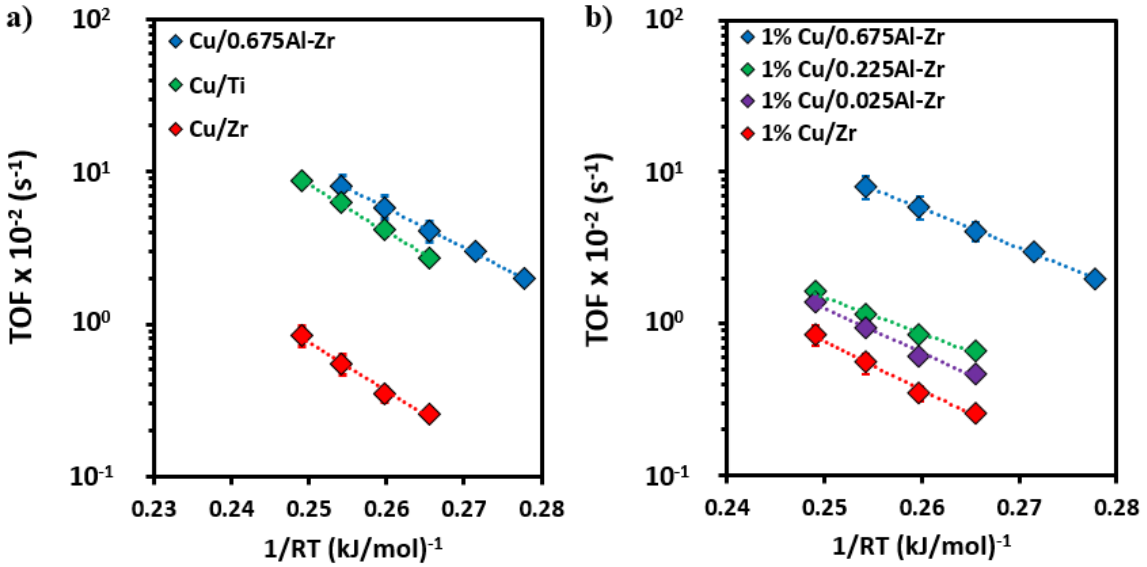

Figure 4.13 Ethanol turn over frequency (TOF) at 71.5 mbar ethanol as a function of temperature (from 160 to 210 °C) for **a)** 1 wt% Cu on ZrO_2 (Zr), TiO_2 (Ti), and 0.675Al-ZrO_2 and **b)** 1 wt% Cu loaded ZrO_2 with varying Al weight loadings. All catalysts were pre-treated in-situ by 450 °C oxidation followed by 400 °C reduction.

Catalyst	TOF at 200°C (10^{-2} s^{-1})
1% Cu/ZrO_2	0.55 ± 0.09
1% Cu/0.025Al-ZrO_2	0.93
1% Cu/0.225Al-ZrO_2	1.14
1% Cu/0.675Al-ZrO_2	8 ± 1
1% Cu/TiO_2	6.22 ± 0.01

Table 4.3 Ethanol dehydrogenation turn over frequency (TOF) at 200 °C and 71.5 mbar ethanol for 1 wt% Cu on ZrO_2, 0.025Al-ZrO_2, 0.225Al-ZrO2, 0.675Al-ZrO2, and TiO_2. Corresponding temperature dependent results are shown in Figure 4.13.

Whereas Figure 4.13 showed how Cu catalysts synthesized on acidic supports (TiO_2 and 0.675Al-ZrO_2) promoted ethanol dehydrogenation, the impact of catalyst pre-treatment was probed by comparing activity after 400 °C reduction in H_2 and oxidation with varying temperature (50 °C, 150 °C, and 450 °C) followed by 400 °C reduction. Figure 4.14 shows ethanol TOF as a function of temperature for 1 wt% Cu/0.675Al-ZrO_2 following the varied pre-treatment, where a clear trend of decreased ethanol TOF with decreasing in-situ oxidation temperature was observed. TOF measured at 200 °C, with

100% selectivity towards acetaldehyde, decreased from 4.8 x 10^{-2} s^{-1} after 450 °C oxidation down to 2.8 x 10^{-2} s^{-1}, 2.4 x 10^{-2} s^{-1}, and 0.59 x 10^{-2} s^{-1} after 150 °C, 50 °C, and no oxidative pre-treatment, respectively. These results are summarized in Table 4.4. Note that the difference in TOF of 1 wt% Cu/0.675Al-ZrO_2 in Figure 4.14 compared to Figure 4.13 following identical pre-treatment was attributed to an increased catalyst activation temperature (from 210 to 230 °C), which induced slight Cu particle sintering. Figure 4.15 shows that the ethanol TOF over 1% Cu/TiO_2 was impacted in an analogous way to that of 1 wt% Cu/0.675Al-ZrO_2 as a function of oxidative pre-treatment temperature with the results summarized in Table 4.5. Interestingly, without oxidative pre-treatment, the TOF over 1 wt% Cu/0.675Al-ZrO_2 of 0.59 x 10^{-2} s^{-1}, was similar to the TOF over 1 wt% Cu/ZrO_2 of (0.55 ± 0.09) x 10^{-2} s^{-1}, as shown in Figure 4.13. It was described previously that dehydroxylation (heat treatment in inert) of Al_2O_3 can effectively modify the surface acid sites.[79] To test whether surface dehydroxylation is playing a role in promoting dehydrogenation activity, the catalyst was thermally treated in He at 450 °C and then reduced at 400 °C. Noticeably, the TOF after 450 °C He treatment was significantly lower compared to the TOF for the sample that was treated in O_2 at the same temperature (Figure 4.15), suggesting that oxidation is necessary during catalyst pre-treatment to burn off adventitious species on the support surface.[66] In the context of the pyridine IR shown in Figure 4.4, the enhanced activity for the samples that were oxidized prior to reduction is correlated with the existence of strong Lewis acid sites.

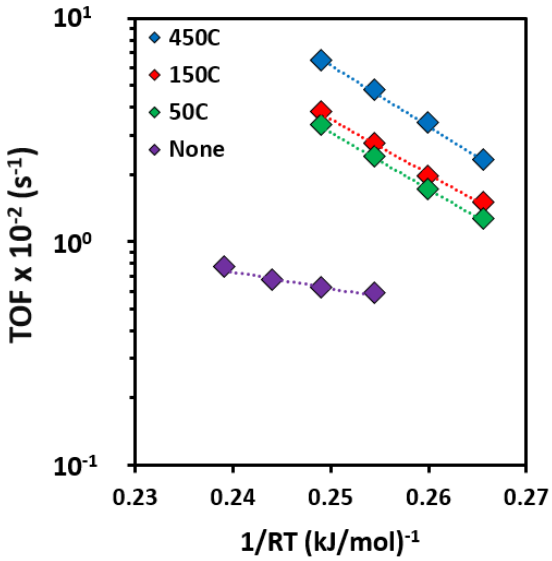

Figure 4.14 Ethanol TOF at 71.5 mbar ethanol over 1 wt% Cu/0.675Al-ZrO_2 as a function of temperature for varying in-situ pre-treatments consisting of 450 °C, 150 °C, 50 °C in O_2, and no oxidative pre-treatment, followed by reduction at 400 °C in H_2.

Pre-Treatment	TOF at 200°C (10^{-2} s^{-1})
450 °C Oxidation 400 °C Reduction	4.8
150 °C Oxidation 400 °C Reduction	2.8
50 °C Oxidation 400 °C Reduction	2.4
No Oxidation 400 °C Reduction	0.59

Table 4.4 Ethanol dehydrogenation turn over frequency (TOF) at 200 °C and 71.5 mbar ethanol for 1 wt% Cu on 0.675Al/ZrO_2 with varying in-situ pre-treatment. Corresponding pre-treatment dependent results are shown in Figure 4.14.

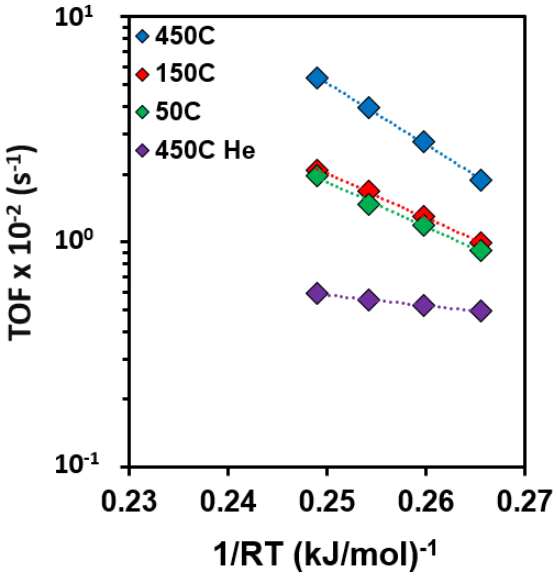

Figure 4.15 Ethanol turn over frequency (TOF) for 1 wt% Cu loaded on TiO_2 as a function of temperature for varying in-situ pre-treatments consisting of 450 °C, 150 °C, 50 °C oxidation, and 450 °C treatment in He, all followed by reduction at 400 °C.

Pre-Treatment	TOF at 200°C (10^{-2} s^{-1})
450 °C Oxidation 400 °C Reduction	3.9
150 °C Oxidation 400 °C Reduction	1.7
50 °C Oxidation 400 °C Reduction	1.5
450 °C He Purge 400 °C Reduction	0.55

Table 4.5 Ethanol dehydrogenation turn over frequency (TOF) at 200 °C and 71.5 mbar ethanol for 1 wt% Cu on TiO_2 with varying in-situ pre-treatment. Corresponding pre-treatment dependent results are shown in Figure 4.15

4.4.3 Ethanol dehydrogenation dependence on Cu particle size

The activity measurements shown in Figure 4.13-4.15 provide evidence that support acid sites promote the TOF for ethanol conversion to acetaldehyde on Cu nanoparticles. This raises an interesting question of whether the support acidity promotes the TOF at all exposed Cu sites, or if the promoting effect is localized at interfacial Cu sites. To probe this question, the TOF for ethanol dehydrogenation was measured as a

function of Cu particle size on ZrO_2 and 0.675Al-ZrO_2. As Cu particle diameter (d) increases, the fraction of exposed sites at the oxide interface decreases with a dependence of $d^{-0.9}$.[80–84] However, the fraction of exposed Cu atoms existing as steps (as compared to terraces) follows the same dependence, which has been commonly used to probe structure sensitivity. To differentiate the role of interfacial Cu sites and Cu step sites, Cu particle size dependent TOF measurements must be executed on multiple supports that are expected to exhibit different interfacial effects.[73] Assuming similar dependences of step and terrace concentrations for Cu particles of a given size regardless of support, differences in particle size dependent TOF seen for Cu on ZrO_2 and 0.675Al-ZrO_2 must be due to a difference in the contribution of interfacial sites. Ethanol TOFs, with 100% selectivity towards acetaldehyde, measured at 200 °C on Cu/ZrO_2 (1.4 – 6 nm diameter) and Cu/0.675Al-ZrO_2 (1.4 – 4.6 nm diameter) as a function of inverse dispersion (and estimated particle size) are shown in Figure 4.16 and Figure 4.17. The ethanol TOF on Cu/ZrO_2 slightly increased with increasing particle size from (0.55 ± 0.09) x 10^{-2} s^{-1} for ~ 1.4 nm Cu to (1.9 ± 0.3) x 10^{-2} s^{-1} for ~ 6 nm Cu. On the other hand, ethanol TOF on Cu/0.675Al-ZrO_2 decreased with increasing particle size from 7.9 x 10^{-2} s^{-1} for ~1.4 nm Cu to (4 ± 1) x 10^{-2} s^{-1} for ~4.6 nm Cu. The TOF shows a positive dependence on 1/dispersion for Cu/ZrO_2 (+0.48 slope) and a negative dependence for Cu/0.675Al-ZrO_2 (-0.45 slope). The difference in slope of ~1 is consistent with what is expected for a transition from a catalyst where interfacial sites are not the primary active site (Cu/ZrO_2) to a catalyst where the interface dominates the catalyst activity (Cu/0.675Al-ZrO_2). The assignments of minimal participation of interfacial sites and complete control of activity by interfacial sites are typically deduced from a slope of 0

and -1, respectively, when plotting TOF versus 1/dispersion.[80,81] It is proposed that the decreased dependencies observed here (0.5 vs. 0 and -0.5 vs. -1) are due to the slight overestimation of Cu dispersion from the overoxidation of surface Cu sites (formation of Cu^{2+} rather than Cu^{+}), which is hypothesized to be more prevalent with smaller particle sizes.[85]

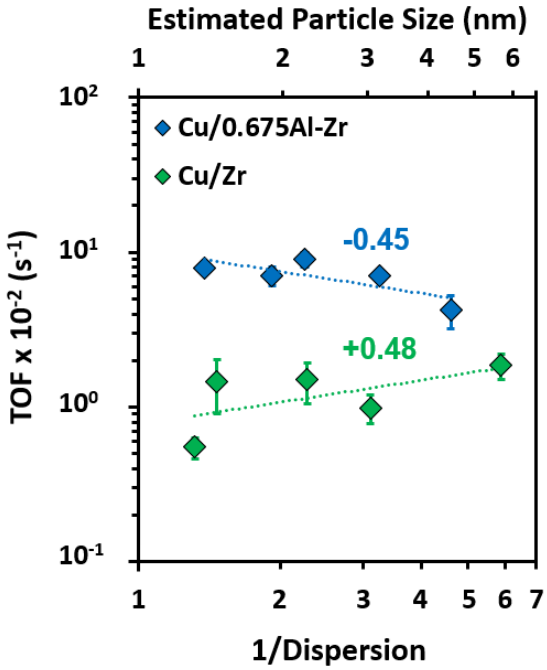

Figure 4.16 Ethanol TOF at 200 °C and 71.5 mbar ethanol over Cu loaded on ZrO_2 (Zr) and 0.675Al-ZrO_2 as a function of 1/dispersion (~ Cu particle size). The dotted lines show the linear trend to data with corresponding slopes displayed. All catalysts were pre-treated in-situ by 450 °C oxidation followed by 400 °C reduction.

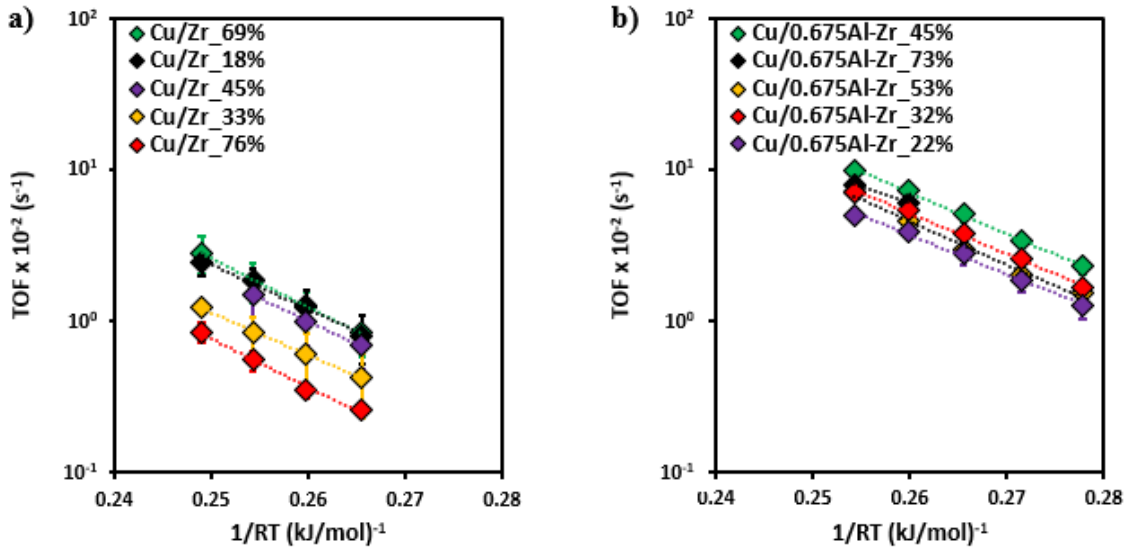

Figure 4.17 Ethanol turn over frequency (TOF) as a function of temperature ranging from 160 to 230 °C with 71.5 mbar ethanol feed on **a)** Cu with various dispersions (18 to 76%) loaded on ZrO_2 (Zr), pre-treated by 450 °C oxidation followed by 400 °C reduction, and **b)** Cu with various dispersions (22 to 73%) loaded on 0.675Al-ZrO_2 pre-treated by 450 °C oxidation followed by 400 °C reduction.

4.4.4 Effect of ethanol partial pressure on ethanol dehydrogenation

The particle size dependent trends in Figure 4.16-4.17 showed how support acid sites not only promote dehydrogenation TOF, but also suggested a shift of the active sites from that of all exposed Cu sites to interfacial Cu when Cu interacts with stronger Lewis acid sites. To provide further insight into the role of support acid sites on promoting ethanol conversion on Cu, ethanol dehydrogenation was executed over 1 wt% Cu/0.675Al-ZrO_2, Cu/TiO_2, and Cu/ZrO_2 at 210 °C with decreasing ethanol partial pressures from 71.5 mbar to 1.3 mbar as shown in Figure 4.18 (a).

At 71.5 mbar ethanol, 1 wt% Cu/TiO_2 showed a dehydrogenation TOF of (7.1 ± 0.6) x 10^{-2} s^{-1} and 1 wt% Cu/0.675Al-ZrO_2 showed a TOF of (10 ± 2) x 10^{-2} s^{-1}, which were respectively 20 and 28-fold enhanced compared to the TOF of 1 wt% Cu/ZrO_2 of (0.36 ± 0.05) x 10^{-2} s^{-1}. However, at 1.3 mbar, 1 wt% Cu/TiO_2 showed a TOF of (0.37 ± 0.06) x

10^{-2} s^{-1} and 1 wt% Cu/0.675Al-ZrO_2 showed a TOF of (0.43 ± 0.05) x 10^{-2} s^{-1}, which were respectively only 4 and 5-fold enhanced compared to the TOF of 1 wt% Cu/ZrO_2 of (0.09 ± 0.04) x 10^{-2} s^{-1}. Qualitatively similar ethanol partial pressure dependent trends were observed for 1 wt% Cu/TiO_2 and Cu/0.675Al-ZrO_2 where TOF decreased continuously with decreasing ethanol pressure and approached a linear trend below 45.5 mbar ethanol. On the other hand, 1 wt% Cu/ZrO_2 exhibited TOF that were ethanol pressure independent above 45.5 mbar, below which the TOF decreased linearly with ethanol pressure. Most interestingly, at low ethanol partial pressures the TOF enhancement of 1 wt% Cu/TiO_2 and 1 wt% Cu/0.675Al-ZrO_2 decreased and the TOF converged towards that of 1 wt% Cu/ZrO_2. This demonstrates that the ethanol partial pressure, which controls ethanol or reactive intermediate coverage on Cu and support acid sites, influences how significantly support acid sites participate in ethanol dehydrogenation. Additionally, it is possible to compare ethanol dehydrogenation TOF at 190 °C and 71.5 mbar for 1 wt% Cu/ZrO_2 in Figure 4.13 to that of nanoporous, unsupported Cu (np-Cu)[86] at 190 °C and ~ 56 mbar ethanol, which shows excellent agreement with values of (0.35 ± 0.04) x 10^{-2} s^{-1} and 0.33 x 10^{-2} s^{-1} (site density of ~1 x 10^{19} sites/mm^2 for np-Cu), respectively. Since the TOF of 1 wt% Cu/ZrO_2 showed ethanol pressure independence for pressures above 45.5 mbar, it was expected that there was no impact on dehydrogenation TOF when comparing 71.5 or 56 mbar ethanol. This, this comparison provides additional evidence that bare ZrO_2 does not play a role in promoting Cu dehydrogenation activity and the reaction proceeds over the exposed Cu surface sites.

To directly probe the impact of Lewis acid sites on ethanol dehydrogenation TOF, 1 wt% Cu/0.675Al-ZrO_2 and Cu/ZrO_2 were exposed to a co-feed of pyridine, increasing from 1.95 to 11.7 mbar, with a constant ethanol pressure of 45.5 mbar and temperature of 210 °C, as shown in Figure 4.18 (b). Both catalysts showed a similar trend where dehydrogenation TOF decreased with increasing pyridine pressure, until the TOF became constant above 8 mbar pyridine. The TOF for 1 wt% Cu/0.675Al-ZrO_2 decreased from 8.2 x 10^{-2} s^{-1} (no pyridine) to 0.19 x 10^{-2} s^{-1} (11.7 mbar pyridine), a 43-fold decrease, and for 1 wt% Cu/ZrO_2, the TOF decreased from 0.89 x 10^{-2} s^{-1} to 0.07 x 10^{-2} s^{-1}, a 13-fold decrease. The TOF for 1 wt% Cu/0.675Al-ZrO_2 and Cu/ZrO_2 converged to only a 3-fold difference with a co-feed of 11.7 mbar pyridine, which is similar to the difference that was observed at the lowest ethanol partial pressures without pyridine in Figure 4.18 (a). Pyridine adsorption was shown to be in equilibrium with the flowing gas phase, rather than being irreversibly bound, as activity was restored after stopping the flow of pyridine into the reactor (Figure 4.19).

After reaching a constant TOF as a function of pyridine partial pressure (11.7 mbar pyridine) the ethanol partial pressure was decreased, as shown in Figure 4.18 (c). With decreasing ethanol pressure, the ethanol dehydrogenation TOF of 1 wt% Cu/0.675Al-ZrO_2 and Cu/ZrO_2 decreased and at 6.5 mbar ethanol the TOF of 1 wt% Cu/0.675Al-ZrO_2 and Cu/ZrO_2 were both 0.02 x 10^{-2} s^{-1}, showing a complete convergence of TOF at the lowest considered ethanol pressures (all pressure dependent results, with acetaldehyde selectivity of 100%, are summarized in Table 4.6). This demonstrates that the support acid sites most effectively promote ethanol conversion to acetaldehyde on Cu when operating at the

highest ethanol pressures and that the promotion was negated at low ethanol pressure with in-situ poisoning of support acid sites.

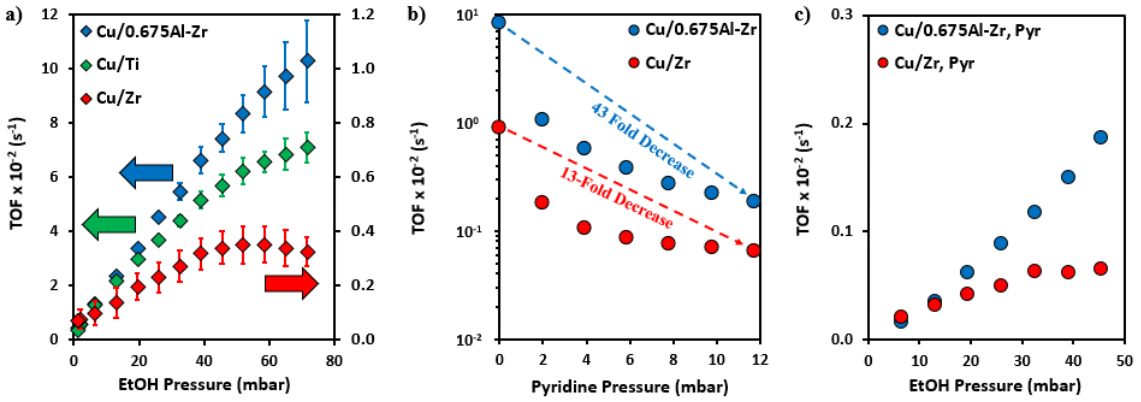

Figure 4.18 a) Ethanol TOF at 210 °C as a function of ethanol partial pressure. Primary axis for 1 wt% Cu loaded on 0.675Al-ZrO_2 and TiO_2 (Ti) and secondary axis for 1 wt% Cu loaded on ZrO_2 (Zr). **b)** Ethanol TOF at 210 °C as a function of pyridine partial pressure with a cofeed of 45.5 mbar ethanol. **c)** Ethanol TOF at 210 °C as a function of ethanol partial pressure with a cofeed of 11.7 mbar pyridine. All catalysts were pre-treated in-situ by 450 °C oxidation followed by 400 °C reduction.

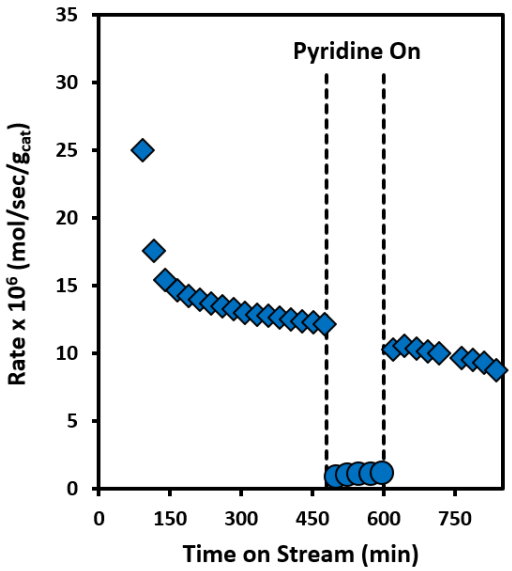

Figure 4.19 Ethanol dehydrogenation reaction rate on 1 wt% Cu loaded 0.675Al-ZrO_2 as a function of time on stream at 210 °C and with an inlet flow of 45.5 mbar of ethanol. At 480 minutes (8 hours), 11.7 mbar of pyridine was cofed onto the catalyst with 45.5 mbar of ethanol for 2 hours (until 600 minutes). Rates dropped by a factor of 12 and remained constant until the pyridine flow was shut off and dehydrogenation rates returned to their original values, correcting for catalyst deactivation independent of pyridine.

Catalyst	TOF at 71.5 mbar EtOH (10^{-2} s^{-1})	TOF at 1.3 mbar EtOH (10^{-2} s^{-1})	TOF at 71.5 mbar EtOH, 11.9 mbar pyridine (10^{-2} s^{-1})	TOF at 6.5 mbar EtOH, 11.9 mbar pyridine (10^{-2} s^{-1})
1% Cu/ZrO_2	0.36 ± 0.05	0.09 ± 0.04	0.07	0.02
1% $Cu/0.675Al\text{-}ZrO_2$	10 ± 2	0.43 ± 0.05	0.19	0.02
1% Cu/TiO_2	7.1 ± 0.6	0.37 ± 0.06	--	--

Table 4.6 Ethanol dehydrogenation turn over frequency (TOF) at 210 °C and varying inlet pressures of EtOH and pyridine for 1 wt% Cu on ZrO_2, $0.675Al/ZrO_2$, and TiO_2. Corresponding pre-treatment dependent results are shown in Figure 4.18.

To summarize the experimental observations, it was shown that:

1) Support acid sites promoted ethanol dehydrogenation by Cu while maintaining the inherent acetaldehyde selectivity of Cu.
2) The most significant activity promotion was observed at higher ethanol partial pressures, where it was also observed that on acidic supports, interfacial Cu sites were the dominant active site involved in the RLS, while on weakly acidic supports, all Cu surface sites were active.
3) The promotional effect of support acid sites could be completely negated by operating at low ethanol pressures and co-feeding pyridine at saturation coverage.

4.5 Discussion

The combination of in-situ characterization and detailed reaction kinetics measurements suggested that Lewis acid sites on metal oxide supports can promote the activity of ethanol dehydrogenation to acetaldehyde on Cu nanoparticles. The question that must be considered is how the Lewis acids promote ethanol conversion TOF while maintaining inherent Cu selectivity.

The addition of 0.675 wt% Al^{3+} to ZrO_2 generated strong Lewis acid Al_{IV} sites, but only after pre-treatment with in-situ oxidation at 450 °C followed by in-situ reduction at 400 °C, see Figure 4.4. In correlation with this, it was observed that the ethanol TOF was also only promoted on $Cu/0.675Al\text{-}ZrO_2$ following the sequential oxidation-reduction pre-

treatment, see Figure 4.14. Interestingly, CO probe molecule IR showed no change in the Cu characteristics as a function of pre-oxidation treatment (see Figure 4.20). The pre-treatment dependent activity measurements coupled with the pre-treatment dependent characterization of the acid and Cu sites provides evidence that strong Lewis acid sites promoted the ethanol TOF by playing a direct role in the reaction mechanism. This conclusion is further substantiated by the in-situ pyridine poisoning experiments shown in Figure 4.18 (b) and Figure 4.19, where it was seen that selective poisoning of the support acid sites significantly decreased the catalytic activity. It has been well documented that strong Lewis acid sites drive facile O-H bond cleavage, but have a large activation barrier for C_{α}-H bond cleavage.[33,34] Therefore, we propose that the strong Lewis acid Al_{IV} sites on 0.675Al-ZrO_2, which are also characteristic of γ-Al_2O_3 (see Figure 4.6), directly promoted the dehydrogenation TOF by facilitating ethanol O-H bond cleavage.

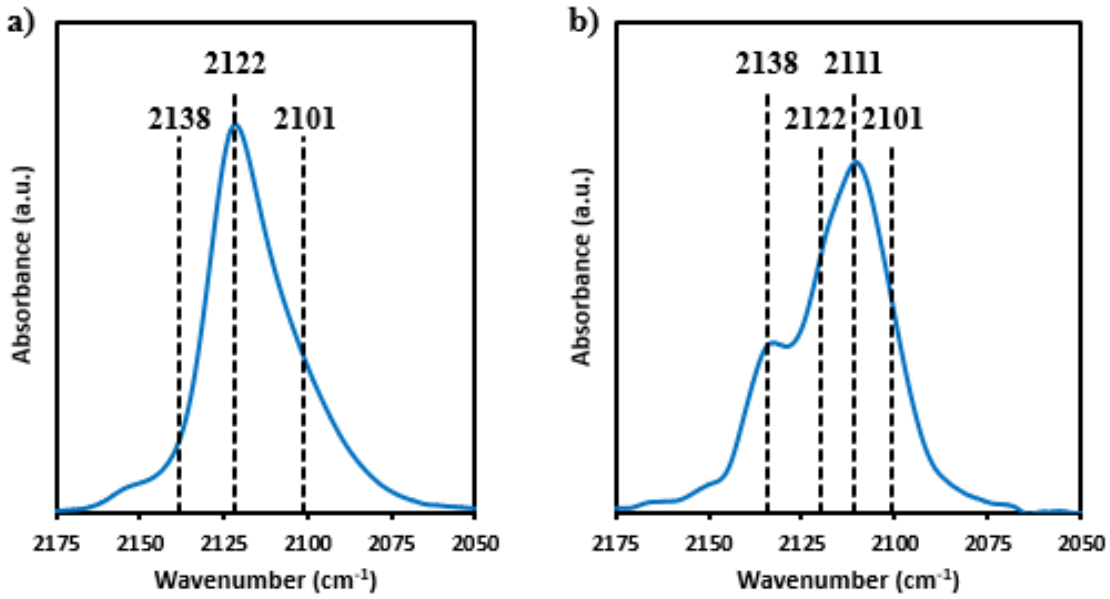

Figure 4.20 In-situ IR spectra of CO adsorbed at -130 °C and at saturation coverage on **a)** 1 wt% Cu loaded on 0.675Al-ZrO_2 pre-treated by 400 °C reduction and **b)** on 1 wt% Cu loaded on TiO_2 pre-treated by 450 °C oxidation followed by 400 °C reduction.

Interestingly, CO probe molecule IR suggested that the strong Lewis acid sites on 1 wt% Cu/0.675Al-ZrO_2 also modified Cu by generating a larger fraction of $Cu^{\delta+}$ compared to Cu^0 sites, as evidenced by a two-fold increase in the relative intensity of the CO vibrational mode at 2122-2124 cm^{-1} when comparing 1 wt% Cu/ZrO_2 to Cu/0.675Al-ZrO_2 (see Figure 4.11). It is proposed that this effect was induced by the strong Lewis acid sites drawing electron density from interfacial Cu sites[73] through a chemical compensation effect[87], through which it is suggested that low valence Al^{3+} on ZrO_2 (higher valence Zr^{4+}) can generate a local electron deficit that is then compensated by the introduction of Cu, which can donate electrons to the Al-doped ZrO_2, generating interfacial $Cu^{\delta+}$ sites. To test the effect of the $Cu^{\delta+}$ on reactivity, the number of interfacial Cu sites was varied through the control of Cu particle size over ZrO_2 and 0.675Al-ZrO_2. Figure 4.16 shows the Cu-support interface shifted from having a minimal effect on dehydrogenation TOF (Cu/ZrO_2) to dominating dehydrogenation activity (Cu/0.675Al-ZrO_2), suggesting that by promoting the formation of interfacial Cu sites, strong Lewis acid sites on the support also indirectly promoted ethanol dehydrogenation TOF. However, the selectivity towards acetaldehyde remained at 100% for all catalysts. This suggested that for 1 wt% Cu/0.675Al-ZrO_2, C_α-H bond activation occurred at interfacial Cu sites that dictated the reaction selectivity, while the strong Lewis acid sites of the support facilitated O-H bond cleavage.

Based on this analysis, a reaction mechanism was proposed, as shown in Scheme 3.1. First, ethanol adsorbed to a support acid site (Step 1), after which the support Lewis acid site induced O-H bond cleavage, forming surface ethoxy species (Step 2). Next, at the Cu-support interface, the ethoxy diffused from the acid site to an interfacial Cu site (Step

3). C_α-H bond cleavage (Step 4) then occurred at interfacial Cu sites, followed by acetyl desorption to produce acetaldehyde (Step 5). 2 H's formed from the two bond cleavage steps (Step 2 and Step 4) and, after diffusing from the support to the Cu sites (Step 6), associatively desorbed from the Cu surface (Step 7). This process is discussed further below.

1. $\mathbf{CH_3CH_2OH(g) + *_{acid} \rightleftharpoons CH_3CH_2OH\ *_{acid}}$
2. $\mathbf{CH_3CH_2OH\ *_{acid} + *_{base} \rightleftharpoons CH_3CH_2O\ *_{acid} + H\ *_{base}}$
3. $\mathbf{CH_3CH_2O\ *_{acid} + *_{Cu} \rightleftharpoons CH_3CH_2O\ *_{Cu} + *_{acid}}$
4. $\mathbf{CH_3CH_2O\ *_{Cu} + *_{Cu} \rightleftharpoons CH_3CHO\ *_{Cu} + H\ *_{Cu}}$
5. $\mathbf{CH_3CHO\ *_{Cu} \rightleftharpoons CH_3CHO(g) + *_{Cu}}$
6. $\mathbf{H\ *_{base} + *_{Cu} \rightleftharpoons H\ *_{Cu} + *_{base}}$
7. $\mathbf{2H\ *_{Cu} \rightleftharpoons H_2(g) + 2\ *_{Cu}}$

Scheme 4.1. Reaction mechanism of ethanol dehydrogenation over Cu/support. $*_{Cu}$ represents Cu adsorption sites, $*_{base}$ represents support basic sites, and $*_{acid}$ represents Lewis acid sites.

Drawing from reports in literature, it was initially assumed that C_α-H bond cleavage (Step 4) was the rate limiting step (RLS) for the dehydrogenation reaction.[4,20,26,27] Based on this assumption, a rate expression was derived using the quasi-equilibrium approximation, as shown in equation 4.1. All corresponding derivations and assumptions for rate expressions are detailed in Appendix. Dehydrogenation TOF as a function of ethanol pressure in Figure 4.18(a) was fit to the rate expression for 1 wt% Cu/0.675Al-ZrO_2, Cu/TiO_2, and Cu/ZrO_2 across the probed ethanol pressure range (1.3 to 71.5 mbar). Comparisons between the model predicted pressure dependences and the experimentally measured dependences are shown in Figure 4.21. It was seen that the model poorly matched

the experimental data, particularly for the 1 wt% Cu/0.675Al-ZrO_2 and Cu/TiO_2 catalysts. Alternatively, there was consistency between the experimental pressure dependences and model fits when O-H bond cleavage was assumed as the RLS and used to generate a rate equation, see equation 4.2 and Figure 4.22. This suggests that O-H bond cleavage controlled dehydrogenation activity for the two catalysts with strong Lewis acid sites on the support, which is not consistent with literature reports showing O-H bond activation to be facile over metal oxide supports with strong acid sites.[33,34]

To address this apparent discrepancy, it was proposed that the active site and RLS would shift as a function of ethanol pressure and thus the coverage of reactants and intermediates on Cu and on the support.[81] Specifically, it was proposed that at higher ethanol pressures, O-H bond cleavage occurred facilely on support acid sites and C_α-H cleavage was the RLS occurring at the Cu-support interface, while at low ethanol pressures, the reaction proceeded exclusively over the Cu surface with O-H cleavage as the RLS.

$$\text{rate} = \frac{\mathbf{k_4 K_{eff} P_{EtOH}}/(P_{H_2})^{\mathbf{1/2}})}{\left(\mathbf{1+K_{eff} P_{EtOH}}/(P_{H_2})^{\mathbf{1/2}}\right)^{\mathbf{2}}} \qquad \textbf{equation 4.1}$$

$$\text{rate} = \frac{\mathbf{k_2 K_1 P_{EtOH}}}{(\mathbf{1+K_1 P_{EtOH}})} \qquad \textbf{equation 4.2}$$

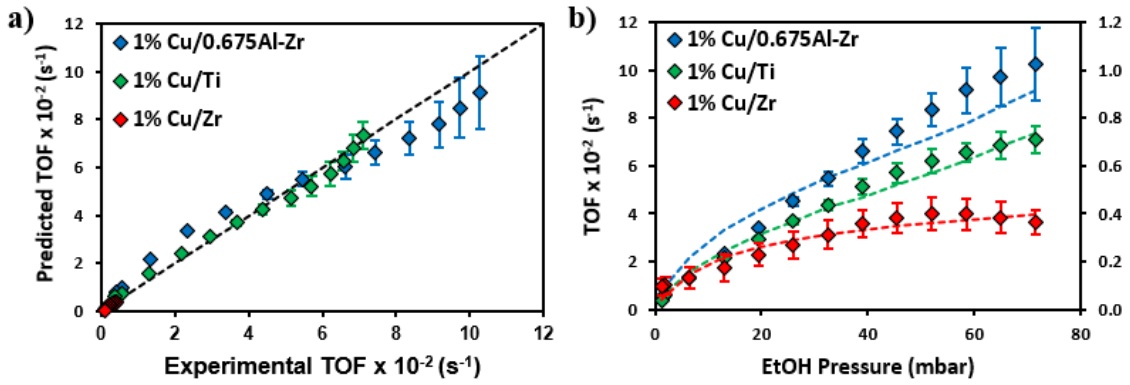

Figure 4.21 Ethanol turn over frequency (TOF) predicted by a best fit to equation 4.1 plotted against the corresponding experimental ethanol TOF for 1 wt% Cu loaded on ZrO_2 (Zr), TiO_2 (Ti), and 0.675Al-ZrO_2 on a) a parity plot where unity corresponds to goodness of fit and on b) Figure 4.18a showing ethanol TOF as a function of ethanol pressure.

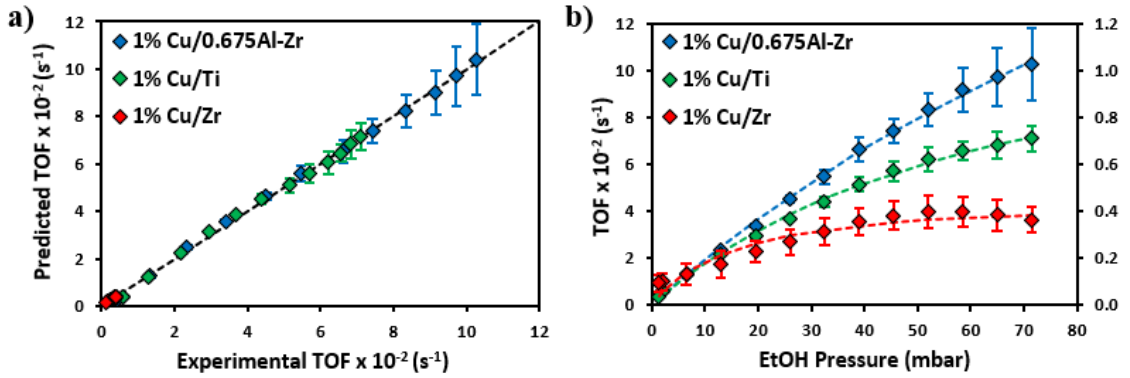

Figure 4.22 Ethanol turn over frequency (TOF) predicted by a best fit to equation 4.2 plotted against the corresponding experimental ethanol TOF for 1 wt% Cu loaded on ZrO_2 (Zr), TiO_2 (Ti), and 0.675Al-ZrO_2 on **a)** a parity plot where unity corresponds to goodness of fit and on **b)** Figure 4.18a showing ethanol TOF as a function of ethanol pressure.

To test whether a shift in RLS would provide a consistent fit with experimental data, the rate expression with C_α-H cleavage as the RLS (equation 4.1) was fit to the experimental data in Figure 4.18(a) with ethanol pressures at and above 45.5 mbar, which was chosen based on the Cu-ZrO_2 TOF saturation suggesting a significant coverage of intermediates on Cu. The rate expression derivations are explained in detail in the Appendix (derivations correspond to fits in Figures 4.21 and 4.22). For equation 4.1, k_4 corresponded to the rate constant of the RLS, K_{eff} corresponded to several equilibrium

constants (see Appendix), P_{EtOH} corresponded to the ethanol feed pressure, and P_{H2} corresponded to the pressure of H_2 in the effluent. Similarly, the rate expression with O-H cleavage as the RLS (equation 4.2) was fit to the experimental data at ethanol pressures below 45.5 mbar. For equation 4.2, k_2 corresponded to the rate constant of the RLS, K_1 corresponded to the equilibrium constant for ethanol adsorption, and P_{EtOH} corresponded to the ethanol feed pressure. The parity plot in Figure 4.23, see Figure 4.24 for best fit to Figure 4.18(a), summarizes these findings, where it was observed that the model including a RLS shift from O-H to C_α-H bond cleavage with increasing ethanol pressure fit well with the experimental data for all 3 catalysts.

The kinetic parameters for the best fit for equation 4.1 (ethanol pressure $\geq$ 45.5 mbar) and equation 4.2 (ethanol pressure < 45.5 mbar) provided further insight into the reaction mechanism depicted in Scheme 3.1. At higher ethanol pressures with C_α-H bond cleavage as the RLS, the rate constants (k_4) for 1 wt% Cu/0.675Al-ZrO_2 and Cu/TiO_2 were, respectively, 181 and 26-fold larger than k_4 of 1 wt% Cu/ZrO_2, see Table 4.7. It is proposed that the presence of $Cu^{\delta+}$ sites on supports with strong Lewis acid sites promoted the rate limiting C-H bond activation step, which is evidenced by the increased k_4.[88,89] In the case of the model fits for an O-H cleavage RLS at lower ethanol pressures, the rate constants (k_2) for 1 wt% Cu/0.675Al-ZrO_2 and Cu/TiO_2 were, respectively, 56 and 21-fold larger than k_2 for 1 wt% Cu/ZrO_2. These differences in the RLS O-H rate constant between Cu on strongly and weakly acidic supports are smaller than differences between the C-H activation rate constants at higher ethanol pressure, but still are significant. It is proposed that without in-situ pyridine poisoning, the interfacial $Cu^{\delta+}$ sites on supports with strong

Lewis acid sites still mildly promoted O-H activation, which resulted in enhanced rate constants.

Based on the comparison of model predictions of the experimental data, we propose an ethanol partial pressure and support acidity dependent reaction mechanism. At low ethanol pressures support effects were minimized, and the reaction primarily proceeded on Cu surface sites with O-H bond cleavage as the RLS. This is consistent with recent DFT studies performed at low ethanol coverage on Cu.[4] However, at higher ethanol partial pressures the Cu surface became poisoned by reaction intermediates and when strong acid sites exist on the support, the reaction was pushed to the Cu-support interface. The strong Lewis acid sites or modified interfacial Cu sites facilitated O-H bond cleavage by reducing the activation barrier for the reaction step, thereby shifting the RLS to C_α-H bond cleavage. Additionally, where C_α-H activation occurred on all Cu surface sites when on ZrO_2, the active sites shifted to interfacial Cu sites in the presence of strong Lewis acid sites, which further promoted ethanol TOF. Thus, it is proposed that the promotional effect of strong Lewis acid sites on ethanol dehydrogenation TOF at high ethanol pressures was two-fold: facilitation of O-H bond cleavage and modification of interfacial Cu sites charges, although the relative contribution of each effect on ethanol TOF has not been deconvoluted. Additionally, comparing ethanol dehydrogenation TOF at 190 °C for 1 wt% Cu/ZrO_2 in Figure 4.13 to the TOF of nanoporous, unsupported Cu (np-Cu)[86], there was excellent agreement with values of 0.35 ± 0.04 s^{-1} and 0.33 s^{-1} (the site density ~1×10^{19} sites/m^2 for np-Cu), respectively. This provides additional evidence that ZrO_2 does not participate in

the reaction mechanism and ethanol dehydrogenation occurs exclusively over Cu sites without the presence of strong Lewis acid sites.

One question that arises from the proposed mechanism is how far away from Cu-support interface sites does O-H activation occur on support acid sites. To provide some insights into this it is important to consider that while adsorbed ethoxy on the oxide surface may be mobile under reaction conditions, the pathway for H_2 desorption likely dictates the distance from the Cu interface where support acid sites participate. A recent analysis of the hydrogen spillover from Pt nanoparticles to TiO_2 and Al_2O_3 (the reverse of the processed described here for H* diffusion on the oxide to Cu and desorption from Cu) showed that H* diffusion over the Al_2O_3 surface was limited to very short distances from the metal particle and had a 10^{10} times slower diffusion rate than H* over TiO_2.[90] Based on this analysis, it is suggested that O-H bond cleavage with subsequent diffusion of H* to Cu could only occur near the Cu-support interface over 0.675Al-ZrO_2. The similar promotional effects on dehydrogenation TOF by TiO_2 and 0.675Al-ZrO_2 strongly suggest that O-H activation happens very near to or at the Cu-support interface.

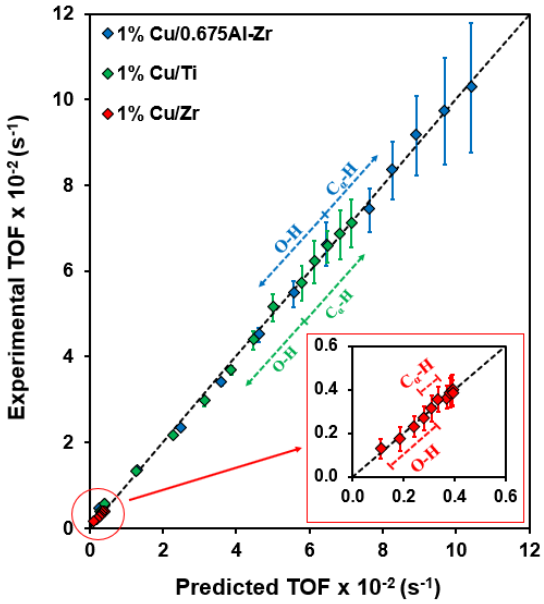

Figure 4.23 Ethanol TOF for 1 wt% Cu over ZrO_2 (Zr), TiO_2 (Ti), and 0.675Al-ZrO_2 predicted from equation 4.1 (C_α-H cleavage as RLS) and equation 4.2 (O-H cleavage as RLS) from microkinetic model of Scheme 4.1 compared to experimental TOF. Inset shows the corresponding TOF comparison for Cu-Zr. Dashed parity lines included as a reference.

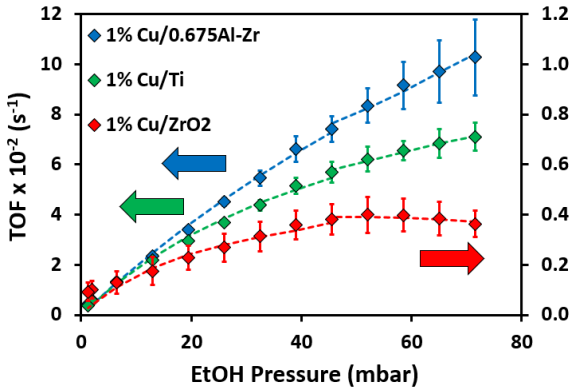

Figure 4.24 Ethanol turn over frequency (TOF) predicted by a best fit to equation 4.1 (≥ 45.5 mbar ethanol) and equation 4.2 (< 45.5 mbar ethanol) plotted against the corresponding experimental TOF for 1 wt% Cu loaded on ZrO_2 (Zr), TiO_2 (Ti), and 0.675Al-ZrO_2 on Figure 4.18 (a) showing ethanol TOF as a function of ethanol pressure.

O-H Abstraction	K_1 ($mbar^{-1}$)	k_2 (s^{-1})
1% Cu/0.675Al-ZrO_2	0.006	32
1% Cu/TiO_2	0.02	12
1% Cu/ZrO_2	0.04	0.57
C-H Abstraction	**K_{eff} ($mbar^{-1/2}$)**	**k_4 (s^{-1})**
1% Cu/0.675Al-ZrO_2	0.0006	290
1% Cu/TiO_2	0.004	42
1% Cu/ZrO_2	0.01	1.6

Table 4.7 Equilibrium (K_1 and K_{eff}) and rate (k_2 and k_4) constants for the best fits of equation 4.2 (O-H cleavage as RLS) below 45.5 mbar ethanol and equation 4.1 (C_α-H cleavage as RLS) at and above 45.5 mbar ethanol. $K_{eff} = K_1K_2K_3K_6^{1/2}K_7^{1/2}$.

4.6 Conclusion

This chapter elucidated the impact of oxide support acidity on the rate of ethanol dehydrogenation to acetaldehyde over Cu catalysts and the corresponding reaction mechanism. At higher ethanol pressures, Cu loaded onto oxide supports with strong Lewis acid sites exhibited ethanol TOF that was promoted by more than an order of magnitude compared to Cu on weakly acidic supports. Alternatively, at lower ethanol pressures and with the addition of in-situ poisoning of acidic sites by pyridine, the TOF was similar for all three catalysts and independent of the support. Cu particle size dependent studies provided strong evidence that the addition of strong Lewis acid sites to ZrO_2 shifted the dehydrogenation active sites from all surface Cu sites to interfacial Cu. The kinetic measurements combined with microkinetic modeling suggest that at low ethanol pressures the reaction proceeds over relatively clean Cu surfaces with a RLS of O-H cleavage and little impact from the support acid sites. However, at high ethanol pressures the reaction is initiated at Lewis acid sites that induce facile O-H cleavage followed by the RLS of C_α-H cleavage at interfacial Cu sites. This study showed the role support acid sites play in

promoting the dehydrogenation of alcohols at high ethanol coverages by facilitating O-H bond cleavage and modifying interfacial Cu sites. This work directly demonstrates the cooperative effects between interfacial metal and support sites for driving catalytic processes.

4.7 References

(1) Witzke, M. E.; Dietrich, P.; Ibrahim, M. Y. S.; Al-Bardan, K.; Triezenberg, M. D.; Flaherty, D. Spectroscopic Evidence for Origins of Size and Support Effects on Selectivity of Cu Nanoparticle Dehydrogenation Catalysts. *Chem. Commun.* **2017**, *53*, 597–600.

(2) Moteki, T.; Flaherty, D. W. Mechanistic Insight to C–C Bond Formation and Predictive Models for Cascade Reactions among Alcohols on Ca- and Sr-Hydroxyapatites. *ACS Catal.* **2016**, *10*, 4170–4183.

(3) Su, S. CatalyticDdehydrogenation of Methanol to Water-Free Formaldehyde. *Chem. Eng. Technol.* **1991**, *17*, 34–40.

(4) Wang, Z.; Xu, Y.; El-soda, M.; Lucci, F. R.; Madix, R. J.; Friend, C. M.; Sykes, E. C. H. Surface Structure Dependence of the Dry Dehydrogenation of Alcohols on Cu(111) and Cu(110). *J. Phys. Chem. C* **2017**, *121* (23), 12800–12806.

(5) Chen, W.; Cubuk, E. D.; Montemore, M. M.; Reece, C.; Madix, R. J.; Friend, C. M.; Kaxiras, E. A Comparative Ab Initio Study of Anhydrous Dehydrogenation of Linear-Chain Alcohols on Cu(110). *J. Phys. Chem. C* **2018**, *122*, 7806–7815.

(6) Kozlowski, J. T.; Davis, R. J. Heterogeneous Catalysts for the Guerbet Coupling of Alcohols. *ACS Catal.* **2013**, *3* (7), 1588–1600.

(7) Wu, L.; Moteki, T.; Gokhale, A. A.; Flaherty, D. W.; Toste, F. D. Production of Fuels and Chemicals from Biomass: Condensation Reactions and Beyond. *Chem* **2016**, *1*, 32–58.

(8) Sushkevich, V. L.; Ivanova, I. I.; Taarning, E. Mechanistic Study of Ethanol Dehydrogenation over Silica-Supported Silver. *ChemCatChem* **2013**, *5* (8), 2367–2373.

(9) Goulas, K. A.; Song, Y.; Johnson, G. R.; Chen, J. P.; Gokhale, A. A.; Grabow, L. C.; Toste, F. D. Selectivity Tuning over Monometallic and Bimetallic Dehydrogenation Catalysts: Effects of Support and Particle Size. *Catal. Sci. Technol.* **2018**, *8*, 314–327.

(10) Neurock, M.; Tao, Z.; Chemburkar, A.; Hibbitts, D.; Iglesia, E. Theoretical Insights into the Sites and Mechanisms for Base Catalyzed Esterification and Aldol Condensation Reactions over Cu. *Faraday Discuss.* **2017**, *197*, 59–86.

(11) Young, Z. D.; Hanspal, S.; Davis, R. J. Aldol Condensation of Acetaldehyde over Titania, Hydroxyapatite, and Magnesia. *ACS Catal.* **2016**, *6* (5), 3193–3202.

(12) Sacia, E. R.; Balakrishnan, M.; Deaner, M. H.; Goulas, K. A.; Toste, F. D.; Bell, A. T. Highly Selective Condensation of Biomass-Derived Methyl Ketones as a Source of Aviation Fuel. *ChemSusChem* **2015**, *8* (10), 1726–1736.

(13) Takezawa, N.; Iwasa, N. Steam Reforming and Dehydrogenation of Methanol: Difference in the Catalytic Functions of Copper and Group VIII Metals. *Catal.*

Today **1997**, *36* (1), 45–56.

(14) Sitthisa, S.; Resasco, D. E. Hydrodeoxygenation of Furfural over Supported Metal Catalysts: A Comparative Study of Cu, Pd and Ni. *Catal. Letters* **2011**, *141* (6), 784–791.

(15) Freitas, I. C.; Damyanova, S.; Oliveira, D. C.; Marques, C. M. P.; Bueno, J. M. C. Effect of Cu Content on the Surface and Catalytic Properties of Cu/ZrO 2 Catalyst for Ethanol Dehydrogenation. *J. Mol. Catal. A Chem.* **2014**, *381*, 26–37.

(16) Sun, J.; Wang, Y. Recent Advances in Catalytic Conversion of Ethanol to Chemicals. *ACS Catal.* **2014**, *4* (4), 1078–1090.

(17) Tu, Y.; Chen, Y. Effects of Alkali Metal Oxide Additives on Cu/SiO2 Catalyst in the Dehydrogenation of Ethanol. *Ind. Eng. Chem. Res.* **2001**, *40*, 5889–5893.

(18) Tu, Y. J.; Chen, Y. W. Effects of Alkaline-Earth Oxide Additives on Silica-Supported Copper Catalysts in Ethanol Dehydrogenation. *Ind. Eng. Chem. Res.* **1998**, *37* (1), 2618–2622.

(19) Kumar, A.; Ashok, A.; Bhosale, R. R.; Ali, M. In Situ DRIFTS Studies on Cu , Ni and CuNi Catalysts for Ethanol Decomposition Reaction. *Catal. Letters* **2016**, *146* (4), 778–787.

(20) Colley, S. W.; Tabatabaei, J.; Waugh, K. C.; Wood, M. A. The Detailed Kinetics and Mechanism of Ethyl Ethanoate Synthesis over a Cu/Cr2O3 Catalyst. *J. Catal.* **2005**, *236* (1), 21–33.

(21) Rioux, R. M.; Vannice, M. A. Hydrogenation/Dehydrogenation Reactions: Isopropanol Dehydrogenation over Copper Catalysts. *J. Catal.* **2003**, *216* (1–2), 362–376.

(22) Crivello, M. E.; Pérez, C. F.; Mendieta, S. N.; Casuscelli, S. G.; Eimer, G. A.; Elías, V. R.; Herrero, E. R. N-Octyl Alcohol Dehydrogenation over Copper Catalysts. *Catal. Today* **2008**, *133–135* (1–4), 787–792.

(23) Ashok, A.; Kumar, A.; Bhosale, R.; Saleh Saad, M. A.; AlMomani, F.; Tarlochan, F. Study of Ethanol Dehydrogenation Reaction Mechanism for Hydrogen Production on Combustion Synthesized Cobalt Catalyst. *Int. J. Hydrogen Energy* **2017**, *42* (37), 23464–23473.

(24) Akdim, O.; Cai, W.; Fierro, V.; Provendier, H.; van Veen, A.; Shen, W.; Mirodatos, C. Oxidative Steam Reforming of Ethanol over Ni–Cu/SiO2, Rh/Al2O3 and Ir/CeO2: Effect of Metal and Support on Reaction Mechanism. *Top. Catal.* **2008**, *51* (1–4), 22–38.

(25) Koitaya, T.; Shiozawa, Y.; Yoshikura, Y.; Mukai, K.; Yoshimoto, S.; Yoshinobu, J. Systematic Study of Adsorption and the Reaction of Methanol on Three Model Catalysts: Cu(111), Zn-Cu(111) and Oxidized Zn-Cu(111). *J. Phys. Chem. C* **2017**, *121*, 25402–25410.

(26) Bowker, M.; Madix, R. J. XPS, UPS, and Thermal-Desorption Studies of Alcohol Adsorption on Cu(11): I. Methanol. *Surf. Sci.* **1980**, *95*, 190–206.

(27) Li, H.; Henkelman, G. Dehydrogenation Selectivity of Ethanol on Close-Packed Transition Metal Surfaces: A Computational Study of Monometallic, Pd/Au, and Rh/Au Catalysts. *J. Phys. Chem. C* **2017**, *121* (49), 27504–27510.

(28) Boucher, M. B.; Marcinkowski, M. D.; Liriano, M. L.; Murphy, C. J.; Lewis, E. A.; Jewell, A. D.; Mattera, M. F. G.; Kyriakou, G.; Flytzani-Stephanopoulos, M.; Sykes, E. C. H. Molecular-Scale Perspective of Water-Catalyzed Methanol Dehydrogenation to Formaldehyde. *ACS Nano* **2013**, *7* (7), 6181–6187.

(29) Madix, R. J.; Telford, S. G. Primary and Secondary Kinetic Isotope Effects for Methoxy Dehydrogenation and Cu(110): Absence of Tunnelling Corrections. *Surf. Sci.* **1995**, *328* (3), L576–L581.

(30) Shan, J.; Lucci, F. R.; Liu, J.; El-Soda, M.; Marcinkowski, M. D.; Allard, L. F.; Sykes, E. C. H.; Flytzani-Stephanopoulos, M. Water Co-Catalyzed Selective Dehydrogenation of Methanol to Formaldehyde and Hydrogen. *Surf. Sci.* **2016**, *650*, 121–129.

(31) Wachs, I. E.; Madix, R. J. The Selective Oxidation of CH3OH to H2CO on a Copper(110) Catalyst. *J. Catal.* **1978**, *53* (2), 208–227.

(32) Eren, B.; Kersell, H.; Weatherup, R. S.; Heine, C.; Crumlin, E. J.; Friend, C. M.; Salmeron, M. B. Structure of the Clean and Oxygen-Covered Cu(100) Surface at Room Temperature in the Presence of Methanol Vapor in the 10–200 MTorr Pressure Range. *J. Phys. Chem. B* **2018**, *122*, 548–554.

(33) Christiansen, M. a.; Mpourmpakis, G.; Vlachos, D. G. Density Functional Theory-Computed Mechanisms of Ethylene and Diethyl Ether Formation from Ethanol on γ-Al2O3(100). *ACS Catal.* **2013**, *3* (9), 1965–1975.

(34) DeWilde, J. F.; Czopinski, C. J.; Bhan, A. Ethanol Dehydration and Dehydrogenation on γ-Al2O3: Mechanism of Acetaldehyde Formation. *ACS Catal.* **2014**, *4* (12), 4425–4433.

(35) Ho, C. R.; Shylesh, S.; Bell, A. T. Mechanism and Kinetics of Ethanol Coupling to Butanol over Hydroxyapatite. *ACS Catal.* **2016**, *6* (2), 939–948.

(36) Sato, A. G.; Volanti, D. P.; Freitas, I. C. De; Longo, E.; Maria, J.; Bueno, C. Site-Selective Ethanol Conversion over Supported Copper Catalysts. *Catal. Commun.* **2012**, *26*, 122–126.

(37) Sutton, J. E.; Danielson, T.; Beste, A.; Savara, A. Below-Room-Temperature C–H Bond Breaking on an Inexpensive Metal Oxide: Methanol to Formaldehyde on CeO $_2$ (111). *J. Phys. Chem. Lett.* **2017**, *2* (111), 5810–5814.

(38) Chokkaram, S.; Srinivasan, R.; Milburn, D. R.; Davis, B. H. Conversion of 2-Octanol over Nickel-Alumina, Cobalt-Alumina, and Alumina Catalysts. *J. Mol. Catal. A Chem.* **1997**, *121* (2–3), 157–169.

(39) Mattos, L. V.; Jacobs, G.; Davis, B. H.; Noronha, F. B. Production of Hydrogen from Ethanol: Review of Reaction Mechanism and Catalyst Deactivation. *Chem. Rev.* **2012**, *112* (7), 4094–4123.

(40) Phung, T. K.; Lagazzo, A.; Rivero Crespo, M. Á.; Sánchez Escribano, V.; Busca, G. A Study of Commercial Transition Aluminas and of Their Catalytic Activity in the Dehydration of Ethanol. *J. Catal.* **2014**, *311*, 102–113.

(41) Zhang, M.; Huang, Y.; Li, R.; Li, G.; Yu, Y. A DFT Study of Ethanol Adsorption and Dehydrogenation on Cu/Cr2O3 Catalyst. *Catal. Letters* **2014**, *144* (11), 1978–1986.

(42) Ro, I.; Liu, Y.; Ball, M. R.; Jackson, D. H. K.; Chada, J. P.; Sener, C.; Kuech, T. F.; Madon, R. J.; Huber, G. W.; Dumesic, J. A. Role of the Cu-ZrO 2 Interfacial Sites for Conversion of Ethanol to Ethyl Acetate and Synthesis of Methanol from CO 2 and H 2. *ACS Catal.* **2016**, *6*, 7040–7050.

(43) Yu, X.; Zhai, S.; Zhu, W.; Gao, S.; Yan, J.; Yuan, H.; Chen, L.; Luo, J.; Zhang, W.; Wang, Z. The Direct Transformation of Ethanol to Ethyl Acetate over Cu/SiO 2 Catalysts That Contain Copper Phyllosilicate. *J. Chem. Sci.* **2014**, *126* (4), 1013–1020.

(44) Basagiannis, A. C.; Panagiotopoulou, P.; Verykios, X. E. Low Temperature Steam Reforming of Ethanol over Supported Noble Metal Catalysts. *Top. Catal.* **2008**, *51* (1–4), 2–12.

(45) Bond, G. C.; Namijo, S. N. An Improved Procedure for Estimating the Metal Surface Area of Supported Copper Catalysts. *J. Catal.* **1989**, *118* (2), 507–510.

(46) Luys, M.; Van Oeffelt, P. H.; Brouwer, W.; Pijpers, A. P.; Scholten, J. J. F. Surface and Sub-Surface Oxidation of Copper and Supported Copper Catalysts by Nitrous Oxide. *Appl. Catal.* **1989**, *46*, 161–173.

(47) Chinchen, G. C.; Hay, C. M.; Vandervell, H. D.; Waugh, K. C. The Measurement of Copper Surface Areas by Reactive Frontal Chromatography. *J. Catal.* **1987**, *103* (1), 79–86.

(48) Hinrichsen, B. O.; Genger, T.; Muhler, M. Chemisorption of N2O and H2 for the Surface Determination of Copper Catalysts.Pdf. *Chem. Eng. Technol.* **2000**, *23*, 956–959.

(49) Sirita, J.; Phanichphant, S.; Meunier, F. Quantitative Analysis of Adsorbate Concentrations by Diffuse Reflectance FT-IR. *Anal. Chem.* **2007**, *79*, 3912–3918.

(50) Manríquez, M. E.; López, T.; Gómez, R.; Navarrete, J. Preparation of TiO2-ZrO2 Mixed Oxides with Controlled Acid-Basic Properties. *J. Mol. Catal. A Chem.* **2004**, *220* (2), 229–237.

(51) Wang, S.; Iglesia, E. Substituent Effects and Molecular Descriptors of Reactivity in Condensation and Esterification Reactions of Oxygenates on Acid-Base Pairs at TiO2 and ZrO2 Surfaces. *J. Phys. Chem. C* **2016**, *120* (38), 21589–21616.

(52) Connell, G.; Dumesic, J. A. The Generation of Brønsted and Lewis Acid Sites on the Surface of Silica by Addition of Dopant Cations. *J. Catal.* **1987**, *105* (2), 285–298.

(53) McFarland, E. W.; Metiu, H. Catalysis by Doped Oxides. *Chem. Rev.* **2013**, *113* (6), 4391–4427.

(54) Metiu, H.; Chrétien, S.; Hu, Z.; Li, B.; Sun, X. Chemistry of Lewis Acid-Base Pairs on Oxide Surfaces. *J. Phys. Chem. C* **2012**, *116* (19), 10439–10450.

(55) Garvie, R. C.; Nicholson, P. S. Phase Analysis in Zirconia Systems. *J. Am. Ceram. Soc.* **1972**, *55* (6), 303–305.

(56) Digne, M.; Sautet, P.; Raybaud, P.; Euzen, P.; Toulhoat, H. Use of DFT to Achieve a Rational Understanding of Acid-Basic Properties of γ-Alumina Surfaces. *J. Catal.* **2004**, *226* (1), 54–68.

(57) Chakraborty, B.; Viswanathan, B. Surface Acidity of MCM-41 by in Situ IR Studies of Pyridine Adsorption. *Catal. Today* **1999**, *49* (1–3), 253–260.

(58) Zaki, M. I.; Hasan, M. a.; Al-Sagheer, F. a.; Pasupulety, L. In Situ FTIR Spectra of Pyridine Adsorbed on SiO2-Al2O3, TiO2, ZrO2 and CeO2: General Considerations for the Identification of Acid Sites on Surfaces of Finely Divided Metal Oxides. *Colloids Surfaces A Physicochem. Eng. Asp.* **2001**, *190* (3), 261–274.

(59) Liu, X. DRIFTS Study of Surface of γ-Alumina and Its Dehydroxylation. *J. Phys. Chem. C* **2008**, *112* (13), 5066–5073.

(60) Liu, C.; Sun, J.; Smith, C.; Wang, Y. A Study of ZnxZryOzmixed Oxides for Direct Conversion of Ethanol to Isobutene. *Appl. Catal. A Gen.* **2013**, *467*, 91–97.

(61) Sun, J.; Zhu, K.; Gao, F.; Wang, C.; Liu, J.; Peden, C. H. F.; Wang, Y. Direct Conversion of Bio-Ethanol to Isobutene on Nanosized ZnxZryOzmixed Oxides with Balanced Acid - Base Sites. *J. Am. Chem. Soc.* **2011**, *133* (29), 11096–11099.

(62) Tamura, M.; Shimizu, K. I.; Satsuma, A. Comprehensive IR Study on Acid/Base Properties of Metal Oxides. *Appl. Catal. A Gen.* **2012**, *433–434*, 135–145.

(63) Morterra, C.; Ghiotti, G.; Boccuzzi, F.; Coluccia, S. An Infrared Spectroscopic Investigation of the Surface Properties of Magnesium Aluminate Spinel. *J. Calaysis* **1978**, *51*, 299–313.

(64) Liu, X.; Truitt, R. E. DRFT-IR Studies of the Surface of γ-Alumina. *J. Am. Chem. Soc.* **1997**, *119* (41), 9856–9860.

(65) Busca, G. Structural, Surface, and Catalytic Properties of Aluminas. *Adv. Catal.* **2014**, *57*, 319–404.

(66) Balajka, J.; Hines, M.; DeBenedetti, W.; Komora, M.; Pavelec, J.; Schmid, M.; Diebold, U. High Affinity Adsorption Leads to Molecularly Ordered Interfaces on TiO2 in Air and Solution. *Science* **2018**, *361*, 786–789.

(67) Bezrodna, T.; Puchkovska, G.; Shimanovska, V.; Chashechnikova, I.; Khalyavka, T.; Baran, J. Pyridine-TiO2surface Interaction as a Probe for Surface Active Centers Analysis. *Appl. Surf. Sci.* **2003**, *214* (1–4), 222–231.

(68) Hadjiivanov, K.; Knozinger, H. FTIR Study of CO and NO Adsorption and Coadsorption on a Cu/SiO2 Catalyst: Probing the Oxidation State of Copper. *Phys. Chem. Chem. Phys.* **2001**, *3* (6), 1132–1137.

(69) Subramanian, N. D.; Kumar, C. S. S. R.; Watanabe, K.; Fischer, P.; Tanaka, R.; Spivey, J. J. A DRIFTS Study of CO Adsorption and Hydrogenation on Cu-Based Core-Shell Nanoparticles. *Catal. Sci. Technol.* **2012**, *2* (3), 621–631.

(70) Fisher, I. A.; Bell, A. T. In Situ Infrared Study of Methanol Synthesis from H2/ CO over Cu/SiO2 and Cu/ZrO2/ SiO2. *J. Catal.* **1998**, *178*, 153–173.

(71) Raval, R.; Parker, S. F.; Pemble, M. E.; Hollins, P.; Pritchard, J.; Chesters, M. A. FT-Rairs, Eels and Leed Studies of the Adsorption of Carbon Monoxide on Cu(111). *Surf. Sci.* **1988**, *203* (3), 353–377.

(72) Hollins, P.; Pritchard, J. Interactions of CO Molecules Adsorbed on Oxidised Cu(111) and Cu(110). *Surf. Sci.* **1983**, *134* (1), 91–108.

(73) Ro, I.; Resasco, J.; Christopher, P. Approaches for Understanding and Controlling Interfacial Effects in Oxide Supported Metal Catalysts. *ACS Catal.* **2018**, *8*, 7368–7387.

(74) Barton, D. G.; Shtein, M.; Wilson, R. D.; Soled, S. L.; Iglesia, E. Structure and Electronic Properties of Solid Acids Based on Tungsten Oxide Nanostructures. *J. Phys. Chem. B* **1999**, *103* (4), 630–640.

(75) Kohler, M. A.; Cant, N. W.; Wainwright, M. S.; Trimm, D. L. Infrared Spectroscopic Studies of Carbon Monoxide Adsorbed on a Series of Silica-Supported Copper Catalysts in Different Oxidation States. *J. Catal.* **1989**, *117* (1), 188–201.

(76) Hansen, P. L.; Wagner, J. B.; Helveg, S.; Rostrup-Nielsen, J. R.; Clausen, B. S.; Topsøe, H. Atom-Resolved Imaging of Dynamic Shape Changes in Supported Copper Nanocrystals. *Science* **2002**, *295* (5562), 2053–2055.

(77) Kasatkin, I.; Kniep, B.; Ressler, T. Cu/ZnO and Cu/ZrO2 Interactions Studied by Contact Angle Measurement with TEM. *Phys. Chem. Chem. Phys.* **2007**, *9*, 878–883.

(78) Wang, Q.-N.; Shi, L.; Li, W.; Li, W.-C.; Si, R.; Schüth, F.; Lu, A.-H. Cu Supported on Thin Carbon Layer Coated Porous SiO2 for Efficient Ethanol Dehydrogenation. *Catal. Sci. Technol.* **2018**, *8*, 472–479.

(79) Morterra, C.; Magnacca, G. A Case Study: Surface Chemistry and Surface Structure of Catalytic Aluminas, as Studied by Vibrational Spectroscopy of Adsorbed Species. *Catal. Today* **1996**, *27*, 497–532.

(80) Cargnello, M.; Doan-Nguyen, V. V. T.; Gordon, T. R.; Diaz, R. E.; Stach, E. A.; Gorte, R. J.; Fornasiero, P.; Murray, C. B. Control of Metal Nanocrystal Size Reveals Metal-Support Interface Role for Ceria Catalysts. *Science* **2013**, *341* (6147), 771–773.

(81) Foppa, L.; Margossian, T.; Kim, S. M.; Mueller, C.; Copéret, C.; Larmier, K.; Comas-Vives, A. Contrasting the Role of Ni/Al2O3 Interfaces in Water-Gas Shift and Dry Reforming of Methane. *J. Am. Chem. Soc.* **2017**, *139*, 17128–17139.

(82) Shekhar, M.; Wang, J.; Lee, W.-S.; Williams, W. D.; Kim, S. M.; Stach, E. A.; Miller, J. T.; Delgass, W. N.; Ribeiro, F. H. Size and Support Effects for the Water–Gas Shift Catalysis over Gold Nanoparticles Supported on Model Al2O3 and TiO2. *J. Am. Chem. Soc.* **2012**, *134* (10), 4700–4708.

(83) Williams, W. D.; Shekhar, M.; Lee, W. S.; Kispersky, V.; Delgass, W. N.; Ribeiro, F. H.; Kim, S. M.; Stach, E. A.; Miller, J. T.; Allard, L. F. Metallic Corner Atoms in Gold Clusters Supported on Rutile Are the Dominant Active Site during Water-Gas Shift Catalysis. *J. Am. Chem. Soc.* **2010**, *132* (40), 14018–14020.

(84) Yang, F.; Liu, D.; Zhao, Y.; Wang, H.; Han, J.; Ge, Q.; Zhu, X. Size Dependence of Vapor Phase Hydrodeoxygenation of M-Cresol on Ni/SiO2 Catalysts. *ACS Catal.* **2018**, *8*, 1672–1682.

(85) Larmier, K.; Tada, S.; Comas-Vives, A.; Copéret, C. Surface Sites in Cu-Nanoparticles: Chemical Reactivity or Microscopy? *J. Phys. Chem. Lett.* **2016**, *7* (16), 3259–3263.

(86) Shan, J.; Janvelyan, N.; Li, H.; Liu, J.; Egle, T. M.; Ye, J.; Biener, M. M.; Biener, J.; Friend, C. M.; Flytzani-Stephanopoulos, M. Selective Non-Oxidative Dehydrogenation of Ethanol to Acetaldehyde and Hydrogen on Highly Dilute NiCu Alloys. *Appl. Catal. B Environ.* **2017**, *205*, 541–550.

(87) Hu, Z.; Li, B.; Sun, X.; Metiu, H. Chemistry of Doped Oxides: The Activation of Surface Oxygen and the Chemical Compensation Effect. *J. Phys. Chem. C* **2011**, *115* (7), 3065–3074.

(88) Narsimhan, K.; Michaelis, V. K.; Mathies, G.; Gunther, W. R.; Griffin, R. G.; Roman-Leshkov, Y. Methane to Acetic Acid over Cu-Exchanged Zeolites: Mechanistic Insights from a Site-Specific Carbonylation Reaction. *J. Am. Chem. Soc.* **2015**, *137* (5), 1825–1832.

(89) Narsimhan, K.; Iyoki, K.; Dinh, K.; Román-Leshkov, Y. Catalytic Oxidation of Methane into Methanol over Copper-Exchanged Zeolites with Oxygen at Low Temperature. *ACS Cent. Sci.* **2016**, *2* (6), 424–429.

(90) Karim, W.; Spreafico, C.; Kleibert, A.; Gobrecht, J.; Vandevondele, J.; Ekinci, Y.; Bokhoven, J. A. Van. Catalyst Support Effects on Hydrogen Spollover. *Nature* **2017**, *541* (7635), 68–71.

Chapter 5. The Effect of Support Acid Sites on the Mechanism for Ethyl Acetate Conversion

5.1 Summary

Selective ethyl acetate deoxygenation to diethyl ether serves as a particularly interesting reaction due to it serving as a potential analog to the conversion of methanol to dimethyl ether in the industrial methanol-to-gasoline (MTG) process. Here, we provided preliminary insights onto the reaction mechanism of ethyl acetate conversion over metal oxide supports over varying acidity and basicity: MgO (non-acidic, strongly basic), γ-Al_2O_3 (strongly acidic, non-basic), and ZrO_2 (moderately acidic, moderately basic). By employing temperature and H_2O partial pressure dependent studies, together with γ-Al_2O_3 surface poisoning through Na doping, it was proposed that ethyl acetate conversion is exclusively facilitate by Lewis acid sites and the production of ethyl acetate occurs indirectly through the dimerization of surface ethoxide intermediates.

5.2 Introduction

Catalytic materials with the ability to deoxygenate and/or form C-C bonds from reactants during catalytic processes are of interest in industrial processes. Reactions that can generate lower oxygen content and longer carbon chains include ethanol conversion to 1,3-butadiene,[1–3] aldol condensation,[4–8] biomass conversion,[9] and water-gas shift,[10,11] and ester deoxygenation and/or hydrogenolysis.[12–14] A particularly important industrial process involving the reduction of oxygen content with the subsequent growth of carbon chains is the methanol-to-gasoline (MTG) process developed by ExxonMobil, which converts methanol to dimethyl ether, which is further converted to light olefins that are then

converted to gasoline.[15] The deoxygenation of ethyl acetate to diethyl ether offers a potential alternative, but analogous biosynthetic process to MTG. Recently, the yeast *Kluyveromyces marxianus* has been shown as an effective host for biosynthesis of ethyl acetate from sugars, suggesting that ethyl acetate may be an interesting platform chemical to study for further conversion to hydrocarbons. Additionally, it was found that diethyl ether could be converted to a similar blend of hydrocarbons as seen in the MTG process, suggesting a potentially interesting alternative pathway for hydrocarbon production.[16] Therefore, studying the mechanism of ethyl acetate deoxygenation to diethyl ether can serve as an important building block for designing systems for biomass conversion to gasoline-like blends.

Currently, ethyl acetate conversion has been studied primarily over active metal catalysts such as Cu, Rh, or Pt, under reductive environments to primarily produce ethanol[13,17–23] with diethyl ether observed as a by-product.[13,21,22] The mechanism for ethyl acetate conversion has been suggested to start with the dissociative adsorption of ethyl acetate to form an acetyl and ethoxy intermediate, which can directly produce acetaldehyde and ethanol, respectively.[23,24] Additionally, diethyl ether can be formed directly from ethyl acetate through a hydrogenolysis, or deoxygenation, process involving the selective hydrogenation of ethyl acetate's carbonyl group. On the other hand, diethyl ether, as well as ethylene, formation have also been attributed to the dehydration of ethoxy intermediates over the active metal[21] or the corresponding metal oxide support.[13,22] However, a mechanistic analysis of the conversion of ethyl acetate over metal oxide supports is lacking,

making it difficult to evaluate the inherent reactivity of the active metal compared to its corresponding support.

In Scheme 5.1, a simplified diagram is shown corresponding to the expected reaction pathways during ethyl acetate conversion. Pathway 1 corresponds to deoxygenation of ethyl acetate's carbonyl (C=O) group, leading to the direct formation of diethyl ether, a reaction that is expected to be of importance of active metals capable of activating H_2 gas. The formation of all other products is initiated by the cleavage of ethyl acetate's C-O bond, forming ethanol through pathway 2, acetaldehyde through pathway 3, and carbon dioxide through pathway 4. Additionally, it is well known that over metal oxide supports ethanol intermediates are further converted to ethylene and diethyl with the subsequent formation of H_2O, as represented by pathways 2a and 2b, respectively.

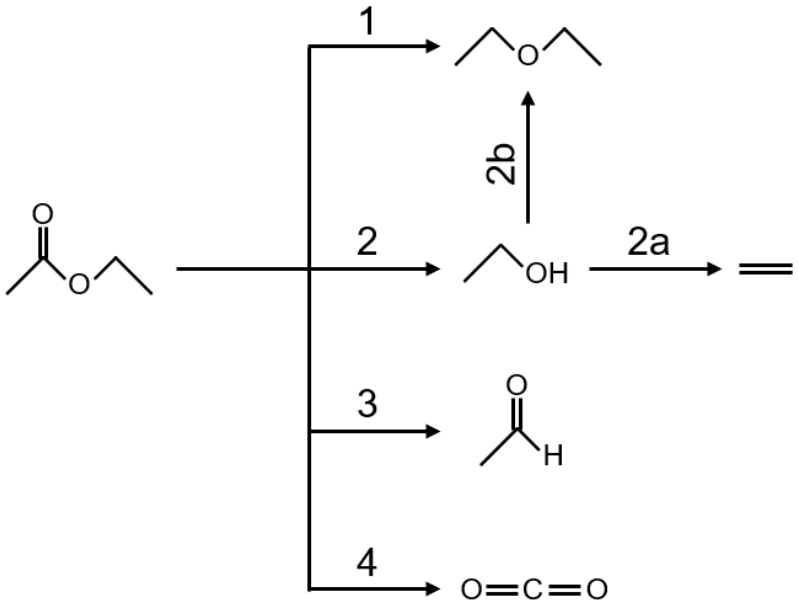

Scheme 5.1 Overview of reaction pathways during ethyl acetate conversion with **1)** direct ethyl acetate deoxygenation (C=O bond cleavage) to diethyl ether. Other pathways involve C-O bond cleavage towards the formation of **2)** ethanol, **3)** acetaldehyde, and **4)** carbon dioxide. Note that **2a)** corresponds to the dehydration of ethanol intermediates to ethylene and **2b)** the etherification of ethanol intermediates to diethyl ether with subsequent formation of H_2O with both pathways

Metal oxide supports with acid-base pair sites are potential model systems to study ethyl acetate deoxygenation to diethyl ether because acid-base pairs have been shown to control mechanistic steps in alcohol dehydration[25–28] as well as aldol condensation[4–8] that may be important during ethyl acetate conversion. For both processes, Lewis acid sites initiate the reaction by attacking the reactant's alcohol or carbonyl group, forming surface alkoxy, acetyl, or enolate species. Lewis base sites work cooperatively with the acid sites by accepting hydrogen species from the reactant. For alcohol dehydration, the base sites help induce O-H bond cleavage by accepting H while the acid site attacks O. On the other hand, during aldol condensation, while the acid site stabilizes the acetyl carbonyl group, the base sites helps induce Cα-H bond cleavage by accepting H, forming a carbo-anion that is an important intermediate for C-C bond formation during the condensation process.[10] Understanding these two reaction pathways can aid in predicting the corresponding reaction mechanism for ethyl acetate conversion as support Lewis acid sites are expected to attack both the carbonyl group oxygen and the ether group oxygen.

In this work, the mechanism of ethyl acetate conversion to diethyl ether is elucidated based on the active surface's corresponding acid-base pair sites. Support surface characterization is coupled with kinetic evaluation to identify the active sites for different ethyl acetate conversion pathways as well as their dependence of reaction temperature, ethyl acetate partial pressures, as well as the impact of reaction intermediate co-feeds.

5.3 Materials and Methods

5.3.1 Preparation of Metal Oxide Supports

For each experiment, MgO (20 nm particle size), γ-Al_2O_3 (~20 nm particle), and m-ZrO_2 (~20 nm particle size) were loaded into each reaction cell as delivered by US Nanomaterials. All materials were pre-treated in-situ for all experiments with 450 °C oxidation followed by 400 °C reduction, unless stated otherwise.

5.3.2 BET Surface Area

Specific surface area based on the Brunaeur-Emmett-Teller (BET) theory was measured for MgO, γ-Al_2O, and m-ZrO_2 using a Micromeritics 3Flex Porosimeter.

5.3.3 CO_2 and NH_3 Temperature Programmed Desorption

Temperature programmed desorption (TPD) was conducted using a Micromeritics AutoChem 2920 instrument. In each experiment, 100 mg of catalyst material was placed in a quart u-tube reactor. The catalyst was first degassed in Ar flowing at 50 mL min^{-1} at 150 °C for 30 minutes after which it was oxidized in-situ with O_2 flowing at 50 mL min^{-1} at 450 °C for 1 hour and reduced in-situ with 10% H_2/Ar flowing at 50 mL min^{-1} at 400 °C for 1 hour. Following these steps, the catalyst was cooled to 50 °C in Ar, after which the probe molecule 10% CO_2/He or NH_3/He was flowed over the catalyst for 30 minutes. Next, the catalyst was purged with Ar for 30 minutes to eliminate any weakly bound or physiosorbed species. Finally, the catalyst temperature was increased from 50 °C to 450 °C, under Ar, at a rate of 10 °C/min. An in-line TCD was used to measure CO_2 and NH_3 desorption as a function of temperature during the TPD with the peak area corresponding to the number of probe molecules desorbed.

5.3.4 In-situ CO_2 and Pyridine Probe Molecule IR Characterization

In-situ IR Spectroscopy was carried out using a Nicolet iS10 FTIR spectrometer with a mercury cadmium telluride (MCT) detector cooled by LN2. HFC-202 and HFC-302 mass flow controllers (Teledyne Hastings) controlled gas flow rates to the reactor bed in a Harrick Low Temperature Reaction chamber with ZnSe windows mounted inside a ThermoScientific Praying Mantis diffuse reflectance adapter set. All gases were passed across a cold trap maintained between -30 to -50 °C with an IPA/LN2 mixture, a Drierite desiccant to absorb trace moisture and a carbonyl trap made of SiO_2 chips heated to 250 °C. N_2 gas was fed through the Praying Mantis to expel gas phase molecules outside of the reaction chamber to minimize noise generated by gas phase signatures in the background. Diffuse Reflectance Infrared Fourier Transform Spectroscopy (DRIFTS) was employed to generate spectra showing absorbance as a function of vibrational frequency (cm^{-1}). Note that absorbance was calculated by taking the log of inverse reflectance (Abs = log(1/R)), as previously discussed.[29] The reaction chamber bed was first complete filled with the support material, MgO, γ-Al_2O, and m-ZrO_2. Extra care was ensured to generate a flat and homogenous layer of the catalyst at the lip of the chamber bed. Background spectra were collected for the pre-treated catalyst under Ar at 50 °C for CO_2 and pyridine probe molecule IR and were subtracted from the spectra taken with the adsorbed probe molecule. In all cases no surface carbonate species were detected in the background spectrum of the freshly pretreated catalysts, suggesting the bands between 1450 and 1650 cm^{-1} exclusively corresponded to adsorbed CO_2 or pyridine on support basic and acid sites, respectively.

For the IR experiments, catalysts were oxidized with O_2 (50 mL min^{-1}) at 450 °C for 1 hour and then reduced with 10% H_2/Ar (100 mL min^{-1}) at 400 °C for 1 hr. The catalysts were then cooled under Ar (50 mL min^{-1}) and held at 50 °C, after which Ar was bubbled through pyridine and 10% CO_2/He (50 mL min^{-1}) was fed directly to deliver the probe molecule to the reaction chamber. It was assumed that equilibrium between the gas and pyridine liquid phase was achieved in the bubbles. CO_2 and pyridine were delivered to the reaction chamber until the absorbance saturated (~20 min). The chamber was then purged with Ar until the spectra remained constant (~20 min) to remove any gas phase or physisorbed pyridine.

5.3.5 Steady state ethyl acetate conversion kinetics

Prior to testing the dehydrogenation activity of all support materials, it was necessary to ensure that mass transfer effects did not play a role on the reaction rates observed. Therefore, ethyl acetate conversion rates for MgO, γ-Al_2O, and m-ZrO_2 were observed as a function of superficial velocity, see Figure 5.1, showing mass transfer effects were negligible across all superficial velocities. 50 mL min^{-1} was selected as the superficial velocity for all kinetic experiments. To prevent heat transfer and/or pressure drop effects on the reaction rates, 180 mg of the support material was further diluted by physically mixing with 900 mg of SiO_2 sand. The diluted catalyst was then loaded into a 1/2" quartz reactor packed with quartz wool and held within a rectangular aluminum block for optimized heat transfer. A home-made temperature controller was used to achieve desired reaction temperatures. All gas flows were controlled by mass flow controllers and an in-line bubbler was used to deliver gas phase ethyl acetate and was used to bubble ethyl acetate

and used as a diluent to control the ethyl acetate partial pressure. The reaction effluent was quantified in a GC that injected the effluent once every 24 minutes and a 6' Haysep D column was used to separate species with quantification by in-line thermoconductivity (TCD) and flame ionization detectors (FID). Ethyl acetate conversion was kept less than 5% for all studies, unless state otherwise, to ensure the system was in the differential reactor regime.

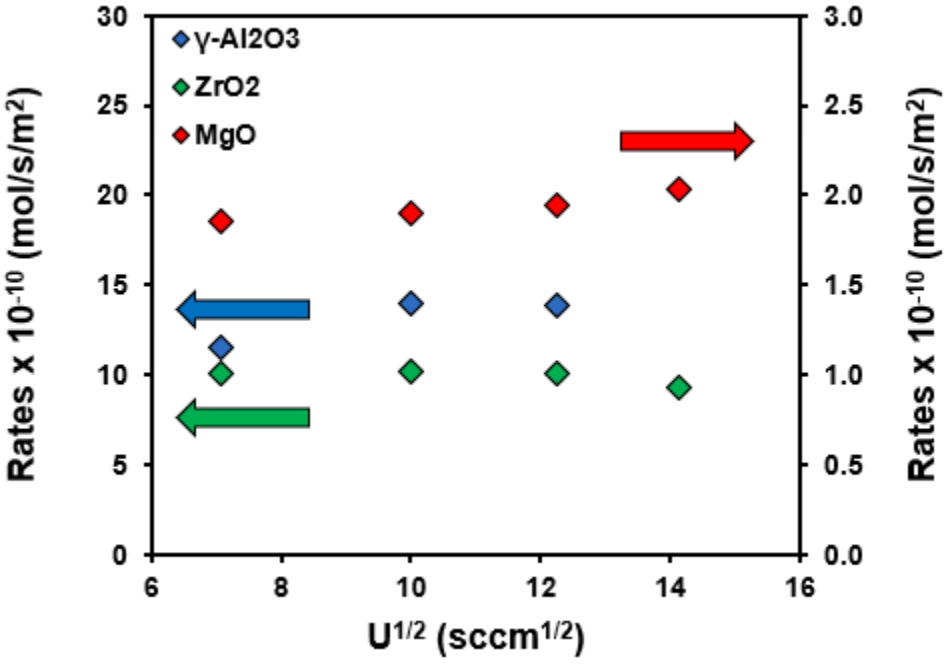

Figure 5.1 External Mass Transfer Effects. Ethyl acetate conversion rates at 340 °C and 40 mbar ethyl acetate as a function of the square root of the superficial velocity in volumetric rate of $cm^3\ min^{-1}$. MgO, ZrO_2, and γ-Al_2O_3 showed rates that were independent of the superficial velocity in the range of 50 to 200 $cm^3\ min^{-1}$. A superficial velocity of 50 $cm^3\ min^{-1}$ was chosen for all kinetic experiments.

5.3.5.1 Ethyl acetate conversion as a function of temperature

For temperature dependent ethyl acetate conversion experiments catalysts were pre-treated by oxidation at 450 °C for 1 hr with O_2 at 50 mL min^{-1} followed by reduction at 400 °C for 1 hr with H_2 at 5 mL min^{-1}. Following pre-treatment, catalysts were activated by flowing 40 mbar ethyl acetate at 340 °C with a superficial velocity of 50 mL min^{-1} for

8 hrs. After activation, the reactor was cooled to and maintained at 290 °C for 2 hours under a constant feed of 40 mbar of ethanol. Next, the temperature was increased (2 °C/min) to and held at 300 °C for 2 hours and this was repeated for each 10 °C step up to 340 °C.

5.3.5.2 Ethyl acetate conversion as a function of EA and H_2O pressure

For ethyl acetate pressure dependent dehydrogenation experiments, all catalysts were pre-treated by oxidation at 450 °C for 1 hour followed by reduction at 400 °C for 1 hour, with catalyst activation induced by 40 mbar ethyl acetate at 230 °C for 8 hrs. After activation, while maintaining a constant temperature of 230 °C, the ethyl acetate partial pressure was successively decreased from 40 ethyl acetate mbar to 1.3 mbar in steps of 5 mbar by adjusting the flow rates of He that bubbled ethyl acetate and He that acted as a diluent. The reaction system was held at each pressure for two hours to allow steady state to be reached and conversion was held at or under 5% at all conditions, unless stated otherwise.

For water pressure dependent dehydrogenation experiments, catalysts were pre-treated and activated in the same protocol. After catalyst activation, He was introduced into a second bubbler holding water, to co-feed 0.55 mbar pyridine with 40 mbar ethyl acetate into the reactor. After holding for 2 hours, the water pressure was increased to 2.75 mbar in steps of 0.55 mbar (each pyridine pressure was held for 2 hours) while maintaining constant ethyl acetate pressure (40 mbar), reaction temperature (430 °C), and superficial velocity (50 mL min^{-1}).

5.4 Results

5.4.1 Metal oxide support selection through characterization

In-situ CO_2 and NH_3 temperature programmed desorption (TPD) experiments were employed to estimate the surface density of acid and base sites on MgO, γ-Al_2O_3, and ZrO_2. As CO_2 is a commonly used probe molecule for metal oxide support basic sites, the peak area of the CO_2-TPD spectra in Figure 5.2 (a) are proportional to the number of basic sites on the catalyst surface. As each support has different surface areas as predicted by BET measurements with MgO, γ-Al_2O_3, and ZrO_2 having specific surface areas of 60, 125, and 26 m^2/g, respectively, the total number of surface acid and base sites were normalized to these surface areas as site densities, see Table 5.1. Using CO_2-TPD, the base site density from largest to smallest was MgO ≈ ZrO_2 >> γ-Al_2O_3. On the other hand, using a common probe molecule for surface acid sites, NH_3-TPD experiments, Figure 5.2 (b), predicted the acid site densities from largest to smallest to be γ-Al_2O_3 ≈ ZrO >> MgO.

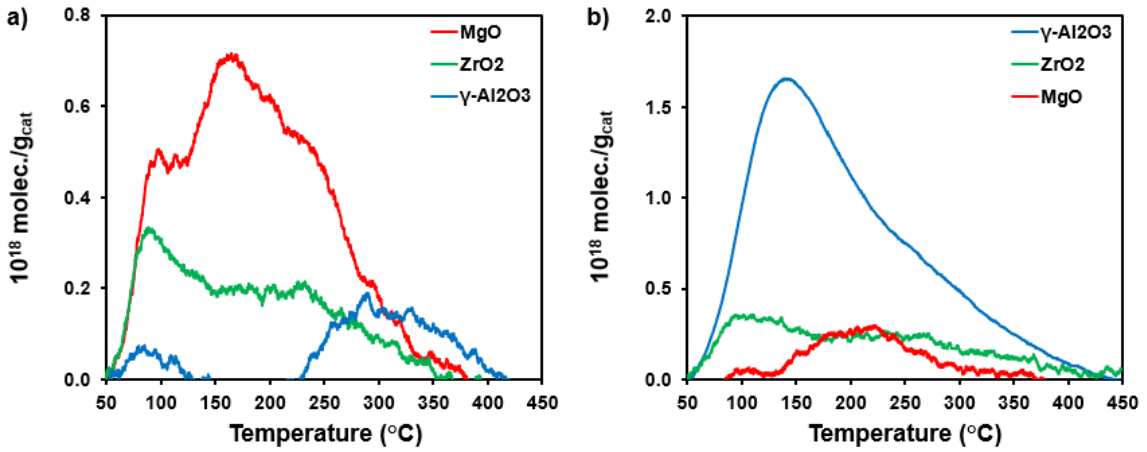

Figure 5.2 Temperature programmed desorption studies using a) CO_2 and b) NH_3 as probe molecules that were adsorbed at 50 °C and at saturation coverage. Following adsorption, catalysts were purged in Ar gas while ramping the catalyst temperature from 50 to 450 °C at 10 °C min^{-1}. Note, catalysts were pre-treated with 450 °C oxidation followed by 400 °C reduction.

While TPD experiments provide a quantitative estimate of surface sites, in-situ pyridine and CO_2 probe molecule IR experiments were employed to gain clear insights into the relative strengths of surface acid and base sites on MgO, γ-Al_2O_3, and m-ZrO_2. Figure 5.3 (a) shows IR spectra of CO_2 adsorbed at saturation cover over the three supports pre-treated by 450 °C oxidation followed by 400 °C reduction. Here, IR spectra are presented in the frequency range (1200-1800 cm^{-1}) where surface carbonates formed from CO_2 adsorption can be identified, with different frequencies corresponding to different strengths of support base sites. The carbonate species that were observed, listed from strongest to weakest, were unidentate (u) at 1596 cm^{-1}, chelating bidentate (cb) at 1655 cm^{-1}, and bridging bidentate at 1300 cm^{-1} (the carbonate structures are discussed in detail in Figure 1.3). Noticeably, while MgO has all 3 types of base sites, no distinct stretches appear for γ-Al_2O_3, suggesting it has particularly weak surface basicity, as has been discussed previously in literature.[30]

Figure 5.3 (b) shows IR spectra of pyridine adsorbed at saturation coverage over the three supports after identical pre-treatment as discussed above for probe molecule CO_2-IR. IR spectra are presented in the frequency range (1550-1650 cm^{-1}) where vibrational modes are assigned to pyridine adsorbed to Lewis acid sites termed ω_{8a} in literature, previously showing that the strength of Lewis acid sites in the ω_{8a} band region increases with increasing vibrational frequency.[31–33] Thus, the spectra in Figure 5.3 (b) have been divided into regions 1, 2, and 3, which correspond to strong, moderate, and weak Lewis acid sites, respectively. These spectra qualitatively show that MgO has relatively weak acid sites as the main IR band near 1600 cm^{-1} has a signal to noise ratio near 1:1, where it was

determined that the stretches near 1630 and 1640 cm^{-1} were simply noise in the spectra. On the other hand, both γ-Al_2O_3 and m-ZrO_2 have a larger number of acid sites, although γ-Al_2O_2 is the only support with strong acid sites as shown by its pyridine adsorption stretches at frequencies above 1615 cm^{-1} (region 1).

The combination of TPD and IR experiments revealed that MgO has a surface with exclusively strong basic sites while γ-Al_2O_3 has a surface with exclusively strong acid sites. Therefore, it was expected that each support would not have significant contribution from acid-base pairs for during ethyl acetate conversion and would serve as model systems for understanding the ethyl acetate conversion pathway through exclusively surface base or acid sites. On the other hand, TPD and IR experiments showed that the ZrO_2 surface has a combination of moderate acid and moderate base sites, suggesting that ZrO_2 has an abundance of acid-base pairs, which are expected to control ethyl acetate conversion differently than either MgO or γ-Al_2O_3. Note that the acid and base site densities together with the relative strength of each site based on IR experiments are summarized in table 5.1 below.

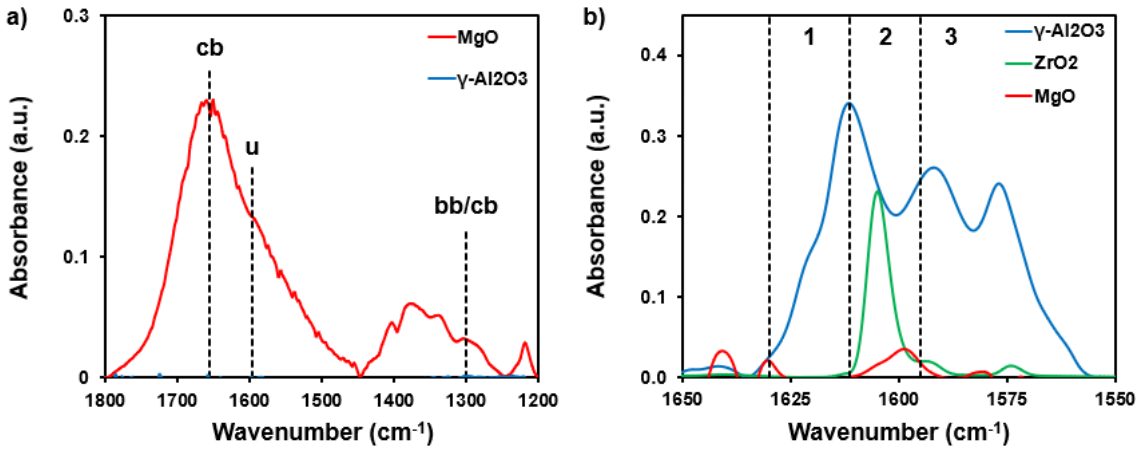

Figure 5.3 IR spectra of a) CO_2 and b) pyridine adsorbed at 50 °C and at saturation coverage on MgO, γ-Al_2O_3, and ZrO_2 pre-treated in-situ by 450 °C oxidation followed by 400 °C reduction. For a) CO_2 IR, cb, u, and bb correspond to chelating bidentate, unidentate, and bridging bidentate carbonates, respectively. For b) pyridine IR, zones 1, 2, and 3 correspond to strong, moderate, and weak acid sites, respectively.

Catalyst	Acid Site Density (NH_3/nm^2)	Base Site Density (CO_2/nm^2)	Relative Strength (acid, base)
MgO	0.6	2.9	Weak, Strong
γ-Al_2O_3	2.1	0.2	Strong, Weak
ZrO_2	2.9	1.9	Moderate, Moderate

Table 5.1 Summary of catalyst acid and base site density from TPD experiments, see Figure 5.2, and the relative acid and base site strength from IR experiments, see Figure 5.3.

5.4.2 Effect of support acid and base sites on ethyl acetate conversion

To compare the activity and product selectivity of MgO, γ-Al_2O_3, and ZrO_2, ethyl acetate conversion was executed at an ethyl acetate partial pressure of 40 mbar diluted in H2 following pre-treatment of the catalysts with in-situ oxidation at 450 °C followed by reduction at 400 °C. Total flow rate dependent measurements were made to ensure the rate of mass transport to the catalysts' surface did not influence the observed kinetics, examples of which are shown for the three supports in Figure 5.1. Ethyl acetate conversion was maintained below 5% for all experiments, ensuring differential kinetics. Temperature

dependent ethyl acetate conversion rates for MgO, γ-Al_2O_3, and ZrO_2 between 290 and 360 °C are shown in Figure 5.4.

Using 340 °C (0.196 mol/kJ) as an example, γ-Al_2O_3 and ZrO_2 showed total ethyl acetate conversion rates 13.8 x 10^{-10} mol s^{-1} m^{-2} and 11.8 and 10^{-10} mol s^{-1} m^{-2}, which were respectively 6 and 5-fold larger compared to the rates over MgO of 2.2 x 10^{-10} mol s^{-1} m^{-2}. Although the total rates were quite different the product selectivity over MgO and ZrO_2 were quite similar with selectivity to diethyl ether (DEE), ethanol (EtOH), and CO_2 being 31-34%, 38-44%, and 14%, respectively. On the other hand, γ-Al_2O_3 promoted ethyl acetate conversion to primarily DEE and ethylene (EY) with selectivity of 42% and 41%, respectively, while EtOH was a minor product with 10% selectivity. Note that for all three catalysts and under all reaction conditions, acetaldehyde (AcetH) was a minor product with less than 5% selectivity. The observed apparent activation barriers for each product over each support are summarized in Table 5.2 with all activation barriers in units of kJ mol^{-1}.

Table 5.2 shows that the apparent activation barrier for DEE formation was relatively similar for all catalysts at 66, 87, and 77 kJ mol^{-1} for MgO, γ-Al_2O_3, and ZrO_2, respectively. Noticeably, the barrier for EtOH formation decreased from 173 kJ mol^{-1} for MgO to 135 kJ mol^{-1} for γ-Al_2O_3 to 89 kJ mol^{-1} for ZrO_2 while the barrier for ethylene formation was similar for MgO and ZrO_2 (162 and 179 kJ mol^{-1}, respectively), it was reduced to 103 kJ mol^{-1} for γ-Al_2O_3. Finally, the barriers for CO_2 were quite similar for all three catalyst, though ZrO_2 did slightly reduce the observed barrier.

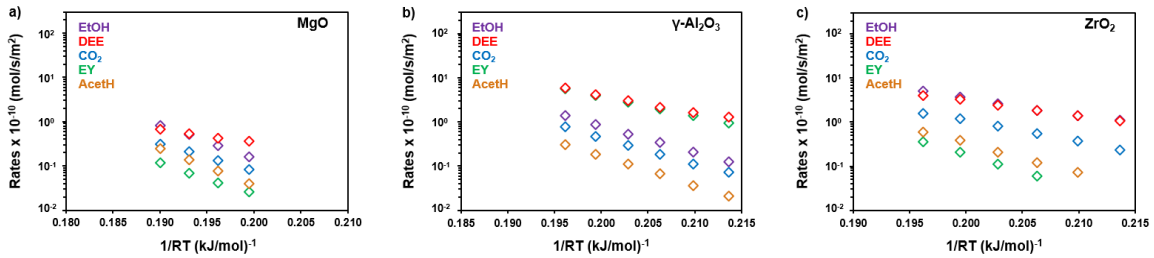

Figure 5.4 Ethyl acetate conversion rates normalized per catalyst surface area (from BET measurements) at 40 mbar ethyl acetate as a function of temperature from 290 to360 °C for **a)** MgO, **b)** γ-Al_2O_3, and **c**) ZrO_2. All catalysts were pre-treated in-situ by 450 °C oxidation followed by 400 °C reduction.

	kJ/mol			
Catalyst	DEE	EtOH	EY	CO_2
MgO	66	173	162	139
γ-Al_2O_3	87	135	103	135
ZrO_2	77	89	179	111

Table 5.2 Apparent activation barriers for ethyl acetate conversion to diethyl ether (DEE), ethanol (EtOH), ethylene (EY), and carbon dioxide (CO_2) with 40 mbar ethyl acetate between 290 and 360 °C. Corresponding ethyl acetate conversion rates as a function of inverse temperature are shown in Figure 5.4

5.4.3 Effect of H_2O partial pressure on ethyl acetate conversion

Based on simple stoichiometric predictions, it was expected that surface H species would help promote ethyl acetate (8 H species) conversion to the primary products ethanol (12 H species) and diethyl ether (10 H species). Therefore, it was of interest to probe the effects of the dissociative adsorption of H_2O onto support acid and base sites (as well as acid-base pairs), which was predicted to promote the generation of surface H species that could help promote ethyl acetate conversion. To conduct this test, ethyl acetate conversion was run over metal oxide supports with varying levels of acidity and basicity: MgO (strongly basic, weakly acidic), γ-Al_2O_3 (weakly basic, strongly acidic), and ZrO_2 (moderately basic, moderately acidic). After pre-treating the catalysts with in-situ oxidation at 450 °C followed by reduction at 400 °C, the supports were introduced to a continuous stream of 40 mbar ethyl acetate at 340 °C (360 °C for MgO). Upon reaching steady state under an ethyl acetate environment, each support was introduced to 0.6 mbar

HPLC-grade H_2O and after holding for 2 hours, the H_2O partial pressure was increased up to 2.8 mbar while keeping the ethyl acetate partial pressure and reaction temperature constant. The H_2O pressure dependent rates for the 5 products observed (CO_2, ethylene, acetaldehyde, ethanol, and diethyl ether), are shown in Figure 5.5. Starting with ethyl acetate conversion over MgO, see Figure 5.5 (a), only ethanol production was enhanced with increasing H_2O pressure, increasing from (0.41 ± 0.01) to (0.81 ± 0.09) x 10^{-10} mol sec^{-1} m^{-2}. All other products decreased slightly, keeping the overall reaction conversion constant (~0.25%). Over MgO, ethyl acetate was converted to two major products, ethanol (29% selectivity) and diethyl ether (47% selectivity). The introduction of H_2O increased the selectivity to ethanol while decreasing the selectivity to diethyl ether where at 2.8 mbar H_2O the selectivity to ethanol and diethyl ether became 52% and 35%, respectively. CO_2, ethylene and acetaldehyde were all minor products with CO_2 having the highest selectivity without H_2O of 14%.

Although the H_2O partial dependence of the ethyl acetate conversion products over γ-Al_2O_3 were qualitatively similar to that over MgO, the rates and product selectivity distribution was quite different as shown in Figure 5.5 (a) and (b). The first difference is the total reaction conversion, which was 4.9% over γ-Al_2O_3, a 20-fold enhancement compared to MgO. As discussed previously, before the introduction of H_2O, the two major products for ethyl acetate conversion over γ-Al_2O_3 were EY and DEE, with 40% and 44% selectivity, respectively. The equal distribution of these two products over γ-Al_2O_3 has previously been reported for ethanol dehydration reactions where surface ethoxy species dominated the support surface,[27] suggesting that ethoxy species are also abundant surface

species during the conversion of ethyl acetate. Increasing H_2O partial pressure over γ-Al_2O_3 promotes the rate of ethanol production 7-fold from (1.17 ± 0.18) x 10^{-8} mol^{-1} g_{cat}^{-1} with no H_2O co-feed to (7.98 ± 1.17) x 10^{-10} mol sec^{-1} m^{-2} at 2.8 mbar H_2O. Diethyl ether production was increased more modestly from (5.87 ± 0.85) x 10^{-10} mol sec^{-1} m^{-2} to (7.63 ± 0.53) x 10^{-10} mol sec^{-1} m^{-2}, while ethylene decreased from (5.30 ± 0.07) x 10^{-10} mol sec^{-1} m^{-2} to (4.48 ± 0.24) x 10^{-10} mol sec^{-1} m^{-2}. Correspondingly, the selectivity to ethanol increased from 9% to 38% while the selectivity of ethylene decreased from 40% to 21% and the selectivity of diethyl ether decreased from 44% to 37%.

Ethyl acetate conversion over ZrO_2 had different rates, H_2O pressure dependencies, and product selectivity distributions than either MgO or γ-Al_2O_3. Before the introduction of H_2O, the total product rates over ZrO_2 of (7.95 ± 0.25) x 10^{-10} mol sec^{-1} m^{-2} were comparable to that of γ-Al_2O_3 of (13.3 ± 0.77) x 10^{-10} mol sec^{-1} m^{-2}. However, the product selectivity over ZrO_2, before introduction of H_2O, was similar to that of MgO, which had comparable selectivity towards diethyl ether (39% compared to 47%) and an increase in ethanol selectivity (42% compared to 29%). However, upon the introduction of H_2O to ZrO_2, the rates of CO_2, ethanol, and diethyl ether increased 8-fold, 19-fold, and 7-fold at 2.8 mbar H_2O, respectively, with no meaningful changes in the rates of ethylene or acetaldehyde. With a co-feed of 2.8 mbar H_2O over ZrO_2, ethanol became the primary product with 68% selectivity compared to 24% and 8% selectivity to diethyl ether and CO_2, respectively. Additionally, the total product rates were increased 12-fold from (7.95 ± 0.25) x 10^{-10} mol sec^{-1} m^{-2}) with no H_2O co-feed to (92.95 ± 10.89) x 10^{-10} mol sec^{-1} m^{-2} with 2.8 mbar H_2O. Taken together, it is clear that a co-feed of H_2O with ethyl acetate primarily

promotes the conversion of ethyl acetate to ethanol, though to different extents over the three supports.

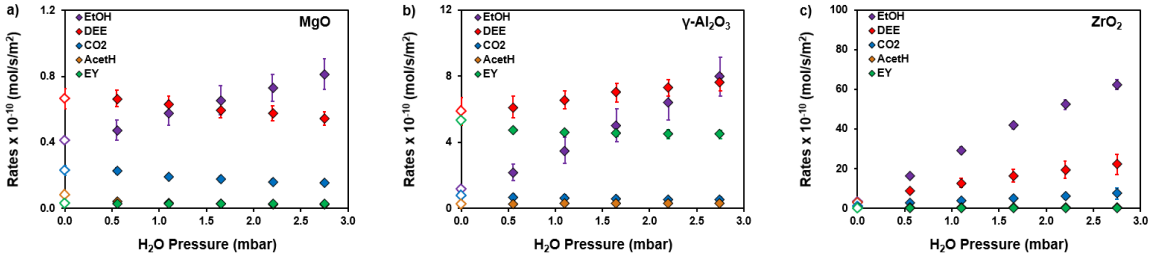

Figure 5.5 Ethyl acetate conversion rates at 340 °C (360 °C for MgO) as a function of water partial pressure with ethyl acetate pressure of 40 mbar. Reaction rates of all observed products: diethyl ether (red), ethylene (green), ethanol (purple), carbon dioxide (green), and acetaldehyde (orange) as a function of H_2O co-feed partial pressure for a) MgO, b) γ-Al_2O_3, and c) m-ZrO_2. All catalysts were pre-treated in-situ by 450 °C oxidation followed by 400 °C reduction.

In previous work, it has been shown that adventitious species from the ambient environment may effectively poison metal oxide support sites and such species may be cleaned off the surface through high temperature, in-situ oxidation.[34,35] Therefore, an analogous study was performed over γ-Al_2O_3 and ZrO_2 using an H_2O pressure dependence study under identical reaction conditions as discussed in Figure 5.5 (40 mbar ethyl acetate, 340 °C oxidation) with the difference being that the 450 °C in-situ oxidation step was omitted during catalyst pre-treatment. Comparing the H_2O pressure dependent results for ethyl acetate conversion over γ-Al_2O_3 with in-situ oxidation, see Figure 5.5 (b), and without in-situ oxidation, see Figure 5.6 (a), it is clear that the rates for all products are identical within experimental error, suggesting that the formation ambient species do not poison the catalysts or that the ambient species do not poison the active sites for ethyl acetate conversion.

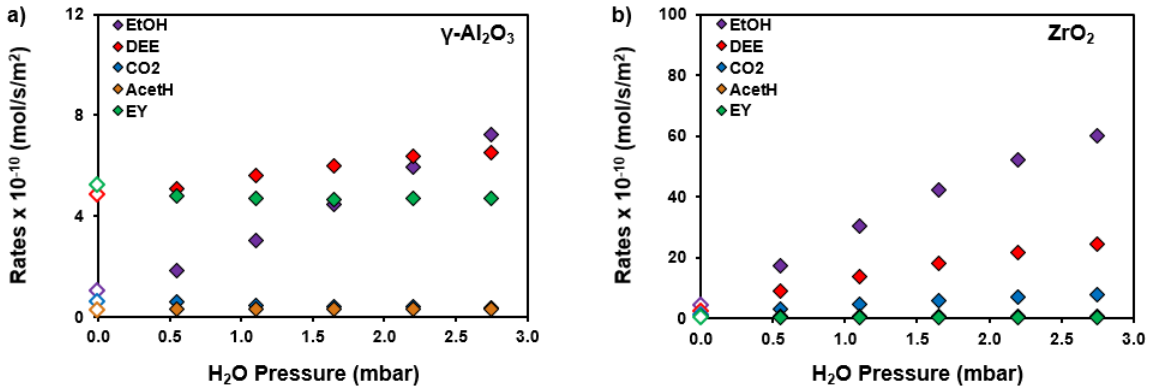

Figure 5.6 Ethyl acetate conversion rates at 340 °C as a function of water partial pressure with ethyl acetate pressure of 40 mbar. Reaction rates of all observed products: diethyl ether (red), ethylene (green), ethanol (purple), carbon dioxide (green), and acetaldehyde (orange) as a function of H_2O co-feed partial pressure for a) γ-Al_2O_3 and b) ZrO_2. All catalysts were pre-treated in-situ by 400 °C reduction only.

5.4.4 Effect of Na dopant on catalyst activity for ethyl acetate conversion

To test whether the product selectivity can be controlled by poisoning specific active sites, 0.5% and 5.0% by weight of Na was added to γ-Al_2O_3 and tested with temperature dependent ethyl acetate conversion experiments as shown in Figure 5.7. First, comparing the rates of γ-Al_2O_3 and 0.5Na-Al_2O_3 at 340 °C (0.196 mol kJ^{-1}) showed a 20% decrease in total ethyl acetate conversion with activity dropping from 13.75 x 10^{-10} mol sec^{-1} m^{-2} to 10.95 x 10^{-10} mol sec^{-1} m^{-2}. Interestingly, ethylene and diethyl ether experienced the largest drops in activity after doping γ-Al_2O_3 with 0.5 wt% Na. Ethylene rates decreased from 5.57 x 10^{-10} mol sec^{-1} m^{-2} to 3.60 x 10^{-10} mol sec^{-1} m^{-2} and diethyl rates decreased from 5.76 x 10^{-10} mol sec^{-1} m^{-2} to 4.62 x 10^{-10} mol sec^{-1} m^{-2}, changes of 35% and 20%, respectively. Additionally, although the selectivity to ethylene decreased from 41 to 33%, the selectivity to diethyl remained constant at 42% when comparing γ-Al_2O_3 to 0.5Na-Al_2O_3.

Next, comparing 0.5Na-Al_2O_3 to 5 wt% Na loaded on γ-Al_2O_3 (5Na-Al_2O_3) at 340 °C (0.196 mol kJ^{-1}), see Figure 5.7, a significant, 3-fold decrease in total rates was observed

from 10.97 x 10^{-10} mol sec^{-1} m^{-2} to 3.59 x 10^{-10} mol sec^{-1} m^{-2}. The rates for ethylene production dropped 16-fold from 3.60 x 10^{-10} mol sec^{-1} m^{-2} to 0.23 x 10^{-10} mol sec^{-1} m^{-2}, respectively, while diethyl ether rates dropped 4-fold from 4.62 x 10^{-10} mol sec^{-1} m^{-2} to 1.08 x 10^{-10} mol sec^{-1} m^{-2}. While the rates for acetaldehyde and CO_2 also decreased, the rates for ethanol stayed constant, even when compared to the un-doped γ-Al_2O_3. Consequentially, for 5Na-Al_2O_3, product selectively changed dramatically form γ-Al_2O_3 and 0.5Na-Al_2O_3 as the ethanol, diethyl ether, and ethylene selectivity became 47%, 30%, and 6%, respectively. Interestingly, after doping γ-Al_2O_3 with 5 wt% Na, the product selectivity and rates approached that of MgO. To summarize the impact of doping γ-Al_2O_3 on ethyl acetate conversion, the addition of a dilute amount of Na (0.5 wt%, ~1 Na/nm^2) decreased the rates of ethylene and diethyl ether by 20-30%, decreasing ethylene selectivity, but maintaining a constant diethyl ether selectivity. The addition of 5 wt % Na (~ 10 Na/nm^2) decreased the reaction rates of ethylene and diethyl ether dramatically, while having no effect on ethanol, which resulted in ethanol becoming the dominant products while the activity and product selectivity approached that observed over MgO.

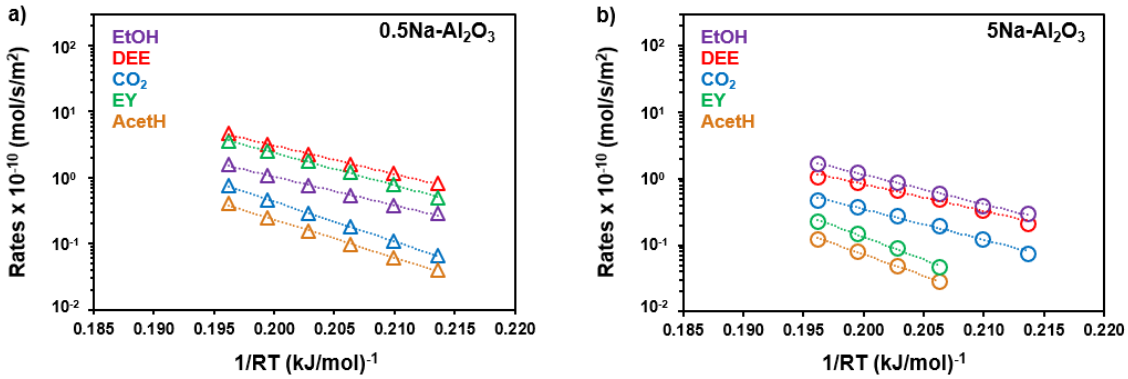

Figure 5.7 Ethyl acetate conversion rates normalized per catalyst surface area (from BET measurements) at 40 mbar ethyl acetate as a function of temperature from 290 to 340 °C for **a)** 0.5 wt% Na loaded on γ-Al_2O_3, and **c**) 5.0 wt% Na loaded on γ-Al_2O_3. All catalysts were pre-treated in-situ by 400 °C reduction only. The corresponding temperature dependent rates of un-doped γ-Al_2O_3 are shown in Figure 5.4 (b).

	10^{10} mol sec^{-1} m^{-2} at 340 °C				
Catalyst	**DEE**	**EtOH**	**EY**	**CO_2**	**AcetH**
γ-Al_2O_3	5.76	1.35	5.57	0.76	0.30
0.5Na-Al_2O_3	4.62	1.59	3.60	0.75	0.41
5Na-Al_2O_3	1.08	1.68	0.23	0.47	0.12
MgO	0.54	0.99	0.03	0.18	0.03

Table 5.3 Summary of rates (10^{10} mol sec^{-1} m^{-2}) at 340 °C and 40 mbar ethyl acetate pressure for ethyl acetate conversion to diethyl ether (DEE), ethanol (EtOH), ethylene (EY), carbon dioxide (CO_2), and acetaldehyde (AcetH) over γ-Al_2O_3, 0.5 wt% Na loaded on γ-Al_2O_3 (0.5Na-Al_2O_3), 5.0 wt% Na loaded on γ-Al_2O_3 (5Na-Al_2O_3), and MgO.

5.5 Discussion

The combination of in-situ characterization and reaction kinetics suggested helped develop some new insights into ethyl acetate conversion over metal oxide supports. First, the results described in this chapter suggested that the active sites for ethyl acetate conversion are predominantly Lewis acid sites based on the enhanced reaction rates of γ-Al_2O_3 (strongly acidic) and ZrO_2 (moderately acidic) compared to MgO (weakly acidic). However, although the total product rates for ZrO_2 and γ-Al_2O_3 were similar at 13.75 x 10^{-10} mol sec^{-1} m^{-2} and 11.76 x 10^{-10} mol sec^{-1} m^{-2}, respectively, the product distributions were

quite different, see Figure 5.4 and 5.5. While the major products over γ-Al_2O_3 were ethylene and diethyl ether with 40% and 44% selectivity, respectively, the major products over ZrO_2 were ethanol and diethyl ether with 42% and 39% selectivity, respectively. Although the surface acid site density for the two supports was similar, 2.1 sites/nm^2 and 2.9 sites/nm^2 for γ-Al_2O_3 and ZrO_2, respectively, γ-Al_2O_3 was unique in having strong acid sites, which ZrO_2 lacked, as shown by pyridine-IR experiments in Figure 5.3 (b). This suggests that strong acid sites are the active sites for ethylene formation as the production of ethylene was 15-fold larger on γ-Al_2O_3 than ZrO_2. Additionally, ethyl acetate conversion to equimolar amounts of ethylene and diethyl ether (84% total selectivity) over γ-Al_2O_3 is quite similar to previous reports on the kinetics of ethanol dehydration over γ-Al_2O_3, which suggested that the active site of both products were Lewis acidic in nature, but also non-equivalent.[27] It was proposed that while ethylene was produced from an adsorbed ethanol molecule, diethyl ether was produced from surface ethoxy dimers. Thus, it is quite likely that Lewis acid sites on γ-Al_2O_3 would cleave the C-O bond in ethyl acetate, forming ethanol and ethoxy-like surface intermediates that would then follow a similar reaction pathway as feeding pure ethanol over the support.

Although we previously reported, in chapter 4, that in situ oxidative pre-treatment of supports can help promote the activation of strong acid species[34], in this work in situ oxidative pre-treatment had no impact on ethyl acetate conversion rates and product selectivity as evidenced by the comparison of Figure 5.5 and 5.6. These contrasting results may be simply due to the high reaction temperature in this work (340 °C) compared to that

in chapter 4 (210 °C), suggesting that under more extreme reaction conditions, the strong Lewis acid sites were activated without the introduction of oxidative pre-treatment.

Finally, the poisoning of support sites with Na dopants helped to provide additional evidence that Lewis acid sites are the active sites for ethyl acetate conversion. As shown in Figure 5.7, with increasing weight loading of Na onto γ-Al_2O_3, the ethyl acetate conversion rates and product selectivity approached that of MgO. The addition of Na worked to make the surface of γ-Al_2O_3 catalytically like that of MgO, in the scope of its surface acidity because while γ-Al_2O_3 is a non-basic support, MgO is a strongly basic support. So, reaction rates and product selectivity converging with the convergence of the acid site properties of the two supports, while the base site properties were dramatically different, strongly suggested that the support Lewis acid sites were the exclusive active sites for ethyl acetate conversion as opposed to basic sites or acid-base pairs. However, it should be noted that acid-base pairs appeared to help facilitate H_2O onto the support surface as evidenced by the significantly enhancement of reaction rates with increasing H_2O partial pressure, as opposed to that observed over MgO or γ-Al_2O_3, as shown in Figure 5.5.

5.6 Conclusion

Although incomplete, the work in this chapter provided new insights into the reaction mechanism for ethyl acetate conversion over metal oxide supports. First, as evidenced by product selectivity and relative rates over γ-Al_2O_3, diethyl ether is formed indirectly from ethyl acetate, through surface ethoxy intermediates. Second, based on the different reaction rates over MgO, γ-Al_2O_3, and ZrO_2, as well as the impact of poisoning the γ-Al_2O_3 with Na dopants, we propose that the active site for ethyl acetate conversion

are exclusively Lewis acid sites, as opposed to basic sites or acid-base pairs. Further work would need to be completed in order to more deeply investigate the ethyl acetate reaction mechanism to then develop predictive power on methods of optimizing diethyl ether formation from ethyl acetate.

5.7 References

(1) Taifan, W.; Li, Y.; Baltrus, J. P.; Zhang, L.; Frenkel, A. I.; Baltrusaitis, J. Operando Structure Determination of Cu and Zn on Supported MgO/SiO2 Catalysts during Ethanol Conversion to 1,3-Butadiene. *ACS Catal.* **2019**, *9* (1), 269–285.

(2) Taifan, W. E.; Baltrusaitis, J. In-Situ Spectroscopic Insights on the Molecular Structure of the MgO/SiO2 Catalytic Active Site During Ethanol Conversion to 1,3-Butadiene. *J. Phys. Chem. C* **2018**, *122* (36), 20894–20906.

(3) Angelici, C.; Velthoen, M. E. Z.; Weckhuysen, B. M.; Bruijnincx, P. C. A. Effect of Preparation Method and CuO Promotion in the Conversion of Ethanol into 1,3-Butadiene over SiO2–MgO Catalysts. *ChemSusChem* **2014**, *7* (9), 2505–2515.

(4) Ngo, D. T.; Tan, Q.; Wang, B.; Resasco, D. E. Aldol Condensation of Cyclopentanone on Hydrophobized MgO. Promotional Role of Water and Changes in Rate-Limiting Step upon Organosilane Functionalization. *ACS Catal.* **2019**, *9* (4), 2831–2941.

(5) Wang, S.; Iglesia, E. Entropy-Driven High Reactivity of Formaldehyde in Nucleophilic Attack by Enolates on Oxide Surfaces. *J. Am. Chem. Soc.* **2018**, *140* (2), 775–782.

(6) Makshina, E. V.; Dusselier, M.; Janssens, W.; Degrève, J.; Jacobs, P. A.; Sels, B. F. Review of Old Chemistry and New Catalytic Advances in the On-Purpose Synthesis of Butadiene. *Chem. Soc. Rev.* **2014**, *43* (22), 7917–7953.

(7) León, M.; Díaz, E.; Ordóñez, S. Ethanol Catalytic Condensation over Mg-Al Mixed Oxides Derived from Hydrotalcites. *Catal. Today* **2011**, *164* (1), 436–442.

(8) Wang, S.; Goulas, K.; Iglesia, E. Condensation and Esterification Reactions of Alkanals, Alkanones, and Alkanols on TiO2: Elementary Steps, Site Requirements, and Synergistic Effects of Bifunctional Strategies. *J. Catal.* **2016**, *340*, 302–320.

(9) Jae, J.; Mahmoud, E.; Lobo, R. F.; Vlachos, D. G. Cascade of Liquid-Phase Catalytic Transfer Hydrogenation and Etherification of 5-Hydroxymethylfurfural to Potential Biodiesel Components over Lewis Acid Zeolites. *ChemCatChem* **2014**, *6* (2), 508–513.

(10) Di Cosimo, J. I.; Díez, V. K.; Xu, M.; Iglesia, E.; Apesteguía, C. R. Structure and Surface and Catalytic Properties of Mg-Al Basic Oxides. *J. Catal.* **1998**, *178* (2), 499–510.

(11) Ginés, M. J. L.; Amadeo, N.; Laborde, M.; Apesteguía, C. R. Activity and Structure-Sensitivity of the Water-Gas Shift Reaction over Cu-Zn-Al Mixed Oxide Catalysts. *Appl. Catal. A, Gen.* **1995**, *131* (2), 283–296.

(12) Brands, D. S.; Poels, E. K.; Bliek, A. Ester Hydrogenolysis over Promoted Cu/SiO2catalysts. *Appl. Catal. A Gen.* **1999**, *184* (2), 279–289.

(13) Claus, P.; Lucas, M.; Lücke, B.; Berndt, T.; Birke, P. Selective Hydrogenolysis of

Methyl and Ethyl Acetate in the Gas Phase on Copper and Supported Group VIII Metal Catalysts. *Appl. Catal. A Gen.* **1991**, *79* (1), 1–18.

(14) Zell, T.; Ben-David, Y.; Milstein, D. Unprecedented Iron-Catalyzed Ester Hydrogenation. Mild, Selective, and Efficient Hydrogenation of Trifluoroacetic Esters to Alcohols Catalyzed by an Iron Pincer Complex. *Angew. Chemie - Int. Ed.* **2014**, *53*, 4685–4689.

(15) Keil, F. J. Methanol-to-Hydrocarbons: Process Technology. *Microporous Mesoporous Mater.* **1999**, *29* (1–2), 49–66.

(16) Whitcraft, D. R.; Verykios, X. E.; Mutharasan, R. Recovery of Ethanol from Fermentation Broths by Catalytic Conversion to Gasoline. *Ind. Eng. Chem. Process Des. Dev.* **1983**, *22* (3), 452–457.

(17) Okumura, K.; Kiotaka, A.; Yasuhiro, I. Structural Transformation and Low-Pressure Catalysis for Ethyl Acetate Hydrogenation of Rh/One-Atomic-Layer GeO2/SiO2. *J. Phys. Chem. B* **1997**, *5647* (97), 9984–9990.

(18) Zhu, Y.; Wang, X.; Shi, L. Hydrogenation of Ethyl Acetate to Ethanol over Bimetallic Cu-Zn /SiO2 Catalysts Prepared by Means of Coprecipitation. *Bull. Korean Chem. Soc.* **2014**, *35* (1), 141–146.

(19) Gursahani, K. I.; Alcalá, R.; Cortright, R. D.; Dumesic, J. a. Reaction Kinetics Measurements and Analysis of Reaction Pathways for Conversions of Acetic Acid, Ethanol, and Ethyl Acetate over Silica-Supported Pt. *Appl. Catal. A Gen.* **2001**, *222* (1–2), 369–392.

(20) Schittkowski, J.; Tölle, K.; Anke, S.; Stürmer, S.; Muhler, M. On the Bifunctional Nature of Cu/ZrO2 Catalysts Applied in the Hydrogenation of Ethyl Acetate. *J. Catal.* **2017**, *352*, 120–129.

(21) Ferretti, O. A.; Bournonville, J. P.; Mabilon, G.; Martino, G.; Candy, J. P.; Basset, J.-M. Surface Organometallic Chemistry on Metals : Part IV. Selective Hydrogenation of Ethyl Acetate to Ethanol on Rh---Sn/SiO2 Bimetallic Catalysts: A Mechanistic Study. *J. Mol. Catal.* **1991**, *67* (3), 283–294.

(22) Minachev, K.; Avaev, V.; Ryashentseva, M. Hydrogenation of Ethyl Acetate on Re/Gamma Alumina Catalyst. *J. Chem. Inf. Model.* **2013**, *53* (2), 1689–1699.

(23) Evans, J. W.; Wainwright, M. S.; Cant, N. W.; Trimm, D. L. Structural and Reactivity Effects in the Copper-Catalyzed Hydrogenolysis of Aliphatic Esters. *J. Catal.* **1984**, *88* (1), 203–213.

(24) Agarwal, A. K.; Cant, N. W.; Wainwright, M. S.; Trimm, D. L. Catalytic Hydrogenolysis of Esters: A Comparative Study of the Reactions of Simple Formates and Acetates over Copper on Silica. *J. Mol. Catal.* **1987**, *43* (1), 79–92.

(25) Roy, S.; Mpourmpakis, G.; Hong, D.-Y.; Vlachos, D. G.; Bhan, A.; Gorte, R. J. Mechanistic Study of Alcohol Dehydration on γ-Al2O3. *ACS Catal.* **2012**, *2* (9), 1846–1853.

(26) DeWilde, J. F.; Chiang, H.; Hickman, D. A.; Ho, C. R.; Bhan, A. Kinetics and Mechanism of Ethanol Dehydration on γ-Al2O3: The Critical Role of Dimer Inhibition. *ACS Catal.* **2013**, *3* (4), 798–807.

(27) DeWilde, J. F.; Czopinski, C. J.; Bhan, A. Ethanol Dehydration and Dehydrogenation on γ-Al2O3: Mechanism of Acetaldehyde Formation. *ACS Catal.* **2014**, *4* (12), 4425–4433.

(28) Knaeble, W.; Iglesia, E. Kinetic and Theoretical Insights into the Mechanism of Alkanol Dehydration on Solid Brønsted Acid Catalysts. *J. Phys. Chem. C* **2016**, *120* (6), 3371–3389.

(29) Sirita, J.; Phanichphant, S.; Meunier, F. Quantitative Analysis of Adsorbate Concentrations by Diffuse Reflectance FT-IR. *Anal. Chem.* **2007**, *79*, 3912–3918.

(30) Morterra, C.; Magnacca, G. A Case Study: Surface Chemistry and Surface Structure of Catalytic Aluminas, as Studied by Vibrational Spectroscopy of Adsorbed Species. *Catal. Today* **1996**, *27*, 497–532.

(31) Digne, M.; Sautet, P.; Raybaud, P.; Euzen, P.; Toulhoat, H. Use of DFT to Achieve a Rational Understanding of Acid-Basic Properties of γ-Alumina Surfaces. *J. Catal.* **2004**, *226* (1), 54–68.

(32) Morterra, C.; Ghiotti, G.; Boccuzzi, F.; Coluccia, S. An Infrared Spectroscopic Investigation of the Surface Properties of Magnesium Aluminate Spinel. *J. Calaysis* **1978**, *51*, 299–313.

(33) Liu, X.; Truitt, R. E. DRFT-IR Studies of the Surface of γ-Alumina. *J. Am. Chem. Soc.* **1997**, *119* (41), 9856–9860.

(34) Hanukovich, S.; Dang, A.; Christopher, P. The Influence of Metal Oxide Support Acid Sites on Cu Catalyzed Non-Oxidative Dehydrogenation of Ethanol to Acetaldehyde. *ACS Catal.* **2019**, *9*, 3537–3550.

(35) Karim, W.; Spreafico, C.; Kleibert, A.; Gobrecht, J.; Vandevondele, J.; Ekinci, Y.; Bokhoven, J. A. Van. Catalyst Support Effects on Hydrogen Spillover. *Nature* **2017**, *541* (7635), 68–71.

Chapter 6. Conclusions and Future Outlook

6.1 Summary

The focus of this dissertation was to study metal oxide supported Cu catalysts and the role Cu-support interfacial effects play in both the ability to effectively characterize the Cu surface (Part 1, Chapter 3) and in promoting the activity for ethanol dehydrogenation to acetaldehyde (Part 2, Chapter 4). For the first part, cryogenic CO probe molecule IR was employed to show that overoxidation of the Cu surface during N_2O-TPR characterization caused the overestimation of Cu particle dispersion. Cryogenic NO chemisorption was proposed as a technique that could effectively quantify the extent of overoxidation and effectively correct Cu dispersion estimates. In part 2, Cu loaded on ZrO_2 and Al-doped ZrO_2 was studied to show the impact of Cu-support interface effects on both the ethanol dehydrogenation reaction active site and activity. It was proposed that by doping ZrO_2 with strong Lewis acid, Al^{3+} sites, the rate limiting step was changed, modifying the Cu active site and promotion reaction dehydrogenation activity.

6.2 General Conclusions

The following conclusions were drawn from the culmination of the work, as described in this dissertation:

- Temperature dependent N_2O oxidation during N_2O-TPR characterization induced the overoxidation of the Cu surface, forming Cu^{2+} sites, as opposed to Cu^{+}.
- The co-chemisorption of CO and NO as probe molecules was shown to be an effective way to identify and differentiate Cu^{+} and Cu^{2+} sites .

- ZrO_2 supported Cu particle size dependence studies suggested that oxidation is more facile on undercoordinated Cu facets with N_2O overoxidation occurring to a higher degree over smaller Cu particles.
- The particle size dependence studies also suggested that complete surface oxidation is more difficult on larger Cu particles, which revealed that the optimum N_2O oxidation temperature is also particle size dependent.
- Due to the difficulty with predicting the optimal N_2O oxidation temperature for Cu characterization, cryogenic NO chemisorption was proposed as a technique that could quantify the degree of overoxidation to properly correct dispersion estimates
- NO-TPD was not a feasible method for quantifying Cu^{2+} sites due to the formation of nitrate and nitrite species on the catalyst surface during the temperature ramp. Therefore, NO pulse chemisorption has been proposed as an alternative technique for which a known quantity will be pulsed onto Cu at cryogenic temperatures and the quantity of adsorbed NO can be used to estimate the number of Cu^{2+} sites.
- The combination of pyridine and CO probe molecule IR showed that doping ZrO_2 with Al^{3+} at surface coverage generated strong Lewis acid sites that were able to withdraw electron density from interfacial Cu sites, effectively creating new interfacial $Cu^{\delta+}$ sites.
- Temperature dependent studies for ethanol dehydrogenation over Cu loaded on ZrO_2 and Al-doped ZrO_2 showed that turn over frequency (TOF) of dehydrogenation was promoted 10-fold with Cu of similar dispersion loaded on Al-doped ZrO_2, compared to bare ZrO_2.

- Pre-treatment dependent studies for ethanol dehydrogenation over Cu loaded on Al-doped ZrO_2 showed that in situ high temperature oxidative pre-treatment was key in activating strong acid sites on the Al-doped ZrO_2, which in turn would promote reaction TOF 10-fold
- Cu particle size dependent studies for ethanol dehydrogenation over ZrO_2 and Al-doped ZrO_2 suggested that when loaded on ZrO_2 the reaction was not Cu structure sensitive, but when loaded on Al-doped ZrO_2, interfacial Cu sites became the dominant active sites for dehydrogenation
- The combination of ethanol and pyridine partial pressure dependent studies suggested that at the limit of low ethanol partial pressure and saturation coverage of pyridine, the TOF for Cu loaded on ZrO_2 and Al-doped ZrO_2 converge as the promotional role of strong Lewis acid sites is minimized
- By fitting a microkinetic model to the pressure dependent results, it was proposed that at high ethanol partial pressures, the Cu surface becomes poisoned with reactive intermediates, and supports with strong Lewis acidity help facilitate O-H bond cleavage, making C_α-H bond cleavage the rate limiting step (RLS) at interfacial Cu sites. In contrast, at low ethanol partial pressures the reaction rate is minimally dependent on the support and the RLS switches to O-H bond cleavage over the entire Cu surface.

6.3 Outlook on Future Work

Though chapter 5 worked to develop a more comprehensive understanding of the ethyl acetate conversion mechanism over metal oxide supports, the research could be

expanded two different ways. The first is to study the mechanism of the conversion of ethyl acetate analogs such as ethyl propanoate (5 carbons instead of 4) or methyl formate (3 carbons instead of 4). Developing an understanding of the effects of carbon change length of esters on their ability to deoxygenate would provide important knowledge for industrial processes that require effective deoxygenation processes to make gasoline-like products.

The second approach would be to study the reaction mechanism of ethyl acetate hydrogenolysis over active metal catalysts such as Pt. Because hydrogenolysis is a process in which bonds breakage is induced by dissociated molecular hydrogen, such a reaction is not possible over metal oxide supports, as they do not have the ability to dissociate hydrogen at reasonable temperatures. However, active metals such as Pt are well known to be very effective hydrogenation catalysts because of their exceptional ability to dissociate hydrogen. Consequentially, it is also expected that ethyl acetate conversion would be much more facile over active metals as opposed to on metal oxide supports. The focus of this section will be to discuss this second approach and will be explained in detail in the sections below.

6.4 Choice of active metals for ethyl acetate hydrogenolysis

Noble metals based on Pt, Pd, Rh, or Ru come off as the natural selection when optimizing hydrogenation reactions as they promote hydrogenation at modest temperature and pressure.[1] However, these noble metals are limited by their high cost and scarcity as well their propensity to induce non-selective hydrogenation. Thus, for a process such as ethyl acetate hydrogenolysis, where selective formation of diethyl ether is desired, these noble metals would not be the optimal choice. On the other hand, group 11 elements (Cu,

Ag, and Au) are known to be quite selective, but have a large activation barrier for hydrogen dissociation, making them ineffective hydrogenation catalysts.[2,3] Consequentially, bimetallic metal alloys (i.e. Cu-Pt or Cu-Ni) have been studied as a means of tuning the catalysts to exhibit the strengths of both types of metals: facile H_2 dissociation while keeping reactant hydrogenation selectivity towards the desired product(s). One example is shown from previous work that employed Cu-Ni alloys loaded on TiO_2 to selectively hydrogenate the carbonyl of furfural to methylfuran. In this system, due to Ni-TiO_2 strong electronic interactions, the Cu-Ni alloy had surface enriched with Cu while Ni predominantly made up the core of the nanoparticle, though some isolated Ni species existed on the nanoparticle surface. Under reaction conditions, these isolated surface Ni atoms worked to dissociate H_2, inducing H spillover onto the bulk Cu surface, which then selectively reduced fufural to methylfuran.[4]

Recently, novel bimetallic alloys, coined single atom alloys, have been developed to synthesize catalysts that induce facile dissociation of reactants (high hydrogenation activity) and weak binding of intermediates (high hydrogenation selectivity). Here, precious metals (i.e. Pt and Pd) are loaded with very low concentrations onto a Cu host metal, creating single atom Pt on bulk Cu nanoparticles. The selective hydrogenation mechanism is analogous to that described above for the Cu-Ni alloy catalyst in which Pt effectively dissociates H_2 onto the Cu surface, which then can perform selective hydrogenation.[1,2] In our future work, our aim was to develop Pt-Cu single atom alloys to perform selective hydrogenolysis of ethyl acetate to diethyl ether at moderate temperatures.

Our expectation was that single atom Pt would activate hydrogen, while Cu would promote the selective hydrogenation of ethyl acetate's carbonyl group, as predicted from literature.[4]

6.5 Completed work for Pt-Cu single atom alloys

6.5.1 Pt-Cu single atom alloy synthesis

To synthesize PtCu single atom alloys, the host metal Cu was prepared first through the colloidal synthesis technique, as described in detail in Chapter 2. First, 0.421 g Cu nitrate was mixed in 100 mL of HPL H_2O solution for 1 hr in a 3-neck round bottom flask, under Ar protection. Next, 0.785 g PVP was added to the solution and stirred for 1 hr to allow for homogenous mixing of the polymer. Following PVP addition, 0.176 g ascorbic acid, in 10 mL HPLC H_2O (0.1 M) was added to the Cu + PVP solution, and stirred for 1 hr, at which time the solution began to turn a light red color and slowly precipitate, indicating the reduction of Cu species in solution. After ascorbic acid began reducing Cu, 0.393 g of $NaBH_4$ in 26 mL HPLC H_2O (0.4 M) was added drop-wise to the reduced Cu solution and stirred for 1 hr. Note that the solution turns to a dark brown solution almost immediately upon the introduction of $NaBH_4$. Finally, 1 g γ-Al_2O_3 was carefully added to the Cu colloid solution and mixed overnight (between 12 and 15 hours). After mixing, the Cu colloid was vacuum filtered, dried, sieved down to a particle size no larger than 75 μm, and calcined at 350 °C for 4 hours to burn off PVP.

After preparation of the 10 wt% Cu loaded on γ-Al_2O_3 nanoparticles, the particles were reduced in-situ, in a 3-neck round bottom flask, at 400 °C for 1 hr to prepare the Cu particles for galvanic replacement. Following reduction, the catalyst was cooled to 100 °C and a 5mM of HCl was added together with the appropriate amount of H_2PtCl_6 solution

and mixed in HPLC H_2O with a total volume of 50 mL. The solution was then added to the 3-neck flask, with an attached reflux column, and stirred for 30 minutes. The PtCu slurry was then vacuum filtered, dried, and sieved.

6.5.2 Pt-Cu single atom alloy characterization

6.5.2.1 Inductively coupled plasma

Pt-Cu single atom alloys were synthesized through a Cu colloid synthesis protocol followed by galvanic replacement of surface Cu with Pt as described above. To prepare the PtCu alloys for inductively coupled plasma (ICP) analysis, the catalysts were digested overnight (~12 hours) in aqua regia (3 parts 30% HCl and 1 part 70% HNO_3). The digested solution was then syringe filtered as a means of separating the Pt and Cu ions in solution from the γ-Al_2O_3 support particles with only small Pt and Cu ions being able to travel through the filter. The filtrate was then used with the ICP, which was calibrated using Cu nitrate and Pt chloride standards bought from Sigma Aldrich and the results for the Pt-Cu single atom alloy is summarized in Table 6.1. The ICP results reveal that the nominal weight loadings of both Cu and Pt were proper estimates of the actual weight loading of each, showing that 100%, within ICP experimental error, of Pt successfully replaced surface Cu atoms. Table 2 summarizes the two PtCu catalyst that were synthesized, 2 wt% Pt, 10 wt% Cu ($PtCu_{15}$) and 0.1 wt% Pt, 10 wt% Cu ($PtCu_{300}$), which were both loaded on a γ-Al_2O_3 support. Note the Pt_xCu_y nomenclature represents the atomic ratio of Pt (x) relative to Cu (y) normalized to the Pt content.

Element	Nominal Weight Loading (%)	Actual (ICP)
Cu	10	9.5
Pt	0.1	0.099

Table 6.1 ICP analysis of $PtCu_{100}$ particles post-digestion with aqua regia with nominal weight loading of Cu and Pt shown with respect to the actual weight loading observed through ICP.

Catalyst	Pt Content (weight %)	Cu content (weight %)
$PtCu_{15}$	1.8	10
$PtCu_{300}$	0.099	9.5

Table 6.2 ICP analysis of $PtCu_{15}$ and $PtCu_{300}$ particles post-digestion with aqua regia with the observed weight percent shown of Pt and Cu for each nanoparticle.

6.5.2.2 Probe molecule CO FTIR

Based on previous studies, it was expected that dopant Pt atoms would have a mild driving force to segregate to the surface of a Cu host nanoparticle.[5] However, the introduction of CO to the PtCu alloy was expected to significantly increase the propensity of Pt to surface segregate.[5–7] In situ CO probe molecule IR was employed to study these two phenomena by effectively identifying Pt species on the surface of the Cu nanoparticle. First the PtCu alloy catalysts were reduced in-situ at 400 °C in 10% H_2/Ar (50 mL min^{-1}) for 1 hour. The sample was then cooled to 25 °C in Ar (50 mL min^{-1}) and after reaching the desired temperature, a background spectrum was collected. Next, 10% CO/Ar (50 mL min^{-1}) was flowed over the catalyst bed for 30 minutes at 25 °C. Following the CO treatment, Ar was flowed to purge the catalyst of any gas phase or weakly bound physisorbed CO species. Subsequent IR spectra were collected after 5 and 20 minutes of purging under Ar. Next, the catalyst bed temperature was raised to 50 °C and held, under CO, at 50 °C for 30 minutes, after which the catalyst was cooled back to 25 °C, Ar purge

was introduced, and the analogous spectra were taken as described above. These steps were repeated for CO treatments at 100 °C and 200 °C, respectively.

The results of the CO treatment experiments for $PtCu_{15}$ and $PtCu_{300}$ loaded on γ-Al_2O_3 are shown in Figures 6.1 and 6.2, respectively. Figure 6.1 (a) shows spectra after a 5 minute Ar purge for $PtCu_{15}$ for which a CO stretch at 2053 cm^{-1}, assigned to small Pt ensembles on the Cu surface,[8–10] is observed with CO treatment at all four measured temperatures (25, 50, 100, and 200 °C). After 200 °C treatment, a second IR stretch at 2020 cm^{-1} is observed, which has been assigned to atomically dispersed Pt particles on the Cu surface.[8,9,11] Purging in Ar for 20 minutes, see Figure 6.1 (b), shows that CO bound to Pt with a vibrational frequency of 2152 cm^{-1} is resistant to the inert purge while the CO-Pt stretch at 2020 cm^{-1} disappears with extended purge time. These observations further support the previous CO-Pt site assignments as CO adsorbed to small Pt nanoparticles is known to be thermally resistant up to 200 °C.[12] On ther other hand, atomically dispersed Pt is expected to be well coordinated to neighboring Cu atoms, making the corresponding Pt-CO bond quite weak, as has been shown for atomically dispersed Pt that is well-coordinated to metal oxide supports.[12,13] Figure 6.2 shows analogous spectra for $PtCu_{300}$, for which CO adsorbed to small Pt ensembles (2053 cm^{-1}) and to atomically dispersed Pt (2022 cm^{-1}) is visible after CO treatment at all temperatures. Similar to $PtCu_{15}$, after 200 °C treatment a large number of atomically disprsed Pt segregated to the surface of $PtCu_{300}$, as seen by a significant growth of the Pt-CO band at 2022 $cm^{-1.}$ Note the relative resistance to the Ar purge was similar for $PtCu_{300}$ compared to $PtCu_{15}$, as CO bound to small Pt ensembles was resistant to the Ar purge while CO bound to the atomically dispersed Pt

atoms desorbed in an Ar environment at 25 °C. The results obtained through CO-IR suggest the PtCu alloy is dynamic in nature, particularly under reactive environments with surface segregation of small Pt ensembles occuring at lower CO treatment temperatures than that of atomically dispersed Pt atoms.

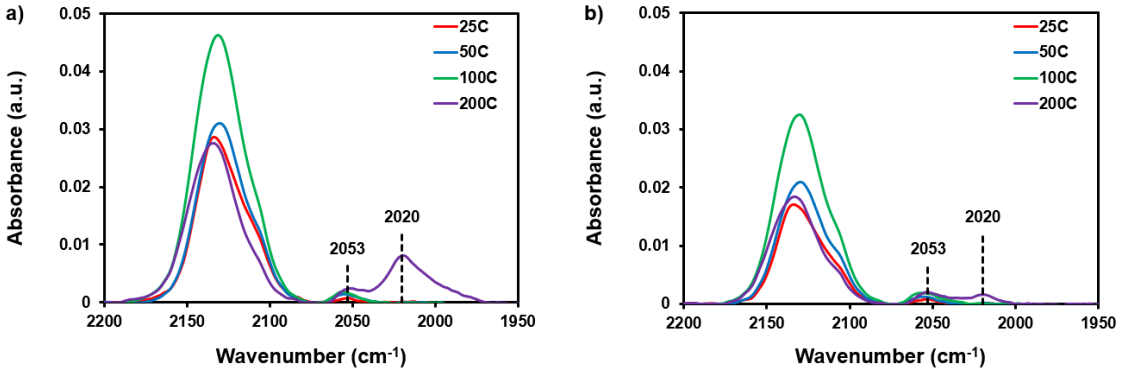

Figure 6.1 In situ IR spectra of CO adsorbed at 25 °C and at saturation coverage after a 5-minute Ar purge (a) and a 20-minute Ar purge (b) on $PtCu_{15}$ loaded on γ-Al2O3 with varying in situ CO treatment temperatures. $PtCu_{15}$ was pre-treated in situ by 400 °C reduction. Note, these IR spectra were recorded before the XAS experiments.

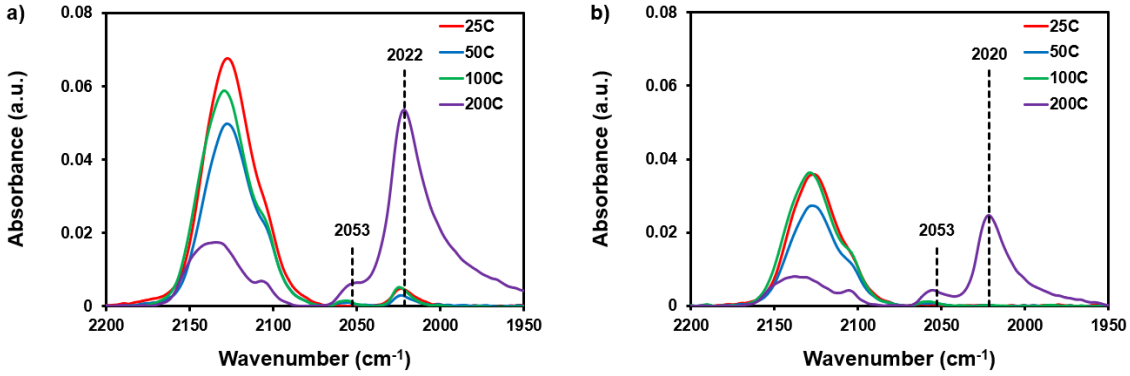

Figure 6.2 In situ IR spectra of CO adsorbed at 25 °C and at saturation coverage after a 5-minute Ar purge (a) and a 20-minute Ar purge (b) on $PtCu_{300}$ loaded on γ-Al_2O_3 with varying in situ CO treatment temperatures. $PtCu_{300}$ was pre-treated in situ by 400 °C reduction. Note, these IR spectra were recorded before the XAS experiments.

6.5.2.3 X-ray absorption spectroscopy

X-ray absorption spectroscopy was employed to identify the oxidation state of Pt with XANES and Pt-Pt and Pt-Cu coordination with EXAFS. Monitoring the oxidation

state of Pt before any reductive pre-treatment would provide preliminary evidence of the location of Pt after the alloy synthesis through galvanic replacement. For example, if the Pt atoms are cationic, it would be indicative of Pt being at the surface of Cu, as it would have become oxidized from the ambient environment. However, if the Pt atoms are metallic, then they reside in the Cu sub-surface as bulk oxidation would not have occurred under ambient conditions. The XANES spectra in Figure 6.3 (a) of the $PtCu_{50}$ after degassing in He at 50 °C for 30 minutes reveals that the Pt atoms are metallic when comparing the sample's white line intensity to that of the Pt foil reference. Previous studies have shown how the white line intensity of Pt is quite large when Pt is either in the Pt^{2+} or Pt^{4+} state.[12,13] In Figure 6.3 (a), the white line intensity of $PtCu_{15}$ is quite low and comparable to the metallic Pt foil reference. This suggests that in $PtCu_{15}$'s native (non-treated) state, Pt sits below the Cu surface and is thus resistant to surface oxidation by the ambient environment.

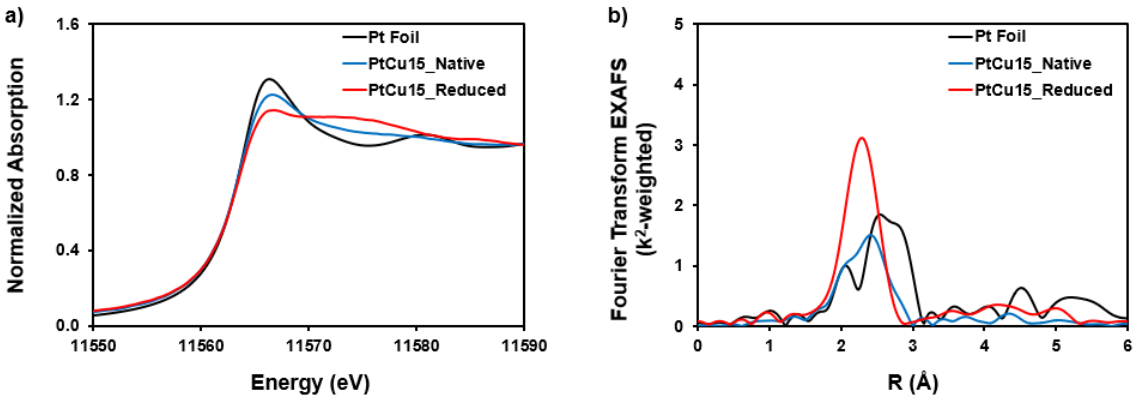

Figure 6.3 XAS of $PtCu_{50}/Al_2O_3$ catalysts. (a) XANES and (b) EXAFS spectra collected at 50 °C immediately following $PtCu_{15}$ degassing in He, labelled "$PtCu_{15}$_Native", and immediately following $PtCu_{15}$ reduction at 350 °C, labelled "$PtCu_{15}$_Reduced".

EXAFS was employed to establish the existence of and any potential changes of the coordination number of Pt-Pt, Pt-Cu, and Pt-O bonds. Based on the XANES spectra in

Figure 6.3, it was expected that no Pt-O contribution should have been observed as Pt was in the metallic state upon synthesis and then would be treated under reductive environments during XAS experiments. On the other hand, it was expected that the total Pt coordination (Pt-Pt + Pt-Cu) should change with varying CO pretreatment temperatures as Pt atoms segregate to the surface. Comparing $PtCu_{15}$ to the Pt foil, suggests that there is no Pt-O coordination for the catalyst (expected bond length of 1.9-2.0 Å), providing further evidence that Pt prefers to sit in the sub-surface layer of° the Cu nanoparticles. Additionally, the EXAFS of $PtCu_{15}$ showed only a small Pt-Pt coordination (2.5 – 2.8 Å) in the native state, suggesting that atomically dispersed Pt atoms are the dominant Pt species in the alloy. Upon reduction of $CuPt_{15}$ at 350 °C, the XANES and EXAFS regions are both modified with the EXAFS showing towards shorter bond lengths (2.3 Å), which is preliminary assigned to the formation of new Cu-Pt bonds, suggesting that reduction of the $PtCu_{15}$ in H_2 gas promoted metal alloying, potentially helping to form atomically dispersed Pt species from small Pt ensembles in the Cu nanoparticle bulk. Note that all Pt bond assignments in EXAFS were performed without proper fitting of the spectra and thus represent tentative or preliminary results. Future work with analogous systems would employ rigorous fitting of EXAFS spectra to approximate Pt coordination number to different atoms (O, Cu, and Pt).

Next, corresponding XANES and EXAFS measurements were performed over $PtCu_{15}$ after treatment in CO at 50 °C and 200 °C, see Figure 6.4, with treatment that was identical to that conducted for CO-IR studies shown in Figures 6.1 and 6.2. Since the CO-IR results suggested that treating $PtCu_{15}$ in CO worked to induce Pt surface segregation,

we expected the EXAFS spectra to change as the Pt coordination number would decrease once it diffused to the Cu surface. The change would be more significant after CO treatment at 200 °C as was observed in the CO-IR experiments, see Figure 6.2. Unfortunately, XAS data showed no difference in the local Pt structure after reducing the catalyst and then treating it in CO for 30 minutes. One possible reason for the inconsistency in the results is the change in IR spectra after CO treatment are quite small and would be quite difficult to deconvolute with XAS. However, it has not only been challenging to synthesize reproducible PtCu alloys, but, as shown in Figure 6.5, we have not been able to achieve consistent CO-IR results even after a second run of the same catalyst batch. It should also be noted that XAS spectra for $PtCu_{300}$ were not completed due to a time constriction while visiting the beam-line facility as the unexpectedly low signal-to-noise ratio of the spectra required more beam time than was allotted.

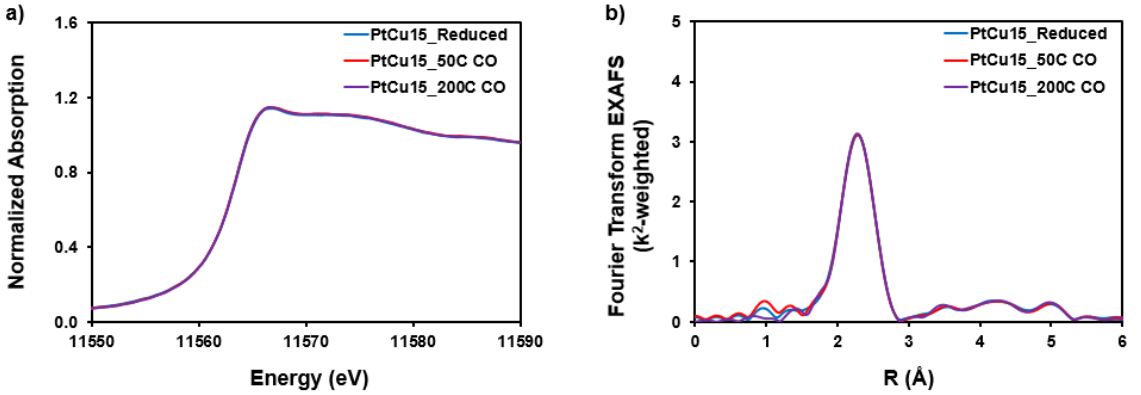

Figure 6.4 XAS of $PtCu_{50}/Al_2O_3$ catalysts. (a) XANES and (b) EXAFS spectra collected at 50 °C immediately following $PtCu_{15}$ reduction at 350 °C, CO treatment at 50 °C, and CO treatment at 200 °C. Note the three spectra are nearly identical and lie on top of each other, particularly in the XANES region.

Due to the inconsistency of the results between CO-IR and XAS experiments, CO-IR of the same batch of $PtCu_{15}$ and $PtCu_{300}$ were taken after returning from the beam-line facility. What was immediately clear, is the CO-IR spectra varied significantly when taken

for the same batch of catalysts before or after the XAS experiments. For $PtCu_{15}$, Pt-CO stretches at 2050 cm^{-1} and 2021 cm^{-1} were qualitatively similar to those of $PtCu_{15}$ spectra taken previously, after CO treatment at 200 °C. The major differences for the spectra of $PtCu_{15}$ is the small changes in the Pt-CO stretches with CO treatment at 50 °C and 200 °C and the significantly reduced Cu-CO stretches visible in the 2100-2150 cm^{-1} range. Analogous similarities and differences are observed for the $PtCu_{300}$ alloy before and after XAS experiments with Pt-CO stretches being qualitatively similar as to the first IR experiment, but with Cu-CO stretches being significantly diminished. Though we currently do not have an explanation for these observed changes, the results do suggest that the PtCu alloys may have undergone structural changes, which also may have impacted the XAS measurements. Consequently, future experiments will have a particular focus on creating reproducible PtCu alloys both in terms of the synthesis technique and the corresponding characterization. This will then provide a pathway for understanding future XAS measurements, which are expected to provide important evidence of Pt segregation to the Cu surface under a CO environment.

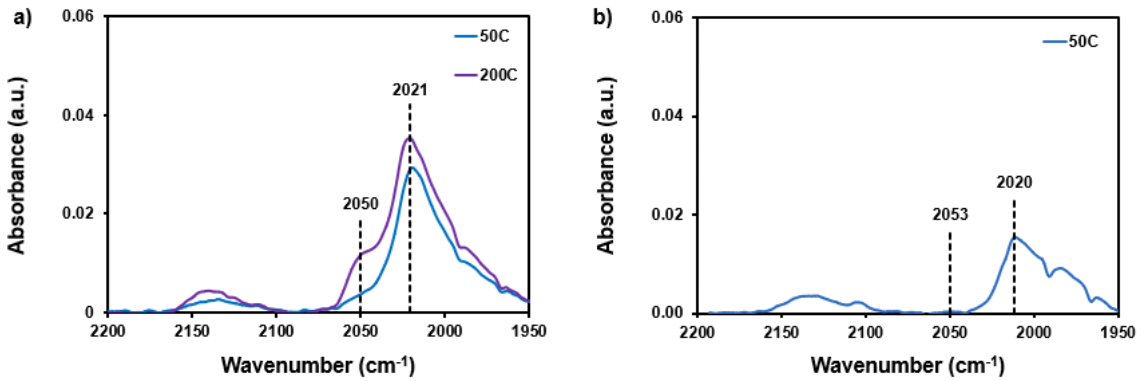

Figure 6.5. In situ IR spectra of CO adsorbed at 50 °C and at saturation coverage after a 5-minute Ar purge on a) $PtCu_{15}$ loaded on γ-Al_2O_3 with varying in situ CO treatment temperatures (50 °C and 200 °C) and b) $PtCu_{300}$ loaded on γ-Al_2O_3 with CO treatment at 50 °C. Both PtCu alloys were pre-treated in situ by 400 °C reduction. Note, these IR spectra were recorded after the XAS experiments.

6.6 Future outlook for Pt-Cu single atom alloys

The work with PtCu single atom alloys discussed in this chapter is incomplete and the following studies would be required to complete the story with the synthesis of PtCu single atom alloys and their impact on the selective conversion of ethyl acetate to diethyl ether through hydrogenolysis. The remaining studies are:

- Developing consistency with PtCu single atom alloy synthesis by observing consistency in alloy characterization using CO probe molecule IR and XAS studies
- Synthesizing a series of PtCu alloys with varying Pt loading to generate alloys that have exclusively atomically dispersed Pt atoms, a combination of atomically dispersed Pt and small Pt clusters, and majority Pt clusters.
- Measuring and comparing the CO probe molecule IR spectra as a function of CO treatment temperature for the alloys with different Pt loadings, as shown in Figures 6.2 and 6.5. These experiments are intended to probe the CO induced surface segregation of the dilute Pt species.

- If the surface segregation dynamics of the atomically dispersed Pt species and small Pt clusters are different then further characterization techniques would be employed to investigate the differences (XAS, CO-TPD, and DFT calculations)
- After achieving consistent PtCu syntheses with the corresponding characterization, the different materials will be tested in their ability to induce ethyl acetate conversion to diethyl ether. The expectation is that the PtCu with the atomically dispersed Pt species should provide the optimum conversion and selectivity towards diethyl ether formation as the Pt species will simply active H_2 gas, allowing the Cu surface to promote hydrogenolysis of ethyl acetate.
- Complete kinetics studies will be performed over each material including temperature, pressure, and Pt particle size dependent studies to gain a detailed understanding of the active site for the reaction as well as the corresponding turn over frequency.
- To summarize, completion of the work discussed in this chapter would help to elucidate the dynamic surface segregation of different sized Pt particles loaded on a larger Cu nanoparticle (PtCu single atom alloy). Then the alloys will be tested for the effective hydrogenolysis of ethyl acetate to diethyl ether, a potentially industrially relevant reaction pathway that is analogous to parts of the MTG (methanol-to-gasoline) process developed by Exxon-Mobil.

6.7 References

(1) Kyriakou, G.; Boucher, M. B.; Jewell, A. D.; Lewis, E. a; Lawton, T. J.; Baber, A. E.; Tierney, H. L.; Flytzani-stephanopoulos, M.; Sykes, E. C. H. Isolated Metal Atom Geometries as a Strategy for Selective Heterogeneous Hydrogenations. *Science* **2012**, *335*, 1209–1212.

(2) Lucci, F. R.; Marcinkowski, M. D.; Lawton, T. J.; Sykes, E. C. H. H2 Activation and Spillover on Catalytically Relevant Pt-Cu Single Atom Alloys. *J. Phys. Chem. C* **2015**, *119* (43), 24351–24357.

(3) Anger, G.; Winkler, A.; Rendulic, K. D. Adsorption and Desorption Kinetics in the Systems H2/Cu(111), H2/Cu(110) and H2/Cu(100). *Surf. Sci.* **1989**, *220* (1), 1–17.

(4) Seemala, B.; Cai, C. M.; Wyman, C. E.; Christopher, P. Support Induced Control of Surface Composition in Cu-Ni/TiO2 Catalysts Enables High Yield Co-Conversion of HMF and Furfural to Methylated Furans. *ACS Catal.* **2017**, *7* (6), 4070–4082.

(5) Darby, M. T.; Sykes, E. C. H.; Michaelides, A.; Stamatakis, M. Carbon Monoxide Poisoning Resistance and Structural Stability of Single Atom Alloys. *Top. Catal.* **2018**, *61* (5–6), 428–438.

(6) Simonovis, J. P.; Hunt, A.; Palomino, R. M.; Senanayake, S. D.; Waluyo, I. Enhanced Stability of Pt-Cu Single-Atom Alloy Catalysts: In Situ Characterization of the Pt/Cu(111) Surface in an Ambient Pressure of CO. *J. Phys. Chem. C* **2018**, *122* (8), 4488–4495.

(7) Oxford, S. M.; Lee, P. L.; Chupas, P. J.; Chapman, K. W.; Kung, M. C.; Kung, H. H. Study of Supported PtCu and PdAu Bimetallic Nanoparticles Using In-Situ X-Ray Tools. *J. Phys. Chem. C* **2010**, *114* (40), 17085–17091.

(8) Therrien, A. J.; Hensley, A. J. R.; Marcinkowski, M. D.; Zhang, R.; Lucci, F. R.; Coughlin, B.; Schilling, A. C.; McEwen, J. S.; Sykes, E. C. H. An Atomic-Scale View of Single-Site Pt Catalysis for Low-Temperature CO Oxidation. *Nat. Catal.* **2018**, *1* (3), 192–198.

(9) Sun, G.; Zhao, Z.-J.; Mu, R.; Zha, S.; Li, L.; Chen, S.; Zang, K.; Luo, J.; Li, Z.; Purdy, S. C.; et al. Breaking the Scaling Relationship via Thermally Stable Pt/Cu Single Atom Alloys for Catalytic Dehydrogenation. *Nat. Commun.* **2018**, *9* (1), 4454.

(10) Chandler, B.; Pignolet, L. DRIFTS Studies of Carbon Monoxide Coverage on Highly Dispersed Bimetallic Pt-Cu and Pt-Au Catalysts. *Catal. Today* **2002**, *65* (1), 39–50.

(11) M.J.Kappers; Maas, J. H. van der. Correlation between CO Frequency and Pt Coordination Number. A DRIFT Study on Supported Pt Catalysts. *Catal. Letters* **1991**, *10*, 365–374.

(12) DeRita, L.; Dai, S.; Lopez-Zepeda, K.; Pham, N.; Graham, G. W.; Pan, X.; Christopher, P. Catalyst Architecture for Stable Single Atom Dispersion Enables

Site-Specific Spectroscopic and Reactivity Measurements of CO Adsorbed to Pt Atoms, Oxidized Pt Clusters, and Metallic Pt Clusters on TiO2. *J. Am. Chem. Soc.* **2017**, *139* (40), 14150–14165.

(13) DeRita, L.; Resasco, J.; Dai, S.; Boubnov, A.; Thang, H. V.; Hoffman, A. S.; Ro, I.; Graham, G. W.; Bare, S. R.; Pacchioni, G.; et al. Structural Evolution of Atomically Dispersed Pt Catalysts Dictates Reactivity. *Nat. Mater.* **2019**.

Appendix

A.1 Reaction Mechanism Derivation (C-H Abstraction as RLS)

$$1.\ CH_3CH_2OH(g) + *_{acid} \overset{K_1}{\rightleftharpoons} CH_3CH_2OH\ *_{acid}$$

$$2.\ CH_3CH_2OH\ *_{acid} + *_{base} \overset{K_2}{\rightleftharpoons} CH_3CH_2O\ *_{acid} + H\ *_{base}$$

$$3.\ CH_3CH_2O\ *_{acid} + *_{Cu} \overset{K_3}{\rightleftharpoons} CH_3CH_2O\ *_{Cu} + *_{acid}$$

$$4.\ CH_3CH_2O\ *_{Cu} + *_{Cu} \xrightarrow{k_4} CH_3CHO\ *_{Cu} + H\ *_{Cu}$$

$$5.\ CH_3CHO\ *_{Cu} \overset{K_5}{\rightleftharpoons} CH_3CHO(g) + *_{Cu}$$

$$6.\ H\ *_{base} + *_{Cu} \overset{K_6}{\rightleftharpoons} H\ *_{Cu} + *_{base}$$

$$7.\ 2H\ *_{Cu} \overset{K_7}{\rightleftharpoons} H_2(g) + 2\ *_{Cu}$$

Rate Expression: $\text{rate} = k_4[EtO\ *_{Cu}][*_{Cu}]$

Intermediates:

$$[EtOH\ *_{acid}] = K_1 P_{EtOH}[*_{acid}]$$

$$[EtO\ *_{acid}] = K_2 \frac{[EtOH\ *_{acid}][*_{base}]}{[H\ *_{base}]} = K_1K_2K_6K_7^{1/2} \frac{P_{EtOH}}{P_{H_2}^{1/2}}[*_{acid}]$$

$$[EtO\ *_{Cu}] = K_3 \frac{[EtO\ *_{acid}][*_{Cu}]}{[*_{acid}]} = K_1K_2K_3K_6K_7^{1/2} \frac{P_{EtOH}}{P_{H_2}^{1/2}}[*_{Cu}]$$

$$[Acet\ *_{Cu}] = \frac{1}{K_5} P_{AcetH}[*_{Cu}]$$

$$[H\ *_{base}] = \frac{1}{K_6K_7^{1/2}} P_{H_2}^{1/2}[*_{base}]$$

$$[H\ *_{Cu}] = \frac{1}{K_7^{1/2}} P_{H_2}^{1/2}[*_{Cu}]$$

Rate Expression:

$$\text{rate} = k_4[\text{EtO}*_{\text{Cu}}][*_{\text{Cu}}] = k_4 K_1 K_2 K_3 K_6 K_7^{1/2} \frac{P_{\text{EtOH}}}{P_{H_2}^{1/2}} [*_{\text{Cu}}]^2$$

$$[*_{\text{Cu}}] = \left(1 + K_1 K_2 K_3 K_6 K_7^{1/2} \frac{P_{\text{EtOH}}}{P_{H_2}^{1/2}} + \frac{1}{K_5} P_{\text{AcetH}} + \frac{1}{K_7^{1/2}} P_{H_2}^{1/2}\right)^{-1}$$

Assumptions:

- No significant H surface coverage, so $\left(\frac{1}{K_7^{1/2}} P_{H_2}^{1/2}\right) = 0$
- No significant acetyl coverage, so $\left(\frac{1}{K_5} P_{\text{AcetH}}\right) = 0$
- $P_{\text{Acet}} = P_{H_2}$ (1:1 stoichiometry)
- $K_{\text{eff}} = K_1 K_2 K_3 K_6 K_7^{1/2}$

$$\text{rate} = \frac{k_4 K_{\text{eff}} \frac{P_{\text{EtOH}}}{P_{H_2}^{1/2}}}{\left(1 + K_{\text{eff}} \frac{P_{\text{EtOH}}}{P_{H_2}^{1/2}}\right)^2} \qquad \textbf{Equation 4.1}$$

*Note that fits are shown in Chapter 4, Figure 4.21 (a) and (b).

A.2 Reaction Mechanism Derivation (O-H Abstraction as RLS)

$$1.\ CH_3CH_2OH(g) + *_{acid} \overset{K_1}{\rightleftharpoons} CH_3CH_2OH\ *_{acid}$$

$$2.\ CH_3CH_2OH\ *_{acid} + *_{base} \xrightarrow{k_2} CH_3CH_2O\ *_{acid} + H\ *_{base}$$

$$3.\ CH_3CH_2O\ *_{acid} + *_{Cu} \overset{K_3}{\rightleftharpoons} CH_3CH_2O\ *_{Cu} + *_{acid}$$

$$4.\ CH_3CH_2O\ *_{Cu} + *_{Cu} \overset{K_4}{\rightleftharpoons} CH_3CHO\ *_{Cu} + H\ *_{Cu}$$

$$5.\ CH_3CHO\ *_{Cu} \overset{K_5}{\rightleftharpoons} CH_3CHO(g) + *_{Cu}$$

$$6.\ H\ *_{base} + *_{Cu} \overset{K_6}{\rightleftharpoons} H\ *_{Cu} + *_{base}$$

$$7.\ 2H\ *_{Cu} \overset{K_7}{\rightleftharpoons} H_2(g) + 2\ *_{Cu}$$

Rate Expression: $\text{rate} = k_2[EtOH\ *_{acid}][*_{base}]$

Intermediates:

$$[EtOH\ *_{acid}] = K_1 P_{EtOH}[*_{acid}]$$

$$[EtO\ *_{acid}] = \frac{1}{K_3}\frac{[EtO\ *_{Cu}][*_{acid}]}{[*_{Cu}]} = \frac{1}{K_3K_4K_5K_7^{1/2}} P_{Acet} P_{H_2}^{1/2}[*_{acid}]$$

$$[EtO\ *_{Cu}] = \frac{1}{K_4}\frac{[Acet\ *_{Cu}][H\ *_{Cu}]}{[*_{Cu}]} = \frac{1}{K_4K_5K_7^{1/2}} P_{Acet} P_{H_2}^{1/2}[*_{Cu}]$$

$$[Acet\ *_{Cu}] = \frac{1}{K_5} P_{AcetH}[*_{Cu}]$$

$$[H\ *_{base}] = \frac{1}{K_6K_7^{1/2}} P_{H_2}^{1/2}[*_{base}]$$

$$[H\ *_{Cu}] = \frac{1}{K_7^{1/2}} P_{H_2}^{1/2}[*_{Cu}]$$

Rate Expression:

$$\text{rate} = k_2[\text{EtOH}*_{\text{acid}}][*_{\text{base}}] = k_2 K_1 P_{\text{EtOH}}[*_{\text{acid}}][*_{\text{base}}]$$

$$[*_{\text{acid}}] = \left(1 + K_1 P_{\text{EtOH}} + \frac{1}{K_3 K_4 K_5 K_7^{1/2}} P_{\text{Acet}} P_{H_2}^{1/2}\right)^{-1}$$

$$[*_{\text{base}}] = \left(1 + \frac{1}{K_6 K_7^{1/2}} P_{H_2}^{1/2}\right)^{-1}$$

Assumptions:

No significant H surface coverage, so $\left(\frac{1}{K_6 K_7^{1/2}} P_{H_2}^{1/2}\right) = 0$

$P_{\text{Acet}} = P_{H_2}$ (1:1 stoichiometry)

$$K_{\text{eff}} = K_3 K_4 K_5 K_7^{1/2}$$

$$\text{rate} = \frac{k_2 K_1 P_{\text{EtOH}}}{\left(1 + K_1 P_{\text{EtOH}} + \frac{1}{K_{\text{eff}}} P_{H_2}^{3/2}\right)(1)}$$

Fitting the above rate expression to experimental data in Figure 4.18a, gave Keff values that were very large (~ 10^7). Applying these values of K_{eff} to EtO*$_{acid}$ showed values that approached 0. Therefore, the surface coverage of ethoxy over both the acid and Cu sites was assumed to be negligible, which is a reasonable assumption when the rate limiting step is O-H abstraction. Therefore, an additional assumption was applied to equation S1:

- No significant ethoxide coverage over support, so $\left(\frac{1}{K_{\text{eff}}} P_{\text{Acet}} P_{H_2}^{1/2}\right) = 0$

$$\text{rate} = \frac{k_2 K_1 P_{\text{EtOH}}}{(1 + K_1 P_{\text{EtOH}})(1)} = \frac{\mathbf{k_2 K_1 P_{EtOH}}}{(\mathbf{1 + K_1 P_{EtOH}})} \qquad \textbf{Equation 4.2}$$

*Note that fits are shown in Chapter 4, Figure 4.22 (a) and (b).